Final Report for NASA Langley Grant NAG-1-1201: Hot Film Wall Shear Instrumentation for Compressible Boundary Layer Transition Research

Principal Investigator:
Steven P. Schneider
Assistant Professor of Aerodynamics
School of Aeronautics and Astronautics
Purdue University
West Lafayette, IN 47907-1282

Period Covered: 1/1/91 to 11/1/92

Project Summary

Experimental and analytical studies of hot film wall shear instrumentation were performed. A new hot film anemometer was developed and tested. The anemometer performance was not quite as good as that of commercial anemometers, but the cost was much less and testing flexibility was improved. The main focus of the project was a parametric study of the effect of sensor size and substrate material on the performance of hot film surface sensors. Both electronic and shock-induced flow experiments were performed to determine the sensitivity and frequency response of the sensors. The results are presented in Micheal Moen's M.S. thesis, which is appended. A condensed form of the results has also been submitted for publication.

Publications

- *Design, Testing, and Analysis of a High-Speed, Time-Resolved Non-Intrusive Skin Friction Sensor System*, by Micheal J. Moen, M.S. Thesis, School of Aeronautics and Astronautics, Purdue University, December, 1992. 195 pages.

- *The effect of sensor geometry and substrate properties on the performance of flush-mount hot film gauges*, by Micheal J. Moen and Steven P. Schneider, submitted to the Third International Symposium on Thermal Anemometry, ASME Fluids Engineering Division Summer Meeting, Washington, DC, June 1993. To be submitted for journal publication.

Appendix

Micheal Moen's thesis is appended, so that it can be made more generally available.

DESIGN, TESTING AND ANALYSIS OF A HIGH-SPEED, TIME-RESOLVED NON-INTRUSIVE SKIN FRICTION SENSOR SYSTEM

A Thesis

Submitted to the Faculty

of

Purdue University

By

Michael Jon Moen

In Partial Fulfillment of the

Requirements for the Degree

of

Master of Science in Aeronautics and Astronautics

December, 1992

ACKNOWLEDGMENTS

The author would like to thank his major professor, Dr. Steven P. Schneider for providing the opportunity to participate in this research. Gratitude is due to the three members of the academic committee, Prof. Steven P. Schneider, Prof. John P. Sullivan and Prof. Mel R. L'Ecuyer for their highly useful input and insight as well as the reading and review of this thesis. Thanks are also extended to Jim Bartlett and his crew at NASA LaRC for their time spent on sensor production, Michael Scott of NASA LaRC for his assistance in the debugging of the sensor system and the members of the machine and electronics staff in the Aerospace Sciences Lab for their continuous help and support. And of course, the author's thanks go out to his many friends and family who provided unending support and encouragement through the good and difficult times of performing this work.

Partial funding for this project was supplied by the NASA LaRC Instrument Research Division under grant NAG-1-1201.

TABLE OF CONTENTS

Page

LIST OF TABLES

LIST OF FIGURES

Figure Page

Figure Page

Figure Page

Figure Page

Appendix
Figure

Appendix
Figure Page

ABSTRACT

Moen, Michael Jon. M.S.A.A., Purdue University, December 1992. Design, Testing and Analysis of a High-Speed, Time-Resolved Non-Intrusive Skin Friction Sensor System. Major Professor: Steven P. Schneider.

While hot wires and cylindrical hot films can obtain fairly high frequency response on the order of 10^5 Hz, flush-mount hot films lag in their relative performance due to the fact that the film is deposited upon a heat conducting substrate. Sensitivity and frequency response of a flush-mount sensor will vary widely depending upon what substrate material (thermal properties) and sensor geometry are chosen. In this research, a flush-mount hot film anemometer system is the subject of a parametric study in order to provide data on the effects of sensor dimension and substrate material for different operational principles so that both the qualitative and quantitative capabilities of a flush-mount sensor may be increased. The parametric study is performed by utilizing both electrical and flow testing. Electrical testing was performed as both voltage step testing and sine wave testing through the use of a function generator in order to optimize the system and obtain performance data. Velocity step testing was performed in a shock tube by passing a shock wave over a flat plate substrate with the flush-mounted sensor. Anemometer and flow conditions were varied to obtain data on frequency response as well as sensitivity. In most cases, results are presented in terms of frequency response and sensor power dissipation. In addition to studying the sensors, an constant temperature anemometer circuit is designed, built and optimized based on theoretical and experimental guidelines. Sample flow cases are analyzed for transition trends and skin friction according to Mirels' quasi-steady model for the boundary layer behind a normal

shock wave over a boundary. Also, an attempt is made to fit the quasi-steady anemometer shock response to steady heat transfer predictions by Kalumuck. Results for static (no-flow) and dynamic (flow) testing of identical aspect ratio sensors show that frequency response increases and sensitivity decreases as the sensor size is decreased. In terms of substrate material, the results show that for both the static and dynamic testing cases, frequency response increases and sensitivity decreases as the unsteady heat transfer parameter β of a homogeneous substrates in increased. A case is shown for a composite sensor where the loss in sensitivity is decreased by using a thermally thin insulating layer between the film and primary substrate, thereby improving the frequency response without sacrificing so much of the sensitivity.

1. INTRODUCTION

Anemometry has been used to characterize fluid flow and produce experimental fluid dynamic data since as early as the 1940's [24]. The first anemometer circuits were constant current circuits in which the frequency response of a hot wire was limited only by the thermal mass of the hot wire. However, with the advent of high speed integrated circuitry, anemometry has since turned to using constant temperature circuits that have much higher operational speeds as well as lower noise characteristics. This feature is desirable when trying to design an anemometer system with high sensitivity, which requires high signal to noise ratios.

One area of fluid mechanics that finds such a sensor useful is transitional flow. As a boundary layer goes from laminar to turbulent, an ordered process occurs that is called transition. Transition is characterized by an ordered breakdown to chaotic flow patterns. One of the ordered phenomena that occurs is called instability waves. In a supersonic boundary layer, instability waves can arise as fluctuations on the order of about one percent of the mean flow with frequencies ranging up around 1 MHz depending upon the Reynolds number of the flow and the thickness of the boundary layer among other properties. Hot wires have been used with some success in the past to detect such phenomena, but only to the order of 100 kHz. One of the largest drawbacks is that hot wires near the wall are intrusive devices, which is a problem of most methods of measuring skin friction and other near wall phenomena. This is where flush-mount hot films become desirable.

Though the flush-mount hot film is the best option for non-intrusive flow measurements, the major drawback of a flush-mount hot film is that the time constant is typically large and very dependent upon the substrate and sensor size. Frequency response performance of the flush-mount hot film is significantly degraded from that of the hot wire. In the past the useful limit of flush-mount films has been to measure the mean skin friction in fluid flow. If the frequency response of the flush-mount sensor can be improved through better understanding of interaction between the film and substrate, then this limitation can be removed and flush-mount films will become an important tool for making time resolved skin friction measurements in all types of flow conditions. The motivation, then, is to gain a better understanding of the electronic circuit interaction with the sensor, and to provide data on the effect of sensor dimension and substrate with the intention of designing a reliable non-intrusive sensor that is capable of making high speed, high-resolution measurements.

1.1. Objectives

The primary objective behind this research is to gain knowledge towards the development of a high-speed, time-resolved skin friction sensor that is capable of capturing small amplitude, high frequency flow phenomena, i.e., instability waves in the transitional compressible boundary layer. This will be done by performing one of the first parametric studies for thin film sensors that combines the use of both electrical testing with a function generator and flow testing with a shock tube intermittent flow facility. The parameters of interest that are varied are the sensor dimension and the sensor substrate material. The data provided will help to clear up the issue of how an anemometer behaves with different types of sensors as well as provide insight towards designing better flush-mount sensors.

Another objective throughout the course of this work is to optimize an anemometer system through the study of architectural changes and response tuning. Most anemometer analysis has been approached from a one-sided perspective of either electrical circuit theory or heat transfer and fluid mechanics. This thesis attempts to cover both bases by (1) designing the anemometer circuit and optimizing for frequency response and stability and (2) designing the sensors and comparing the results from both voltage and velocity step tests for variations in the sensor geometry and substrate material.

1.2. Thesis Organization

This thesis is organized into three main parts. The first part is a discussion of different theories that may pertain to understanding electrical and thermal characteristics of sensor and anemometer operations. In particular, theories are presented that might be useful in modeling the dynamic response of an anemometer circuit to velocity and voltage steps. Basic theories are also presented that might indicate how the substrate affects the thermal response of flush-mount sensors. Clearly, the interactions between the anemometer and sensor in terms of heat transfer, operational speed and operational stability can be quite complicated. In this light, some of the more basic theories are intended to be used only as a guide for system design rather than a basis of comparison for results. In addition, theory is also presented that models the flow regime behind a normal shock wave. This will become important in the case of velocity step testing utilizing the shock tube.

The second main part of the thesis is a discussion pertaining to anemometer architecture, circuit design and sensor design. It is within this section that the effects of different anemometer components were analyzed in order to understand what it would take to optimize the response of the anemometer. The anemometer went through three

primary evolutions that led to its final testing configuration. These architectural changes are presented and discussed along with experimental results of improved performance.

The third part of the thesis is a presentation of the results obtained through both electrical testing and flow testing. In some cases, responses to electrical testing are compared to theoretical models. In other cases, trends in the frequency response, sensitivity and heat transfer are noted for the array of sensors that were used for this research. The response of the sensor in the shock tube is compared to the skin friction predictions of other researchers. A calibration is then applied to an anemometer shock wave response in order to confirm suitable and repeatable operation of the flush-mount film anemometer system. Trends in frequency response and sensitivity are also shown for the array of sensors through the use of the shock tube. The study of the sensor in the shock tube serves to confirm results that were earlier indicated through electrical testing and provides a fairly comprehensive study on the effects of substrate and sensor dimension in the static and dynamic flow conditions.

2. THEORETICAL ANEMOMETER SYSTEM PERFORMANCE

2.1. Literature Search

Historically speaking, work with heated film elements dates back as early as 1931 with the work of Fage and Falkner [13] in which they demonstrated the feasibility of a film type device used to measure skin friction in the subsonic laminar boundary layer. Ludweig [24] carried this one step further by demonstrating a similar system's performance in the subsonic turbulent boundary layer. Enter Liepmann and Skinner [22] who in 1954 showed that a heat transfer type measuring device consisting of a small metal element imbedded in a substrate could be calibrated in the laminar regime and then successfully operated in the laminar as well as the turbulent boundary layer. Suddenly the heat transfer-type gage possessed a significantly wider operating range than two other common techniques of measuring skin friction: the Stanton tube or the floating wall element balance.

The use of anemometry has spanned several different uses from hot wires in subsonic and supersonic flows to hot films being used to detect transition points and transonic airfoil buffeting. While the applications of anemometry are widely varied, anemometry generally experiences two major obstacles across all applications: operational speed and system stability. Roberts et al. [33] used thin film heat transfer sensors to make convective heat transfer measurements in particle laden air within a shock tube. While he gave optimistic reviews for the upper frequency response of such instrumentation on the order of 10^6 Hz, he flatly stated that the performance was limited by low thermal conductivity of the substrate upon which the sensors had been deposited.

As the operational speed capability of electronic instrumentation increases, anemometry has become a reliable means of making measurements in intermittent flow facilities. Davies and Bernstein [10] used film sensors in a shock tube to study the heat transfer and transition to turbulence in a shock-induced boundary layer and Schneider [38] intends to use film type sensors to study boundary layer transition in a quiet flow Ludweig tube. As a result of the ever increasing interest in anemometry techniques, the interaction between the film or wire and the anemometer circuit in terms of speed and stability has become the subject of numerous studies.

Freymuth [16] presents a model for a generic anemometer that incorporates the Wheatstone bridge with the sensor, an amplifier, a capacitance and a test voltage. Using stability equations for the amplifier and bridge that he derived in earlier work, he presents a third order differential equation that models the hot wire anemometer system. This equation can be solved for either a velocity step or a voltage step applied to the system. Then through testing, he shows how the time constants can be backed out of the system. Freymuth also discusses that the hot wire anemometer analysis is not entirely appropriate for a surface mount hot film sensor. This was shown in work by Freymuth and Fingerson [18] in which the response of a conical film sensor to electrical testing was shown to deviate from the response of cylindrical sensors. This difference was attributed to the heat loss across the substrate to the adjacent surfaces upon which the sensor had been deposited. A one dimensional model of the losses was introduced by Bellhouse and Schultz [6] and this resulted in more work by Freymuth [17] in which he modeled non-cylindrical hot films by incorporating the Bellhouse-Schultz model. Freymuth finds that the behavior of a non-cylindrical hot film anemometer can be simulated through his analysis seen in the sine wave testing result. This is evidenced by a "bump" in the amplitude response curve at low frequencies and a decrease in the slope of amplitude response versus frequency plot at higher frequencies.

Work on the subject of anemometer circuitry has also been done by Watmuff. Watmuff [41] describes his system as a seventh order polynomial because he sees effects that are very non-third order while testing. In some of Watmuff's latest work, he presents stability plots for the different poles of the anemometer and shows where certain configurations will tend to become unstable. He describes the effect of offset voltage in the operational amplifier as well as inductance in the control of system stability and response shape with great detail. Both inductance and offset voltage can be tuned to increase the frequency response of the anemometer and tune the response to an optimal shape. The seventh order polynomial utilizes lumped inductive and capacitive elements that are explicitly represented in the coefficients of the polynomial. The result is a seventh order polynomial that accounts for the electrical anomalies that the third order theory does not. This is unlike Freymuth's theory in which all inductances and capacitances are lumped into one time constant that modifies the third order response.

Watmuff and Freymuth have a tendency to lean towards modeling the behavior of the anemometer circuit in terms of electrical stability and frequency response. In other cases, past work has leaned more towards modeling the anemometer system thermally by focusing on the heat transfer characteristics of the sensor. Kalumuck [21] provided a comprehensive steady state calculation of the heat transfer from a flush-mount hot film. His study incorporated a three-dimensional shear flow over a hot film on a semi-infinite substrate. He carried out the parametric study in terms of the conductivity ratio between the substrate and film, the aspect ratio of the sensor and the Peclet number of the flow. His results indicated that for an airflow over a sensor on a glass wall, a large portion of the substrate surface was heated. In addition he found that the conductivity ratio has a strong effect on how much of the heat generated by the sensor is lost to the substrate.

The interaction between the film and substrate is clearly an issue for the operation of the sensor as shown through the work of people such as Kalumuck. In some cases,

people have attempted to isolate the sensor from the substrate. Ajagu and Libby [2] designed a sensor that incorporated a hot wire mounted close to the substrate surface, and then a flush-mounted constant temperature guard heater beneath the hot wire. They reported success in the operational quality of the sensor in that it could be used to make measurements in a large range of flows. Ajagu and Libby only hinted though, as to what frequency response characteristics their sensor possessed and it appeared to be in the low kHz range. In another case, Houdeville et al. [19] eliminated the substrate heat transfer effect by using a surface level hot wire mounted over a small cavity on the substrate. Houdeville reported success in the use of the cavity gauge for both laminar and turbulent flows and their results indicated better frequency response characteristics than the stand flush-mounted hot film. However this did not make up for the increased complexity of sensor construction and fragility. Yet another attempt was made by Reda [32] at reducing heat transfer effects by actually insulating the film sensor and placing the substrate on a guard heater. His sensor consisted of a nickel film deposited on a Kapton film that was glued to a foam substrate. Reda concluded that the guard heater actually gave decreased frequency response performance and that the transient heat conduction in the substrate was still a limiting factor.

2.2. Theoretical Open Loop Thermal Response of Sensor

In order for an anemometer system to have a fast time response to a step change in conditions over the sensor surface, the sensor should have an inherently fast time response capability. The response time is dictated by the thermal mass of the sensor, and in the case of a shear wall sensor, the substrate upon which is sensor is deposited. The problem of determining thin film response can be approached utilizing fluids and heat transfer analysis. The major drawback to such analysis is that it entirely neglects the feedback of a constant temperature anemometer circuit. Therefore such an analysis is

considered to be an open loop analysis of the sensor transient response. The advantage in such an analysis is that it guides the choice of material for both the sensor and substrate.

In its most complex form, the heat transfer from the sensor is treated as an unsteady, three-dimensional problem in which the convection from the substrate and sensor surface is coupled to the conduction from the sensor to the substrate. The heat that is generated by the current, and the temperature coefficient of resistance for the metal film are important issues. In addition, the conductivity of the substrate as well as the corresponding heated footprint around the sensor will also effect the time response. Kalumuck [21] developed the first comprehensive steady, three dimensional film and substrate model, but it is computationally intensive and does not lend itself to a simple solution. However, Kalumuck's work does present some good points for comparison and discussion. In the following pages, the four different heat transfer models are presented and discussed. The purpose of the first three basic analyses is that, although physically incorrect, each analysis gives an insight as to how different film, substrate and film-substrate combinations behave with respect to their thermal time constants. Having this insight acts as a guide for what materials should be used for building a fast response flush-mount sensor. The three basic analyses are schematically represented in Figure 2.1 as well as the more complex three dimensional problem by Kalumuck.

2.2.1. Lumped Capacitance Film

Lumped capacitance is one way of dealing with the heat transfer problem for a body that experiences a sudden change in its thermal environment. Assuming that some body is initially at T_i, a convective condition with a temperature $T_\infty < T_i$ is imposed at time $t = 0$. The validity of the lumped capacitance method is dependent upon the Biot number, Bi. The Biot number is defined as the ratio of the conductive heat transfer resistance to the convective heat transfer resistance, which is shown in equation (2.1).

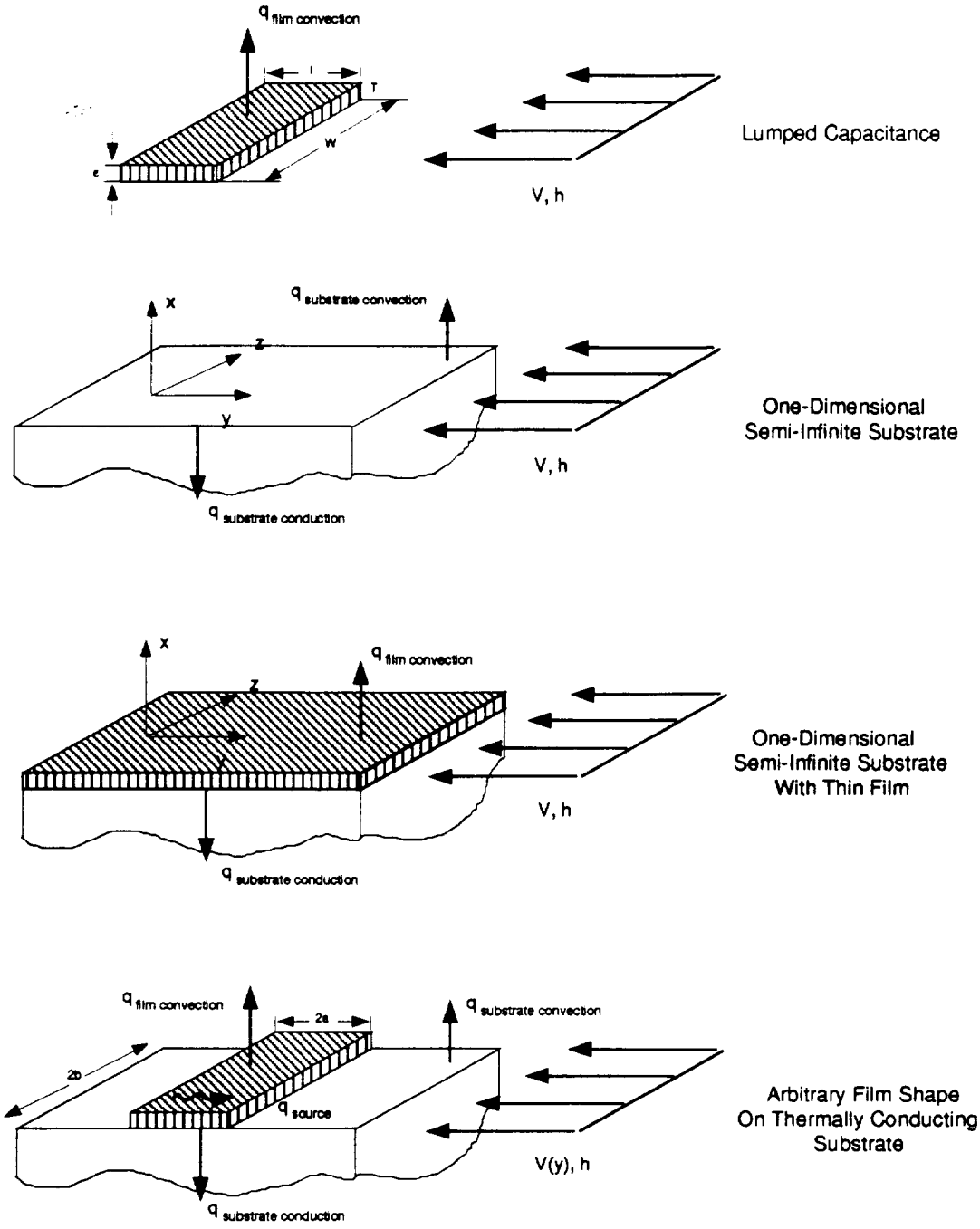

Figure 2.1. Four thermal models for the thin film sensor and the substrate (interacting and non-interacting)

$$Bi = \frac{R_{cond}}{R_{conv}} = \frac{(L/kA)}{(1/hA)} = \frac{hL}{k} \tag{2.1}$$

where h is the heat transfer coefficient, k is the thermal conductivity of the body, A is the surface area of the body and L is a characteristic length. In order for the lumped capacitance model to be deemed sufficient, the requirement must be met that

$$Bi = \frac{hL}{k} \leq 0.1 \tag{2.2}$$

For our thin film, we call the thickness, δ, the characteristic length. An h can be estimated using the simple flat plate laminar boundary layer analogy at a laminar Re in standard air

$$h_L = \frac{Nu_L k_{air}}{L} = 0.664 \frac{k}{L} Re_L^{0.5} Pr^{0.33} \tag{2.3}$$

which results in a Biot number of approximately Bi = 0.003 meaning that a lumped capacitance model could be valid for the transient response of the thin film. There are two major limitations in this case. The first is that lumped capacitance neglects any sort of temperature distribution within the body of question. Because the Biot number is small, it is generally acceptable to disregard temperature distributions within a body. Nonetheless, it is still a limitation. The second limitation is that lumped capacitance entirely neglects the presence of a substrate. The presence of a substrate will actually increase the time constant for film response to a step condition in temperature, so it is a necessary consideration when creating an accurate heat transfer model. What the lumped capacitance model is good for is that it clearly shows what sensor material responds the fastest to changes in its environment.

The lumped capacitance model according to Incropera and DeWitt [20] states that the transient temperature for a body at T_i with no heat generation experiencing a sudden change in thermal environment, T_∞, is given by

$$\frac{\Theta}{\Theta_i} = \frac{T - T_\infty}{T_i - T_\infty} = \exp\left(-\left(\frac{hA_s}{\rho Vc} \right) t \right) \tag{2.4}$$

Within this equation the thermal time constant is defined as

$$\tau_t = \frac{1}{hA_s} \rho Vc \tag{2.5}$$

or A_s and V cancel to leave a characteristic length of the sensor, L. Therefore the open loop response based on lumped capacitance is a function of the body dimensions and thermal capacity as well as the heat transfer coefficient. Since the heat transfer coefficient is defined as

$$h = h\ (Nu, Re, Pr) \tag{2.6}$$

it is obvious that the fluid mechanics associated with the problem have a significant effect on the open loop time response. For example, a smaller time constant is associated with a higher flow velocity. The time constant of equation (2.5) also indicates that smaller sensors will have smaller time constants due to the smaller thermal mass. In the Table 2.1 below, the open loop thermal time constant is listed for several different sensor materials.

Table 2.1. Thermal properties and open loop time constants of sensor material choices

Material	ρ (kg / m³)	C_p (J / kg K)	k (W / m K)	τ (s/m) h = 350	τ (s/m) h = 1000
Ni	8900	444	90.7	3.16×10^{-3}	1.11×10^{-3}
Cr	7160	449	93.7	2.57×10^{-3}	9.00×10^{-4}
Pd	12020	244	71.8	2.30×10^{-3}	8.05×10^{-4}
Pt	21450	133	71.6	2.28×10^{-3}	7.98×10^{-4}
W	19300	132	174	2.03×10^{-3}	7.10×10^{-4}
Au	19300	129	317	1.99×10^{-3}	6.97×10^{-4}

In Figure 2.2 that follows, the temperature transient for lumped capacitance analysis is shown for different film materials.

2.2.2. Semi-Infinite Substrate

This model is the other extreme of the lumped capacitance model in the sense that it models the semi-infinite substrate but neglects the presence of the thin film. The reason why there is any legitimacy to this approximation is that the film has a very small thickness and so it may be neglected in some cases. It is assumed that substrates with higher thermal conductivity allow shorter thermal response times for the flush-mount film than lower thermal conductivity substrates because the substrate is able to conduct heat away from the film faster. The assumption in this problem is that a substrate is at a temperature T_i. At an instant in time, t = 0, a temperature T_∞ is imposed as a convective boundary condition. Arts and Camci [1] give an equation that describes the temperature distribution throughout the body

$$\frac{T(x,t)-T_i}{T_\infty - T_i} = \operatorname{erfc}\left(\frac{x}{2\sqrt{\alpha t}}\right) - \left(\exp\left(\frac{hx}{k}+\frac{h^2\alpha t}{k^2}\right)\right)\left(\operatorname{erfc}\left(\frac{x}{2\sqrt{\alpha t}}+\frac{h\sqrt{\alpha t}}{k}\right)\right) \qquad (2.7)$$

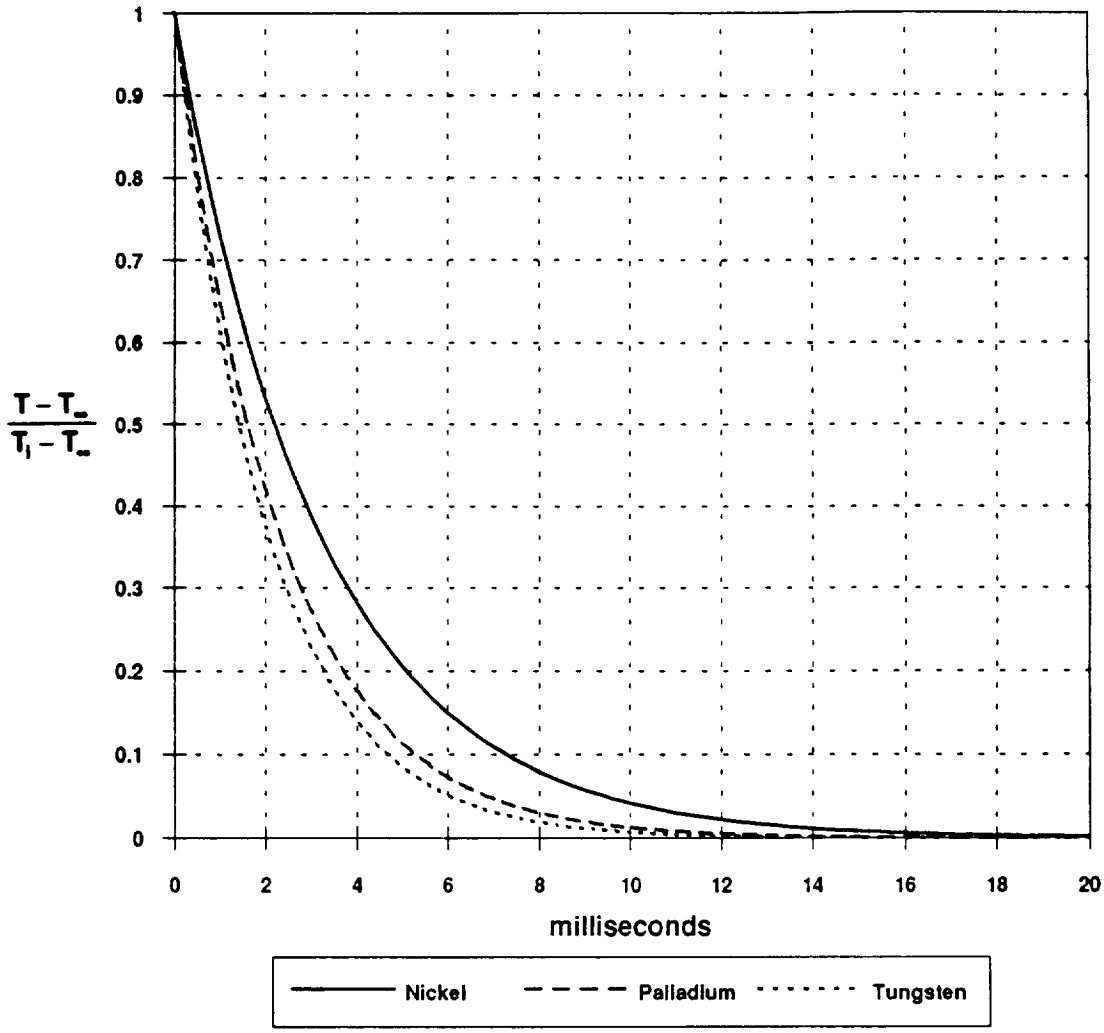

Figure 2.2. Open loop time response of a thin metal film subjected to a step in convective conditions based on lumped capacitance model

The only plane of interest is at the body surface, x = 0. Therefore, equation (2.8) simplifies to

$$\frac{T(0,t)-T_i}{T_\infty-T_i}=1-\left(\exp\left(\frac{h^2\alpha t}{k^2}\right)\right)\left(\operatorname{erfc}\left(\frac{h\sqrt{\alpha t}}{k}\right)\right) \qquad (2.8)$$

In Figure 2.3 below a plot is shown for the transient surface temperature of a semi-infinite body with a convective boundary condition. Even though the surface temperature appears to change faster for lower thermal conductivity substrates, the heat transfer rate is still higher for the whole body for higher thermal conductivity substrates.

2.2.3. One Dimensional Semi-Infinite Substrate With Film

Sandborn [37] suggests that for high frequency flow oscillations on the order of 10^5, the substrate will not affect the response of the sensor. This would seem to be true in the limit as no substrate will be able to conduct heat away from the sensor fast enough compared to the rate at which heat will be convected away. But like many other analyses, this does not take into consideration the feedback of an anemometer circuit. So neglecting circuit feedback, Sandborn's analysis shows what the film open loop response would be for different film-substrate combinations when subjected to a step change in the temperature.

For a transient operation estimation for high frequency response performance, Sandborn assumes a one dimensional heat transfer problem in which the substrate is treated as an infinitely thick substrate. At some time t = 0, a step in the convective heat transfer is imposed at the film surface. An additional assumption is made that thermal

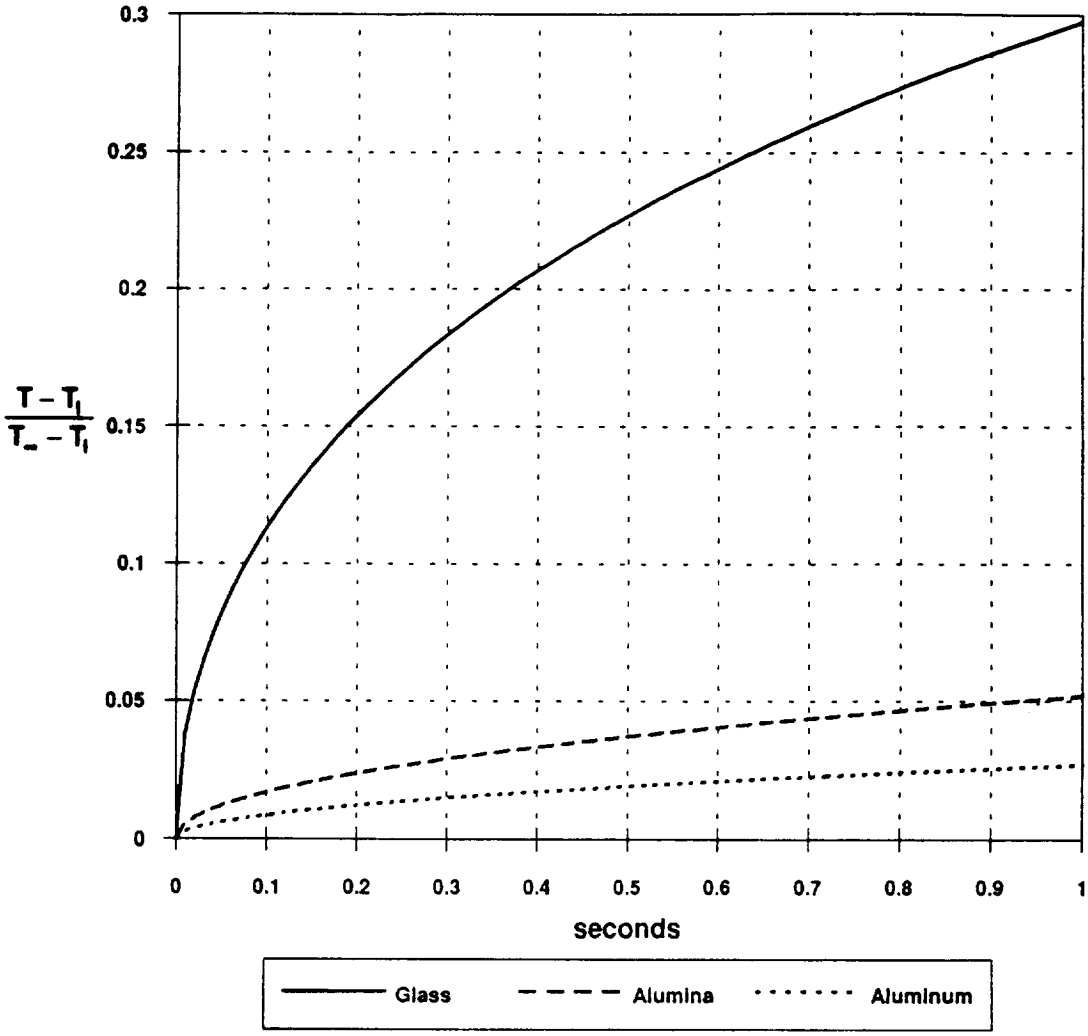

Figure 2.3. Open loop time response of a semi-infinite substrate subjected to a step in convective conditions

radiation between the fluid and the film is neglected. The film has thickness, δ, and goes from $0 < y < \delta$. The governing equation for the film is stated as

$$\frac{\partial T_f}{\partial t} = \frac{k_f}{\rho_f c_f}\frac{\partial^2 T_f}{\partial y^2} \tag{2.9}$$

where T for both the film and substrate is an incremental temperature above or below the initial temperature from time t = 0. The boundary conditions for the film are

$$\text{for } t < 0 \qquad T_f(y) = 0 \tag{2.10}$$

$$\text{for } t > 0 \text{ and } y = 0 \qquad \left(\frac{\partial T_f}{\partial y}\right)_{y=0} = -\frac{1}{k_f}\dot{q}(t)$$

The substrate, which is assumed to be a semi-infinite body, goes from $\delta < y < \infty$. The governing equation for the substrate is similar to the governing equation for the film and is given by

$$\frac{\partial T_s}{\partial t} = \frac{k_s}{\rho_s c_s}\frac{\partial^2 T_s}{\partial y^2} \tag{2.11}$$

and the boundary conditions for the substrate are

$$\text{for } t < 0 \qquad T_s(y) = 0 \tag{2.12}$$

$$\text{for } t > 0 \text{ and } y = \delta \qquad k_f\left(\frac{\partial T_f}{\partial y}\right)_{y=\delta} = k_s\left(\frac{\partial T_s}{\partial y}\right)_{y=\delta}$$

$$\text{and} \qquad T_f(\delta) = T_s(\delta)$$

$$\text{for } y \to \infty \qquad T_s \to 0$$

Through a Laplace transformation exact solutions are found for the temperature distribution in the film and substrate. However, a simplifying assumption is made that

the average film temperature is the same as the surface temperature at y = 0. Therefore, the solution is written for the film temperature as

$$T_f = \frac{1}{k_f}\sqrt{\frac{k_f}{\pi\rho_f c_f}}\int_0^t \frac{q(\lambda)}{\sqrt{t-\lambda}}d\lambda + \tag{2.13}$$

$$\frac{1}{k_f}\sqrt{\frac{k_f}{\pi\rho_f c_f}}\sum_{n=1}^{\infty} 2\sigma^n \int_0^t \frac{q(\lambda)}{\sqrt{t-\lambda}}\left(\exp\left(-\frac{\rho_f c_f n^2\delta^2}{k_f(t-\lambda)}\right)\right)d\lambda$$

where σ is defined as

$$\sigma = \frac{\sqrt{\frac{k_f\rho_f c_f}{k_s\rho_s c_s}} - 1}{\sqrt{\frac{k_f\rho_f c_f}{k_s\rho_s c_s}} + 1} \tag{2.14}$$

Equation (2.13) is expanded into a series where the higher order series terms δ^n are neglected due to the very small film thickness, δ. This results in the following equation

$$T_f = \frac{1}{\sqrt{\pi k_s\rho_s c_s}}\int_0^t \frac{q(\lambda)}{\sqrt{t-\lambda}}d\lambda - q(\lambda)\frac{\delta}{k_f}\left(\frac{k_f\rho_f c_f}{k_s\rho_s c_s} - 1\right) \tag{2.15}$$

A simplified case where a constant heat transfer boundary condition is held above the surface may be applied in order to plot a solution. The fact that the heat transfer is constant invalidates the solution from a standpoint of duplicating experimental results. In actuality, the heat transfer over the surface would decrease as the sensor is cooled off by the air flow. However, the solution still can duplicate trends in the effects of film and substrate material choices. The solution with a constant heat transfer can be represented by the equation

$$\frac{T_f}{q} = \frac{1}{\sqrt{\pi k_s \rho_s c_s}} \int_0^t \frac{d\lambda}{\sqrt{t-\lambda}} - \frac{\delta}{k_f}\left(\frac{k_f \rho_f c_f}{k_s \rho_s c_s} - 1\right) \tag{2.16}$$

and after integrating

$$\frac{T_f}{q} = \frac{2}{\sqrt{\pi k_s \rho_s c_s}} \sqrt{t} - \frac{\delta}{k_f}\left(\frac{k_f \rho_f c_f}{k_s \rho_s c_s} - 1\right) \tag{2.17}$$

Figure 2.4 below shows the effect of different film and substrate combinations on the thermal response to a step in the convective heat transfer. What this result seems to indicate is that regardless of the film material choice, the dominating effect is the substrate. The correction to the heat transfer that the film provides for this particular analysis does not have a large enough magnitude to significantly affect the heat transfer at the film thickness that is dealt with in this work. Unfortunately, this particular one dimensional theory is incapable of dealing with actual sensor dimension, therefore, it restricts the parametric analysis.

2.2.4. Kalumuck's Three Dimensional Film Model

Kalumuck [21] presents a comprehensive theory for the heat transfer from a flush-mount gage. His theory considers an arbitrarily shaped probe on a planar, thermally conducting substrate with an arbitrary heat source distribution exposed to a steady, uniform, incompressible shear flow. Kalumuck solves the complete three dimensional fluid and substrate energy equations in order to obtain the temperature and heat flux distributions for his parametric study. These are

$$\nabla^2 T_f - \frac{s}{\alpha} y \frac{\partial}{\partial x} T_f = 0, \quad y \geq 0 \tag{2.18}$$

$$\nabla^2 T_s = 0, \quad y \leq 0 \tag{2.19}$$

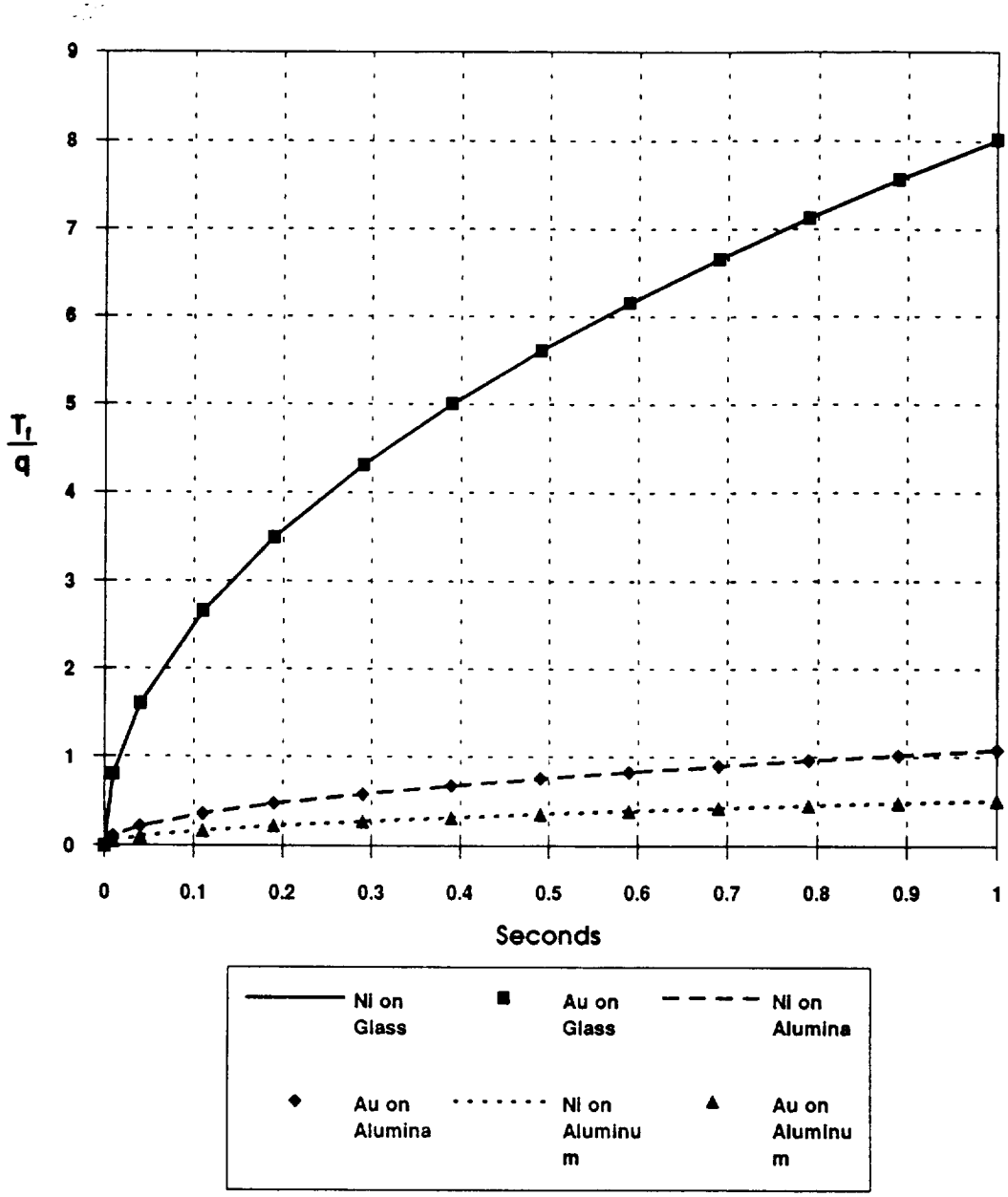

Figure 2.4. Open loop time response for different film substrate combinations subjected to a step in convective conditions based on one dimensional film and substrate model

where s is the fluid velocity gradient, α is the fluid thermal diffusivity and T_f, T_s are the temperatures measured above ambient for the fluid and substrate respectively. These equations are subject to the boundary conditions

$$T_f = T_s \quad \text{at} \quad y = 0 \tag{2.20}$$

$$k_s \frac{\partial T_s}{\partial y} - k_f \frac{\partial T_f}{\partial y} = Q(x,z) \quad \text{at} \quad y = 0 \tag{2.21}$$

$$T_f,\ T_s \rightarrow 0 \quad \text{as} \quad x,\ y \text{ or } z \rightarrow \pm\infty \tag{2.22}$$

where x is the streamwise direction, z is the spanwise direction and y is off the surface. Kalumuck presents his results mainly with respect to the flow Peclet number, sensor aspect ratio, and the conductivity ratio of the substrate to the fluid. The aspect ratio of a sensor is a ratio of the sensor spanwise half-width to the sensor streamwise half-length.

$$\text{Aspect Ratio} = \frac{b}{a} \tag{2.23}$$

The flow Peclet number is defined as

$$Pe = \frac{sL_p}{\alpha} \tag{2.24}$$

where s is the velocity gradient at the wall, L_p is the sensor streamwise length (characteristic length) and α is the fluid diffusivity. The conductivity ratio is a ratio of the substrate thermal conductivity to the fluid thermal conductivity.

$$K = \frac{k_s}{k_f} \tag{2.25}$$

Kalumuck's steady flow analysis cannot provide data on the open loop thermal response of a sensor, but it does provide useful information on the thermal distribution in the sensor and substrate. Alone, this information is useful, but combined with the experimental results of this thesis, the two parts together form a picture that is more clear than either of the individual results. Figure 2.5 is a plot from Kalumuck's work of the heat flux from the sensor surface to the fluid and the substrate for two different conductivity ratios. This theoretical result clearly shows that for a substrate with a higher thermal conductivity, more heat is transferred to the substrate and less heat is transferred to the fluid than sensors mounted on lower thermal conductivity substrates. This result becomes important later when looking at the experimental results of this thesis.

An additional parameter defined by Kalumuck is the sensor Nusselt number. This is defined by

$$Nu = \frac{P_s 2a}{4abk_f \overline{T_p}} \tag{2.26}$$

where P_s is the power dissipated by the sensor and $\overline{T_p}$ is the average sensor temperature. This definition of the Nusselt number can be used to show the change in the heat transfer with the change in shear. Adopting a similar definition to Kalumuck, the flow sensitive portion of the Nusselt number must be isolated. This can be done simply by subtracting off the portion of the Nusselt number that arises from conduction to the substrate.

$$Nu(Pe, K = 0) = Nu(Pe, K) - Nu(Pe = 0, K) \tag{2.27}$$

As a basis for comparison to theory, the flow sensitive Nusselt number can be plotted against the Peclet number. Both of these values are easily obtained in the lab setting. The sensor power dissipation to determine the Nusselt number may be found

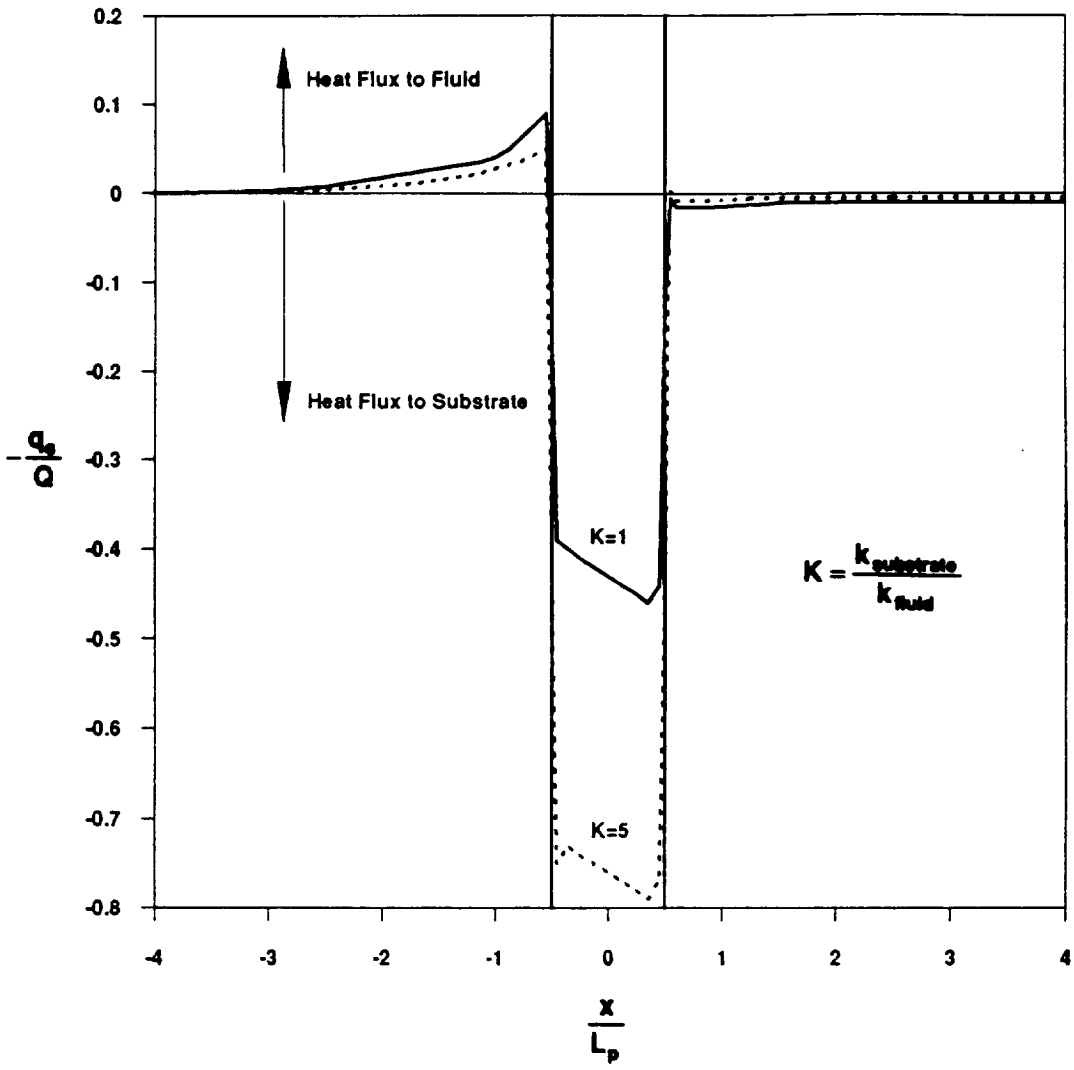

Figure 2.5. Heat flux distribution for flush-mount sensor on conducting substrate in fluid flow comparing different conductivity substrates (taken from Kalumuck)

from a simple bridge balance equation and the sensor temperature is determined through a calibration. The shear for the Peclet number is determined using theory presented by Mirels [27], which will further be discussed in Section 2.4.1.

2.3. Theoretical Feedback Frequency Response of Anemometer System

Much effort has been put into understanding the problems associated with the anemometer circuit such as feedback instabilities and frequency response limitations. Work done by Watmuff [41] and Perry and Morrison [31], shows that two of the most significant factors affecting frequency response and stability are the amplifier offset voltage and the bridge inductance. In general, increased bridge inductance increases the ringing frequency of what is typically described as a third order dynamic response, while increased amplifier offset voltage increases the decay time of the response. The anemometer response can be described as third order because it superimposes damped oscillations onto an exponential decay. Amplifiers with higher offset voltages will have a higher ringing frequency, but the actual frequency response is lower than the response of low offset voltage amplifiers due to the exponential decay of the signal. As the amplifier offset voltage is decreased to zero the anemometer response reaches a more optimum response with less exponential decay. Freymuth [16] presents a third order differential equation to describe the dynamic behavior of a constant temperature anemometer in response to either a voltage step or a velocity step. Freymuth pays more attention to an equation that is capable of optimizing the circuit and presents roots to his equation that model the optimum response to both voltage and velocity steps. Figure 2.6 schematically represents three different models that were employed in analyzing the performance of the anemometer for this work.

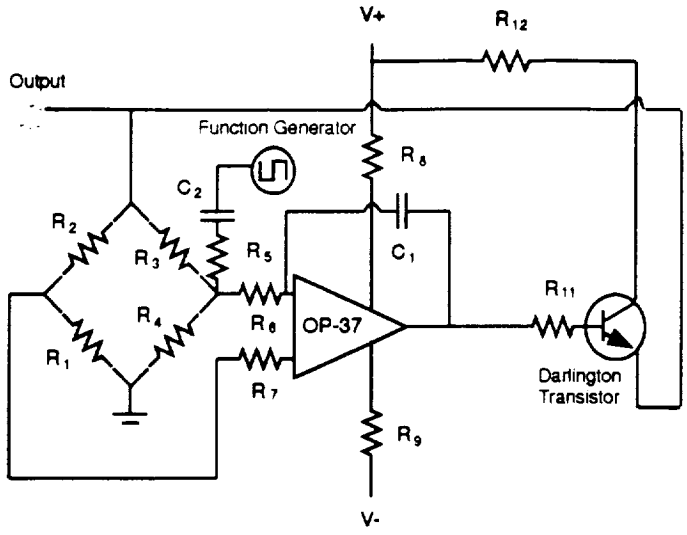

SPICE Model

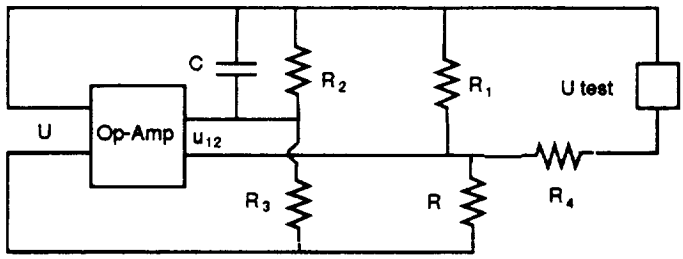

Freymuth's Third Order Model

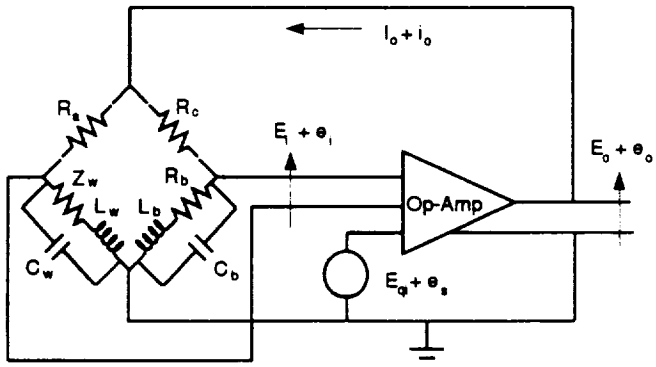

Watmuff's 7th Order Polynomial Model

Figure 2.6. Different electrical circuit models considered for performance analysis of anemometer circuit

2.3.1. SPICE Model

An electrical circuit modeling program called SPICE is available in both public domain and commercial packages. This program is most useful amongst the IC design engineers as a means of developing new IC concepts and layouts. However, it was thought that this program could also be useful as a software testbed for new anemometer architectural designs. The immediate problem that becomes apparent is the program's inability to account for a component such as the hot wire or hot film. A hot film is much different from a passive component in that its resistance changes significantly with an imposed heat transfer. It is this property that is difficult to model in the SPICE software package. Additional problems arose in the fact that a velocity step could not be modeled using SPICE. Even by coupling a current source and a voltage source to model a sensor, the software program still couldn't properly model the anemometer system dynamics.

An attempt was made to model the anemometer circuit in SPICE and this yielded some favorable results in terms of the response shape for an input square wave. However, without the program accounting for a film sensors thermal time constant for a step change in temperature, the predicted frequency response was much faster than the actual experimental frequency response. Therefore, this particular method of analysis for the circuit was not utilized for anything other than showing trends. Results of this analysis are discussed in Appendix B.

2.3.2. Freymuth's Third Order Theory

An ideal anemometer response would appear to be a second order system and in the most basic analysis, one may treat the response to be second order. Freymuth [15], who has done considerable work with the dynamic response of the anemometer circuit, presents his theoretical analysis for a hot wire anemometer by treating it as a third order system. He gives experimental evidence showing that the anemometer is indeed third

order in behavior. However he also states that the third order analysis does not necessarily apply to flush-mount hot films. In order to deal with this he incorporates a correction based on work by Bellhouse and Schultz [6] for the heat transfer to the substrate. In this section the theory is presented for the third order hot wire response to voltage and velocity steps as well as the correction for flush-mount hot films.

Beginning with a simplified constant temperature anemometer circuit, Freymuth [16] develops a general dynamic equation for the response of the system to either a step in velocity or voltage applied to the bridge.

$$\frac{MM''}{G}\frac{d^3u}{dt^3} + M_y\frac{d^2u}{dt^2} + M_x\frac{du}{dt} + u = Sv + n\frac{M}{n+1}\frac{R_1}{R_4}\left(\frac{\gamma U_t}{c/H} + \frac{dU_t}{dt}\right) \qquad (2.28)$$

where M is a time constant associated with the hot wire properties given by

$$M = \frac{(n+1)^2}{2}\frac{R_1}{nR_1 - R_o}\frac{c}{H(V)} \qquad (2.29)$$

The time constant M is made up of the time constant of c/H(V), where H is a heat transfer function which increases with the flow velocity at the sensor surface, and c is the thermal inertia of the wire. Two other time constants, M_x and M_y require adjustment for the optimization of the anemometer response. These are given by

$$M_y = \frac{M}{G}\left(\frac{\gamma M''}{c/H} + M' - GM_B\right) = M\frac{M' - GM_B}{G} \qquad (2.30)$$

$$M_x = \frac{M}{G}\left(\frac{\gamma(M' - GM_B)}{c/H} + \frac{U_b}{U_o}\right) = M\frac{U_b}{GU_o} \qquad (2.31)$$

The sensitivity S of the anemometer is a measure of the anemometer's ability to resolve changes in the heat transfer and is given by

$$S = \frac{U_o}{2}\frac{1}{H}\frac{dH}{dV}\left(1 - \frac{n+1}{G}\left(\frac{n+1}{2}\frac{R_1 g}{nR_1 - R_o}\frac{U_b}{U_o} - \frac{nR_1 + (1-n)R_o/n}{nR_1 - R_o}\frac{U_b - U_o}{U_o}\right)\right) \quad (2.32)$$

This third order differential equation can be treated for two different test conditions. One test condition is where a velocity step is applied. This is done by adjusting the dynamic equation so that the test voltage U_t is equal to zero. The other condition is a step in voltage. The voltage step is applied by adjusting the dynamic equation so that the velocity v is equal to zero. For either condition, the resulting third order equation is solved for its roots. In order to show the dynamic response of the constant temperature anemometer system based on the given circuit parameters, Freymuth introduces a dimensionless representation so that the dynamic response results can be applied generally to all anemometers. The results are plotted in Figures 2.7 and 2.8 for an example set of roots used by Freymuth.

Case 1: $p_1 = p_2 = p_3 = -1$

Case 2: $p_1 = -0.75 + i0.88$, $p_2 = -0.75 - i0.88$, $p_3 = -0.75$

Case 3: $p_1 = -0.5 + i0.87$, $p_2 = -0.5 - i0.87$, $p_3 = -1$

Cases 1, 2 and 3 correspond to the overdamped case, the critically damped case and the underdamped case. The overdamped case yields the slowest frequency response while the underdamped case reaches 3% of the maximum value the quickest. Granted, the ideal response is given by the critically damped case, but an underdamped case is most likely to be useful in intermittent flow applications due to the higher frequency response.

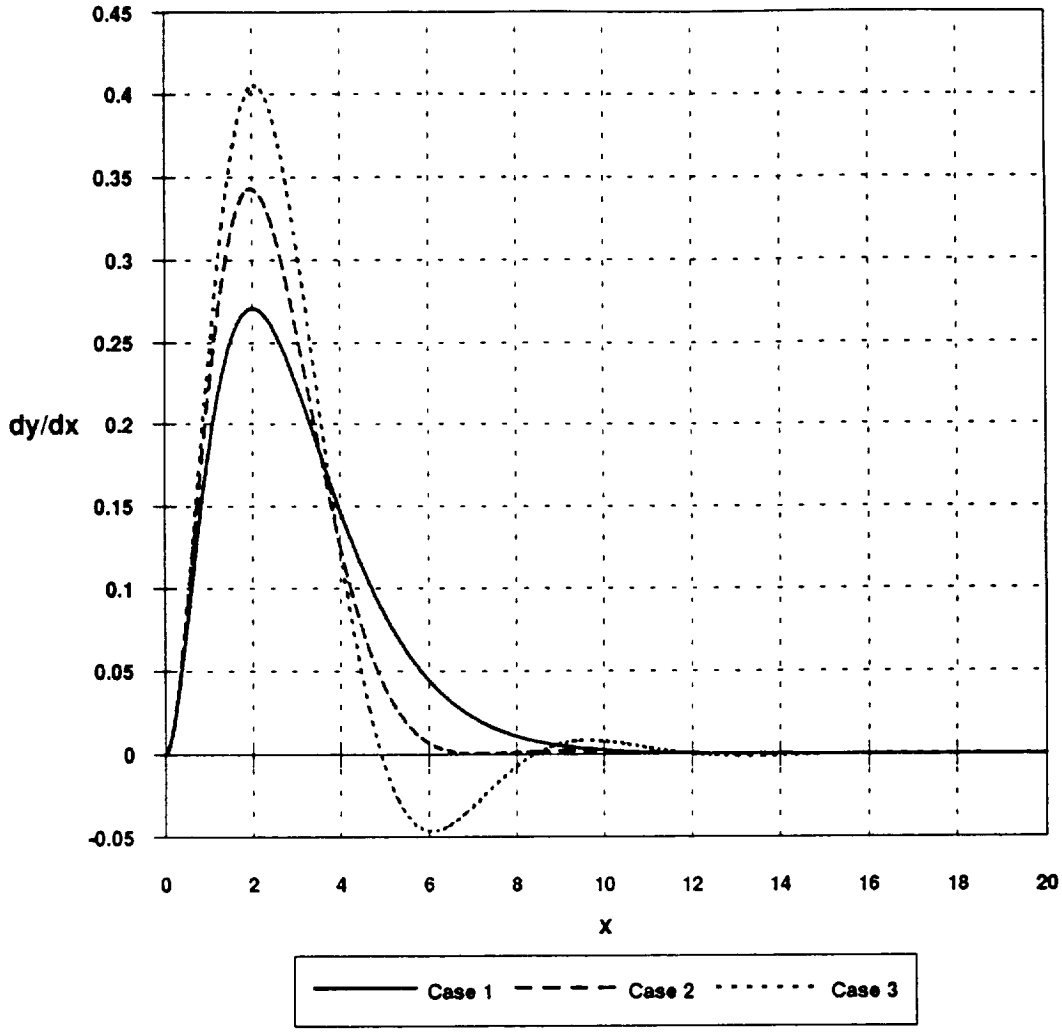

Figure 2.7. Anemometer response to voltage step based Freymuth's third order model

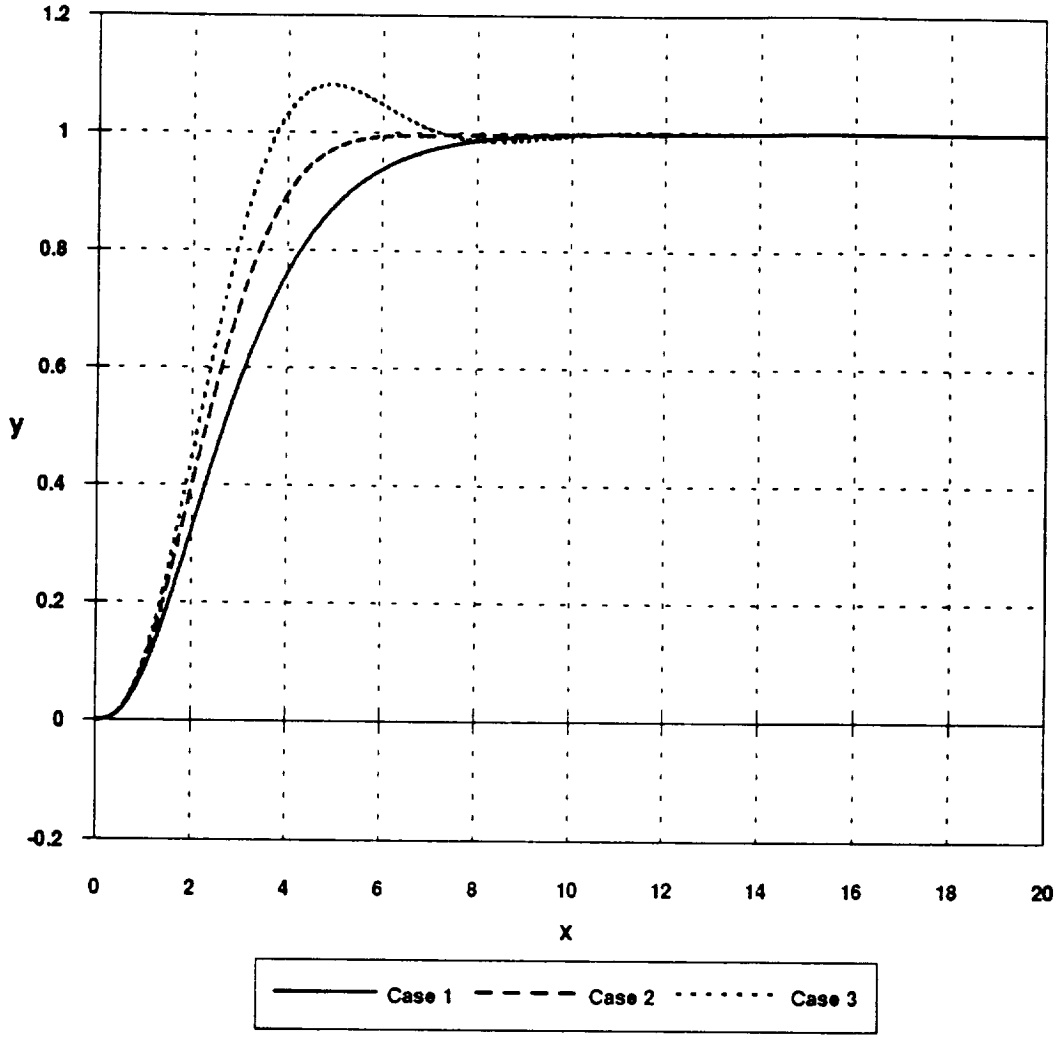

Figure 2.8. Anemometer response to velocity step based on Freymuth's third order model

The anemometer time constants can be determined through sinusoidal and square wave testing, and compared for different anemometer configurations. In addition, the time constants can be used to assist in improving the anemometer frequency response and overall performance.

The correction to this theory for non-cylindrical hot films is based on a heat loss to the substrate upon which the thin film is deposited. In this correction, the anemometer analysis remains essentially the same, but now the film model consists of a film on a substrate with a spanwise width L and a streamwise length *l*. In the hot wire analysis, conduction to the wire supports was neglected, and heat transfer was restricted to convection only. In the non-cylindrical hot film analysis, the heat transfer boundary conditions are given by

$$H(V) = \int_{\xi=0}^{l}\int_{\eta=0}^{L} \hat{h}(V,\xi,\eta)d\xi d\eta \qquad \text{Convection} \qquad (2.33)$$

$$H(V)\left(T_{y=-h} - T_o\right) = lLK\left(\frac{\partial T}{\partial y}\right)_{y=-h} \qquad \text{Conduction} \qquad (2.34)$$

where a Biot number is specified for the sensor as

$$x = \frac{hH(V)}{lLK} \qquad (2.35)$$

Freymuth's [17] analysis drives towards modeling the anemometer system response to a sinusoidal temperature fluctuation and results in a governing response equation that superimposes the voltage responses to sinusoidal test voltage, sinusoidal temperature, and sinusoidal velocity fluctuations into a combined response voltage. From this the response equation is evaluated for a particular anemometer configuration and relative

responses are derived for the temperature, voltage and velocity responses. For the purpose of this research, the relative voltage response to a sinusoidal voltage input is of interest, which is defined by

$$R_u = \frac{u_{test}(\Omega)}{u_{test}(\Omega = 0)} \tag{2.36}$$

where Ω is a non-dimensional circular frequency defined as

$$\Omega = \frac{\omega h^2}{D} \tag{2.37}$$

D being the thermal diffusivity of the substrate. The relative voltage response is evaluated for the following equation.

$$R_u = \frac{1+x}{2+x} \times \left(1 + \frac{(i\Omega)^{1/2}}{x} \frac{\begin{array}{l} \exp[(i\Omega)^{1/2}]\{[(i\Omega)^{1/2}/x]+1\} \\ -\exp[-(i\Omega)^{1/2}]\{[(i\Omega)^{1/2}/x]-1\} \end{array}}{\begin{array}{l} \exp[(i\Omega)^{1/2}]\{[(i\Omega)^{1/2}/x]+1\} \\ +\exp[-(i\Omega)^{1/2}]\{[(i\Omega)^{1/2}/x]-1\} \end{array}} \right) \tag{2.38}$$

The relative voltage response R_u, is plotted in Figure 2.9 for different thin film Biot number values. The Bellhouse-Schultz effect is characterized by a bulging of the curve at small Ω. This differs from the sine wave testing result for a hot wire in which Ω would be much more linear in the small frequency region. This effect will be demonstrated later in the thesis.

2.3.3. Watmuff's Fifth Order Polynomial

Watmuff [41] observes in his work that the constant temperature hot wire anemometer response experiences higher order phenomena than the standard third

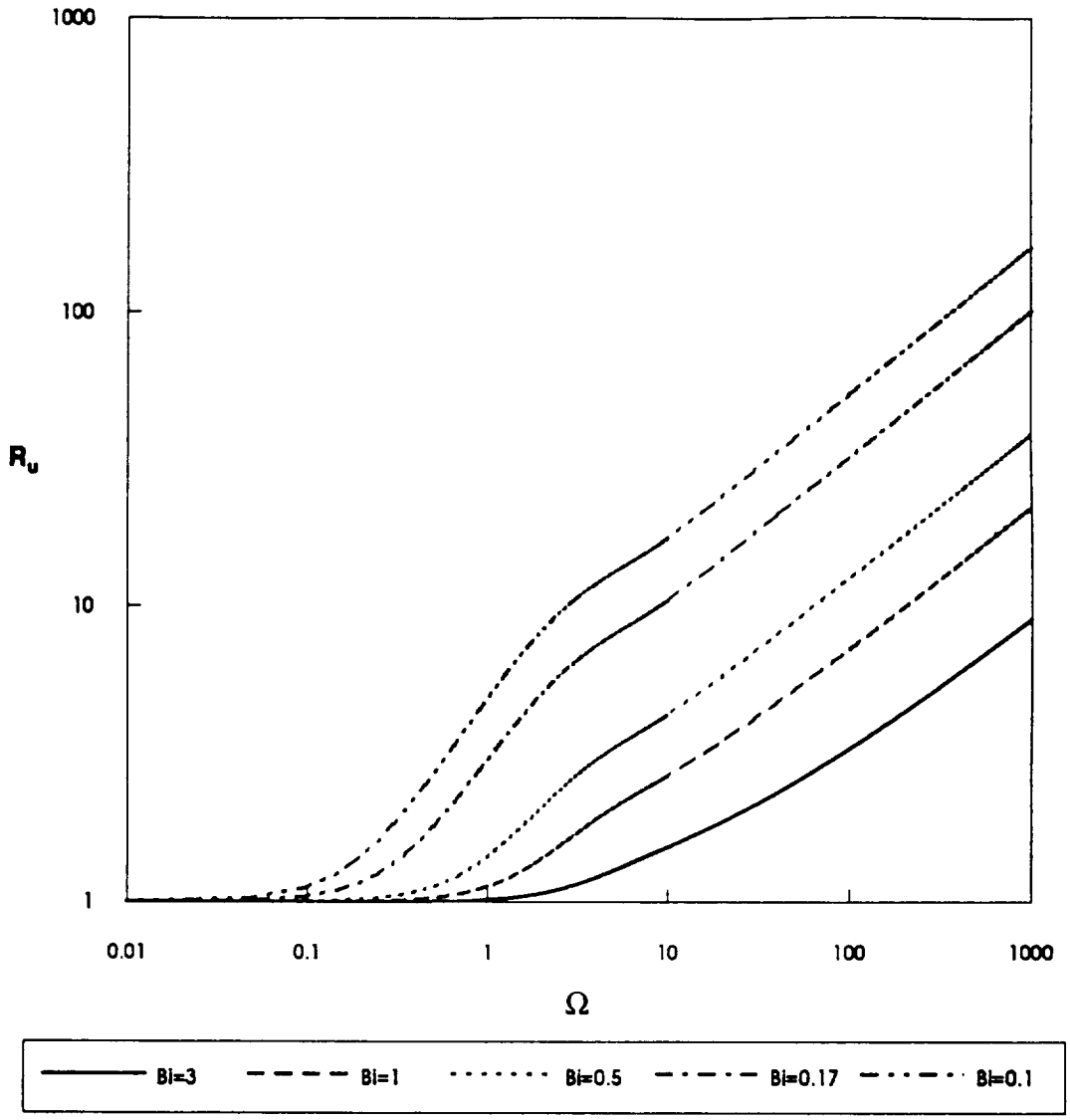

Figure 2.9. Theoretical results of Freymuth's non-cylindrical hot film sine-wave testing model showing the Bellhouse-Schultz effect

order response models presented by such people as Freymuth [16] and Perry and Morrison [31] predict. This led Watmuff to develop a seventh order model. Through his model, Watmuff shows the important effects of bridge inductance and offset voltage in the amplifier. In his simplified fifth order model, transfer functions are given for velocity fluctuations u' and offset voltage perturbations e_s as

$$\frac{e_o}{u'} = \frac{KxR_s(L_bs + R_b + R_c)}{A(s)} \tag{2.39}$$

and

$$\frac{e_o}{e_s} = \frac{KB(s)}{A(s)} \tag{2.40}$$

These transfer functions are combinations of the two polynomials A(s) and B(s) that comprise the fifth order analysis. Both A(s) and B(s) are defined with the Laplace variable s. Watmuff defines A(s) and B(s) as

$$A(s) = A_5s^5 + A_4s^4 + A_3s^3 + A_2s^2 + A_1s + A_0 \tag{2.41}$$

$$B(s) = B_3s^3 + B_2s^2 + B_1s + B_0 \tag{2.42}$$

The constants in both A(s) and B(s) are composed of additional constants as well as the weights, M, for the poles that define the operational amplifier transfer function.

$$\begin{aligned} A_0 &= C_0 + C_{k0} & B_0 &= C_0 \\ A_1 &= C_1 + 2MC_0 + C_{k1} & B_1 &= C_1 \\ A_2 &= C_2 + 2MC_1 + M^2C_0 + C_{k2} & B_2 &= C_2 \\ A_3 &= C_3 + 2MC_2 + M^2C_1 & B_3 &= C_3 \end{aligned} \tag{2.43}$$

$$A_4 = 2MC_3 + M^2C_2 \qquad \text{cont. (2.43)}$$

$$A_5 = M_2C_3$$

The constants C_n are products of the actual anemometer parameters and are defined as

$$\begin{aligned}
C_0 &= (R_b + R_c)(R_a + R_w + \alpha) \\
C_{k0} &= K(R_wR_c - R_aR_b + R_c\alpha) \\
C_1 &= (R_a + R_w + \alpha)L_b + (R_b + R_c)[(R_a + R_w)T_w + L_w] \qquad (2.44) \\
C_{k1} &= K((R_wR_c - R_aR_b)T_w + R_cL_w - R_aL_b) \\
C_2 &= [(R_a + R_w)T_w + L_w]L_b + (R_b + R_c)L_wT_w \\
C_{k2} &= KT_w(R_cL_w - R_aL_b) \\
C_3 &= L_bL_wT_w
\end{aligned}$$

where

$$\alpha = R_w(R_w - R_g)/R_g \qquad (2.45)$$

The result of this analysis is a theory that accounts for the variations in inductance and operational amplifier offset voltage. Figure 2.10 shows how these variations in the inductance L_b can affect the frequency response roll-off point. Watmuff's theory is also sensitive to the properties of the sensor. Figure 2.11 shows how variations in the thermal time constant T_w of the sensor controls the roll-off point for frequency response.

2.4. Operation of a Film Sensor in Flow Conditions

2.4.1. Skin Friction in the Boundary Layer Behind a Normal Shock

The shock tube was used in this work as a means of flow testing the sensor to determine the operational parameters and confirm theoretical trends. It is necessary to

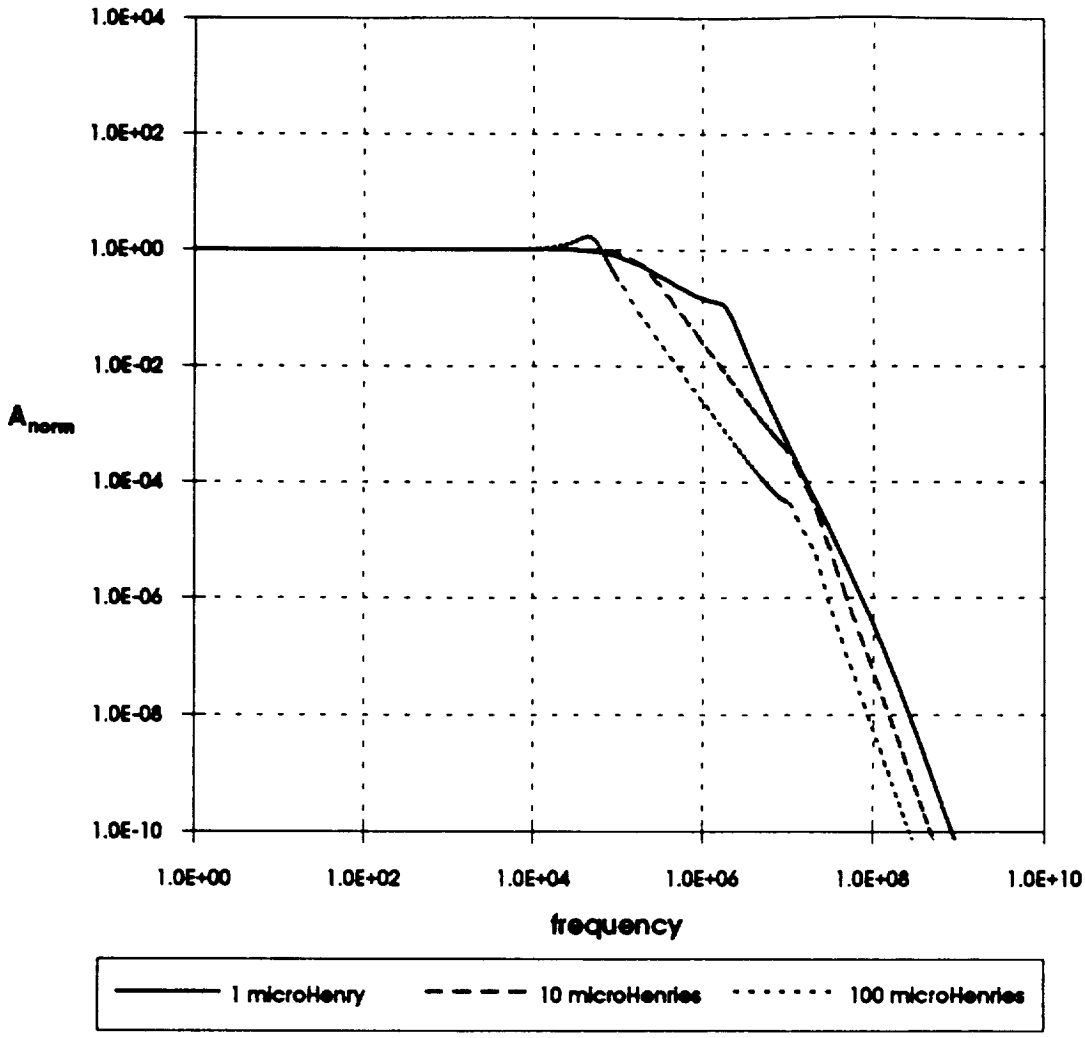

Figure 2.10. The effect of sensor side inductance on frequency response roll-off point based on Watmuff's model

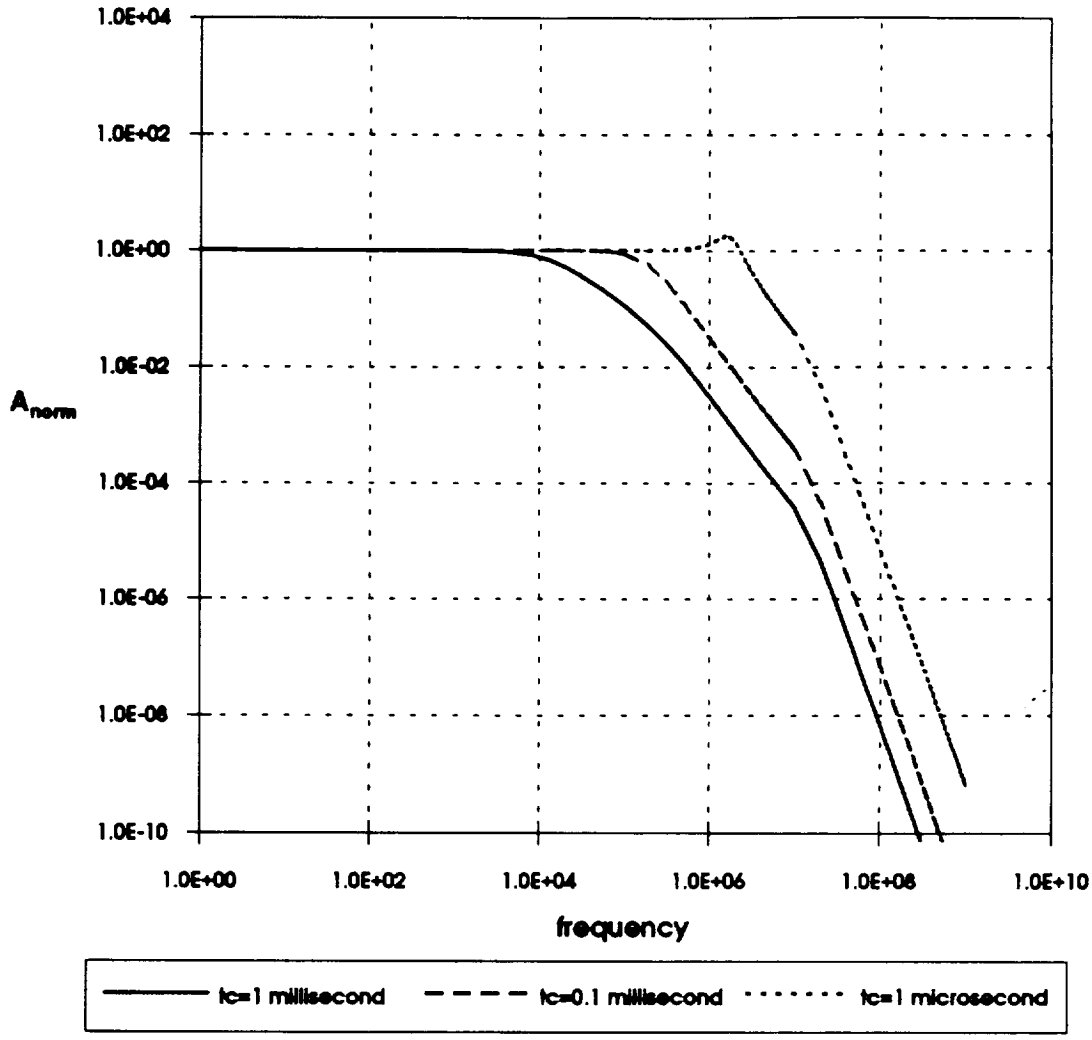

Figure 2.11. The effect of film time constant on frequency response roll-off point based on Watmuff's model (tc = T_w in Watmuff's model)

have a theory that describes the flow seen by the sensor for a flush-mount sensor in the shock tube. Mirels [27] addresses the issue of a laminar boundary layer forming behind a normal shock advancing into a stationary fluid. This solution may be used to determine shear as well as heat transfer at the wall, or in the case of this research, at the surface of the sensor plate model.

As a normal shock wave advances into a stationary fluid with constant velocity, a boundary layer builds behind it. In the lab frame, this boundary layer is time dependent so it sees a change in the heat transfer rate from the wall as the boundary layer builds with time. In order to deal with the time dependency of the problem, a coordinate system is defined in which the observer moves with the shock (see Figure 2.12) creating a quasi-steady frame for the boundary layer. Once the equations are independent of time, similarity may be employed to solve the equations. The coordinate system is defined through

$$\begin{aligned} x' &= x - u_w t & y' &= y \\ u' &= u - u_w & v' &= v \end{aligned} \tag{2.46}$$

The assumption of flow over a flat plate implies that the pressure gradient dp/dx is zero. In addition, it is assumed that the boundary layer is laminar. Then for $x > 0$ we can write continuity, momentum, energy and state equations respectively as follows where the terms $\partial/\partial t = 0$.

$$\frac{\partial \rho u}{\partial x} + \frac{\partial \rho v}{\partial y} = 0 \tag{2.47}$$

$$u\frac{\partial u}{\partial x} + v\frac{\partial u}{\partial y} = \frac{1}{\rho}\frac{\partial}{\partial y}\left(\mu \frac{\partial u}{\partial y}\right) \tag{2.48}$$

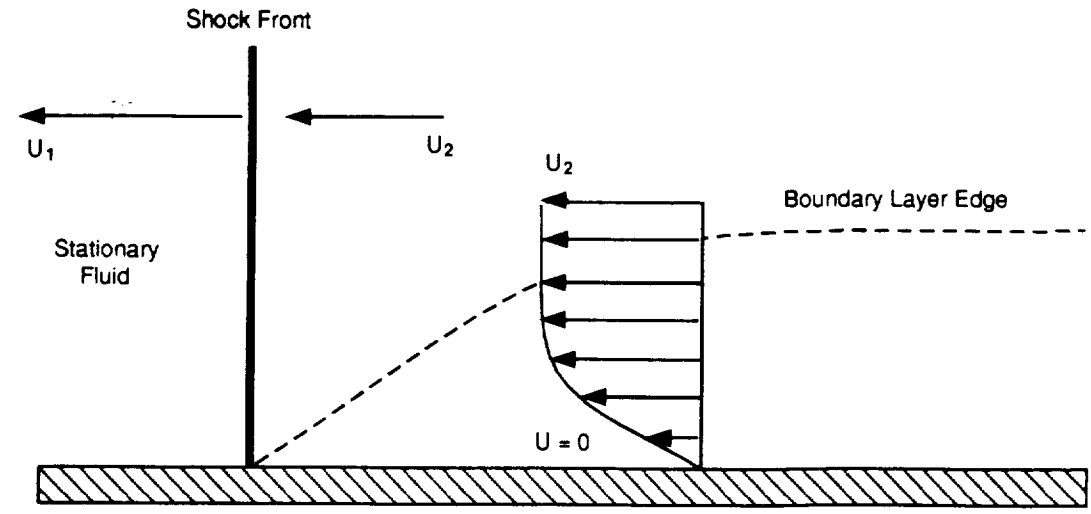

Figure 2.12. Shock and lab fixed reference frames for Mirels' solution to the boundary layer behind a normal shock advancing into a stationary fluid

$$\rho c_p\left(u\frac{\partial T}{\partial x}+v\frac{\partial T}{\partial y}\right)=\frac{\partial}{\partial y}\left(k\frac{\partial T}{\partial y}\right)+\mu\left(\frac{\partial u}{\partial y}\right)^2 \tag{2.49}$$

$$P=\rho RT \tag{2.50}$$

And the boundary conditions for x>0 are

$$u(x,0)=u_w \qquad T(x,0)=T_w$$

$$v(x,0)=0 \tag{2.51}$$

$$u(x,\infty)=u_e \qquad T(x,\infty)=T_e$$

From continuity, a stream function, ψ, is self satisfied through the equations

$$\frac{\rho u}{\rho_w}=\frac{\partial \psi}{\partial y} \qquad \frac{\rho v}{\rho_w}=-\frac{\partial \psi}{\partial x} \tag{2.52}$$

Next, Mirels defines a similarity parameter

$$\eta=\sqrt{\frac{u_e}{2xv_w}}\int_0^y\frac{T_w}{T(x,y)}dy \tag{2.53}$$

Utilizing the similarity parameter, y can be expressed as

$$\psi=\sqrt{2u_e x v_w}\,f(\eta) \tag{2.54}$$

and then the velocities are expressed as

$$\frac{u}{u_e}=f' \tag{2.55}$$

$$\frac{v}{u_e} = -\frac{\rho_w}{\rho}\sqrt{\frac{\nu_w}{2xu_e}}\left(f + 2xf'\frac{\partial \eta}{\partial x}\right) \tag{2.56}$$

The following relations are assumed for the wall where the constants of proportionality have been chosen so that μ and k have the appropriate numerical value at the wall.

$$\mu = \frac{\mu_w}{T_w}T \qquad\qquad k = \frac{k_w}{T_w}T \tag{2.57}$$

It is also assumed that c_p and the Prandtl number, Pr, are constant throughout the boundary layer and are evaluated at the wall temperature. Through the similarity transformation, the momentum equation is written as

$$f''' + ff'' = 0 \tag{2.58}$$

while the boundary conditions are

$$f(0) = 0$$

$$f'(0) = \frac{u_w}{u_e} \qquad\qquad f'(\infty) = 1 \tag{2.59}$$

Through the transformations, the shear at the wall is defined

$$\tau_w = \left(\mu\frac{\partial u}{\partial y}\right)_w = u_e f''(0)\sqrt{\frac{u_e \rho_w \mu_w}{2x}} \tag{2.60}$$

from the definition of the local skin friction coefficient, equation (2.60) can be turned into

$$c_f \sqrt{Re_{xs}} = \frac{-\sqrt{2} f''(0)}{\sqrt{\frac{u_w}{u_e}\left(\frac{u_w}{u_e} - 1\right)}} \tag{2.61}$$

where the Reynolds' number is defined as

$$Re_{xs} = \frac{(u_w - u_e)^2 t}{\nu_2} \tag{2.62}$$

Equation (2.60) can also be used to define a time dependent wall shear that applies at any point on the flat plate time t after the shock has passed that location.

$$\tau_w = \left(\mu \frac{\partial u}{\partial y}\right)_w = u_e f''(0) \sqrt{\frac{u_e \rho_w \mu_w}{2 u_w t}} \tag{2.63}$$

Mirels gives numerical solutions for velocity ratios u_w/u_e ranging from 1.5 to 6 which are shown below in Table 2.2.

Table 2.2: Skin friction coefficients for the laminar shock induced boundary layer as given by Mirels [27]

u_w / u_e	$c_f \sqrt{Re_{xs}}$	$-f''(0)$
1.0	1.128	--
1.5	1.057	0.4578
2.0	1.019	1.0191
3.0	0.979	2.3973
4.0	0.958	4.0623
5.0	0.944	5.9726
6.0	0.935	8.1009

In addition to the standard numerical solution, Mirels solves the weak shock problem as a perturbation solution for cases where

$$\frac{u_w}{u_e} - 1 << 1 \tag{2.64}$$

In this case, the important parameter f''(η) is given by

$$f'' = -\sqrt{\frac{2}{\pi}}\left(\frac{u_w}{u_e} - 1\right)e^{-\eta^2/2} + o\left(\frac{u_w}{u_e} - 1\right)^2 \tag{2.65}$$

In most cases for this research, the shock strength was within the criteria for weak shock waves.

2.4.2. Development of Instabilities

These sensors were designed with the intention of capturing instability waves in the high speed flow. A quick analysis for the rise of instability waves can be done and compared to the experimental responses of the sensors to the shock wave passage. To get a standard lab fixed Reynolds number for each shock event, the Reynolds number is calculated as

$$Re = \frac{u_2 \rho_2 x}{\mu_2} \tag{2.66}$$

where the subscript 2 denotes freestream of the flow induced by the shock wave. In order to calculate μ_2, Sutherland's viscosity law was used, which is defined as

$$\frac{\mu}{\mu_o} = \left(\frac{T}{T_o}\right)^{1.5} \frac{T_o + S}{T + S} \tag{2.67}$$

where for air, T_o = 273 K, $\mu_o = 1.716 \times 10^{-5}$ Ns/m^2 and S = 111 K, or for nitrogen, T_o = 273 K, $\mu_o = 1.663 \times 10^{-5}$ Ns/m^2 and S = 107 K.

According to stability calculations shown in White [42], instability waves arise at a Reynolds number of approximately 90,000 for M = 0. This result sufficiently applies to the range M = 0 - 0.5 so that it may be used as a basis for all experimental comparisons. At the transition point, unstable frequencies can be approximated by

$$2 \times 10^4 = F = \frac{\omega \nu}{u_e^2} \tag{2.68}$$

Therefore, for the velocity case that yields a Reynolds number of 90,000, flow fluctuations should be comparable to the circular velocity ω.

3. FILM SENSOR AND ANEMOMETER SYSTEM DESIGN

Recall that the design goals set forth for this project were to provide a film sensor with a fast open loop frequency response and an anemometer system that was not only high speed, but had low noise and good stability characteristics. One of the major problems associated with the design of anemometer systems is that the literature either concentrates on the electrical aspect of anemometry or the fluid aspect of anemometry. Very few works in literature address the system as a whole considering both the electronics and fluid mechanics as an intimately coupled system. The design of this system does not depart radically from this analytical separation, yet both the sensor and anemometer were designed for maximum frequency response while ensuring that the two would work properly as a whole.

Film design required an understanding of material properties in terms of thermal and electrical conductivity and thermal capacity as well as more mechanical properties such as the material's ability to bond with substrate surfaces. It was also of interest to design similar sensors on different substrates in order to isolate the effects of substrate.

Circuit design began with utilizing a classical anemometer architecture and testing its performance with one particular sensor. Stability was eventually tested with hot wires as well as hot films to ensure that the system would be robust in its design. Attempts were made to maximize frequency response with the given architecture and then test the different sensors with one anemometer configuration.

Once a final configuration was arrived at, tests were at first made electronically, and then in the shock tube to ensure that the anemometer and sensor system gave

repeatable results as well as results that followed the trends shown by the experimental and theoretical work of people such as Mirel, and Davies and Bernstein.

3.1. Film Design

The matter of material selection for the film sensors was considered carefully so that a sensor with a small physical mass as well as small thermal mass could be designed. The objective set forth in this research was to design a system that was capable of a frequency response up to 1 MHz. Theory suggests that in order to design a sensor with a non-feedback thermal response on the order of 1 MHz, it would require pushing the limits of fabrication as well as the budget of this project. Three key factors were considered when designing the sensor:

1. Material Availability and Ease of Fabrication
2. Properties of Substrate Material
3. Properties of Metal Film Material

In reality, the three factors are coupled in the sense that some metals may bond with some substrates but not with others.

3.1.1. Substrate Material Selection

The substrate material was the first item of selection. The most important parameter to consider when choosing a substrate material is the unsteady heat transfer parameter. The unsteady heat transfer parameter describes the speed at which a material responds to changes in the thermal environment. The unsteady heat transfer parameter is sometimes referred to as β and is defined as

$$\beta = \sqrt{k\rho c} = \sqrt{\frac{k^2}{\alpha}} \tag{3.1}$$

where k is the thermal conductivity, c is the specific heat and α is the thermal diffusivity. For the effect of variable thermal properties on the heat transfer from homogeneous materials, Schultz and Jones [39] show that

$$\dot{q}_s = \frac{T_s\sqrt{\pi}}{2}\frac{\beta}{\sqrt{t}} \tag{3.2}$$

Therefore, for any given surface temperature, the substrate heat transfer will increase with increasing β.

To add a little insight, the thermal diffusivity is the measure of a material's ability to store thermal energy. A material will reach equilibrium slower with a small α than with a large α. Large α materials can respond quickly to changes in the thermal environment. However, maximizing α will minimize β. The other factor to consider is the thermal conductivity. As long as the increase in k^2 is larger than the increase in α going from material to material, the trade-off constitutes a better substrate. Table 3.1 lists the important characteristic thermal parameters for some substrate materials.

In terms of the ease of fabrication, an important consideration in choosing a substrate is whether or not a metal film can be deposited on the surface. Surfaces such as aluminum and nickel are obviously a bad choice for the very reason that they are metal and would short out the hot wire. However, sensors are made where a polymeric coat is deposited on a metal substrate before sensor deposition.

For the purpose of this research, three different substrate materials were chosen to make a total of five different sensor plates. Three sensor plates were made from standard soda lime plate glass. Plate glass has properties that are very similar to Pyrex, which is a

common substrate used in fabricating thin films. A fourth sensor plate was made by bonding a 1/32 inch alumina sheet on a 3/32 inch aluminum plate. Alumina has a thermal conductivity roughly four times greater than soda lime glass. Finally, a fifth sensor plate was made by coating a 1/8 inch aluminum plate with a 6 micron film of DuPont Pyralin 2590PI high temperature polymer. The thermal properties of each substrate is listed below in Table 3.2. All three substrates were chosen based on the commonality of their use in flush-mount sensor applications.

In Table 3.2, the thermal impedance of each substrate has been calculated. The thermal impedance is a combination of the individual contribution from each substrate material to the overall thermal resistance of the substrate weighted by its thickness,

$$I_t = \frac{1}{U} = \left(\frac{1}{(L_p / k_p) + (L_s / k_s)} \right)^{-1} \tag{3.3}$$

where k is the thermal conductivity and L is layer thickness for the primary substrate, p, and the secondary substrate, s. In the case of these particular substrates, the alumina substrate sensor has the smallest thermal impedance and correspondingly the greatest heat transfer. At first, one might guess that the aluminum sensor would have the smallest thermal impedance based on the thermal conductivity of the aluminum. The Pyralin coat on the aluminum substrate was designed to be thermally thin. However it is still thick enough to cause the substrate impedance to be greater than the alumina sensor.

3.1.2. Film Material Selection

The material for a thin film is chosen on the basis of its thermal mass, resistivity, depositability and temperature coefficient of resistance. Thermal mass is important because it determines the thermal time constant of the material. Recall from previous

Table 3.1. Thermal parameters of different substrate materials

Substrate Material	Thermal Conductivity k (W/mK)	Specific Heat C_p (J/kgK)	Thermal Diffusivity α (m^2/s)	Unsteady Parameter β ($Ws^{1/2}/m^2K$)
Polystyrene	0.40	1400	2.75×10^{-7}	762
Plate Glass	1.04	795	5.25×10^{-7}	1407
Pyrex Glass	1.36	774	7.93×10^{-7}	1520
Fused Quartz	1.40	750	8.48×10^{-7}	1520
Alumina	35.6	775	1.16×10^{-5}	10460
Nickel	90.9	444	2.31×10^{-5}	18917
Aluminum	204.0	890	9.79×10^{-5}	22169
Diamond	2300.0	509	1.29×10^{-3}	64011

Table 3.2. Thermal properties of sensor substrates utilized in project

Primary Substrate Material	L_p (cm)	k_p (W/mK)	Secondary Substrate Material	L_s (cm)	k_s (W/mK)	Substrate Impedance (cm^2K/W)
Plate Glass	0.317	1.04	N/A	N/A	N/A	30.6
Alumina	0.079	35.6	Aluminum	0.238	204	0.340
Aluminum	0.317	204	Pyralin	6×10^{-4}	0.155	0.543

discussion in section 2.1.1 where the sensor was treated as a lumped heat transfer element. Materials with small specific heats and dimensions have smaller time constants meaning that they are able to adjust to a new temperature more quickly than materials with larger time constants. In the same sense, resistivity becomes an important parameter. If it is necessary to make the smallest possible sensor, a material with a high resistivity is desirable because the higher the resistivity, the smaller the required film thickness for a given film aspect ratio.

Temperature coefficient of resistance (TCR) is important because it determines how much of a resistance change will occur for a change in the temperature. In a sense, materials with a larger TCR will have better resolution in the measurements because a given temperature change will create a larger resistance change and correspondingly a larger current draw from the anemometer to maintain a constant temperature. Depending on the method used to deposit the metal film, the TCR as well as the resistivity of the material may change due to annealing in the crystalline structure. The thermal coefficient of resistance per degree Celsius is defined as

$$TCR = \frac{1}{\Delta T}\frac{R_T - R_c}{R_c} \tag{3.4}$$

The thermal coefficient of resistance is shown for several different materials in Table 3.3. In addition, Figure 3.1 shows the change in resistance for some standard thin metal films over the temperature range of 0 to 100 °C . The TCR indicated in this figure, may not be entirely accurate. Depending upon relative film thickness, changes in resistance can vary from what is generally accepted as the TCR for a given change in the temperature.

The final choice for film sensor material was nickel. It was chosen for the reason that it is easy to deposit on all of the selected substrates, and it is commonly used at

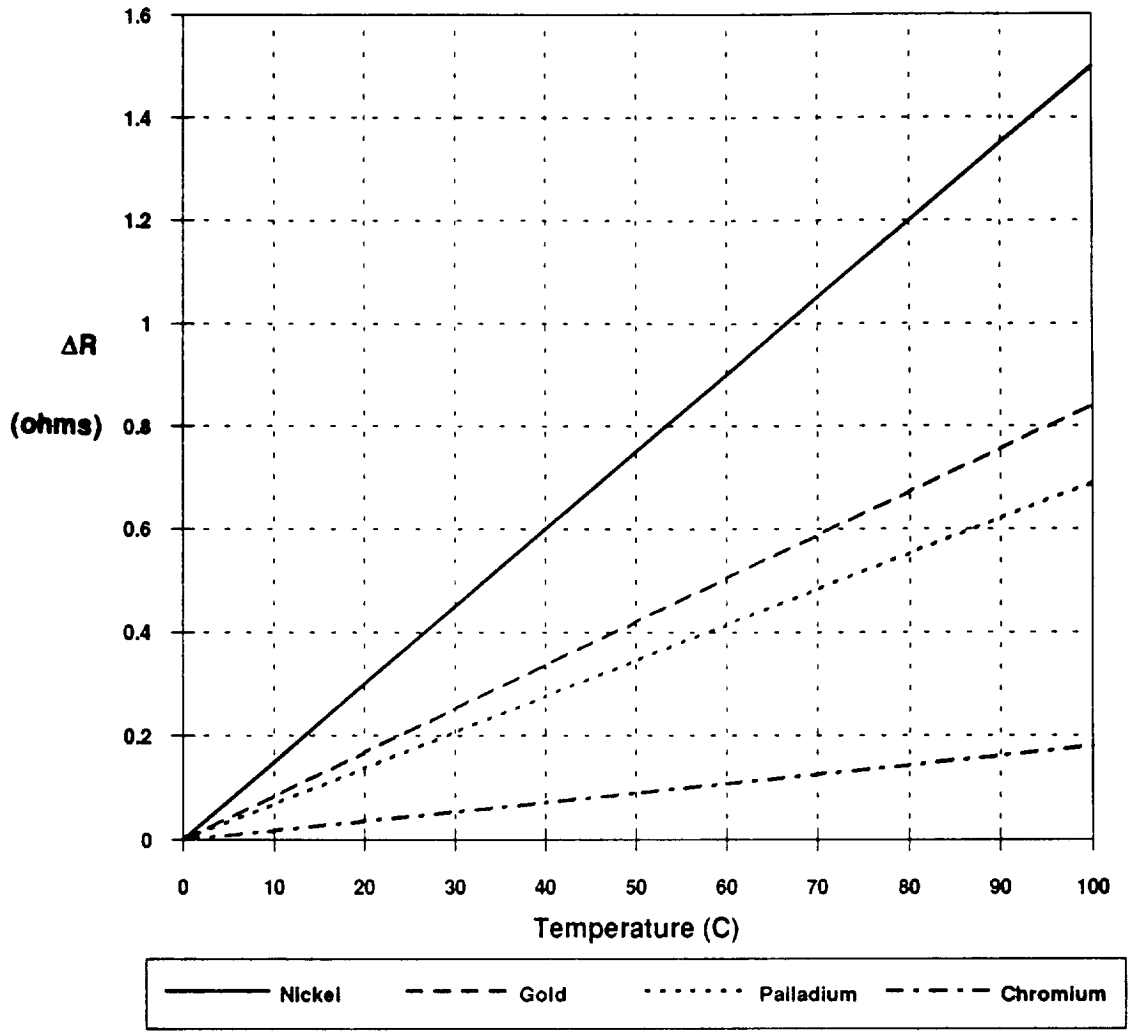

Figure 3.1. Comparison of thermal coefficient of resistance per degree Celsius for different thin film materials based on 3 Ω cold resistance

NASA Langley Research Center (LaRC) for the fabrication of thin film sensors. Three different dimensions were chosen for the sensors in order to isolate the effect of dimension on the frequency response: 5 mil by 0.5 mil, 10 mil by 1 mil and 20 mil by 2 mil. All three dimensions were placed on glass substrates, while 20 mil by 2 mil sensors were placed on the alumina and aluminum substrates.

Table 3.3. Electrical parameters of deposited thin metal films

Material For Thin Film Deposition	Resistivity Before Annealing (μΩ-cm)	Resistivity after Annealing (μΩ-cm)	Temperature Coefficient of Resistance
Nickel	28.5	41.0	0.0050
Aluminum	0.41	0.36	0.0028
Silver	22.2	4.95	0.0028
Platinum	8.7	15.65	0.0025
Palladium	20.3	20.8	0.0023
Titanium	67.1	59.9	0.0007
Chromium	172.5	62.0	0.0006

3.1.3. Fabrication of Final Design

The design requirements set forth for the film sensors were that each sensor should have a cold resistance of approximately 5 Ω. The nickel deposition thickness limitation was in between 1200 and 4000 Angstroms so the required nickel film thickness was calculated to be 2800 Angstroms to obtain the 5 Ω objective. This thickness was calculated based on the correction in bulk resistivity of thin films, which is that thin film nickel has a resistivity half that of the bulk value. The leads leading to the film were to be made of 40,000 Angstrom copper film. This would ensure small lead resistance

relative to the resistance of the nickel film sensor. Each film, regardless of dimension, was designed with a length to width ratio of 10 to reduce cross current sensitivity in the sensor vicinity. All substrates were made to be 0.125 inches thick by 2 inches in length by 1.75 inches in width with a 30 degree sharp leading edge. A sensor array would be designed to go on each substrate that consisted of two sensors with identical sensor dimensions and slightly different lead dimensions. The front sensor would act as the primary testing sensor while the rear sensor was to be utilized as a back up in the event of sensor failure. A not-to-scale diagram detailing the characteristics of the sensor design is shown in Figure 3.2.

Once the materials were selected for film and substrate and the sensor shape was designed, the sensors were fabricated by NASA LaRC. The method used for fabrication was ion gun evaporation, which is a well-developed process that is commonly used by electronics industries for the deposition of thin films on substrates.

Previous to the deposition process, the substrate surface is checked for scratches that might cause an uneven film. Next the surface is atomicly stripped of surface impurities by bombarding the surface with a 10 eV beam. The nickel is energetically evaporated and the clean surface is bombarded with a 65 eV beam. This results in a nickel deposition rate of 2-3 Angstroms per second. This slow rate is desirable in order to avoid non-uniformities in the film layer, which can result in sensor hot spots and premature burn-out. Deposition continues until a film thickness of approximately 2800 Angstroms is achieved (the thickness required for a 5 Ω sensor with the given dimensions). Once the deposition is complete, the film is coated with a photoresist chemical that reacts with the film layer when exposed to ultraviolet light. A mask in the shape of the sensor is placed over the film and the film is exposed to ultraviolet light.

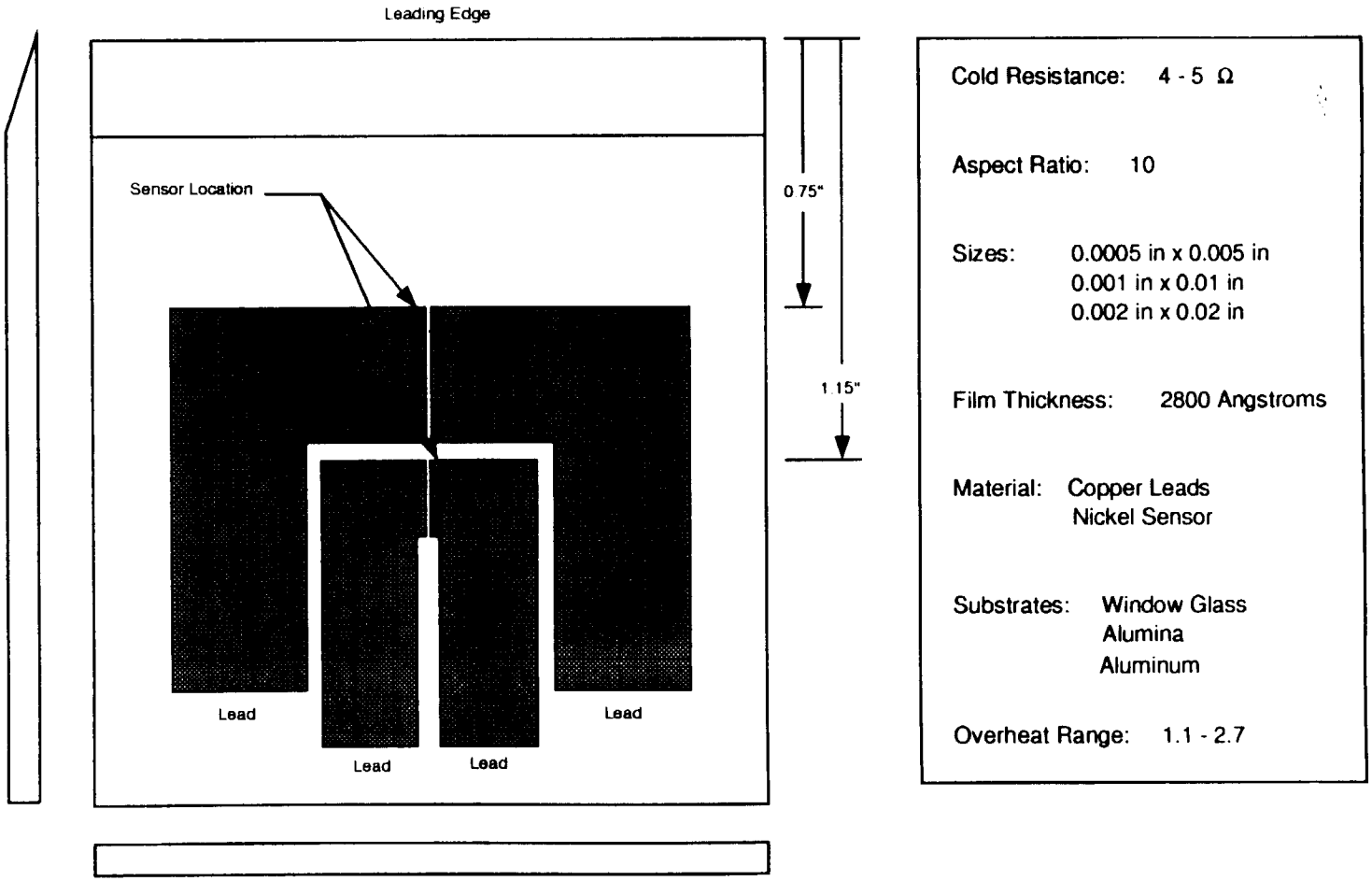

Figure 3.2. Design characteristics of thin film sensors used in this research

This exposure allows all but the sensor film to be etched away by using a chemical bath. Copper leads connecting to the film sensor were deposited next and then thin gauge wire was soft soldered to the ends of the leads.

The cold resistance of each sensor was checked after an operational burn-in period. The cold resistance values are shown in Table 3.4. The cold resistance was found through a thermal calibration which is detailed in Appendix C.

Table 3.4. Cold resistance of tested sensors

Substrate Material	Plate Glass	Plate Glass	Plate Glass	Alumina	Aluminum
Sensor Dimension	5 x 0.5 mil	10 x 1 mil	20 x 2 mil	20 x 2 mil	20 x 2 mil
Rear Cold Resistance	N/A	4.190	3.884	3.654	N/A
Front Cold Resistance	3.141	3.632	3.175	3.452	17.806

3.2. Constant Temperature Anemometer Design

Several different architectures of constant temperature anemometers exist in the commercial field. All designs employ a Wheatstone bridge, but the use of op amps, power amps, and transistors and output buffers varies significantly. The design chosen in this case was chosen because it is elegant in its simplicity. There are two philosophies in the treatment of electronics. One philosophy is to tackle stability and noise problems through the addition of more components. The other philosophy is to avoid stability and noise problems through the elimination of "non-vital" components. The latter philosophy was chosen to pursue the goals of this research.

Recall that Freymuth described a constant temperature anemometer as a third order system. In response to a square wave, the output signal consists of an oscillatory

decay superimposed on an exponential decay. The optimum response to design for is one in which both the exponential decay and oscillatory damping of the response is very fast. In short, the ideal third order response should be made to look like a critically damped second order dynamic response.

3.2.1. Bridge Ratio

The heart of the constant temperature anemometer is the Wheatstone bridge resistor network. The bridge should consist of four resistors: two precision resistors, one control resistor and the sensor. The anemometer operates by running a current through the bridge and holding the sensor at a particular temperature (resistance). As airflow cools the sensor, the resistance of the sensor begins to change. The bridge becomes imbalanced and the operational amplifier picks up this imbalance. The resulting feedback dumps more current into the top of the bridge to bring the sensor back up to the original temperature, thus constant temperature anemometry. The ratio of the bridge is set by the ratio of the two sides of the bridge to each other. For example, if the precision resistor on the control resistor side of the bridge is 40 Ω and the precision resistor on the sensor side of the bridge is 4 Ω, then the bridge ratio is 10:1. An anemometer designed with a 10:1 bridge ratio will decrease the amount of current supplied to the control resistor side in order to balance the bridge resulting in a low power anemometer (and probably lower noise levels). However, the higher power 1:1 bridge is more desirable from a standpoint of operating speed because the bridge arms are equal. Equal bridge arm resistance provides impedance matching between the two arms allowing a higher frequency response.

3.2.2. Operational Amplifiers

If the Wheatstone bridge is the heart of the anemometer, then the operational amplifier is the pacemaker that drives the heartbeat. As mentioned previously, a bridge imbalance set by a change in the heat transfer over a sensor is the input to the operational amplifier. The speed at which the negative feedback loop that has been set up between the op amp and the bridge can adjust is the time constant of the system. The operational amplifier provides gain to the differential signal supplied from the imbalanced bridge.

The op amp is capable of amplifying out to a specific frequency which is indicated by its gain-bandwidth product. The higher the gain bandwidth product, the larger frequency range the op amp will amplify. Not only is it desirable to have a large gain-bandwidth product, but it is also desirable to have a large gain. Large gain translates into a smaller time constant. An important characteristic of all op amps is their point of stability. The negative feedback of an operational amplifier requires a 180 phase shift in the signal in order to remain stable. The gain stability criterion for the typical op amp is a gain of unity. Once this point is reached, the operation may become unstable resulting in signal oscillation. Decompensated op amps are available which tend to become unstable at higher gains than their compensated counterparts. The trade-off is in gain-bandwidth product. For example, the OP-27 is a compensated operational amplifier with a minimum gain of 1 for stability and has a gain-bandwidth product of 6. The OP-37 is a decompensated OP-27 in which the minimum gain for stability is 5. However, its gain-bandwidth product is 60 meaning that the OP-37 has 10 times more frequency range than the OP-27. The operational amplifier used in this circuit is the Burr-Brown OP-37. A typical practice for decompensated amps is to force a premature roll-off of the gain-bandwidth by placing some capacitance around the operational amplifier input and output. This will help to ensure that the stability criterion is maintained.

3.2.3. Amplifier Offset

Every amplifier has an offset voltage between the inverting and non-inverting pins. This offset can have a significant effect on the square wave frequency response as shown in work by Watmuff [41]. An increase in amplifier voltage offset is accompanied by an increase in the ringing frequency of a response and a decrease in the exponential decay rate of the signal amplitude. The OP-37 is a good operational amplifier because it has a low fixed offset voltage. This results in a near optimum response to any input. It is possible to hard wire in a null potentiometer with the operational amplifier to control the amount of offset voltage. Some offset voltage is required to make the circuit "start" when power is supplied to the op amp. However, less offset in the op amp provides a more optimal response. There is a point where it is acceptable to trade off settling time for ringing frequency so it is a good idea to include an offset potentiometer for the op amp to provide some control over the response shape.

3.2.4. Inductance Compensation

In order to make the response appear to be very third order, the design can include a way of adjusting the inductance compensation in the Wheatstone bridge of the circuit. Some amount of inductance is present in the cables between the sensor and the anemometer circuit. Because an inductor in a feedback circuit can sometimes act like a capacitor, an increased ringing can be introduced through mismatched inductance between the cable and the anemometer (similar to stray capacitance). One way of compensating the ringing is to place a variable inductor between the control resistor and ground. This provides control over the damping of the ringing oscillation. In reality, changing the inductance in the circuit changes the location of the zeroes and poles that determine system stability (Watmuff [41]), but that is beyond the scope of this discussion.

3.2.5. Noise Considerations

Noise reduction is an important consideration in the design of a high-speed constant temperature anemometer when the goal is to measure instability waves. There are certain guidelines to follow when designing the circuit. The first most important guideline is to shield the circuit from the power supply and radio waves. If the shields are in any way connected to the circuit, the shields should be grounded. Wire groupings such as the positive, negative and ground wires that come from the power supply should be braided together so that the electromagnetic radiation picked up by each wire cancels each other. Other wires can be shielded using shielding cable, or simply using shielded cable in its place. Components should be placed close together on the board to decrease lead length between components. In addition, the number of necessary components should be minimized. This is particularly true for high speed electronics where the introduction of any additional component may decrease the stability of the circuit. If possible, sockets for IC's should be avoided. Though good gold contact sockets are available, the potential for loose contact and increased stray capacitance arises. Cable lengths can be minimized to decrease the amount of capacitance that is present due to coaxial cable. Precision resistors can be used wherever possible to avoid the increased noise associated with thermal drift. Along the same lines, heat sinks can be placed on power components such as transistors to avoid thermal drift. High quality switches should be used wherever possible if it is in the feedback loop. This will also decrease the possibility of stray capacitance that would lead to circuit instability.

3.2.6. Overheat Setting

Overheat is the primary means of determining how fast the sensor will respond to a change in imposed conditions. The overheat is set by changing the control resistance in the Wheatstone bridge. Because it is in the feedback loop, the means of setting the

control resistance becomes vital. Many anemometers allow a variable setting through a potentiometer or switch array. The best way to set the overheat is to use a fixed resistor value. This eliminates the stray capacitance that is associated with switches and pots. Therefore, it provides a cleaner, more stable circuit.

3.2.7. Current Limitation

If a circuit is going to be designed so that it operates with a fixed rather than variable resistance, then an important consideration is the amount of current that the circuit sends through a sensor at start-up. It is best to design a circuit with some form of current limitation or soft start-up so that a current surge is not imposed on the sensor. One way is to place a resistor on the power line that limits the amount of current that the transistor can dump to the Wheatstone bridge. An adjustable current limiting resistor can then be used to start the circuit with a low current level and then increase the current capability once the circuit is running.

3.3. Optimizing Towards Final Circuit Configuration

The anemometer circuit went through three major stages during the course of this thesis work. All changes were made in order to make it operate with a higher frequency response and lower noise levels while maintaining a robust design that could operate with several different types of sensors. Initial testing was done with a configuration referred to as Anemometer Configuration Prototype (AC-P). After proper anemometer behavior was established, changes were made which resulted in Anemometer Configuration 1 (AC-1). This configuration was a high speed, low noise version of AC-P, yet it still lacked some of the fine tuning that could be accomplished with the anemometer circuit. Additional testing was performed that led to Anemometer Configuration 2 (AC-2). This

configuration became the primary configuration for all voltage and velocity testing that followed (see Appendix A).

3.3.1. Electronic Testing

In order to test and optimize the circuit, electronic testing was used. In particular, square wave testing was performed in order to quantify the effects of minor architectural changes in the anemometer. The anemometer configuration to be tested was set up by connecting a ground referenced Hewlett Packard function generator to the Wheatstone bridge next to the inverting input pin on the operational amplifier and the anemometer output was hooked up to a Gould DSO 400 digital oscilloscope as well as a Hewlett Packard multimeter in order to monitor both the response event and the DC voltage level (see Fig 3.3). A square wave was defined with both frequency and amplitude and then applied to the operational anemometer. The frequency of the square wave was established by making sure that the anemometer ringing due to the front end of the square wave decayed before the trailing end of the square wave arrived. The Gould DSO 400 could be set to capture a single shot of the response event based on the voltage rise that occurred due to the applied square wave allowing the digital data to be dumped to a computer via a RS432 connection for permanent record and future analysis.

3.3.2. Anemometer Configuration Prototype (AC-P)

In the AC-P design (see Fig 3.4), an OP-27 operational amplifier was used in the anemometer circuit with TSI 1210-60 and -20 hot films as well as a 1210T-1.5 hot wire to confirm proper operation and circuit stability. The first task was to increase the circuit speed which was done by trading the OP-27 for an OP-37 operational amplifier (see Figure 3.5). Noise levels were found to be about 50 mV and stability was poor for some overheat settings with the digipot. Removal of the milliameter was found to reduce

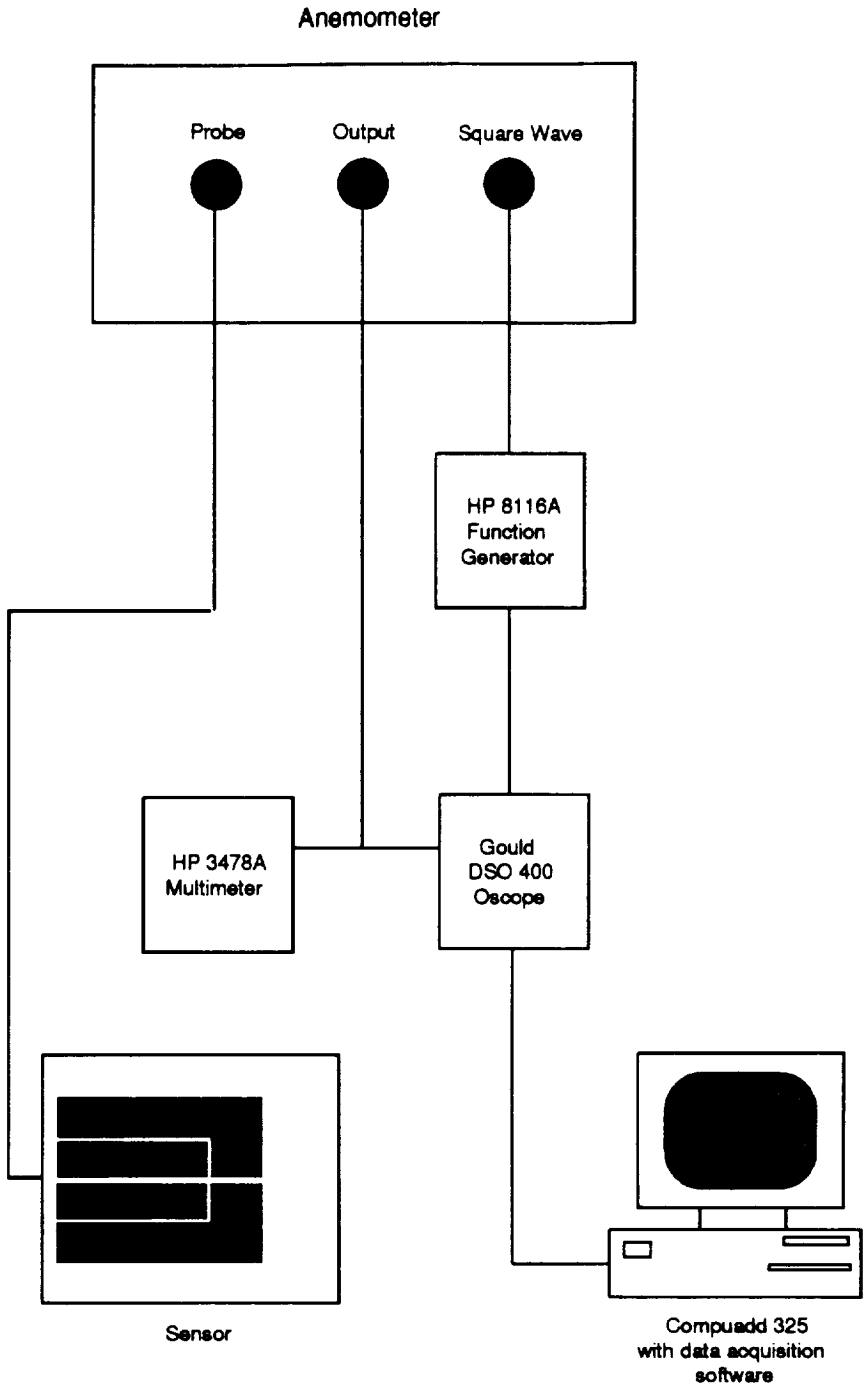

Figure 3.3. Schematic of setup for electronic testing of anemometer configurations

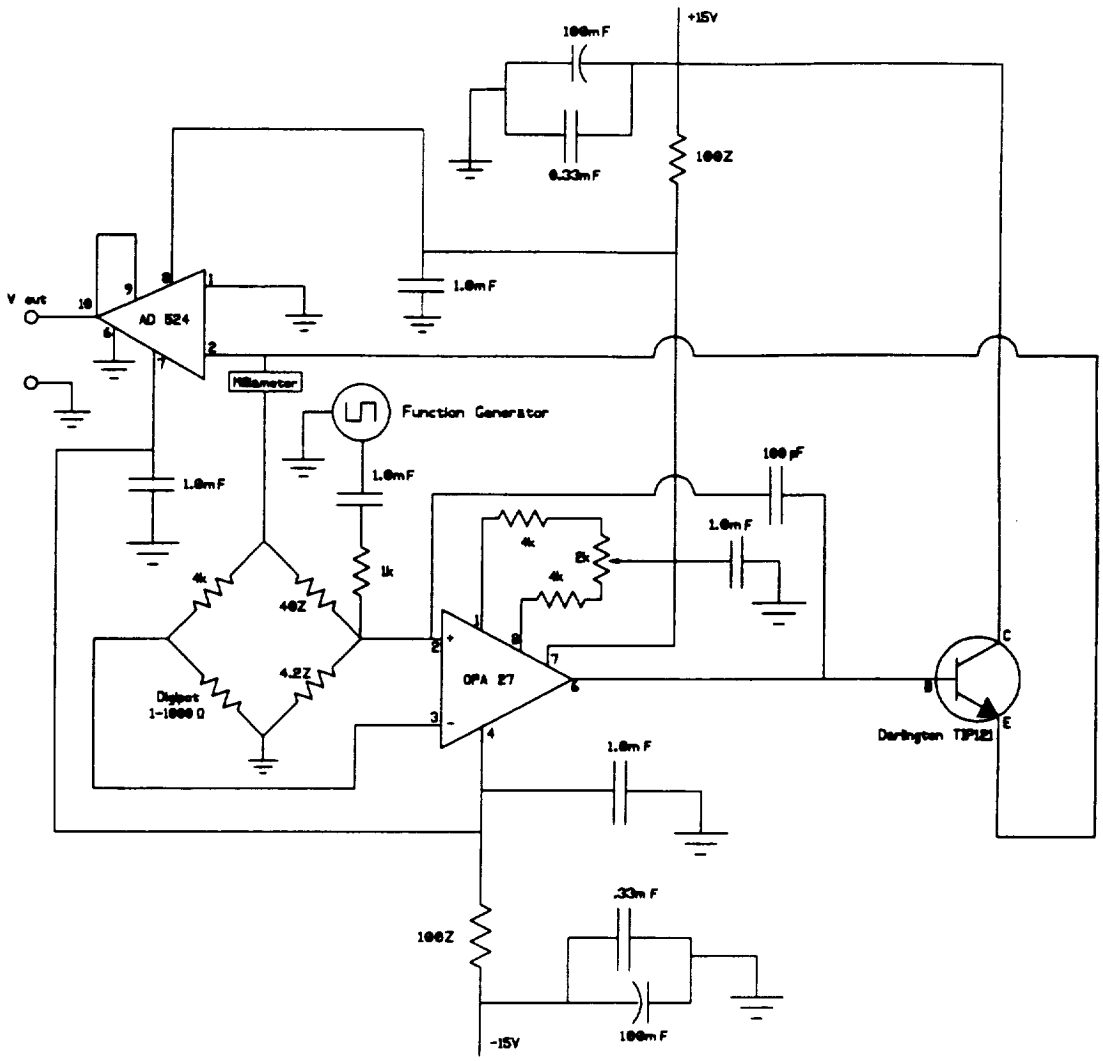

Figure 3.4. Schematic of Anemometer Configuration Prototype used for original circuit run testing

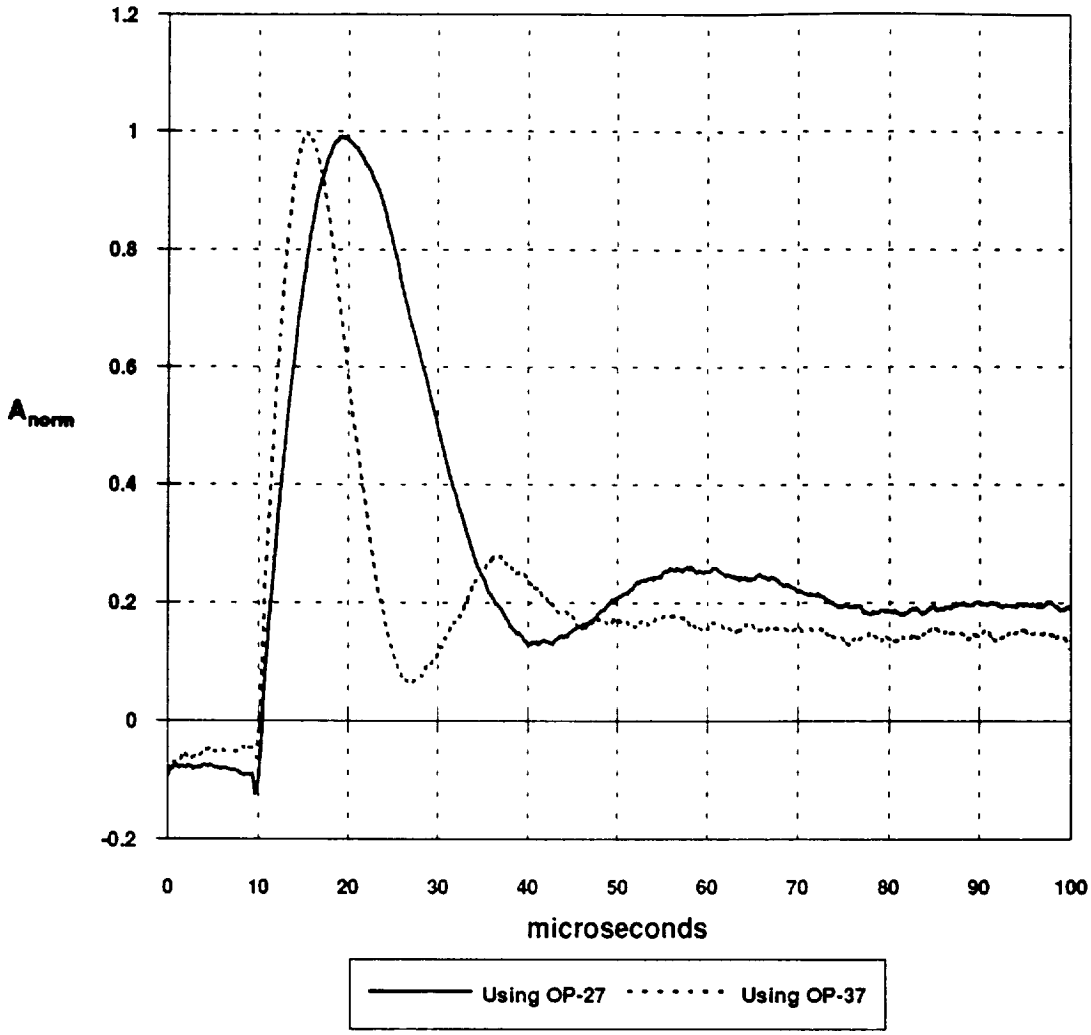

Figure 3.5. Comparative responses to voltage step for the compensated OP-27 and decompensated OP-37

noise by approximately 50% and subsequent replacement of the digipot with a fixed resistor was found to decrease the noise by an additional 80%. Using a fixed resistor required controlling the amount of current that surged through the sensor at anemometer startup. This was done by placing a resistor in the power line that fed to the transistor in the feedback loop.

Significant problems with instability were decreased by using shorter cable lengths (decreased capacitance) between the sensor and anemometer, and elimination of the digipot virtually eliminated remaining instability problems. Problems were further reduced by adjusting the offset null in the operational amplifier to avoid the unstable switching between positive and negative feedback. Finally, eliminating all possibilities of ground loops gave a clean, stable circuit that operated with approximately 3 mV of noise peak-to-peak. This final configuration was called AC-1.

3.3.3. Anemometer Configuration 1 (AC-1)

For AC-1 (see Figure 3.6), operational characteristics were good, but changes could be made that improve the circuit's tunable characteristics. The issue of current limiting presented a problem in itself. Increasing the overheat was accompanied by an increase in the amount of current surging through the sensor at startup as well as during operation. Smaller resistors were needed so as not to current restrict standard anemometer operation running at high overheats, but larger resistors were needed to handle the current surges that accompany startup. Therefore, a 500 Ω Spectrol precision potentiometer was installed to provide control over the amount of current limiting resistance during operation. This caused an increase in the noise level to approximately 8 mV peak-to-peak, but the tradeoff was considered to be acceptable for the remainder of the work, knowing that 3 mV noise levels were possible.

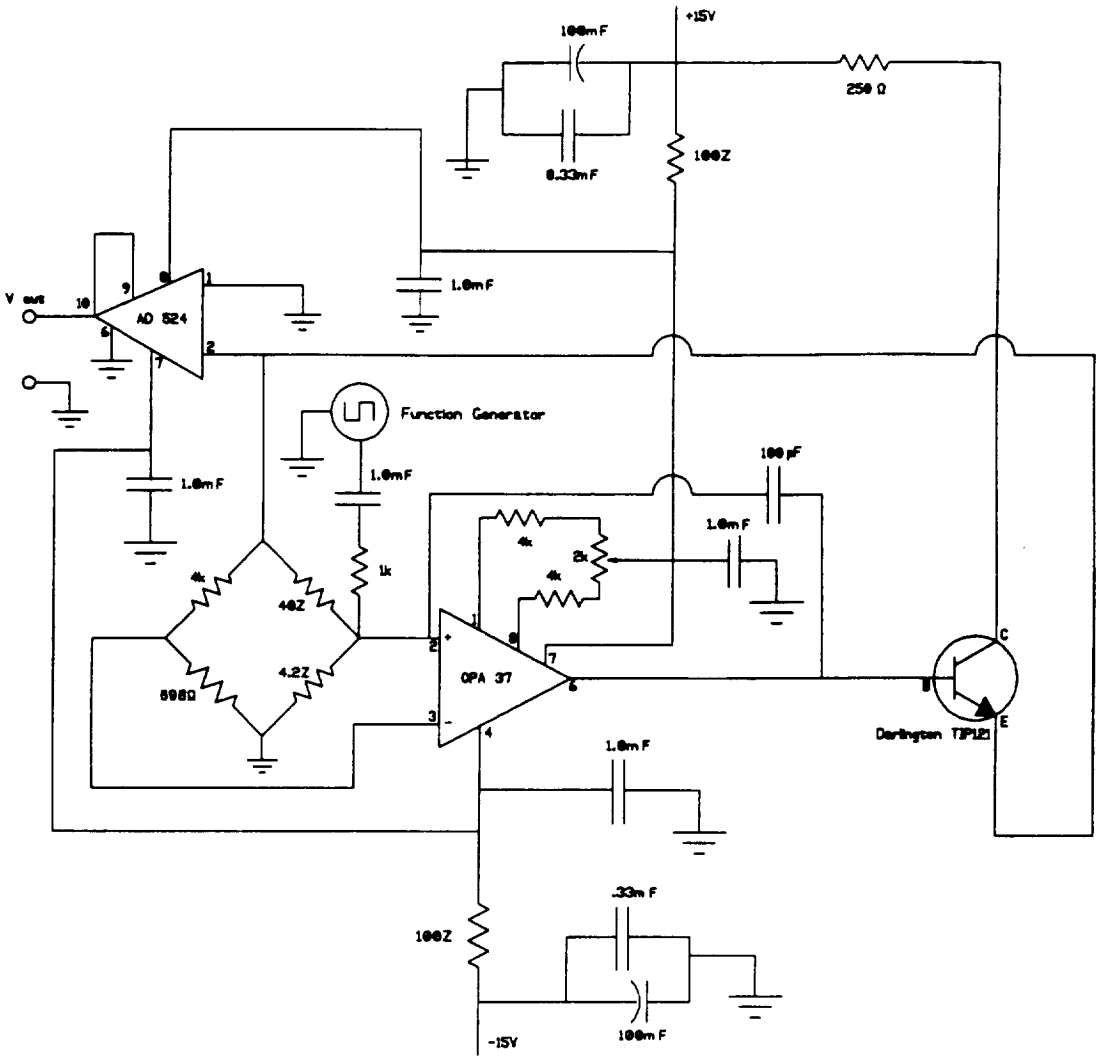

Figure 3.6. Schematic of Anemometer Configuration 1 used for voltage step testing and later improved upon

A trim capacitor was installed around the operational amplifier in place of the 100 pF capacitor as a means of controlling the roll-off frequency of the operational amplifier. The gain of an operational amplifier in closed loop mode rolls off at a frequency indicated by its gain bandwidth product. A capacitor can be used to make the operational amplifier roll off prematurely. This would be of interest if the high frequency end of the operational amplifier is causing unstable behavior. No increase in noise resulted from this component.

A 11-64 μH variable inductor was installed in the bridge between the control resistor and ground. As discussed earlier, the variable inductor can be used to alter the shape of the response. Figure 3.7 shows how this shape was altered by varying the inductance through the available range. With shielding, the noise level while using the inductor increased to about 20 mV. The presence of the inductor coil was difficult to shield against in the airport environment of the Aerospace Sciences Laboratory.

Finally, resistors were placed in series with the input pins of the operational amplifier as well as the base of the transistor. The resistors act to balance and isolate the two inputs thereby increasing the impedance of each operational amplifier input post looking out to the input signal. The resulting control of current leakage and matching of impedances tends to increase the operating speed of the anemometer circuit. The design that resulted from the testing of AC-1 is called AC-2. The response of AC-2 to a square wave is compared to AC-1 in Figure 3.8 where AC-2 has a faster response due to the architectural changes.

3.3.4. Anemometer Configuration 2 (AC-2)

The AC-2 anemometer circuit (see Figure 3.9) is the circuit that all major voltage and velocity step testing was performed with. It is understood that this architecture is only one design in a large field of anemometer designs. The particular architecture

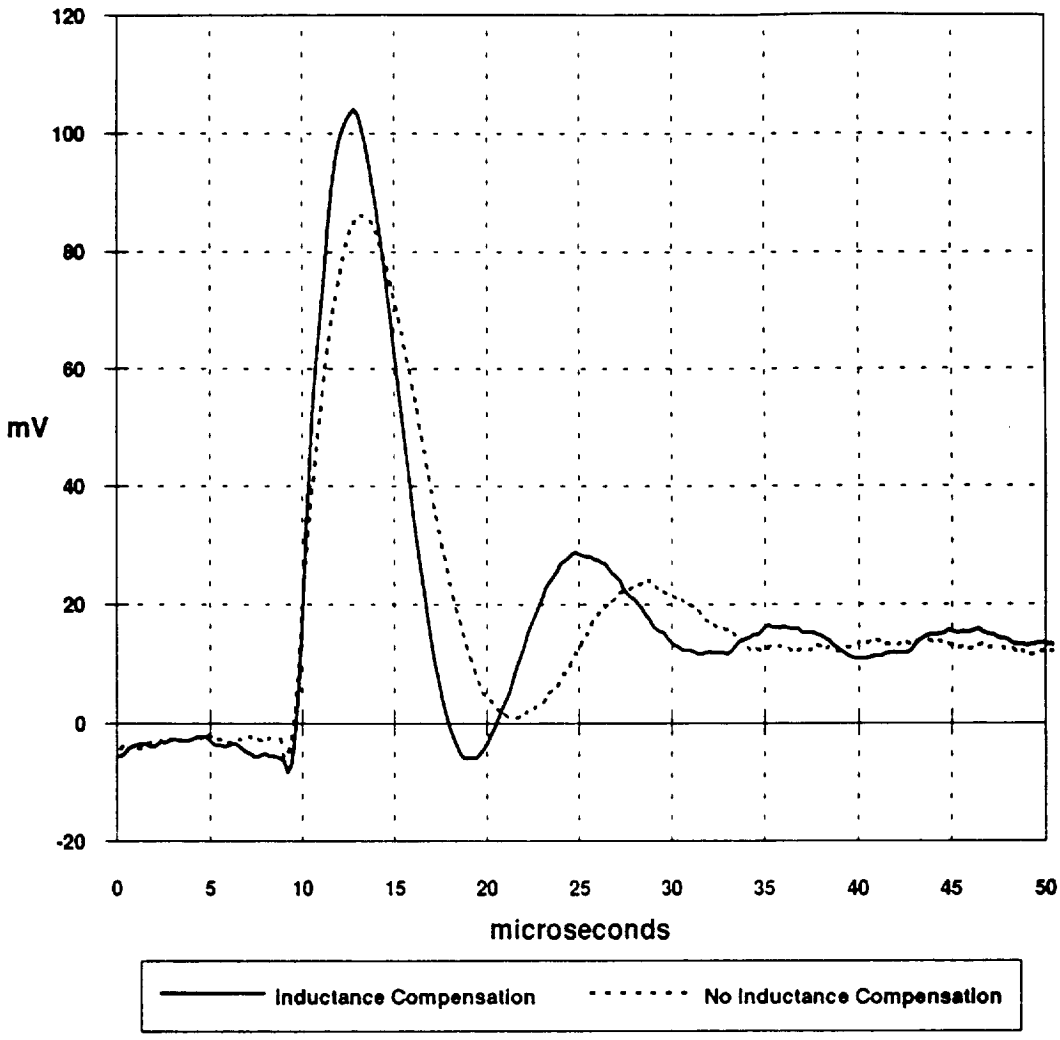

Figure 3.7. Anemometer response to voltage step with and without inductance compensation

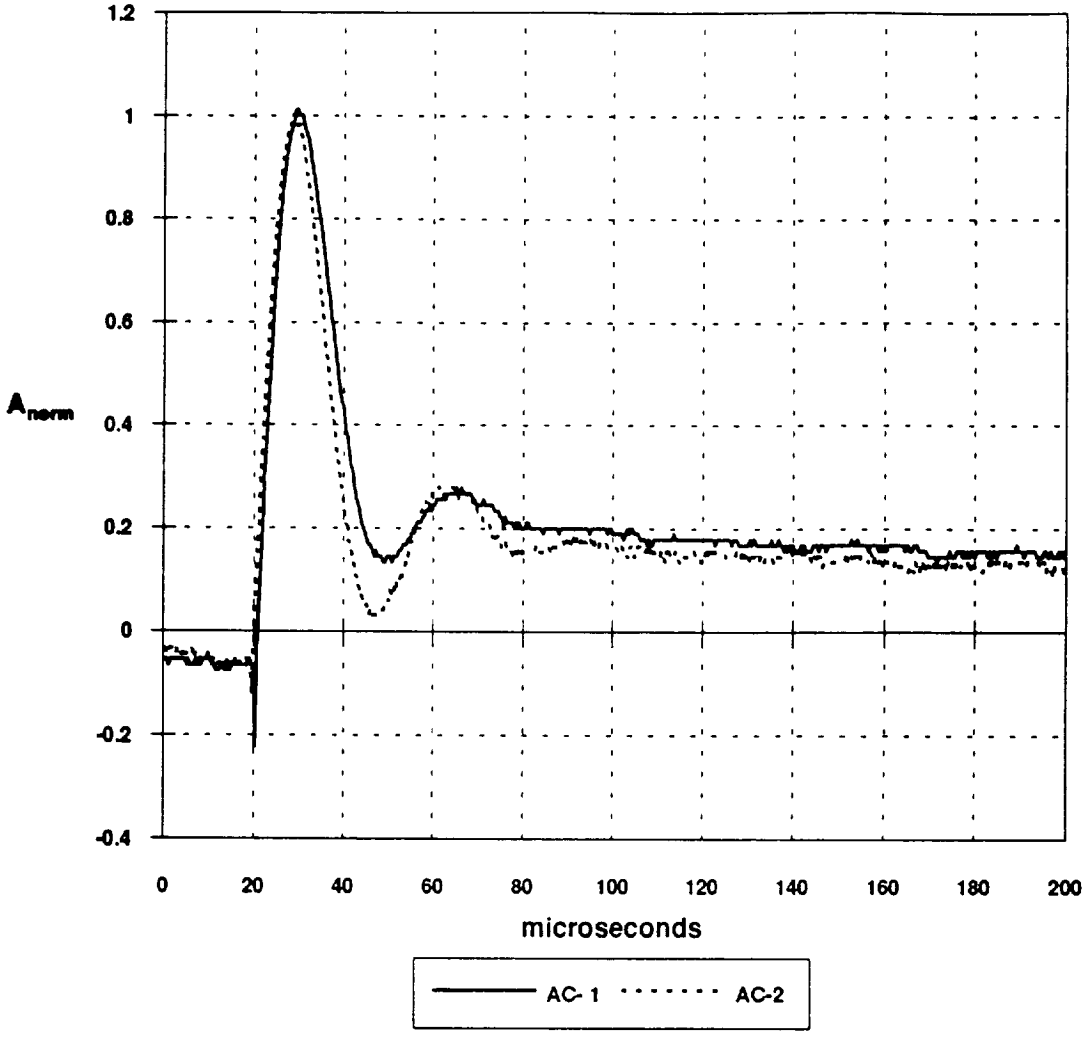

Figure 3.8. Comparative responses to voltage step for AC-1 and AC-2

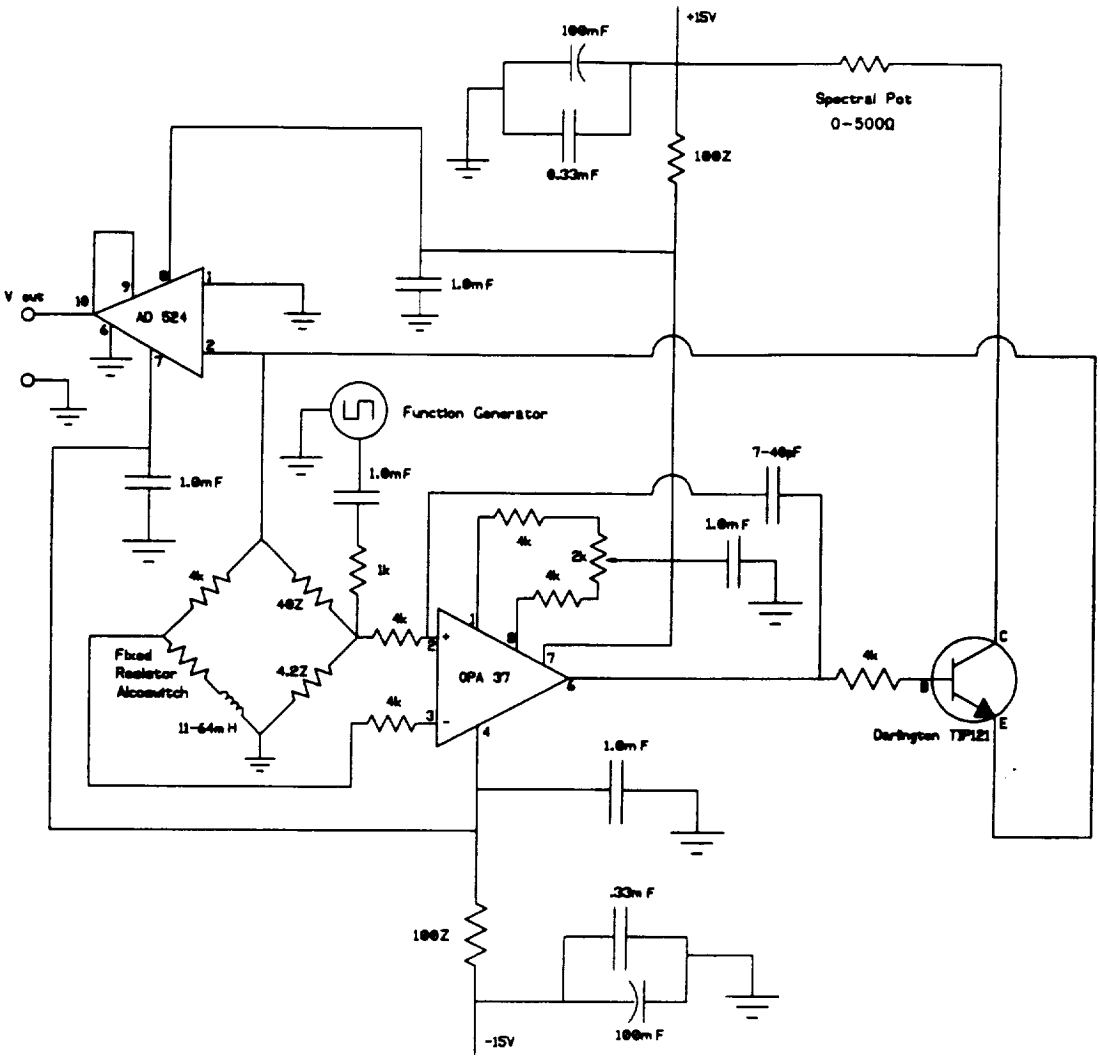

Figure 3.9. Schematic of Anemometer Configuration 2 used as the final configuration for voltage step and velocity step testing

employed for the anemometer design in this thesis is chosen primarily for historical reasons. Because the op amp is set on open loop gain, a higher gain is achieved, but a lower roll-off frequency might be experienced. Answers to the cutoff frequency are partially addressed by running square wave tests with other anemometer architectures and our anemometer appears to be narrowly outperformed by a commercial IFA-100 anemometer designed by TSI . Further gains in frequency response might be achieved by running the op amp with closed loop gain. However, this would sacrifice the sensitivity of the anemometer to detecting velocity and voltage step phenomena.

4. OPTIMIZATION, USE AND ANALYSIS OF FILM SENSORS

4.1. Experimental Methods and Approach to Parametric Study

Sensor testing comprised two main phases. The first phase was electrical testing through the application of both sine waves and square waves. The second phase was flow testing through the use of a shock tube to create velocity steps. The resulting data was compared to trends predicted by different theoretical models for both electrical and thermal properties of the anemometer/sensor system.

The purpose of this research was to study ways of improving the operational speed of anemometer systems. Therefore, the most useful and significant parameter that was obtained through both velocity step and electrical testing was the frequency response. Square wave testing provided a good measure of the frequency response and allowed further refinement of the anemometer for an optimally tuned response. Sine wave testing was used to analyze a particular adjustment for both frequency response and sensitivity. Velocity step testing also resulted in frequency response data, but this data was obtained for real flow situations with varied heat transfer conditions rather than the static case obtained through the electrical testing. In both phases, the sensor dimension and substrate material were independently varied to draw comparisons.

In general, there is a trade-off between sensor frequency response and signal sensitivity. Therefore, another significant parameter that was used to evaluate the operation of the anemometer system was the sensitivity. This was done by recording the response amplitude for larger and larger velocity steps in the shock tube. A flush-mount hot film has a shape associated with the voltage to velocity curve. In this case, a power

series was an effective fit. With higher velocities, small velocity fluctuations become less discernible, so curve fitting the response amplitude and noting the curve slope at successively higher velocity steps gave a good indication of the sensitivity for each sensor.

Part of analyzing the sensitivity is looking at the signal to noise ratio. Making an estimation of the signal to noise ratio gives an indication of what the smallest possible input amplitude is before smaller inputs are obscured in electronic noise. This issue was also investigated through the use of the shock tube by sending successively smaller shock waves over each sensor. For each weak shock wave, the response amplitude was noted as well as the static operational noise due to interfering electromagnetic fields and stray capacitance. The same curve fit used to determine velocity sensitivity could be used to determine at what point the signal became obscured in this operational electronic noise. Once again, the sensor dimension and substrate were independently varied to study the effect of these two characteristics on overall performance.

4.2. Static Power Dissipation

Before the sensors are subjected to velocity or voltage steps, a trend is noted in the static behavior of each sensor. For each overheat there is an output voltage that may be converted into a static power dissipation. The static power dissipation is largely a measure of how much heat is dissipated to the substrate through conduction, but it also includes the heat dissipated to the surrounding fluid through free convection. Static power dissipation is determined through a simple bridge relationship for the anemometer

$$P = I_{sensor} R_{sensor} \tag{4.1}$$

where the sensor current is given by

$$I_{sensor} = \frac{V_{out}}{R_{sen} + R_{cable} + R_{sensor}} \tag{4.2}$$

Figure 4.1 shows the comparative static power dissipation for the 5, 10 and 20 mil glass sensors over a range of overheats. The dissipation is greatest for the 20 mil glass sensor which is indicative of the increased current level required to heat the larger sensor mass and surrounding substrate. In Figure 4.2, the static power dissipation is shown for the 20 mil glass, alumina and aluminum sensors. In this case, the static power dissipation is greatest for the alumina sensor followed by the aluminum then the glass. Recall that the alumina substrate also had the smallest thermal impedance followed by the aluminum then the glass. As the thermal impedance of a substrate decreases, more heat will be conducted into the substrate and the current required to hold a sensor at a constant temperature will increase.

Figures 4.3 and 4.4 are thermal images of identically sized sensors on different substrates running at similar overheats (supplied by Jim Bartlett of NASA LaRC). The pictures were taken while the sensors were in static operation (zero velocity) each with a surface temperature of approximately 165 °F. The light areas in the images correspond to the heated sensor and surrounding substrate and the dark areas correspond to the cooler sensor leads. The sensor substrate in Figure 4.3 is a 0.5 μm SiO_2 layer on 1 mm of epoxy fiberglass composite and has a much lower thermal impedance than the sensor substrate in Figure 4.4 which is made from a 0.5 mm SiO_2 layer on a 10 μm Pyralin layer. The thermal footprint for the lower impedance substrate is much smaller. The reason for this is that a high conductivity substrate will conduct more heat into the substrate relative to the amount that will be convected away from the surface. These pictures will have more significant meaning when the experimental data is obtained in the following sections for comparative frequency response and sensitivity performance.

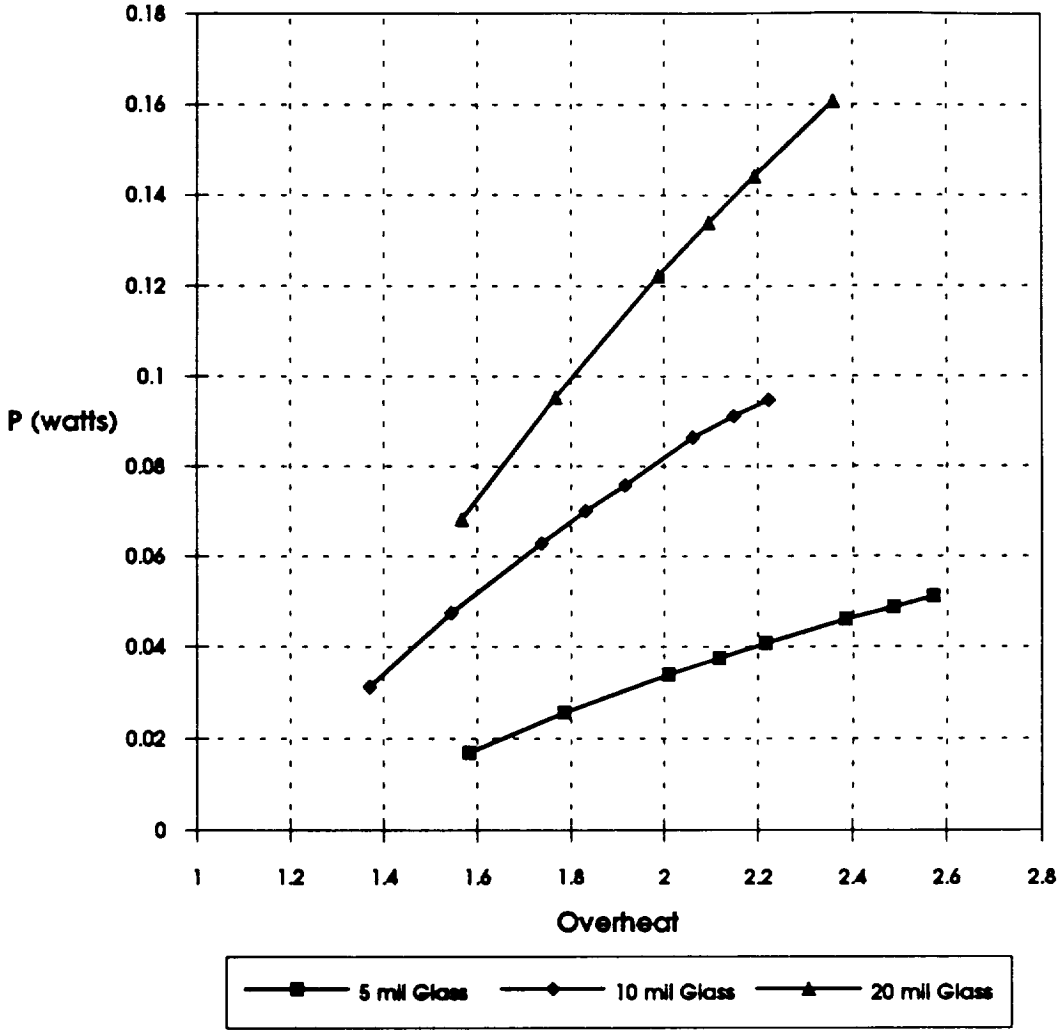

Figure 4.1. Static power dissipation (zero flow) for the 5, 10 and 20 mil glass sensors to indicate heat conducted to substrate

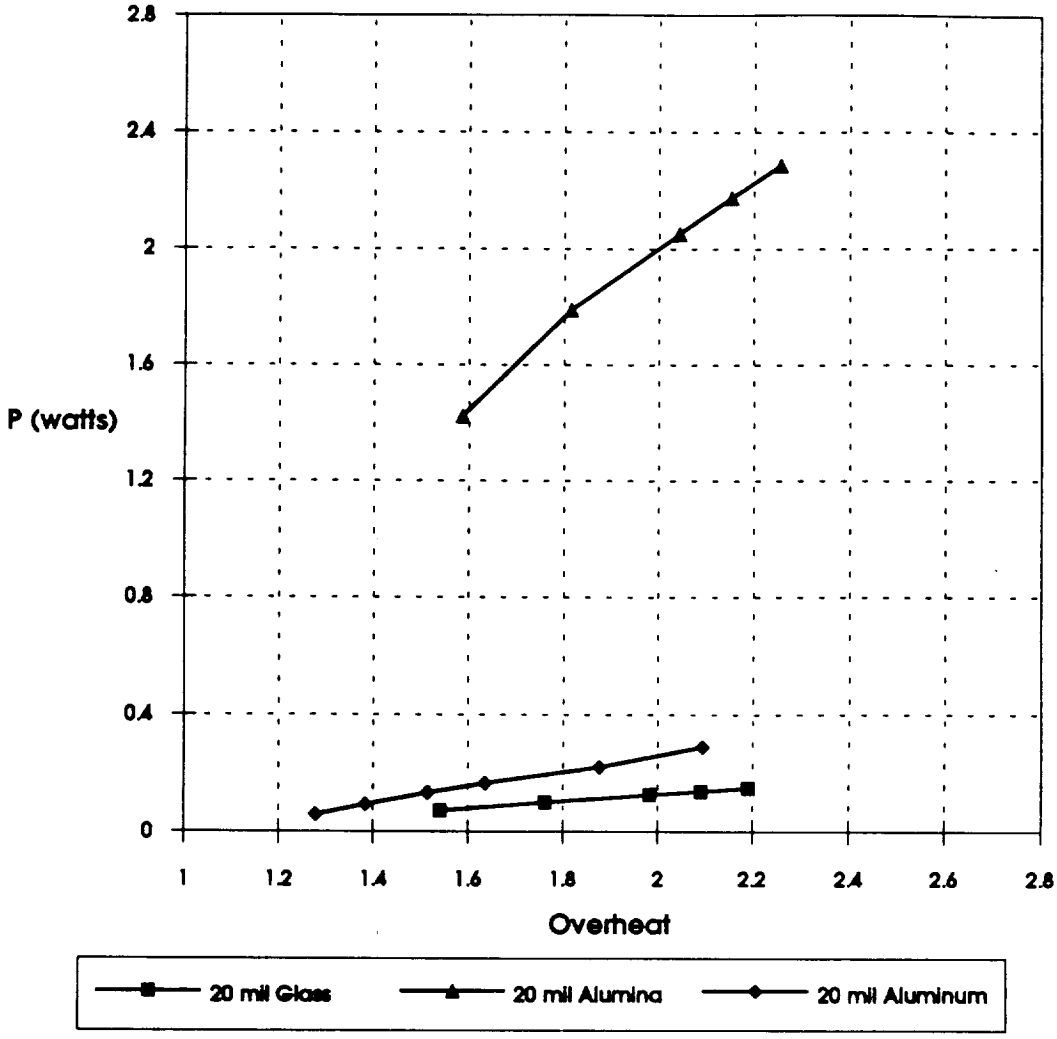

Figure 4.2. Static power dissipation (zero flow) for the 20 mil glass, alumina and aluminum sensors to indicate heat conducted to substrate

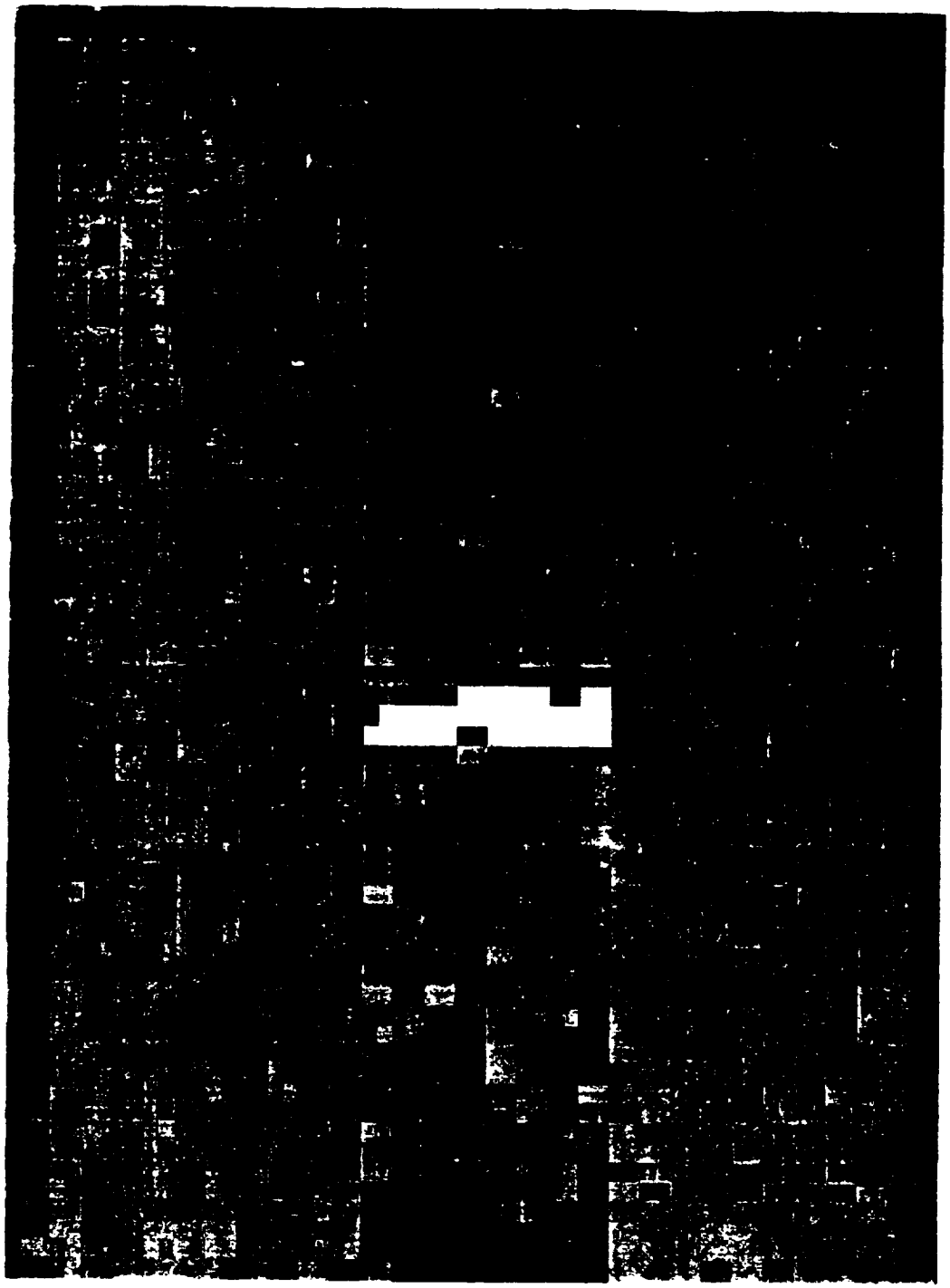

Figure 4.3. Thermal image of operational flush-mount sensor on low thermal impedance substrate (provided by Jim Bartlett of NASA LaRC)

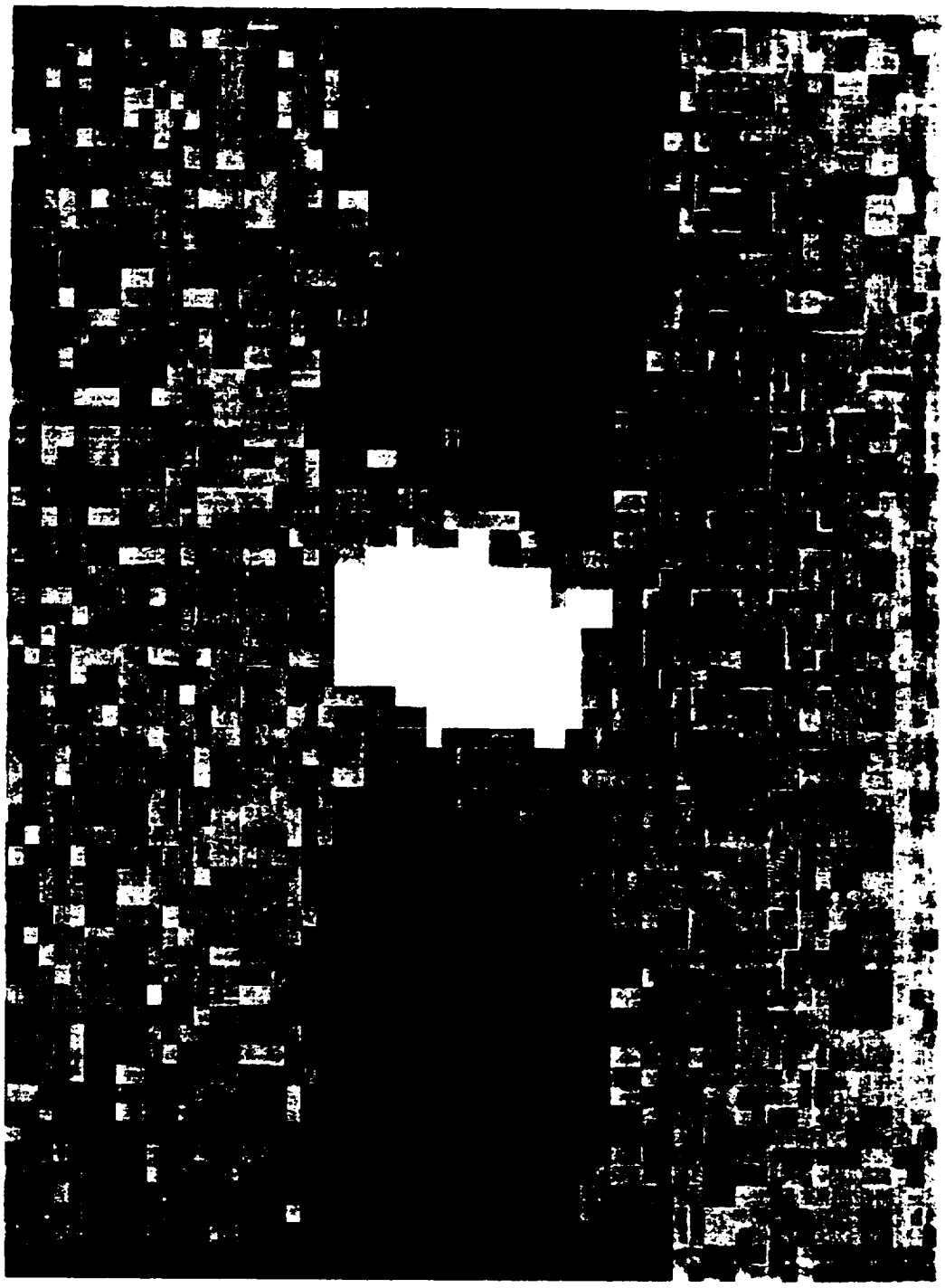

Figure 4.4. Thermal image of operational flush-mount sensor on high thermal impedance substrate (provided by Jim Bartlett of NASA LaRC)

4.3. Experimental Voltage Step Testing

Electrical testing may also be referred to as zero flow testing. It is similar to velocity step testing in that a change in resistance is forced upon the sensor. However, substrate conduction may play a bigger role in sensor operation dynamic flow testing than it does in static testing. It is through voltage step testing that system frequency response can be clearly measured and optimized.

Total system frequency response may be determined through square wave testing because it includes the effect of the sensor dimension and substrate conductivity. In the case of this research, square wave testing is performed in order to quantify the effects of sensor dimension, sensor substrate choice, and minor architectural changes in the anemometer. For each test the anemometer is set up in a configuration using one of the five sensors. The AC-2 anemometer is set up by connecting a ground referenced Hewlett Packard function generator to the Wheatstone bridge next to the inverting input pin on the operational amplifier and the anemometer output is hooked up to a Gould DSO 400 digital oscilloscope as well as a Hewlett Packard multimeter in order to monitor the DC voltage level (see Fig 4.5). Each sensor is set on a horizontal plane and exposure to major convective currents was minimized. An operational overheat is set, which is defined as the ratio of the control resistance to the sensor resistance at zero degrees Celsius. From the point at which the anemometer is turned on, the steady state voltage is monitored until it appears that the voltage change over time has slowed considerably. This helps to avoid the effect of transient heat transfer in the sensor as the substrate underneath the sensor heats up. At this point, the square wave test may begin. A square wave is defined with both frequency and amplitude and then applied to the operational anemometer. The frequency of the square wave is established by making sure that the anemometer ringing due to the front end of the square wave decays before the trailing end of the square wave arrives. The Gould DSO 400 is set to trigger a single shot of the

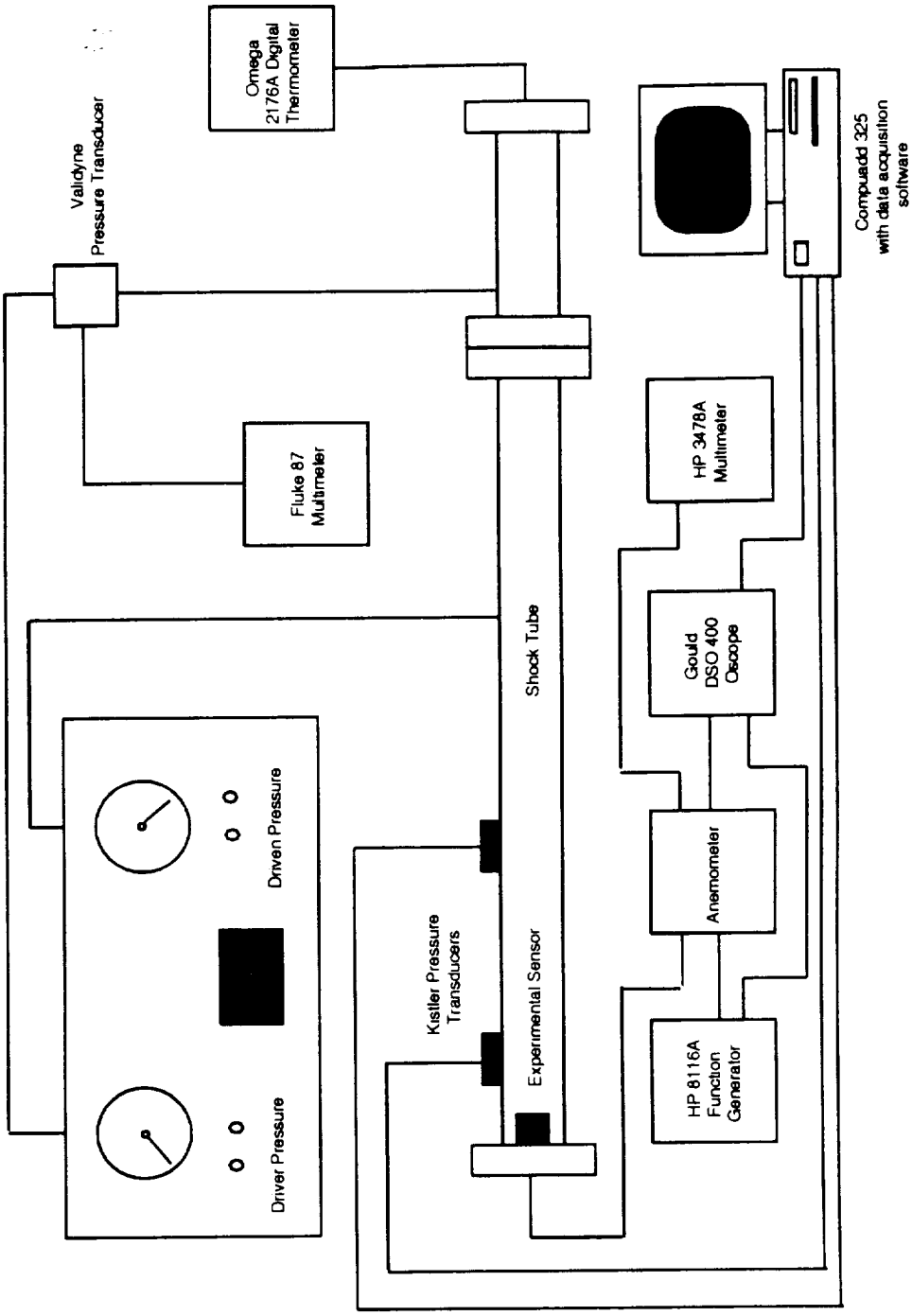

Figure 4.5. Lab setup for performing both voltage and velocity step testing of anemometer systems with sensors

response event based on the voltage rise that occurs due to the applied square wave and the digital data is then dumped to a computer via a RS432 connection for permanent record and future analysis.

One of the first results that became obvious for the AC-2 anemometer is that there is a linear relationship between the input square wave voltage and the resulting response. Figure 4.6 shows how the input square wave relates to the peak voltage of the response monitored on the oscilloscope. Because of the linear relationship, it was very easy to normalize all voltage step test response curves as follows.

$$A_{norm} = A / A_{max} \tag{4.3}$$

Therefore all preceding and following analysis that involved voltage step testing could be normalized by dividing the signal by its peak amplitude

4.3.1. Square Wave Testing and Sensor Dimension

When comparing the effects of sensor dimension through electrical testing, the only parameter of interest was the frequency response. Determination of sensor sensitivity to perturbations was left to flow testing in the shock tube. Recall that frequency response is estimated by taking the inverse of the time that it takes for a signal to respond. Frequency response can be defined in a number of ways. For example, Freymuth defines the frequency response as the point at which the output signal returns to 3% of the response maxima. For the majority of the analysis in this work, the response cut-off frequency is determined from the experimental curve as is shown in Figure 4.7. In other cases such as relating square wave testing to Freymuth's results, the 3% definition is used.

First, the 5, 10 and 20 mil glass sensors were tested for frequency response over a range of overheats while using the AC-2 anemometer. Figure 4.8 shows how the

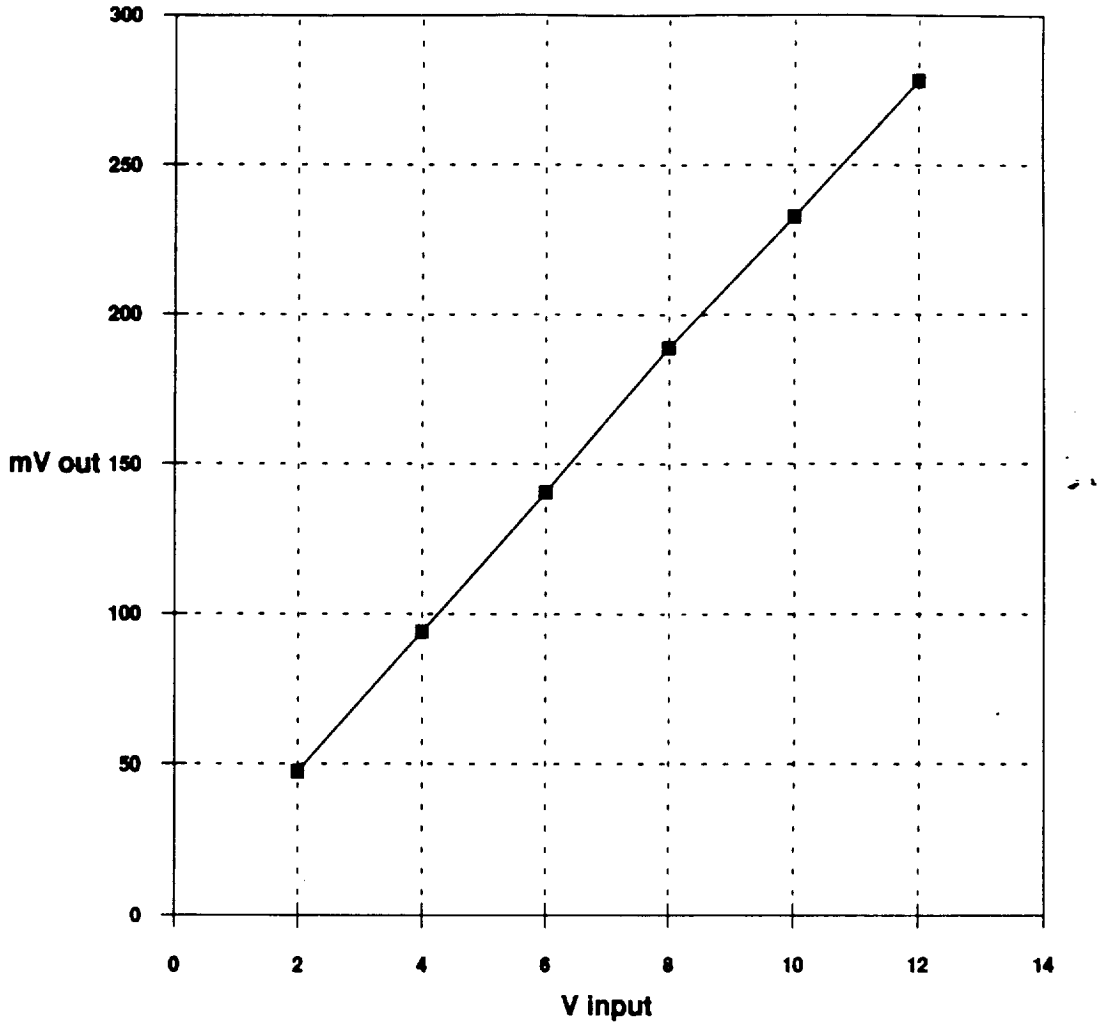

Figure 4.6. Linear relationship between input and output for anemometer square wave testing

C-2

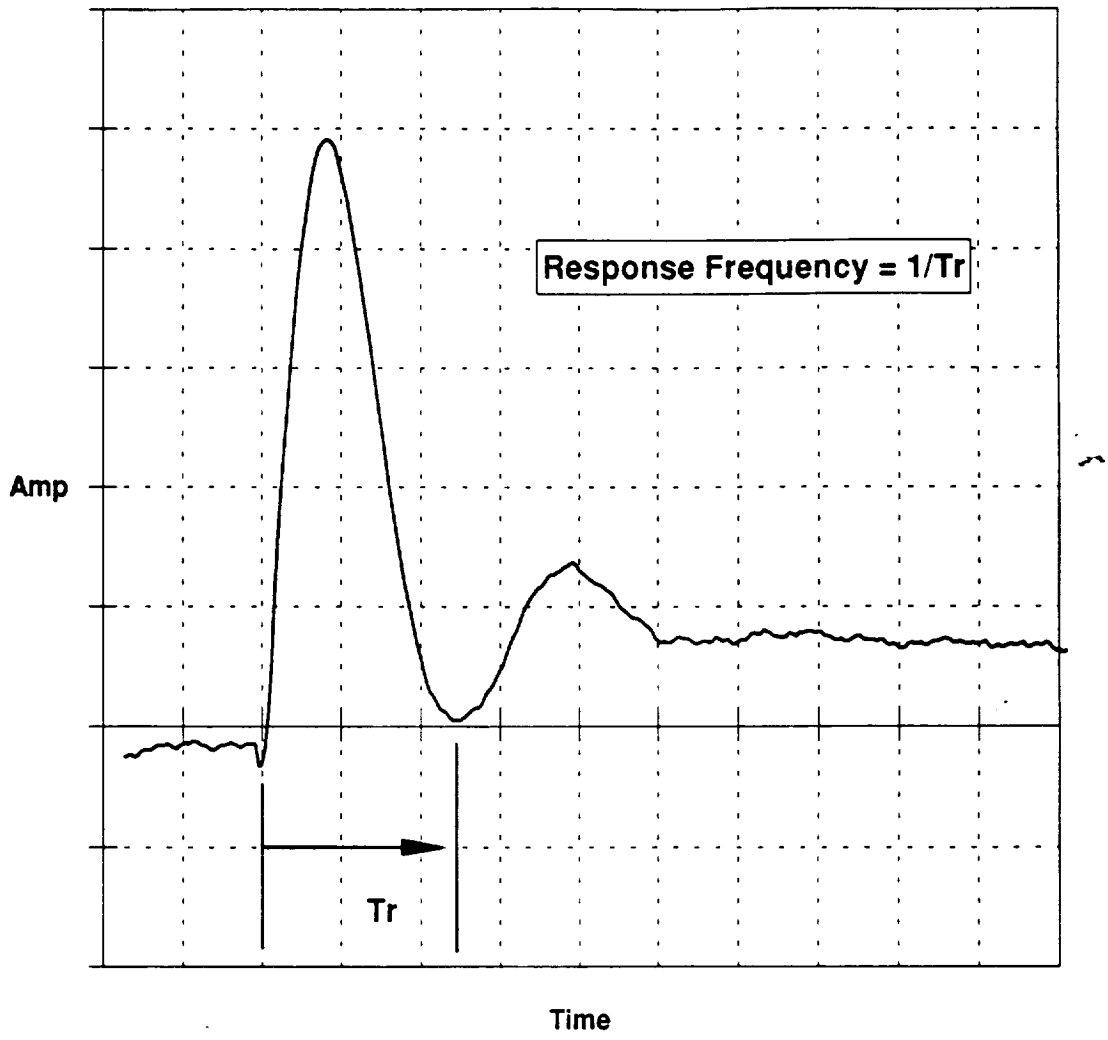

Figure 4.7. Method for determining frequency response in electronic testing

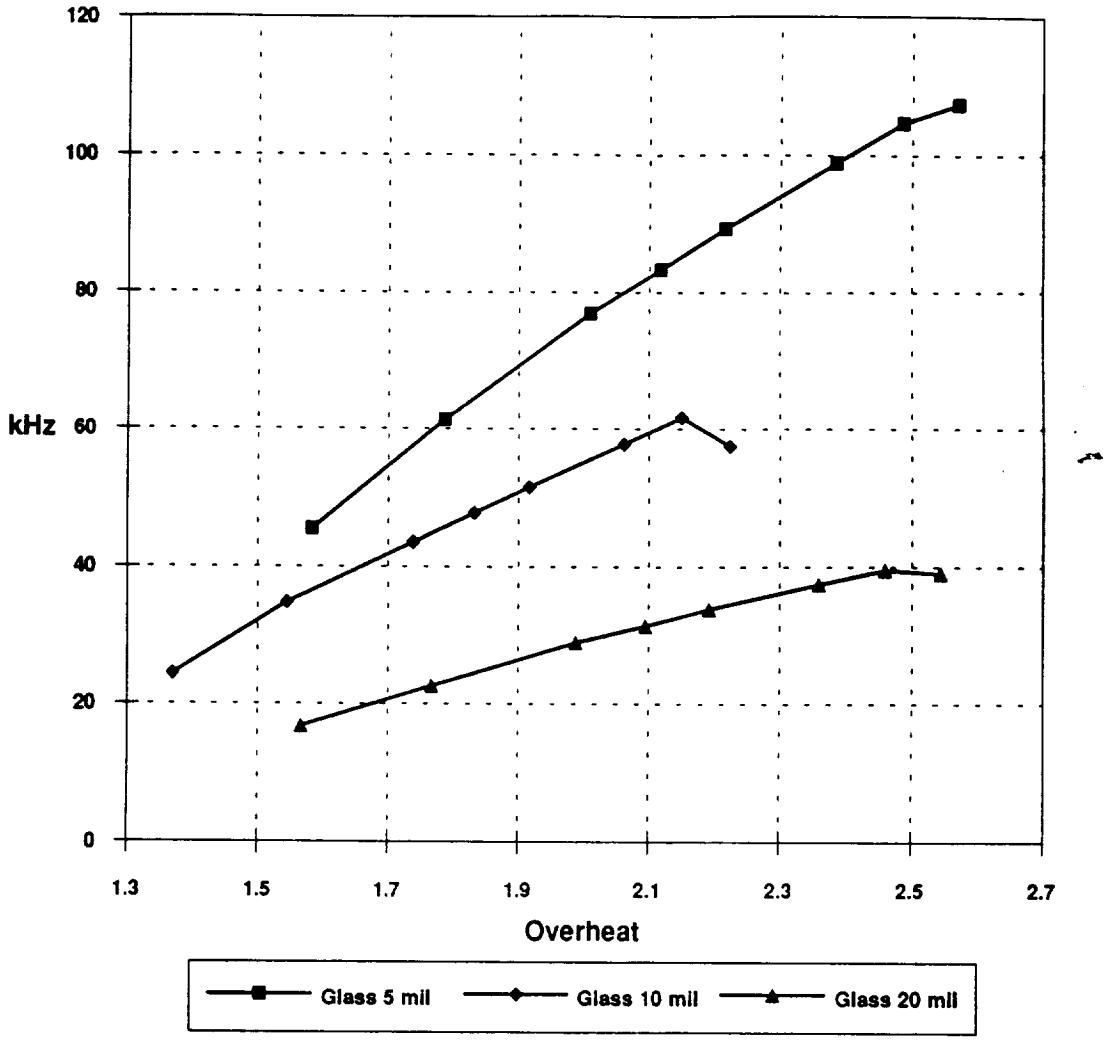

Figure 4.8. Frequency response for different overheats comparing 5, 10 and 20 mil sensors on identical substrate materials using the AC-2 anemometer

frequency response increases as the overheat is increased for all three sensors. The 5 mil glass sensor has superior performance at all overheats shown. Furthermore, for a given change in overheat, there will be a greater change in frequency response for the 5 mil glass sensor than either of the larger sensors. The best obtained frequency response in this test comes from the 5 mil glass sensor at approximately 110 kHz.

For all three sensors, there appears to be a maximum obtainable frequency response. For the 5 and 20 mil sensor sizes, the curve levels out at an overheat of approximately 2.5. Prior to the testing performed in this work, a sample sensor was tested for its maximum overheat. An overheat of 2.5 was provided by Bartlett [private communication] as the point at which sensor degradation occurred. This overheat corresponds to the leveling point for the 5 and 20 mil sensor frequency response whereas the 10 mil glass sensor leveled off at an earlier overheat of approximately 2.2. The decreased frequency response may best be explained as a result of saturation heating and film degradation.

The trends for frequency response performance were confirmed using a TSI IFA-100 anemometer (see Figure 4.9). In general, the frequency response is higher for any given overheat when using the IFA-100 rather than the AC-2. This may be attributed to the difference in bridge designs as well as the available control functions on the IFA-100 for tuning the shape of the square wave response. No clear leveling off appears while testing the 5, 10 and 20 mil glass sensors, but this was due to the fact that the maximum obtained overheat was 2.2. This overheat was not sufficient to reach the degradation point for the sensors. In the case of the 5 mil glass sensor, a frequency response of approximately 110 kHz was obtained at an overheat of 2.2 with the IFA-100. The sensor experienced a failure in a separate test before any higher overheats could be tested. However, it is approximated that the frequency response would be 120 kHz at the

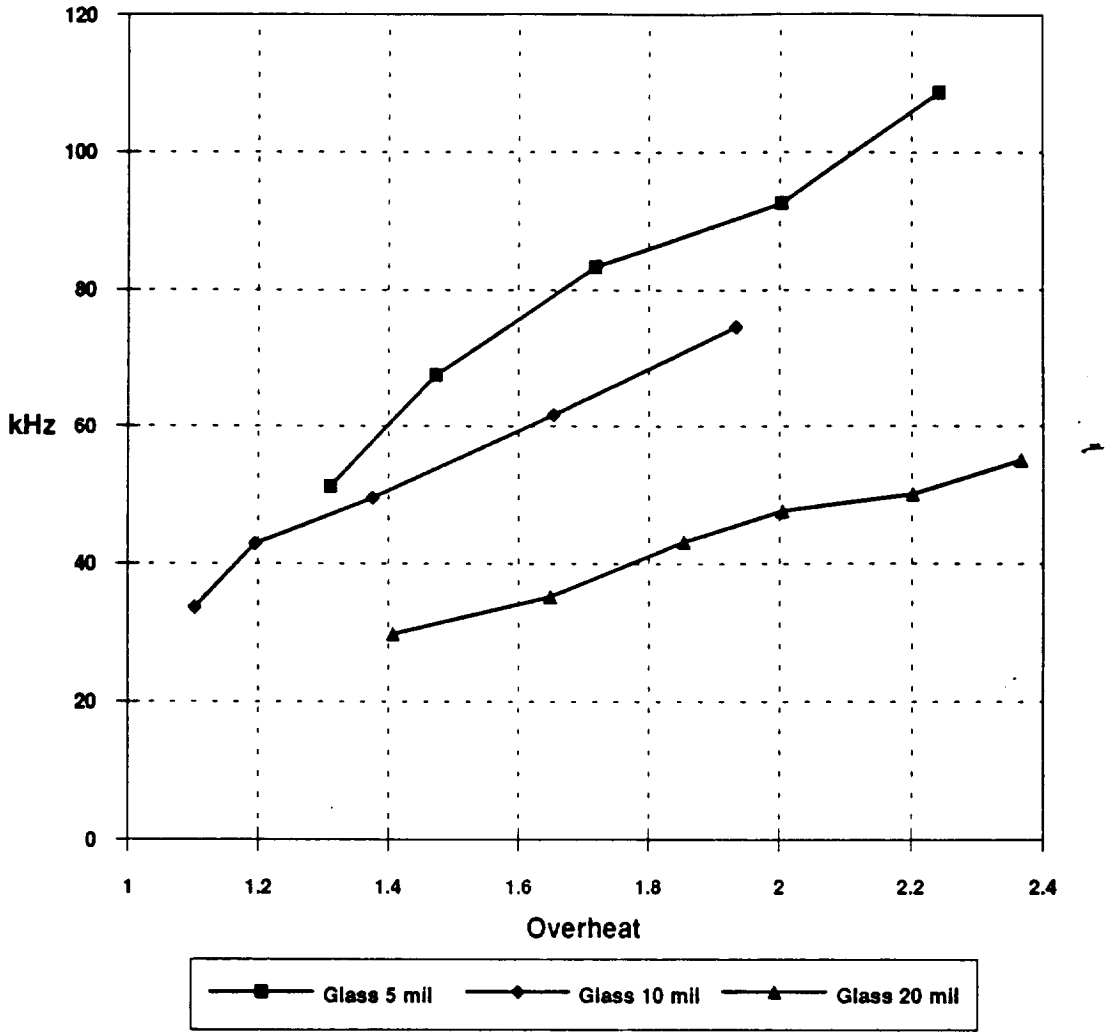

Figure 4.9. Frequency response for different overheats comparing 5, 10 and 20 mil sensors on identical substrate materials using the IFA-100 anemometer

maximum overheat of 2.5. This is only a 10 kHz improvement over the AC-2 anemometer that was built for this work.

The effect of compensating inductance on the bridge of the AC-2 was also analyzed through the voltage step test for different sensor dimensions. Figures 4.10, 4.11 and 4.12 show the three different sized sensors responding to the voltage step test with the inductance compensated AC-2, the non-compensated AC-2 and the IFA-100. In each case of inductance compensation, the inductance was increased across its entire range (11 to 64 μH) until the maximum value was reached. The previously mentioned figures show that for all three sensor sizes, the frequency response performance of the sensors in operation with the AC-2 improves with inductance compensation with the smallest sensor benefiting the most from the compensation. However, the frequency response performance is still slightly off from what can be attained by utilizing the IFA-100.

In all three cases of inductance compensation, the frequency response using the AC-2 closely followed the leveling trend at high overheats shown by the square wave testing without inductance compensation. This seems to confirm the likelihood that something is happening around high overheats near the film degradation point. It is also interesting to note that the increase in frequency response is fairly uniform across the overheat range relative to the non-compensated frequency response. The differential increase in frequency response for a range of overheats due to inductance compensation is shown in Figure 4.13. There is no clear relationship between the overheat and the increased performance due to inductance compensation. It may be that the measurements for increased performance were somewhat obscured in the measurement error on the oscilloscope so the average increase in the frequency response is given for each sensor. This plot shows that as the sensor size decreases, the average increase in frequency response increases.

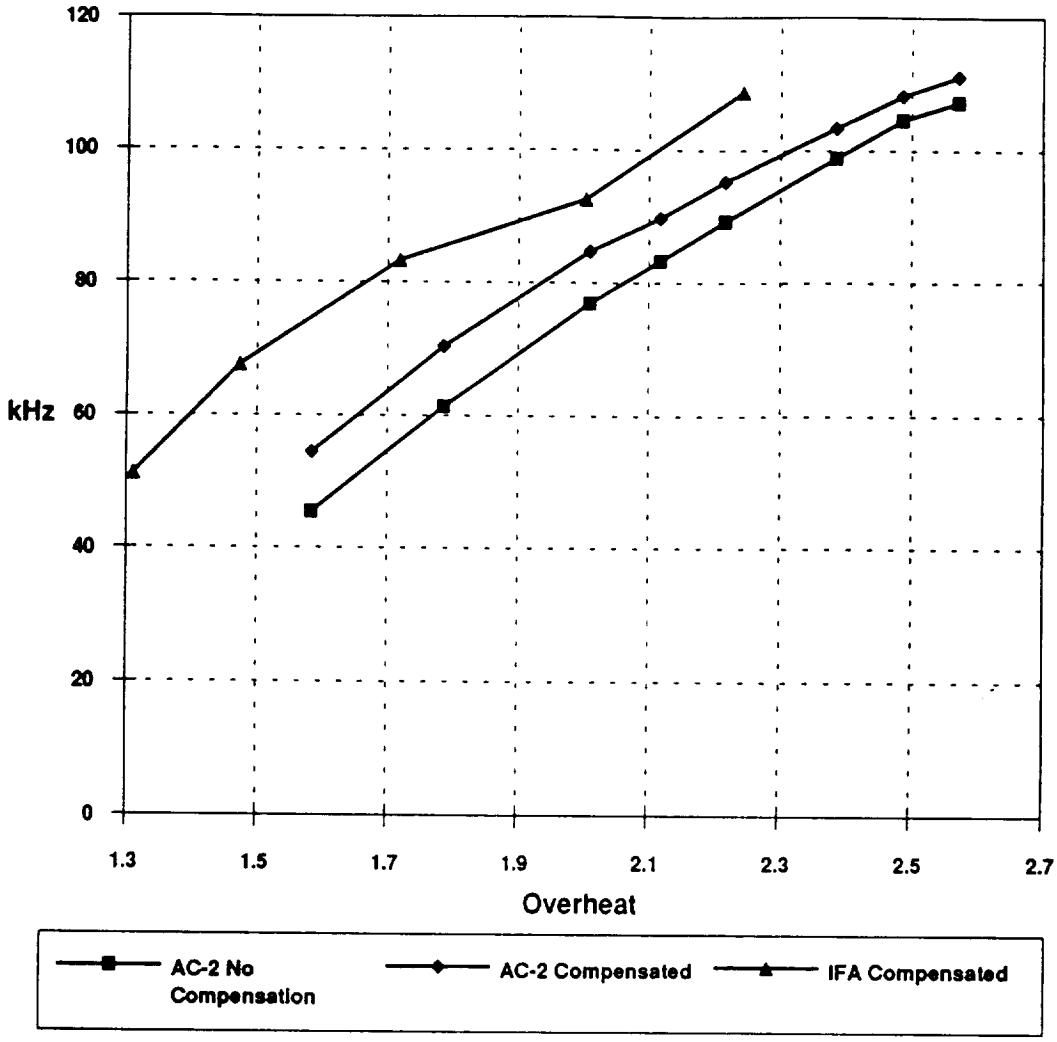

Figure 4.10. Comparison of frequency response for the inductance compensated and non-compensated AC-2 as well as the IFA-100 using the 5 mil glass sensor

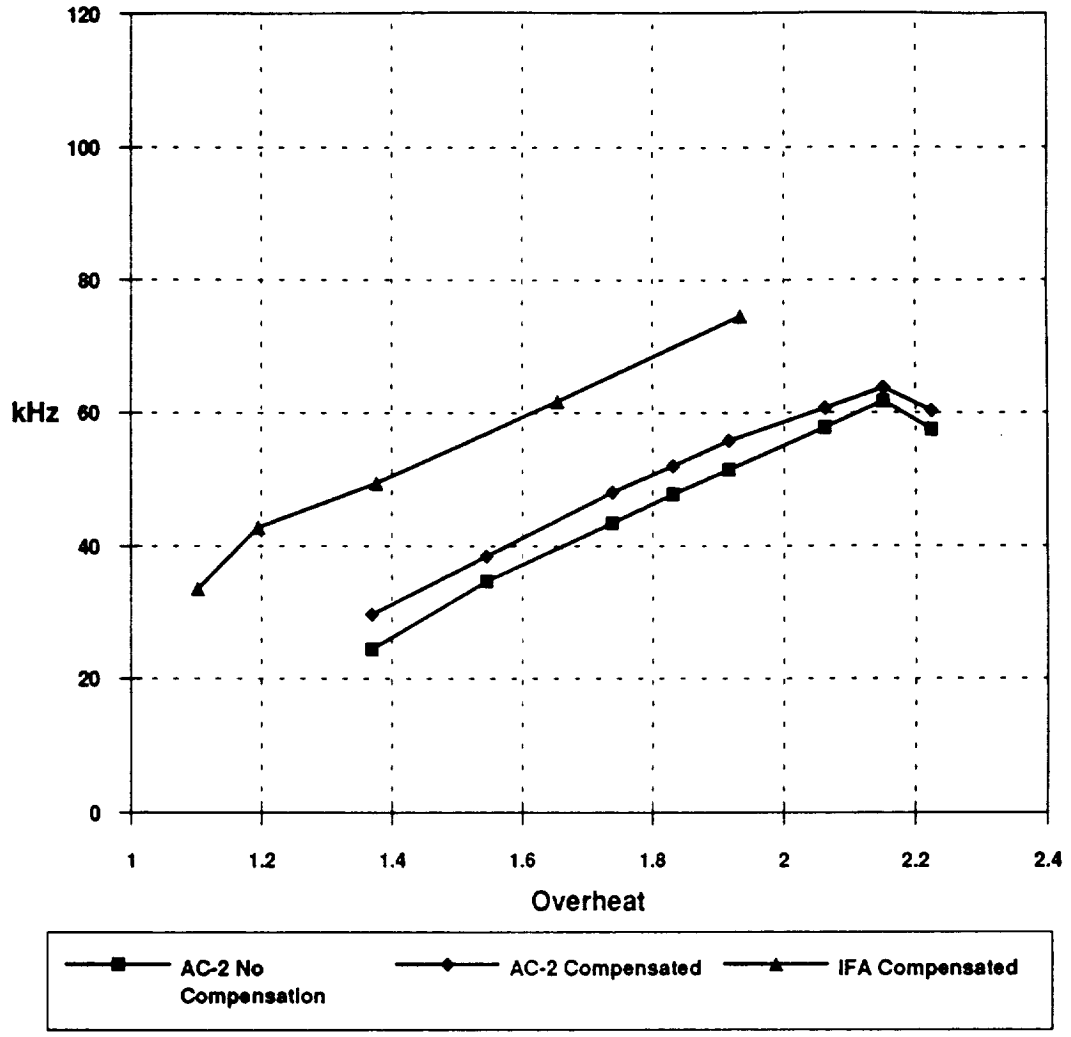

Figure 4.11. Comparison of frequency response for the inductance compensated and non-compensated AC-2 as well as the IFA-100 using the 10 mil glass sensor

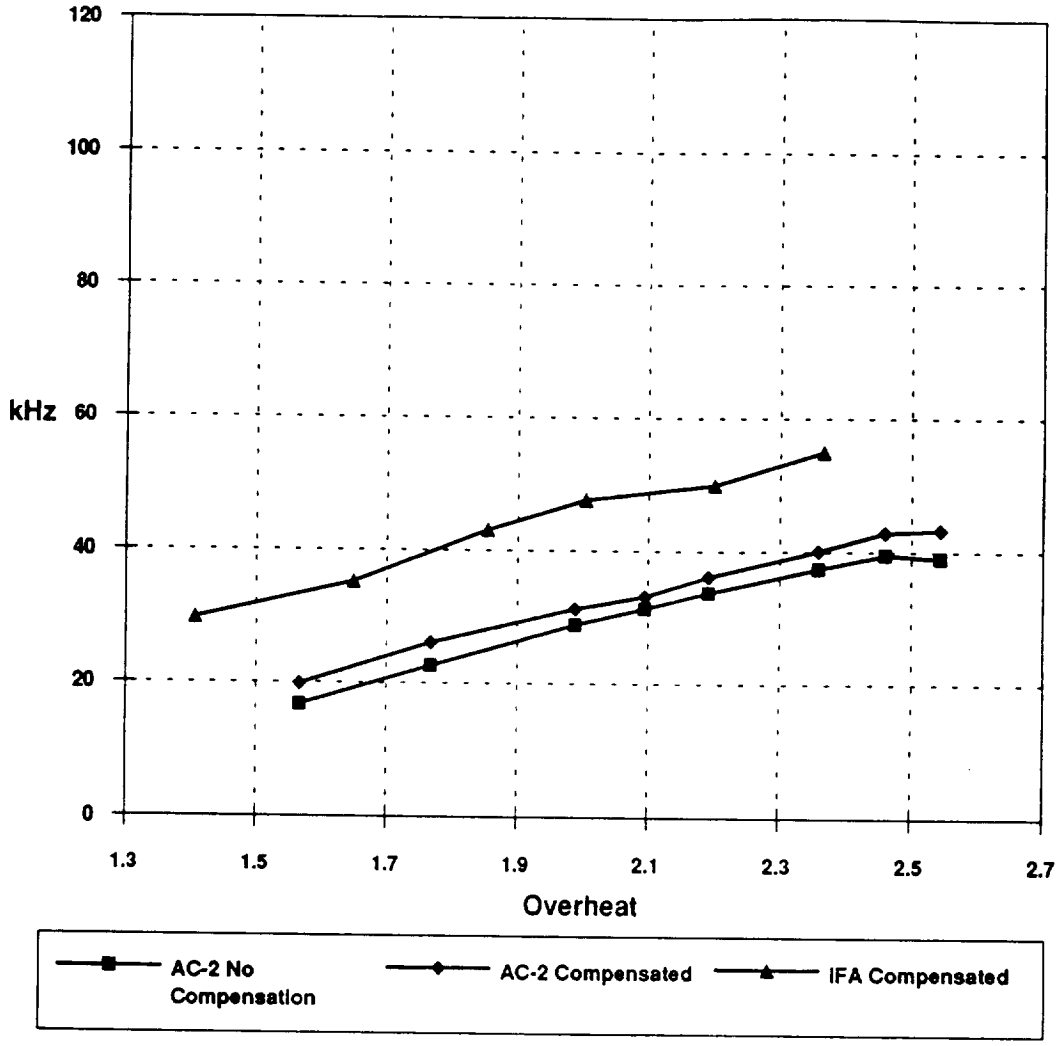

Figure 4.12. Comparison of frequency response for the inductance compensated and non-compensated AC-2 as well as the IFA-100 using the 20 mil glass sensor

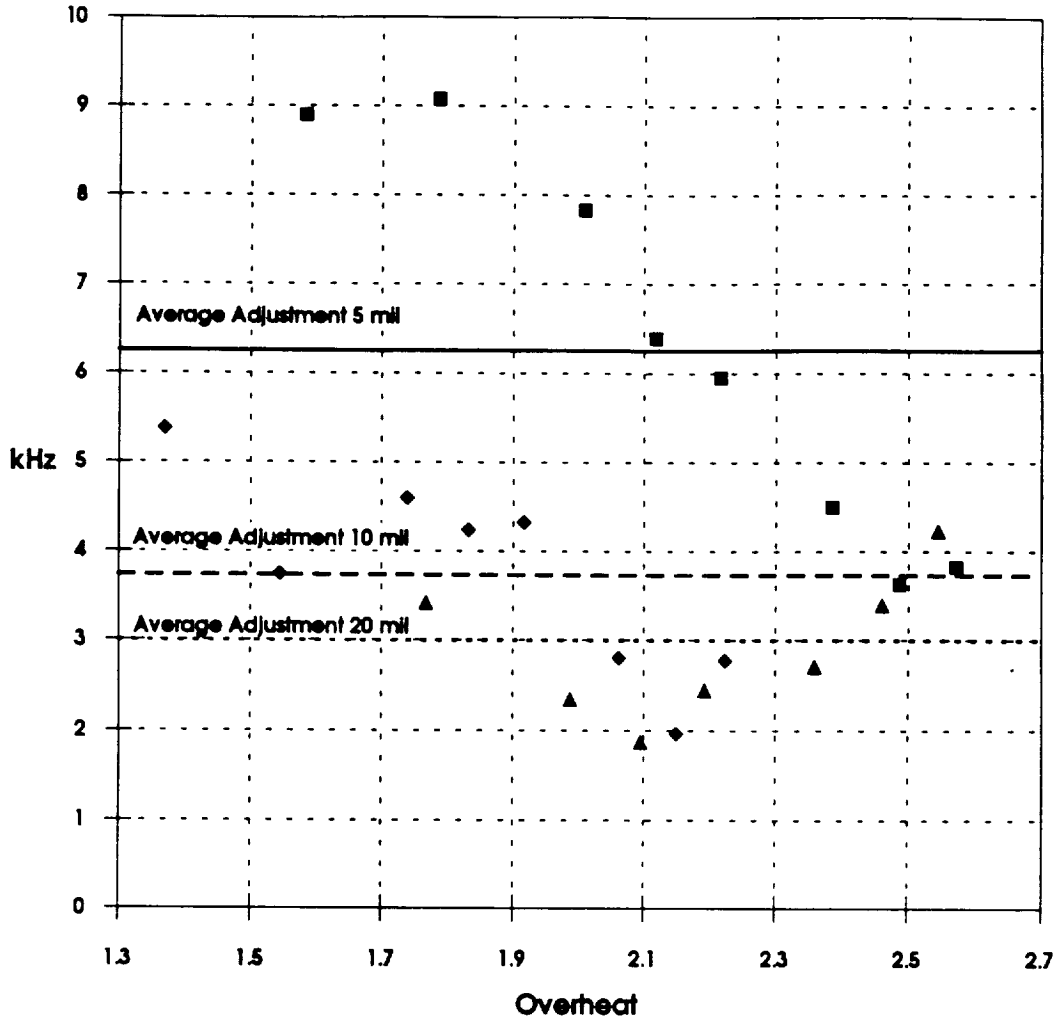

Figure 4.13. Average increase in the frequency response performance due to inductance compensation for the 5, 10 and 20 mil glass sensors

Watmuff's fifth order polynomial analysis showed that as the amount of inductance increased on the bridge, the response rolled off at a lower frequency. However examples of Watmuff's work show that when he increased inductance in his anemometer, the frequency at which his response oscillated (ringing frequency) also increased. Using the definition of frequency response as described in this work, this implies that the frequency response was increasing for increased inductance in his results and this is consistent with the results in this work.

4.3.2. Sine Wave Testing and Sensor Dimension

The principle method for investigating frequency response optimization is the square wave test. Sine wave testing, on the other hand, is a practical way of investigating the anemometer for a given adjustment. Sine wave testing results were obtained for the 5, 10 and 20 mil glass sensors for a selected overheat case of approximately 1.3. Figure 4.14 shows the resulting roll-off points for each sensor in operation with the AC-2 anemometer. This figure shows that for a given overheat the 20 mil glass sensor rolls off the earliest at approximately 16 kHz while the 5 mil glass sensor rolls off at approximately 30 kHz. The point of roll-off can be attributed to the sensor size and the heated area on the surrounding substrate. Larger sensors require more current to maintain a set temperature, which results in more substrate heating. Not only is the thermal time constant of the larger sensor causing a slower adjustment, but the heated footprint on the surrounding substrate also helps to decrease the response time.

Figure 4.14 also shows that the 5 mil glass sensor rolls off at a smaller amplitude than the two larger sensors. This is indicative of the lower sensitivity associated with smaller sensors. This result is important because it shows that sensitivity must be sacrificed for increased frequency response performance. Sine wave testing was performed again, but only after the 5 mil glass sensor had failed. These results are

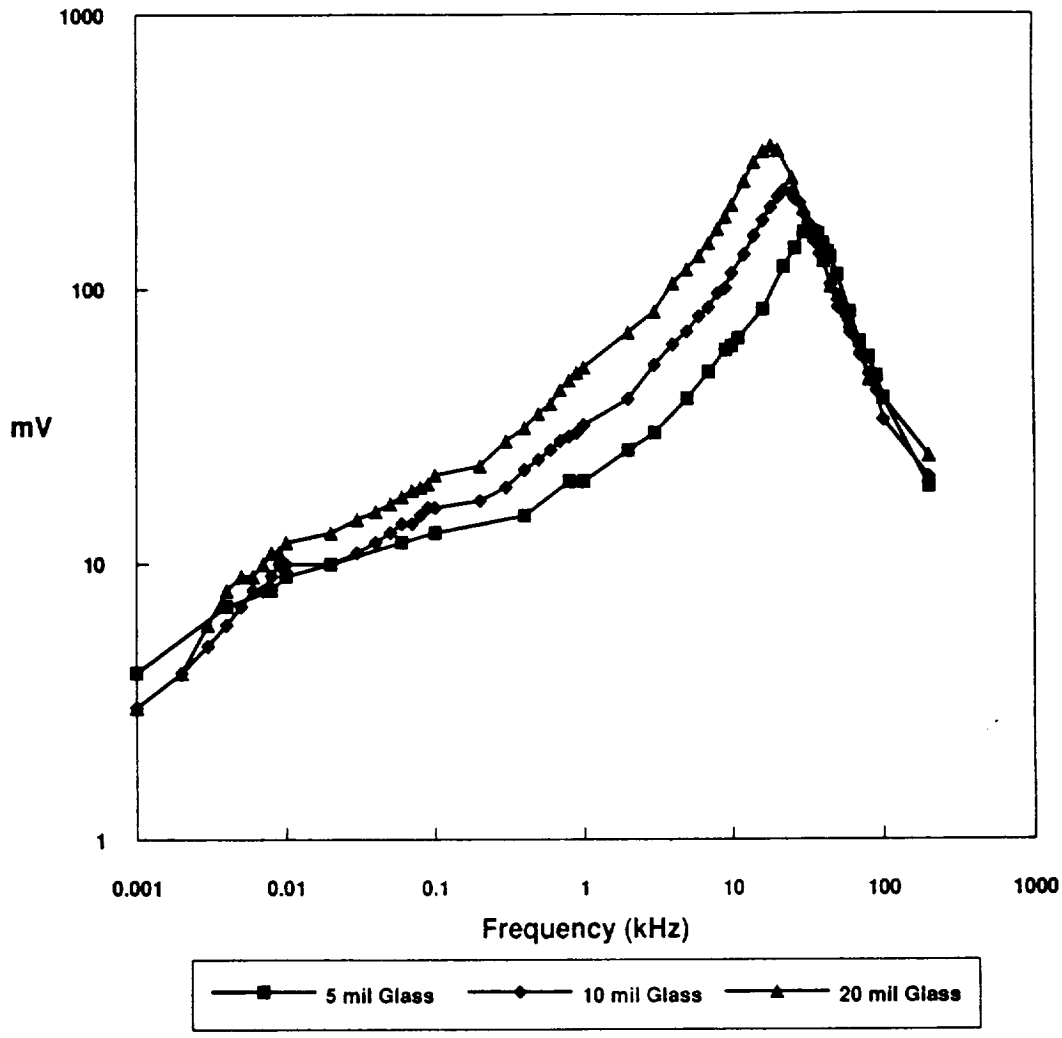

Figure 4.14. Roll-off points for 5, 10 and 20 mil glass sensors at overheat of 1.3 shown through sine wave testing

discussed in more detail in section 4.3.4 where experimental results are compared to Freymuth's theory for hot wire and non-cylindrical hot film anemometers.

4.3.3. Square Wave Testing and Substrate Material

The subject of this test was the comparative frequency response performance for three 20 mil sensors that had been deposited on glass, alumina and polyimide coated aluminum. All three sensors were tested for frequency response across a range of overheats using the IFA-100. Figure 4.15 shows how the frequency response increases for increasing overheat for the 20 mil glass, alumina and polyimide-aluminum sensor. The alumina substrate provides superior frequency response performance followed by the polyimide-aluminum substrate and then the glass substrate. At the highest tested overheat of 2.1, the 20 mil alumina sensor had a frequency response of approximately 160 kHz while the 20 mil glass sensor had a frequency response of approximately 50 kHz at an equivalent overheat. In this case, the previously noted degradation overheat of 2.5 was never reached for any of the three sensors, so the leveling effect was not noticed in this test. However, trends indicate that had the 20 mil alumina sensor been tested at an overheat of 2.5, the frequency response would have probably peaked over 200 kHz.

Recall from Table 3.1 that the unsteady parameter β was used to rate the quality of a substrate. Materials with higher β were considered to respond to thermal changes better because heat transfer was directly proportional to β. In the case of the glass and alumina substrates this trend is true while the alumina-polyimide sensor stands out. However, only the glass substrate is a single material substrate, while the other two substrates are layered. Therefore, a total β cannot be defined for each substrate. This is why a thermal impedance was calculated in Table 3.2. Thermal impedance considers a finite substrate thickness and provides an indicator of how effectively the substrate will transfer heat. Based on estimations of the total substrate thermal impedance that

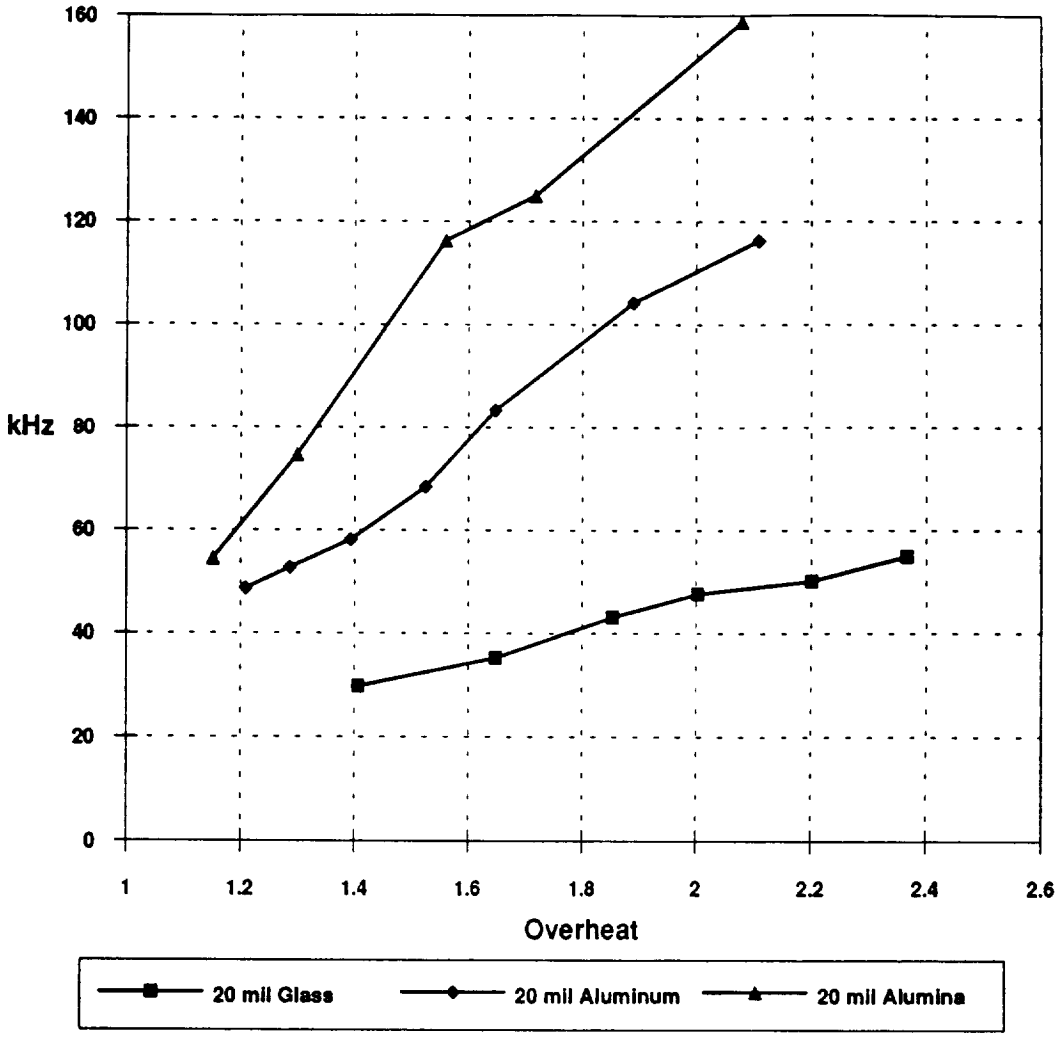

Figure 4.15. Comparison of frequency response for the 20 mil glass, alumina and aluminum sensors subjected to voltage step

accounts for all insulating layers, the alumina substrate should provide the best performance followed by the polyimide-aluminum substrate then the glass substrate. This follows the trends that are shown in Figure 4.15.

Sandborn [37] says that the thickness of the substrate is unimportant during high frequency events making possible the assumption that the substrate is a semi-infinite body for a heat transfer analysis. The problem is that such analyses only treat homogeneous substrates and not substrates with thin insulating layers. If the individual substrate materials were used in homogeneous substrates then the performance trend would be aluminum with the highest response, followed by alumina, then glass, then polyimide. However, in the case where a thin polyimide layer is deposited between the primary aluminum substrate and the film sensor, a six micron polymeric layer can still be sufficient to lower the response below that of alumina, but not that of glass. Perhaps this can better be understood by looking at the relative penetration depths of heat oscillations into a composite layered substrate. Unfortunately, this issue can be rather complicated and went beyond the scope of this thesis.

4.3.4. Fitting Experimental Electronic Testing Results to Theory

Dynamic performance parameters of the anemometer and sensors may be represented by Freymuth's [16] third order hot wire anemometer analysis. In this analysis, the optimum dynamic response of the anemometer is determined by the third order time constant MM"/G. Within this time constant, M is a constant associated with the wire or film sensor and M"/G is a constant associated with the circuitry. Freymuth discussed that this particular analysis may not be accurate for the non-cylindrical film sensor, but it is of interest to further understand the analysis and determine what each parameter implies. The parameters are experimentally determined as follows.

The AC-2 anemometer is tuned for operation to have a response to a square wave that is similar in shape to the response associated with case 3 of Figure 2.7 (see Section 2.3.2). A cut-off frequency is associated with this case that is defined by

$$f = \frac{\Omega x}{2\pi t} \tag{4.4}$$

where Ω is a dimensionless circular frequency that is defined at the -3 db point as shown in Figure 4.16. The equations define the -3 db roll-off as the point where

$$\left|\frac{y}{z}\right| = \frac{1}{\sqrt{2}} \tag{4.5}$$

which comes from the relationship

$$\left|\frac{y}{z}\right| = \left[1 + (a^2 - 2b)\Omega^2 + (b^2 - 2a)\Omega^4 + \Omega^6\right]^{-1/2} \tag{4.6}$$

The time t at which the experimental response signal decreases to 3% of the response maxima is recorded for each sensor in square wave testing mode. According to case 3 in Freymuth's work, the values x = 4.80 and Ω = 1.0 are used. Equation (4.2) then becomes

$$f = \frac{1}{3t} \tag{4.7}$$

Knowing t and using the x as defined by Freymuth for the tuned response, the parameter MM"/G can be obtained from

$$(MM"/G)^{1/3} = \frac{t}{x} \tag{4.8}$$

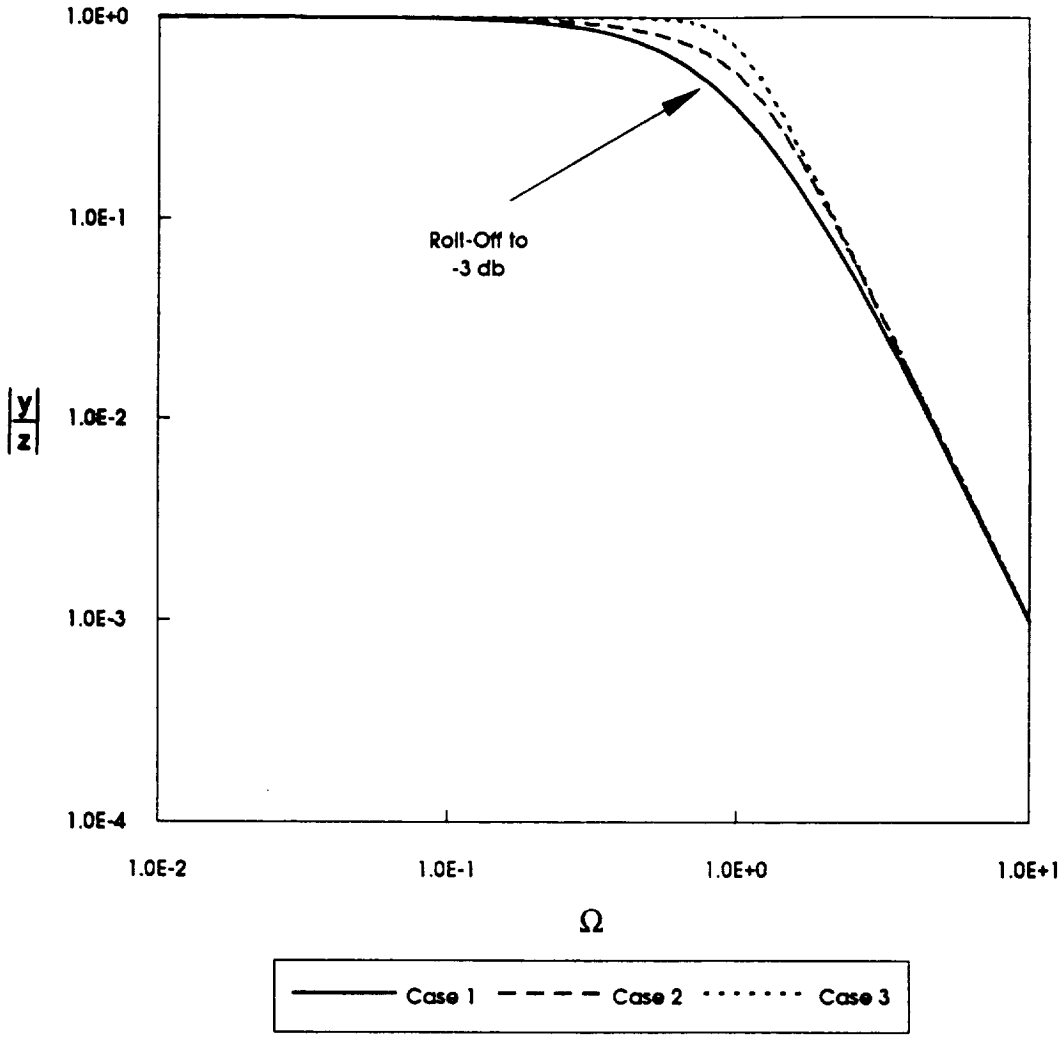

Figure 4.16. Theoretical plot of the -3 db roll-off point that is used to define the cut-off frequency and system time constants for Freymuth's theory

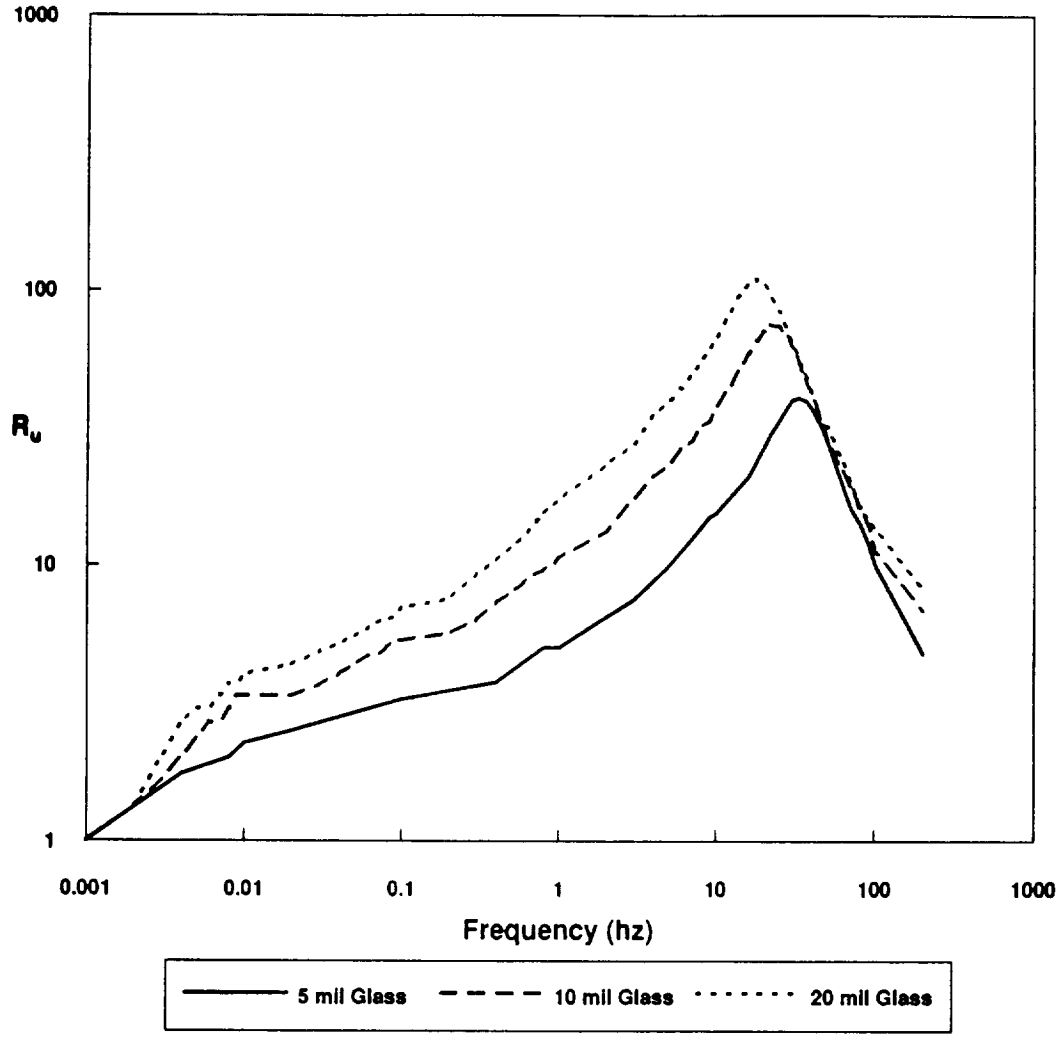

Figure 4.17. Relative response amplitude resulting from sine wave testing of the 5, 10 and 20 mil glass sensors at overheat of 1.4 with zero flow

In order to break this time constant down further, the sine wave test is administered to the anemometer that has been optimized through the square wave testing. A constant amplitude sine wave $\hat{U}_t$ is applied with variation in the frequency and the resulting output amplitude is plotted against the input frequency (see Figure 4.17). The slope of the linear portion of this curve before the roll-off is calculated and used as $d\hat{u}/df$ in the following equation to find the sensor time constant M.

$$M = \frac{n+1}{2\pi\hat{U}_t}\frac{R_4}{R_1}\frac{d\hat{u}}{df}\frac{1}{n} = \frac{(n+1)^2}{2}\frac{R_1}{nR_1 - R_o}\frac{c}{H(V)} \tag{4.9}$$

Now, knowing M and MM"/G the anemometer time constant can be obtained through

$$\left(\frac{M''}{G}\right)^{1/2} = \frac{\left[(MM''G)^{1/3}\right]^{3/2}}{M^{1/2}} \tag{4.10}$$

and also the amplifier relation

$$\frac{U_b}{GU_o} = \frac{a(MM''/G)^{1/3}}{M} \tag{4.11}$$

An initial attempt was made at producing the data for this analysis with mixed results. The anemometer was set with a fixed control resistance, and the 5, 10 and 20 mil glass sensors were tested through a range of frequencies in static operation (zero flow). The overheat for each sensor was slightly different due to differences in the cold resistance yet the result was sufficient for indicating the relationship of the sensor dimension to the sensitivity of the sensor. The output amplitude of the sine wave was plotted against the input frequency and the linear portion of the curve before the roll-off was fit with a straight line (see Figure 4.18). The resulting slopes related strongly to the dimension of

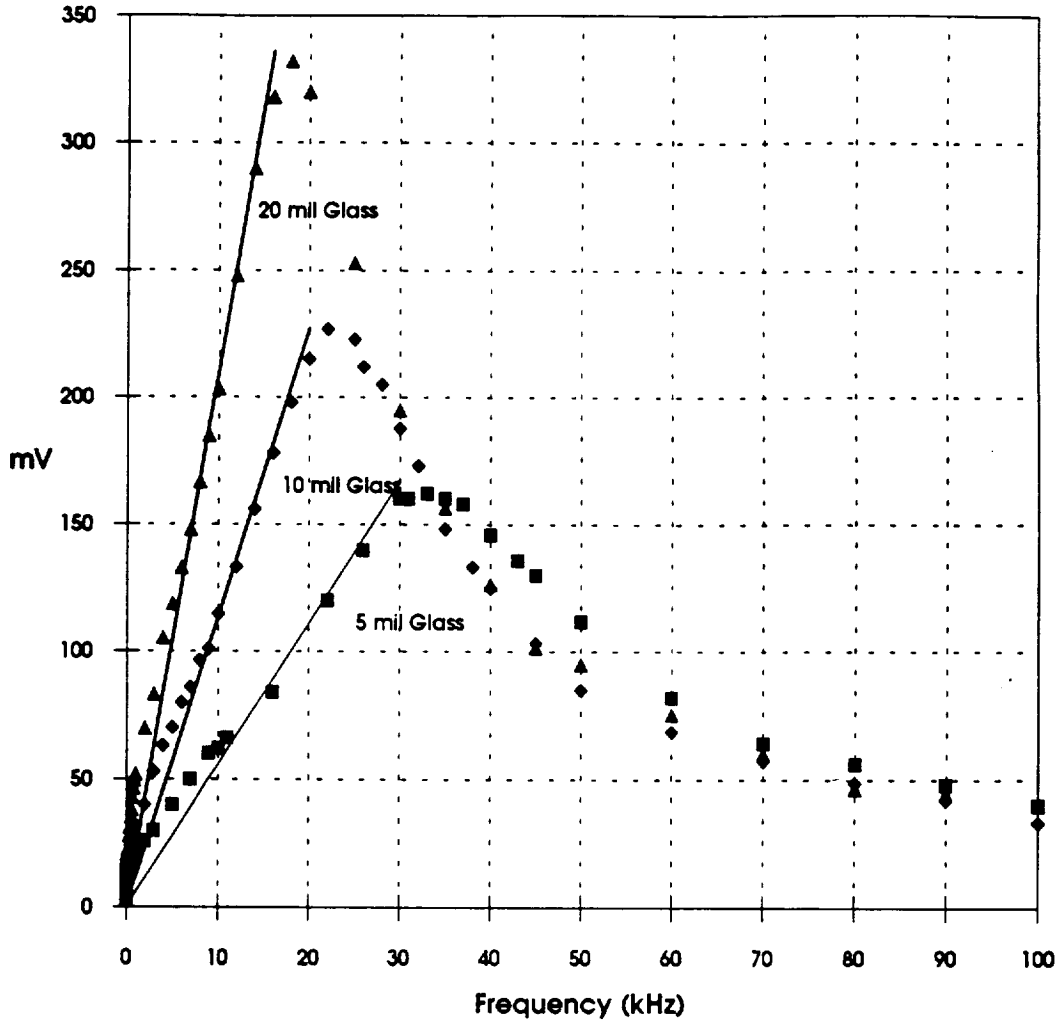

Figure 4.18. Curve fit to the linearized portions of dû/d*f* for determining Freymuth model time constants

the sensor as seen in Table 4.1. In this table the normal length and volumes are ratios of the respective sensor dimension to the 5 mil glass sensor dimensions. Though not exact, from this initial test, it appeared that the increase in amplitude for the increase in frequency scaled nearly to the sensor normal length for a given aspect ratio. This is significant because the sensor time constant M is directly proportional to $d\hat{u}/df$ and so the slope ratio for $d\hat{u}/df$ is the same as the ratio of M for each sensor.

Table 4.1. Sensor lengths and volumes normalized to the smallest sensor dimension compared to the slope of the sine wave test curve

Sensor Dimension	Normal Length	Normal Volume	$d\hat{u}/df$	Slope Ratio
0.5 x 5 mil Glass	1	1	0.005558	1
1 x 10 mil Glass	2	4	0.011360	2.04
2 x 20 mil Glass	4	16	0.020972	3.77

A second attempt was made at electronic testing for the comparison to Freymuth's hot wire theory. By this time, the 5 mil glass sensor had failed and so was not used for this test. The calculated performance parameters are shown below in Table 4.2 for the 10 mil and 20 mil glass substrate sensors.

Recall that $(MM''/G)^{1/3}$ is the third order constant for the dynamic equation and should be constant when the overheat, flow velocity, sensor size and amplifier gain are held constant. A well designed anemometer should have a very small $(MM''/G)^{1/3}$ because the smaller the constant is, the more second order the anemometer behavior becomes. The constant $(M''/G)^{1/2}$ is extracted from the third order constant and should be very small and constant for a given anemometer circuit. The testing results show that $(M''/G)^{1/2}$ is nearly constant from run to run with less than a 5% difference. This amount of error

Table 4.2. Dynamic performance parameters for sensors and anemometer

Parameter	10 mil Glass	20 mil Glass
$(MM''/G)^{1/3}$	1.396×10^{-5}	1.979×10^{-5}
$(M''/G)^{1/2}$	8.878×10^{-9}	9.235×10^{-9}
$d\hat{u}/df$	0.07668	0.20215
M	34.5	90.9
U_y/GU_o	8.093×10^{-7}	4.354×10^{-7}

could easily be attributed to the slope calculation for $d\hat{u}/df$. The difference in the constant U_y/GU_o may be attributed to the fact that the operational amplifier is operating in open loop mode and the transistor in the feedback loop has a gain with a weak dependency on the current load. Because the two sensors draw a different current load on the anemometer system, the supplied gain will be different. The relationship is not so clear on the $d\hat{u}/df$ trend for this test as it was on the previous test. The two sensors were run at nearly identical overheats, but the difference could be sufficient to offset the relationship that was clearly seen before. In addition, there was a change in the way the sine wave was applied to the anemometer circuit. It is likely that this was also responsible for causing the difference.

At this point we could attempt to draw a comparison using Freymuth's theoretical model. Having used the theoretical square wave response curves to calculate the anemometer time constants, the theoretical plots for the response to a velocity step could be drawn and compared to the experimental plots for the same (see Figure 4.19). However, the velocity step that the wire of the third order analysis experiences is very much unlike the velocity step that the shear wall film experiences. Considerable heat

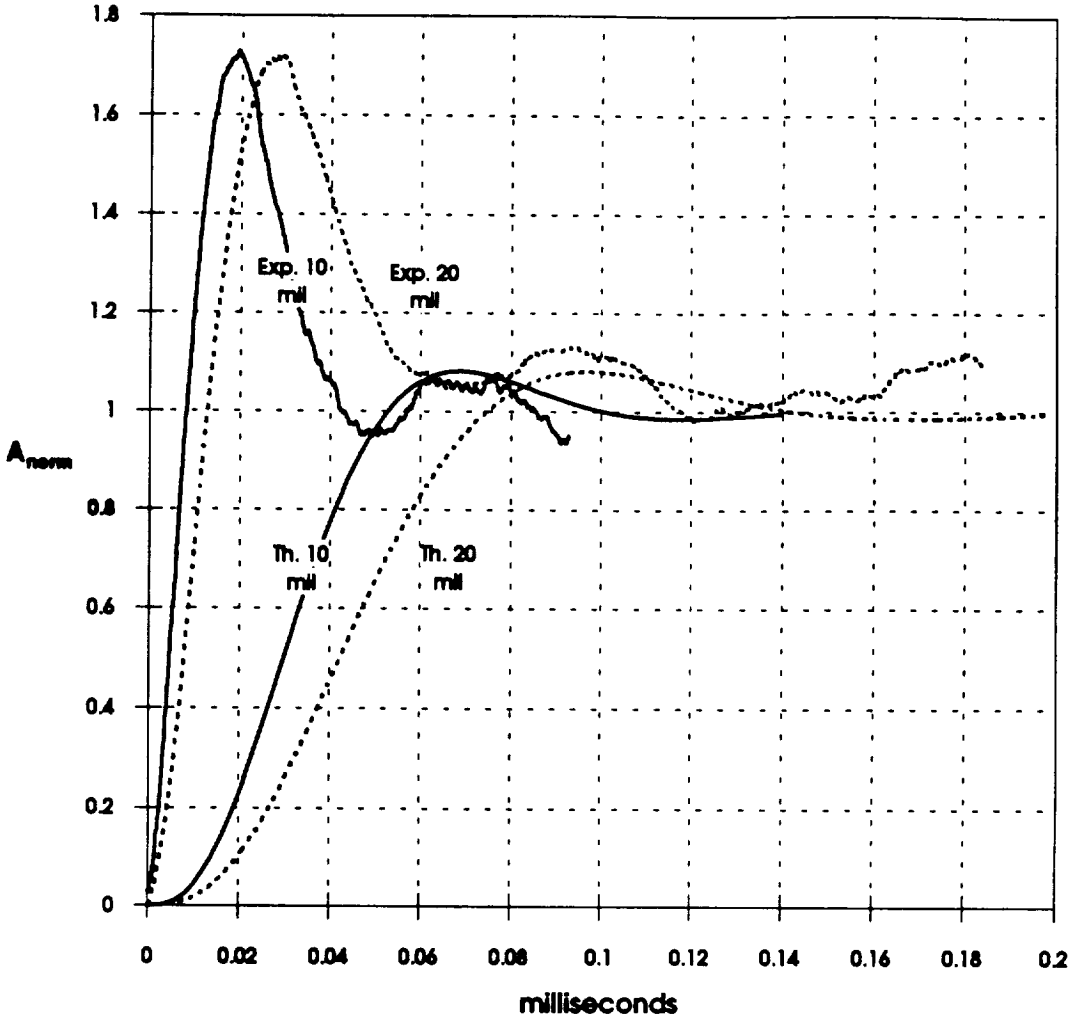

Figure 4.19. Comparison of the experimental velocity step responses and the predicted velocity step responses using Freymuth time constants

losses to the wall as well as the building boundary layer do not present a shape that is all that similar to what is predicted by Freymuth's theory.

Another important comparison is drawn using Freymuth's theory for the non-cylindrical hot film. Recall from Section 2.3.2 in which Figure 2.9 showed the theoretical shape of the sine wave testing curve. As the sensor Biot number decreased, a bulge began to appear that was indicative of the Bellhouse-Schultz effect. This effect arises as a result of the conductive heat transfer from the flush-mount sensor to the substrate. Figure 2.9 shows the relative voltage response defined as

$$R_u = \frac{\hat{u}(\Omega)}{\hat{u}(\Omega = 0)} \tag{4.12}$$

versus the non-dimensional sine wave frequency Ω, which is defined as

$$\Omega = \frac{\omega h^2}{D} \tag{4.13}$$

where h is the heat transfer coefficient, D is the substrate diffusivity and ω is the circular frequency. In addition to the growth of the bulge, the relative response was shown to increase with a decrease in the Biot number. Freymuth speculated that given enough sine wave testing data, the theoretical curves could be matched to the experimental curves resulting in an empirical fit to the Biot number. The Biot number could then be used to rate non-cylindrical sensor performance in terms of frequency response and sensitivity.

A bump similar to what is shown in the theoretical plot of Figure 2.9 is clearly visible in the experimental data of Figure 4.20 confirming the presence of the Bellhouse-Schultz effect. The difference between the curves in Figures 2.9 and 4.20 is that R_u is defined at the beginning test frequency rather than the zero non-dimensional frequency as

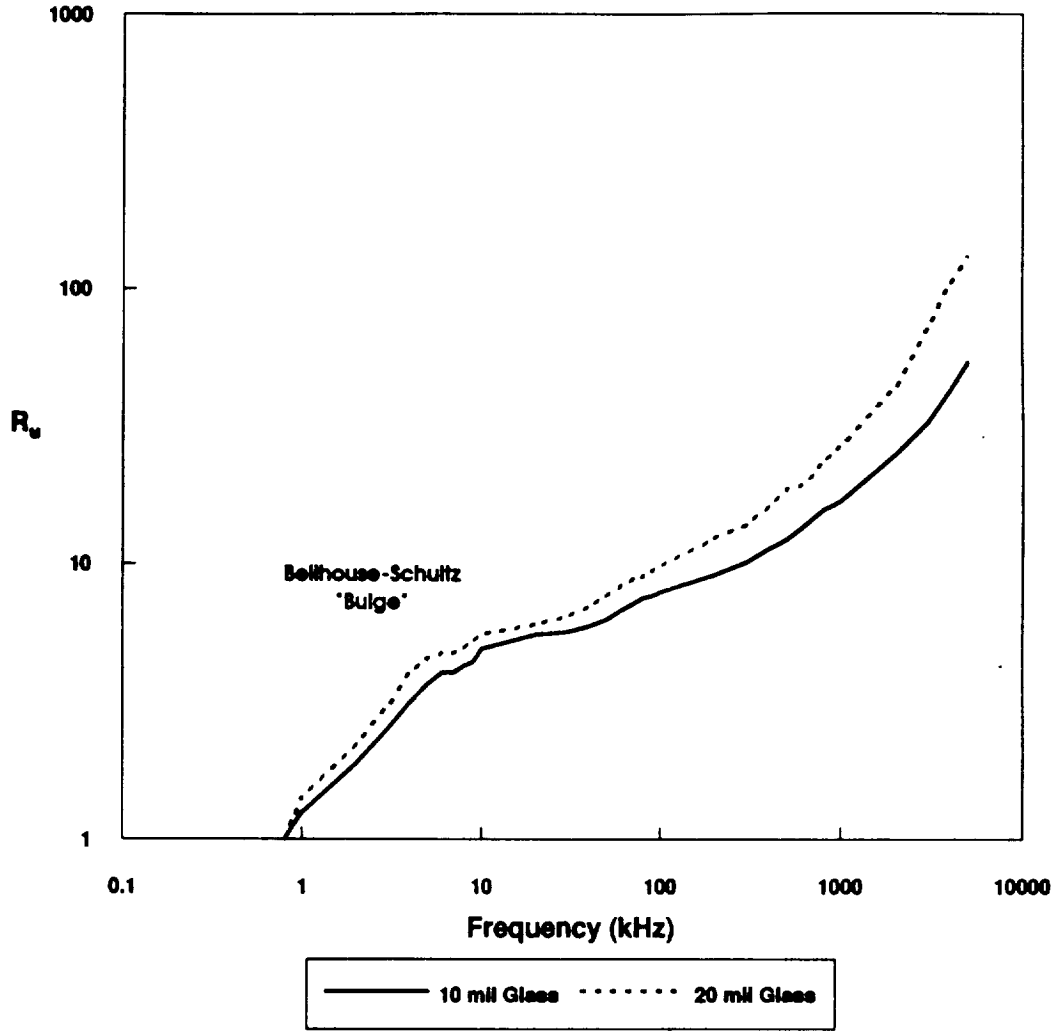

Figure 4.20. Relative response from sine wave testing for the 10 and 20 mil glass sensors showing the Bellhouse-Schultz effect

$$R_u = \frac{\hat{u}(f)}{\hat{u}(f_o)} \tag{4.14}$$

and this data is plotted versus the dimensional frequency. The relative response is defined differently than the theoretical model because the non-dimensional frequency Ω requires making an estimation of h, and the data for doing so is limited. Therefore, the experimental curve cannot be directly correlated to the theoretical curve and no empirical correlation can be found. Clearly it is more desirable to represent the data in Figure 4.20 using the non-dimensional quantities of Figure 2.9, but plotting the data as was done in Figure 4.20 still provides a useful result.

Given the 10 and 20 mil glass sensors with identical aspect ratio, the 20 mil glass sensor shows a larger bulge and a greater sensitivity in Figure 4.20. Since Freymuth shows that relative response increases (as well as the Bellhouse-Schultz bulge) for a given frequency with decreasing Biot number, then the smaller Biot number sensors must correspond to the larger sensor sizes. Practically speaking, according to the definition the Biot number will decrease with increasing sensor size provided the heat transfer characteristics are fairly similar for the test conditions. This is true in the case of the data in Figure 4.20. This confirms the theoretical prediction and shows that the relative response in terms of sensitivity can be improved by decreasing the Biot number i.e. increasing the sensor size.

4.4. Experimental Velocity Step Testing

Experimental velocity step testing was used to determine the effect of sensor dimension and sensor substrate material on frequency response performance as well as sensitivity in the dynamic flow condition. Velocity step testing is a useful tool because it tests the real measurement capabilities of each sensor. For each test the anemometer was

set up in a configuration using one of the five sensors. The anemometer was turned on and allowed to run for about 15 minutes in order to minimize the effect of transients that might occur due to heat transfer to the substrate. A Validyne pressure transducer was connected to the driver gas line in order to monitor the pressure leading up to diaphragm failure. The transducer sent an output voltage to a Fluke 87 multimeter that recorded peak voltages and this was converted into a pressure through a calibration. The pressure of the driven end of the shock tube was recorded on a Heisse vacuum gauge. Two Kistler pressure transducers were located at the far end of the driven section and these were used to monitor the shock passage. The signals from the Kistlers were recorded using a 1 MHz RC Electronics A/D board, which allowed an accurate measurement of the shock velocity by noting the time of passage over each transducer. Using this information along with the bursting pressure of the diaphragm, the temperature and velocity of the flow behind the shock could be deduced. The Gould DSO 400 oscilloscope was set to trigger on the voltage rise in the anemometer signal due to the passage of the shock wave and this response event was sent to the computer through a RS432 interface to be recorded for later analysis (refer back to Figure 4.5).

The sensor was mounted onto the shock tube base plate as indicated in Figure 4.21. This configuration is similar to what was used by Davies and Bernstein when they analyzed the boundary layer development on a flat plate behind a normal shock. Davies and Bernstein gave convincing evidence that Mirels' boundary layer solution for this flow condition was applicable for the quasi-steady regime behind the shock. Therefore, Mirels' solution is consulted for the approximation of velocity shear in this work.

It was necessary to use a consistent definition of frequency response when analyzing the velocity step results. The frequency response of the anemometer sensor was defined as the inverse of the time from when the anemometer first began to respond until the minimum point of the first signal overshoot (see Figure 4.22).

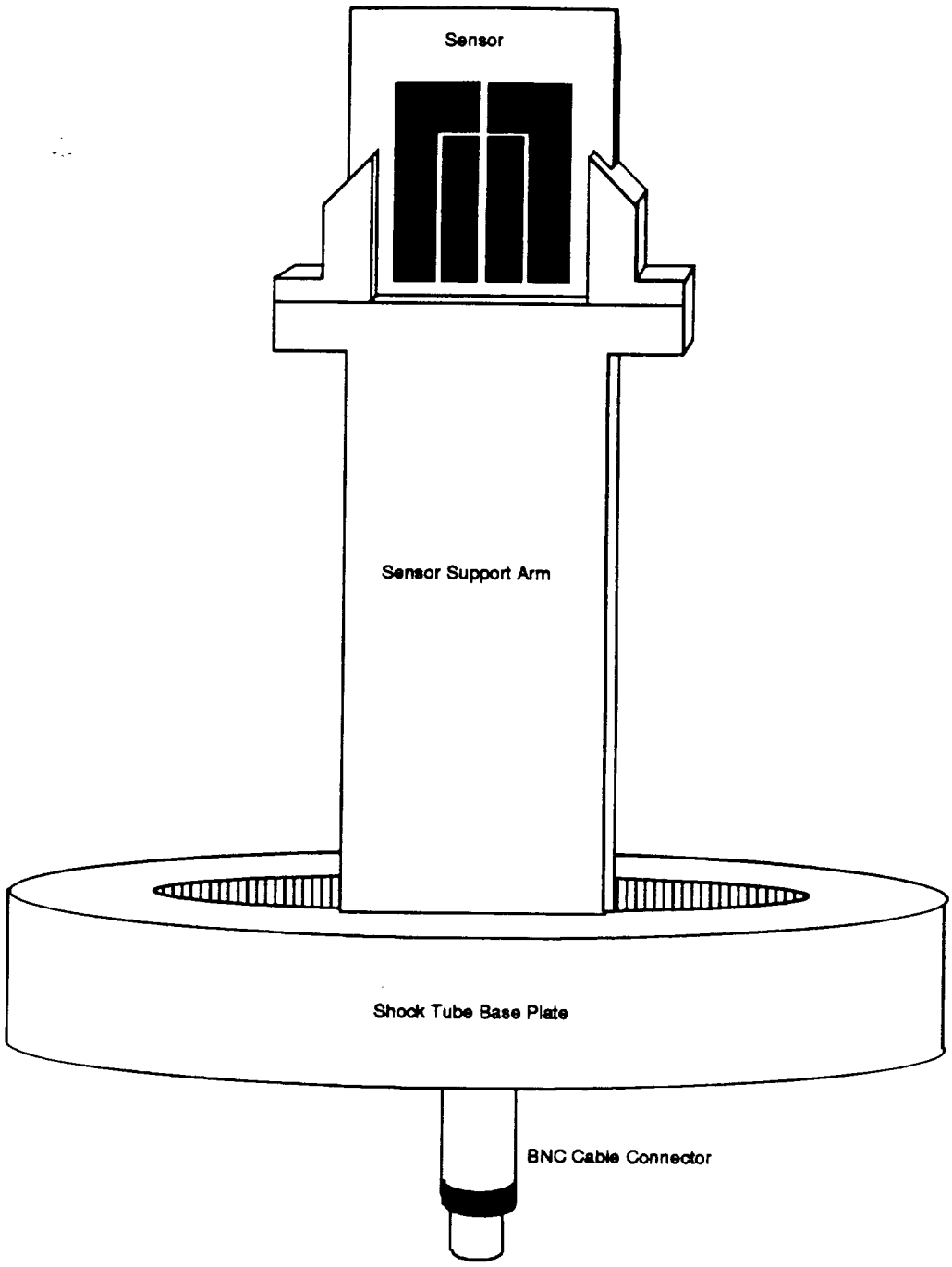

Figure 4.21. Sensor mount configuration on shock tube base plate

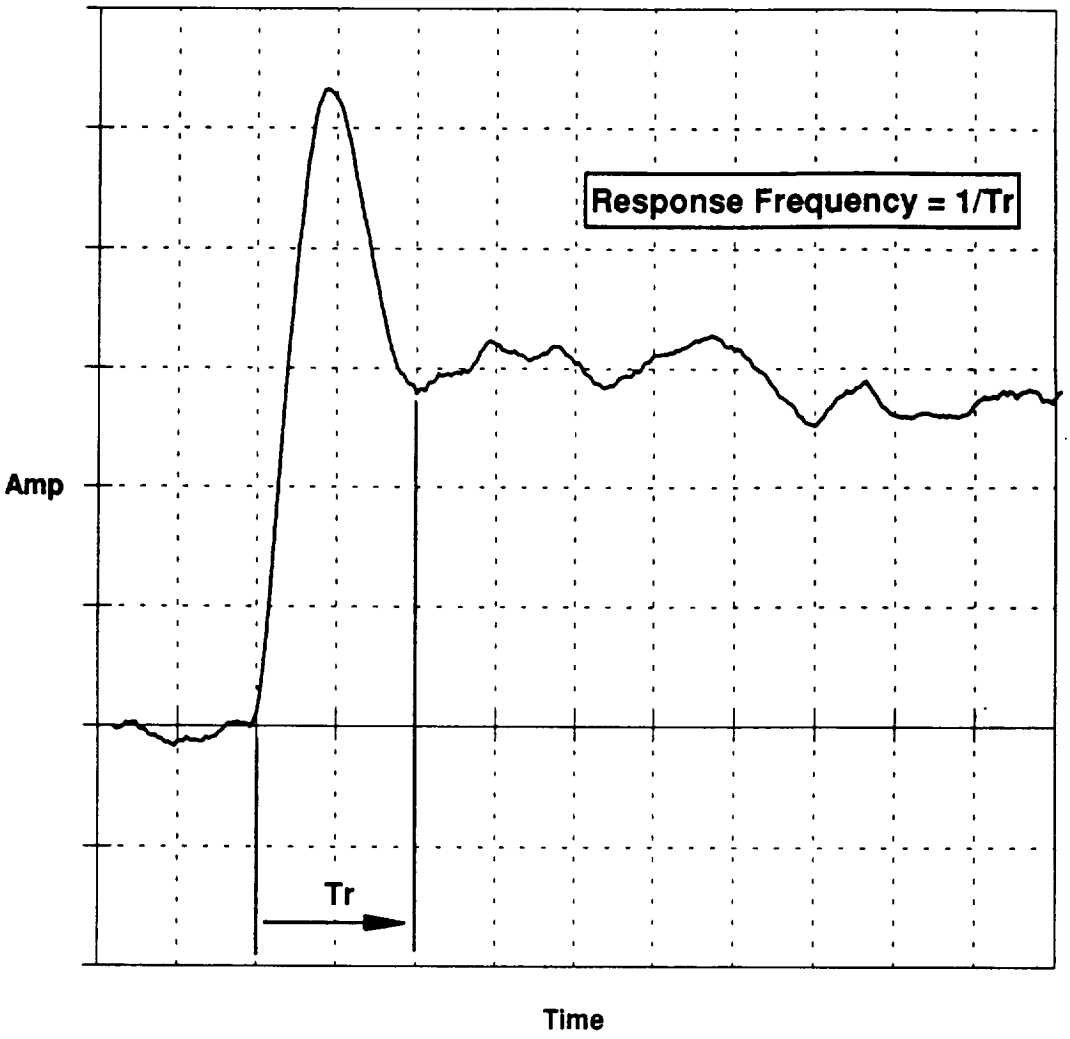

Figure 4.22. Method for determining frequency response in velocity step testing

4.4.1. Velocity Step Testing and Sensor Dimension

To analyze the effects of sensor dimension on flow detection, three key parameters were recorded: the operating point voltage, the frequency response to a passing shock wave and the amplitude of the response. As with the electrical testing, the frequency response was for the analysis of the operational speed for varied sensor dimensions. The operating point voltage and response amplitude were for the analysis of sensitivity to flow fluctuations.

Sensor dimension had an identical effect in the flow situation as it did in the non-flow situation. As could be predicted by Freymuth's hot wire model, the dominating effect was the lumped capacitance time constant as it interacts with the feedback circuit. In voltage step testing, a voltage step is applied to the sensor to heat it and the feedback circuit adjusts the current through the sensor to keep the sensor a constant temperature. In velocity step testing, a step in the velocity (forced convection) removes heat from the sensor and once again the feedback circuit adjusts accordingly.

Figure 4.23 shows the frequency response of the 5, 10 and 20 mil glass substrate sensors as they adjust to similar shock waves (velocity steps) at different overheats. The 5 mil clearly adjusts the fastest of the three with an upper frequency response of 70 kHz at an overheat of 2.1 while the 20 mil adjusts the slowest with an upper frequency response of 29 kHz at an overheat of 2.1. This can be compared to the electrical frequency responses of 82 kHz and 24 kHz at an overheat of 2.1 for the 5 mil and 20 mil glass sensors. The difference in the frequency response is simply attributed to the difference in definition from the electrical testing to the flow testing. As with the electrical testing, the increase in frequency response for a given increase in overheat is the largest for the 5 mil glass sensor. If the trend for the 5 mil glass sensor is extrapolated out to the degradation overheat of 2.5, an upper frequency response of 100 kHz might be possible.

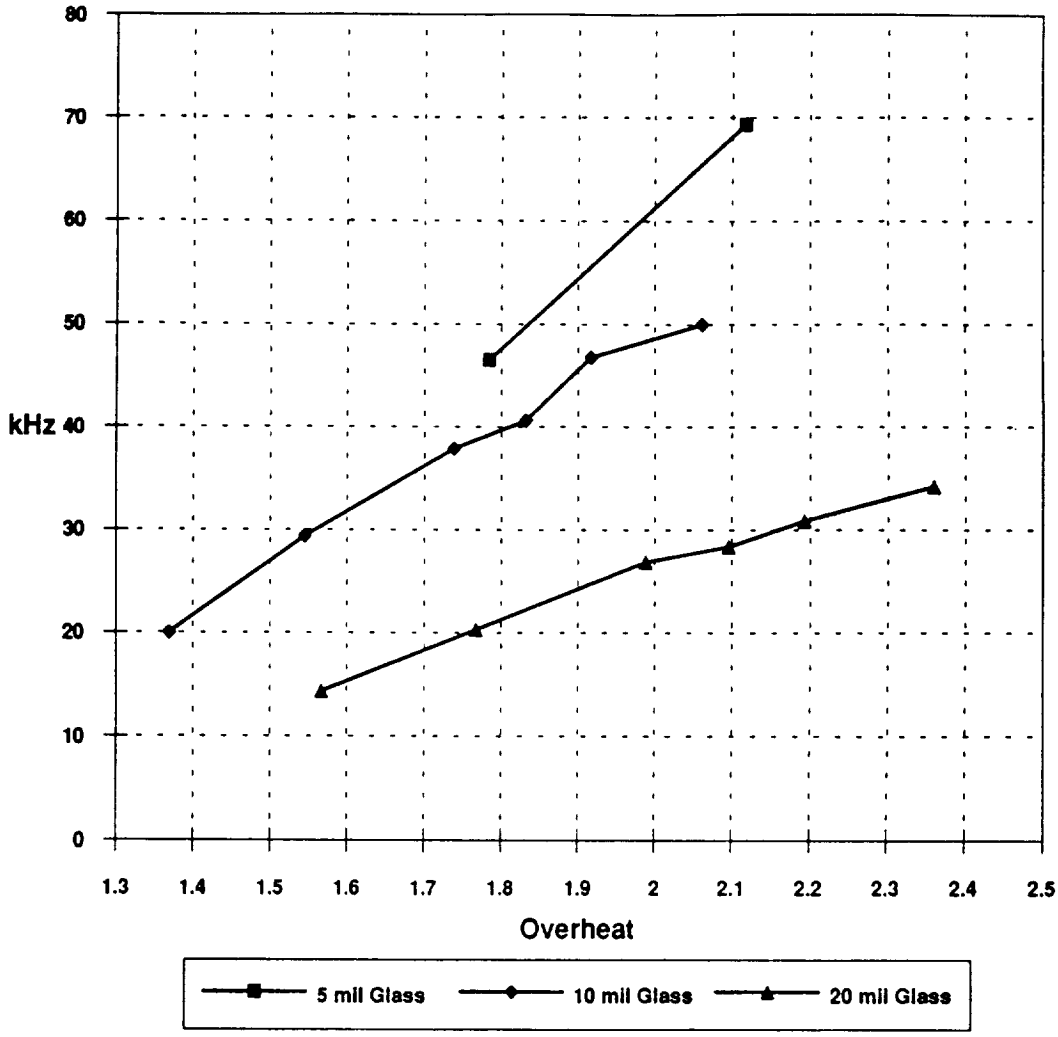

Figure 4.23. Comparative frequency response of the 5, 10 and 20 mil glass sensors as they adjust to similar amplitude velocity steps

To analyze the flow sensitivity, the 10 and 20 mil glass sensors are set at nearly identical overheats and a series of shock waves (velocity steps) is passed over each sensor. The overshoot amplitude is recorded for each velocity step and converted into a non-dimensional power dissipation defined as

$$P_s^* = \frac{P_s - P_{ref}}{P_{ref}} \tag{4.15}$$

where P_{ref} is the static power dissipation and P_s is the total power dissipation. The non-dimensional power dissipation is then plotted against the velocity of the applied step and fit with a power series curve. By representing this data as the differential power dissipation normalized to the reference power dissipation, a clear relationship can be drawn for the relative amount of power dissipated to the flow by each sensor. The more power that is dissipated to the flow for a given velocity step, the more sensitive a sensor is.

Figure 4.24 shows that the 20 mil sensor has superior sensitivity to the smaller sensor size. This figure can be interpreted in two ways. As the velocity step is increased from the zero limit, the anemometer response signal will increase and move out of the interference of the electronic noise. According to the curve fit in Figure 4.24, the 20 mil glass sensor response magnitude increases above the noise level for a smaller velocity than the 10 mil glass sensor. Therefore, in terms of signal to noise, the 20 mil glass sensor performs better than the 10 mil glass sensor. The sensor performance can also be rated by looking at the large velocity response. The slope of the curve fit can be calculated at any point to show how different sensors compare for a differential increase in velocity. The larger the slope for any sensor for a sensor at a given velocity, the more sensitive the sensor. Once again, in this case the 20 mil glass sensor shows the greatest sensitivity followed by the 10 mil glass sensor.

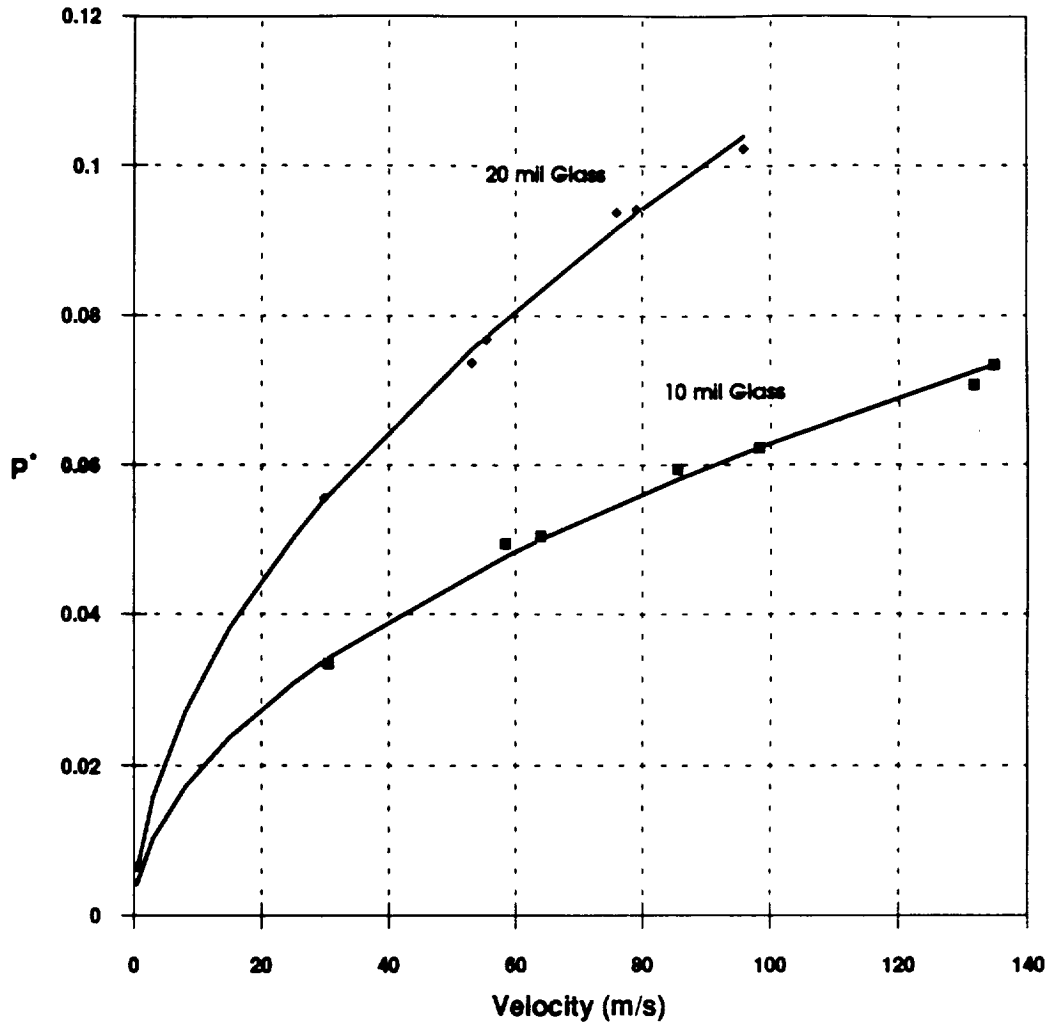

Figure 4.24. Non-dimensional power dissipation during velocity steps for the 10 and 20 mil glass sensors to show flow sensitivity

Recall that Kalumuck looked at the effect of sensor size in terms of Peclet number. For the flow situation, we can also look at the response of each sensor in terms of Peclet number. This requires some knowledge of the shear of the flow and so work by Mirels can be used to estimate the Peclet number of the flow behind the shock. This will be discussed in a later section.

4.4.2. Velocity Step Testing and Substrate Material

The trends for frequency response in the flow situation are similar to what was shown through electrical, or static testing. Substrates with higher thermal impedances adjust more slowly to the flow step than do the lower impedance substrates and cause a slower overall system response. Experimental data for the frequency response of the 20 mil glass and alumina sensors in flow testing is shown in Figure 4.25. Similar strength shock waves were passed over each sensor running at a range of different overheats. The low thermal impedance alumina sensor shows the fastest response with a upper frequency response of 110 kHz at an overheat of 2.2. Meanwhile, the high thermal impedance glass shows the slowest response with an upper frequency response of 45 kHz at an overheat of 2.2. This is consistent with what was shown in the electrical step testing. The aluminum sensor was not included in this figure due to a sensor failure.

Figure 4.26 shows a plot of the non-dimensional power dissipation for different velocities for the 20 mil glass, alumina and aluminum sensors running at similar overheats. In this case, the aluminum sensor seems to have superior sensitivity followed closely by the glass and then the alumina sensor. According to the curve fit in Figure 4.26, the 20 mil aluminum sensor response magnitude seems to increase above the noise level for a smaller velocity than either the 20 mil glass or aluminum sensor. Therefore, in terms of signal to noise, the 20 mil aluminum sensor performs better than the 20 mil glass or aluminum sensor. In terms of the differential increase in response magnitude for

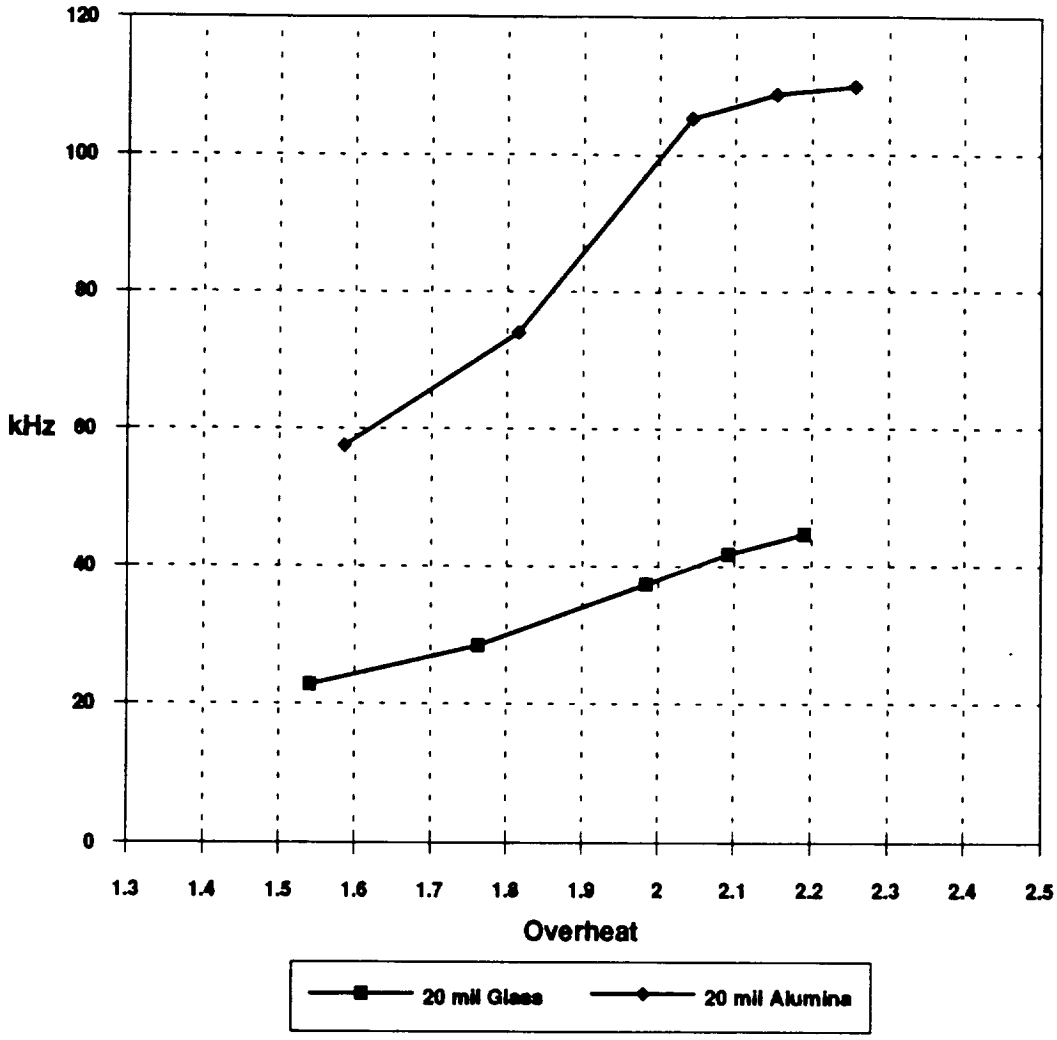

Figure 4.25. Comparative frequency response of the 20 mil glass and alumina sensors as they adjust to similar amplitude velocity steps

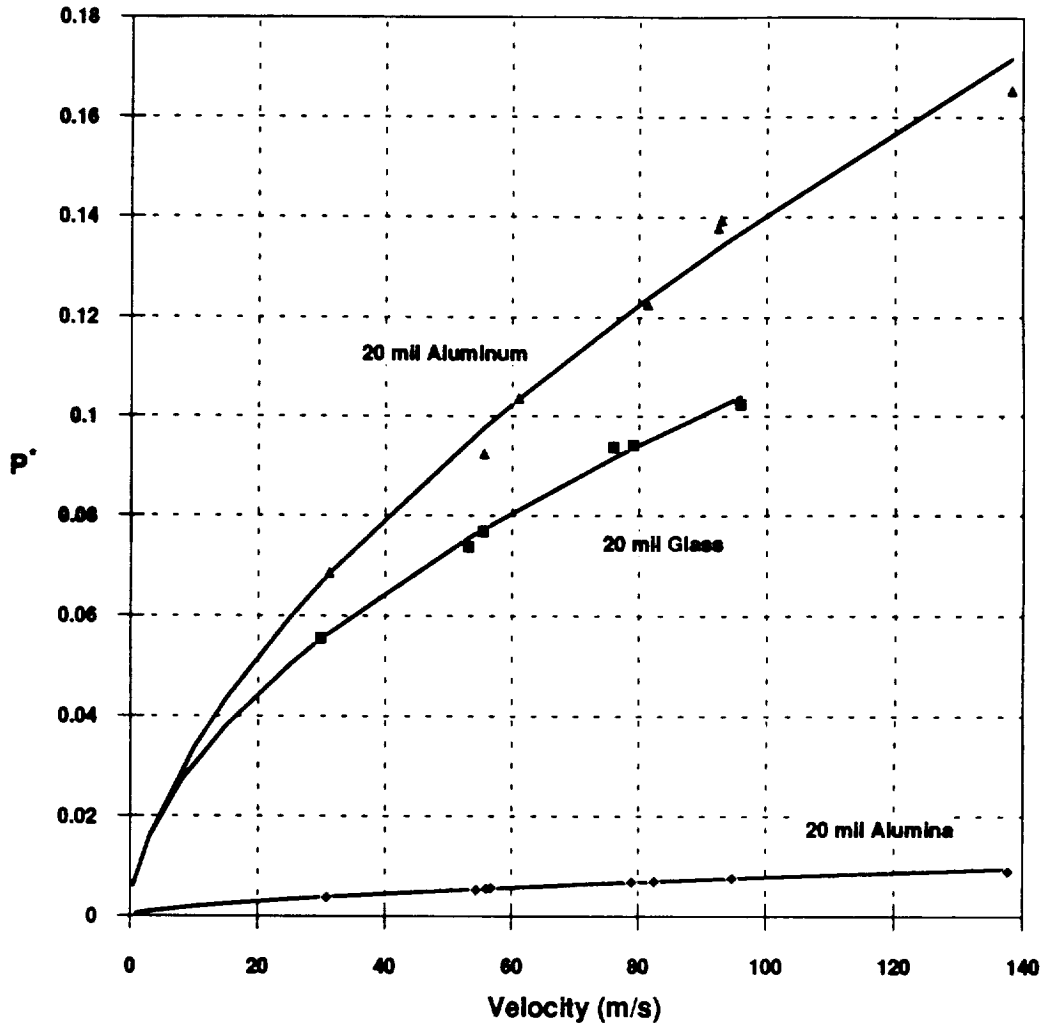

Figure 4.26. Non-dimensional power dissipation during velocity steps for the 20 mil glass, alumina and aluminum sensors to show flow sensitivity

a change in velocity, the aluminum also has superior performance followed by the glass and then alumina sensor meaning that the aluminum sensor has the superior performance.

This is somewhat of a quandary because sensitivity generally goes the opposite direction of frequency response. In electrical testing, the frequency response performance of the aluminum sensor lay between the glass and alumina sensor. Therefore, its sensitivity should also lie between the glass and alumina sensor. However this was not the case. Unfortunately the failure with the aluminum sensor prevented the acquisition of frequency response data in the flow situation.

Recall from section 4.2 where the static power dissipation was discussed. For a high thermal conductivity (low thermal impedance) substrate, the heat transfer in static operation is already high. This was shown in Figure 4.3 where the sensor heated a very small surrounding area of the substrate. More of the heat was penetrating deeper into the substrate rather than heating just the surface of the substrate. Once a flow is established, this higher rate of heat transfer is reflected in the frequency response results because the highly conductive substrate provides more assistance in removing heat from the sensor. However, the higher thermal conductivity substrate also reduces the amount of convective heat transfer relative to the amount of conductive heat transfer thereby decreasing the sensitivity of the sensor. It would appear from these results though, that the best overall performance comes from a highly conductive substrate with a thermally thin insulating layer.

4.4.3. Comparing Experimental Results to Theory

The effect of substrate material on the dynamic flow response was analyzed in more detail by comparing the experimental results to theoretical work by Kalumuck. In the process of doing this, Mirels' work for the building boundary layer behind a shock was utilized. Recall that Kalumuck presented his results in terms of Peclet numbers and

Nusselt numbers for different aspect ratios and conductivity ratios. The effect of aspect ratio cannot be determined in this work because all five sensors were designed with an aspect ratio of 10. Therefore, this analysis is restricted to the comparison of sensors with different conductivity ratios.

The Peclet number as defined by Kalumuck was shown in Part 2 to be

$$Pe = \frac{sL_p}{\alpha} \tag{4.16}$$

where s is the fluid velocity gradient, L_p is the sensor streamwise length and α is the fluid diffusivity. Having used a shock tube to create the velocity steps for sensor analysis, Mirels' solution of the fluid shear in the boundary layer forming behind a shock wave can be used to determine the velocity gradient, s.

$$s = \left(\frac{\partial u}{\partial y}\right)_w = u_e f''(0)\sqrt{\frac{u_e}{2u_w t v_w}} \tag{4.17}$$

where f''(0) is found through either the perturbation solution or the numerical solution depending upon the shock strength criteria discussed in Section 2.4.1. Recall also that Kalumuck defined a Nusselt number as

$$Nu = \frac{P_s 2a}{4abk_f T_p} \tag{4.18}$$

where a is the sensor streamwise half-length, b is the sensor spanwise half-length, P_s is the power dissipated by the sensor, k_f is the fluid conductivity and T_p is the average sensor temperature. Depending on the operating overheat of the sensor, an average temperature can be specified based on the sensor thermal calibration (see Appendix C).

The Nusselt number of interest is the flow sensitive Nusselt number which was defined in Section 2.2.4 as

$$Nu(Pe, K = 0) = Nu(Pe, K) - Nu(Pe = 0, K) \tag{4.19}$$

where Nu(Pe = 0, K) is calculated during static operation and implies pure conduction to the substrate, and Nu(Pe, K) is calculated during dynamic operation and implies combined convection and conduction. The first comparison that can be drawn is shown in Figure 4.27 which plots the total sensor Nusselt number against the flow Peclet number for the most laminar cases obtained during the testing of each sensor. In this figure, the static power dissipation clearly dominates the magnitude of the Nusselt number. Though the conductivity cannot be specified exactly for the multi-layered substrate, it is fair to say that the 20 mil alumina sensor has the highest conductivity ratio while the 20 mil glass sensor has the lowest conductivity ratio. The trend that is shown for the three different substrates fits Kalumuck's prediction that the total Nusselt number should increase with the substrate conductivity ratio.

The closest comparison that can be drawn to Kalumuck's work is a plot that he presents for a sensor with the aspect ratio of 1 (Kalumuck - Figures 3.13 and 4.16). In this case, a sensor with a conductivity ratio of 40 will have a total Nusselt number increasing from approximately 85 to 90 when $Pe^{1/3}$ varies from 2 to 4. The 20 mil glass sensor used in this work, which has a conductivity ratio of approximately 40 has a Nusselt number increasing from 80 to 82 as $Pe^{1/3}$ varies from 2 to 4. The Nusselt number decreases for a given Peclet number as the aspect ratio increases so the experimental data appears to be very close to the theoretical prediction of Kalumuck.

Figure 4.28 shows the flow sensitive portion of the Nusselt number for the 20 mil glass, alumina and aluminum sensors. Once again the closest comparison that can be drawn to Kalumuck's work is the sensor with a conductivity ratio of 50 and an aspect

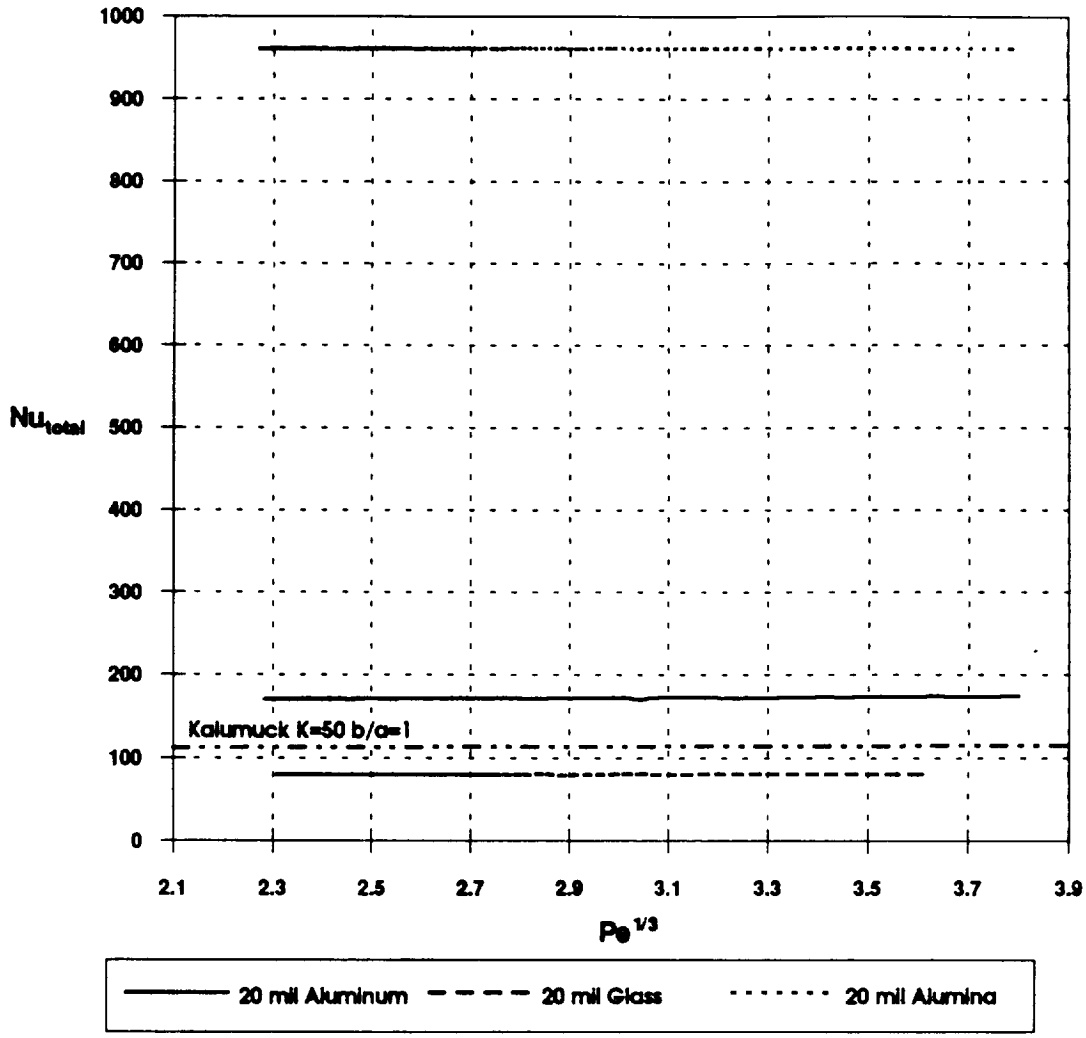

Figure 4.27. Total Nusselt number obtained during one shock tube run for the 20 mil glass, alumina and aluminum sensors as it compares to Kalumuck's work

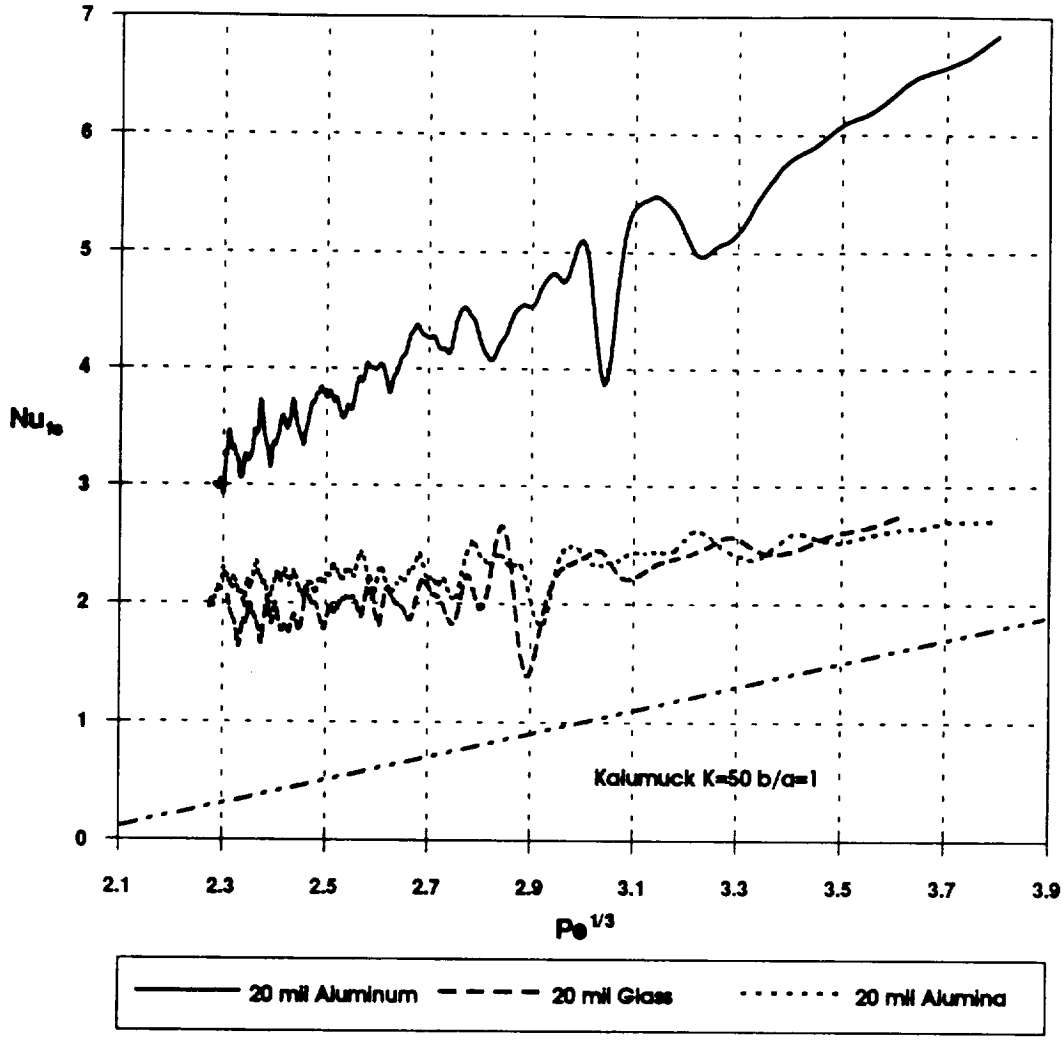

Figure 4.28. Flow sensitive Nusselt number obtained from one shock tube run for the 20 mil glass, alumina and aluminum sensors as it compares to Kalumuck's work

ratio of 1. The experimental result does not fall so close to the prediction as it did with the total Nusselt number, but the data is within the order of magnitude. For a given conductivity ratio and Peclet number, the flow sensitive Nusselt number increases with increasing aspect ratio, so the experimental data may not be so far off from the theoretical predictions after all. What is interesting to note is that the aluminum sensor has such a high flow sensitive Nusselt number in comparison to the alumina and glass sensors. Recall from section 4.4.2 that the polyimide-aluminum sensor had a higher sensitivity than the glass even though the glass was expected to have a higher sensitivity. Figure 4.28 confirms this previous experimental result that the polyimide-aluminum has superior sensitivity in the flow condition. Kalumuck shows that the flow sensitive Nusselt number is numerically close for varying conductivity ratios under 50. This appears to be the case for the glass and alumina sensors. However, the conductivity ratio of the aluminum sensor is much larger than either the glass or alumina sensors, so this prediction may not be suitable.

4.4.4. Flow Shear Characteristics

Recall that Mirels' solution for shear in the quasi-steady regime of the developing boundary layer induced by a shock wave was used to calculate the Peclet number in the comparison to Kalumuck's flush-mount sensor model. Here evidence is given that Mirels' solution is applicable to the sensor response. Liepmann and Skinner [22] show that for the steady flow case, the output of a heated film may be related linearly to the cube root of the flow shear. The output in this case is represented as the dissipated power divided by the differential operating temperature of the heated film above the flow temperature.

$$\text{Anemometer Output Parameter} = \frac{i^2 R}{\Delta T} \tag{4.20}$$

To apply Mirels' skin friction solution, an average about a point is defined for a point in time on a typical anemometer response to a shock wave. Although the skin friction solution varies as a function of time, the averaging is performed in a relatively flat area of the response in order to reduce the signal noise. The theoretical shear is calculated for the point as well as the output parameter as defined in equation (4.20). This results in a calibration plot as shown in Figure 4.29. A Reynolds' number calculation indicates that some points correspond to laminar conditions while some of the larger magnitude shear data may correspond to turbulent conditions, but Figure 4.29 shows the linear relationship as described by Liepmann and Skinner. Since this calibration works well, the boundary layer must be developing approximately in the manner described by the Mirels' solution, and the quasi-steady assumption is approximately valid in this region. Of course, the accuracy of this calibration in a time-resolved sense remains to be determined.

The calibration is applied to a typical anemometer response to a shock wave in Figure 4.30. At first, it appears that the calibration does not apply well to the response. However, the leading edge of the response is a transient phenomena associated with the anemometer circuit that is related to the magnitude of the velocity step. This phenomena is not accounted for in the quasi-steady calibration. In addition, the trailing edge of the response after the surge that occurs at approximately 0.25 msecs is also not accounted for in the calibration due to a pressure wave from the sensor mount that interrupts the boundary layer development (see Appendix E). For the region between 0.05 msecs and 0.25 msecs, the calibration seems to apply with sufficient agreement.

Further work along these lines may be able to show the limits of applicability of the quasi-steady calibration. Also, data taken with an improved sensor mount may show a better agreement of the experimental data and theoretical model for a longer time. Finally, ensemble averaged data could be used to further test the agreement of theory and experimental data.

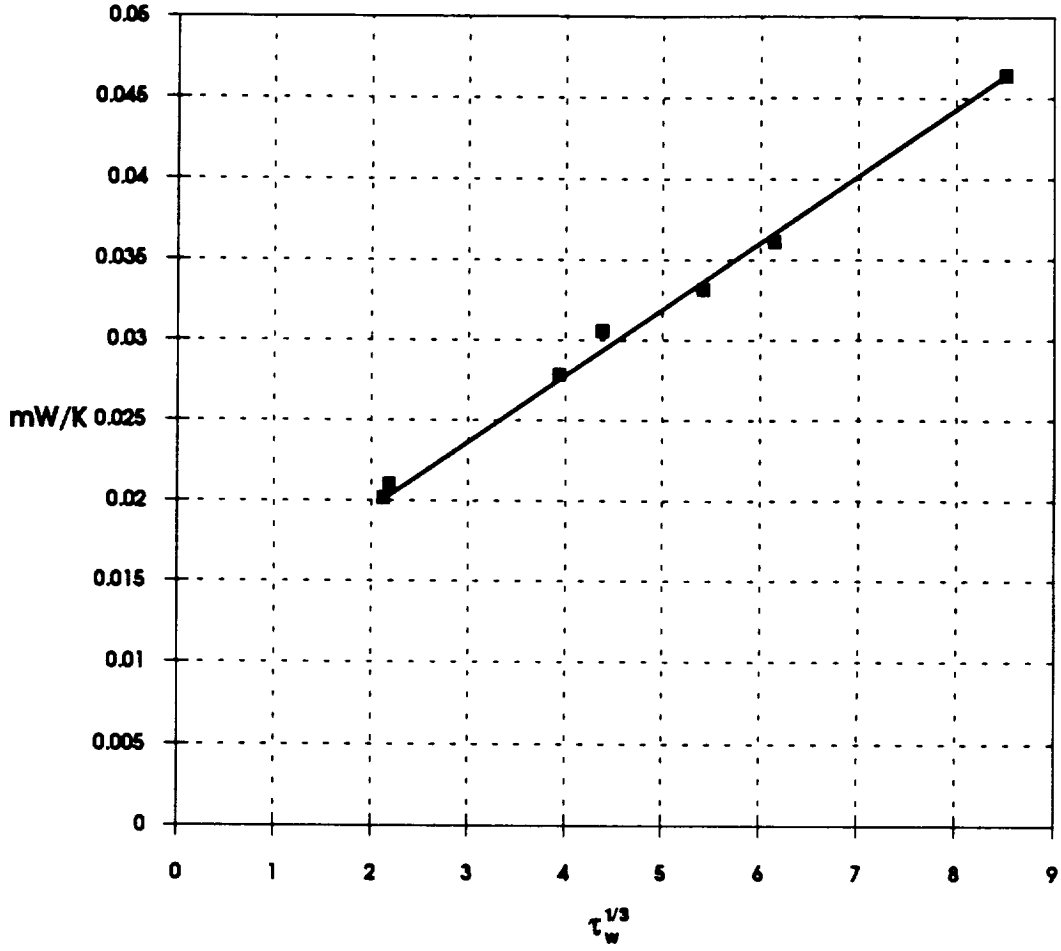

Figure 4.29. Calibration of sensor output using Mirels' quasi-steady solution

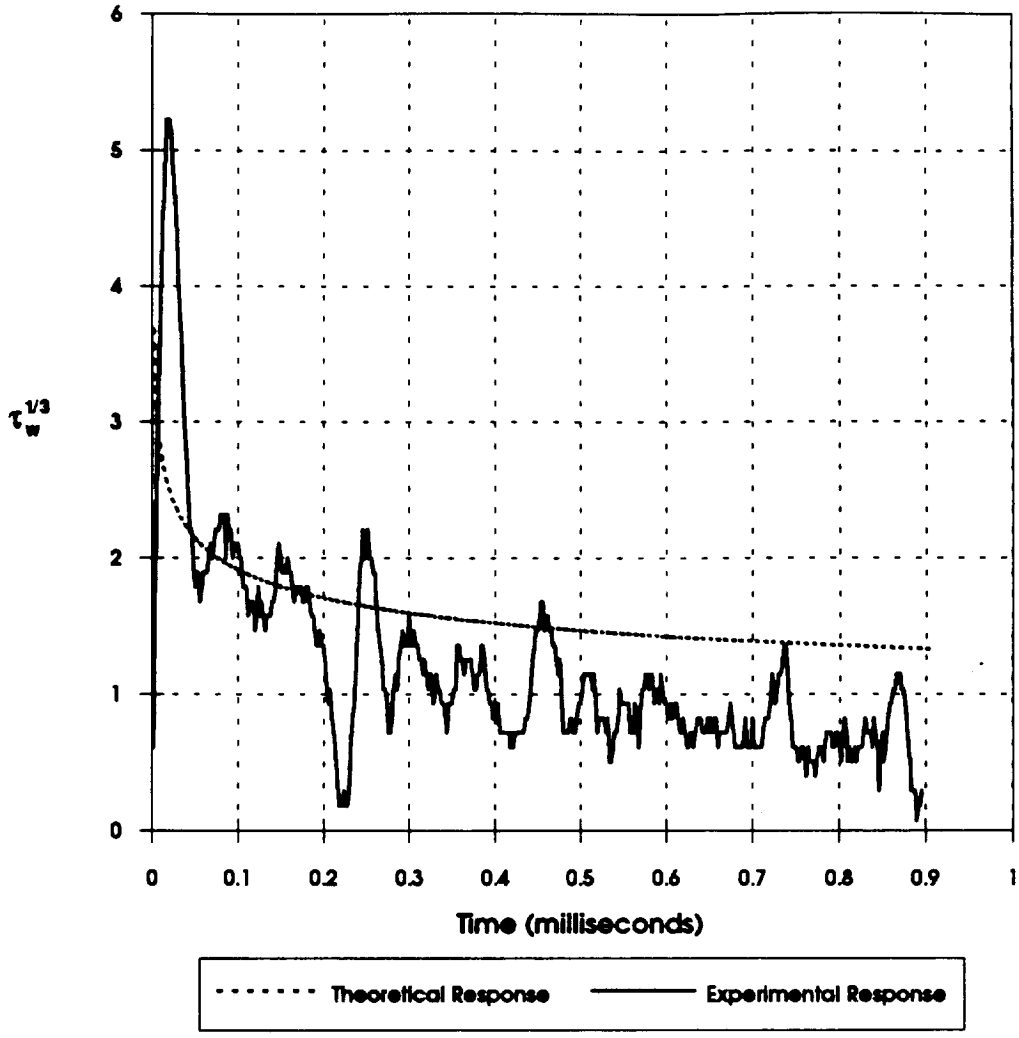

Figure 4.30. Application of calibration to typical anemometer shock wave response

4.4.5. Development of Instabilities and Turbulence In the Flow

As a final point of analysis, boundary layer instability was investigated by running successive shocks at different strengths over one sensor plate in the shock tube. Because all sensor plates were identical in design, the 20 mil glass sensor plate was chosen to make the flow survey due to its high sensitivity. With the 20 mil glass sensor running at a single overheat, four different shocks were passed over the sensor plate and each shock event was recorded.

Mirels' shock induced boundary layer assumes a quasi-steady regime for the building boundary layer which allows us to define a Reynolds' number as

$$Re_{xs} = \frac{(u_w - u_e)^2 t}{\nu_2} \tag{4.21}$$

Recall that stability calculations indicate that instability occurs around a Reynolds' number of 90,000 for the Mach zero case. Figures 4.31 through 4.34 show the amplitude response of each shock event plotted against the transient Reynolds' number defined by equation 4.21. In a lab fixed frame, the heat transfer and skin friction are infinite in theory, but finite in nature at the leading edge of a plate. As the distance x from the leading edge increases, the Reynolds' number increases and the heat transfer and skin friction decrease. This decreasing trend continues until the boundary layer experiences transitional behavior followed by turbulence, and a leap to a higher level of heat transfer and skin friction occurs. Once again this is followed by a decrease in momentum and heat transport as the Reynolds' number continues to increase. This analogy is easily applied to the shock induced boundary layer case by fixing the coordinate system to the shock. For a sensor in one place, the boundary layer grows with the time after the shock passage. Figure 4.31 is perhaps the most laminar case in which a

decline in the amplitude is seen with the increasing Reynolds' number. Figure 4.32 is similarly laminar but small fluctuations that may or may not be attributed to noise are shown in the response. Figure 4.33 is the best response obtained for visualizing the transition to turbulence. Fluctuations are seen prior to a Reynolds' number of 90,000 and following 90,000, the fluctuations increase in magnitude and there is an initial increase in the mean amplitude implying that the boundary layer has become transitional if not turbulent. Figure 4.34 is nearly fully turbulent. While the level of some fluctuations may be attributed to the design of the sensor mount (see Appendix E) the sensor is clearly showing fluctuations in the flow that are more significant than the amount of operational electronic noise present. However, whether or not the fluctuations are related to an underdamped electronic phenomena remains to be an issue.

A fast Fourier transform (FFT) was performed on the four cases to see if any frequency of oscillation dominated the fluctuations seen in the experimental data. A plot of the FFT's showed very little which may be due to the limited amount of points defining the results. In addition, the ambiguity of the FFT may have also been caused by the material step junction between the sensor plate and the mount. Once the shock wave had passed over the step junction , a reflected shock wave or pressure surge was fed upstream in the subsonic flow region causing an unexpected "bounce" in the anemometer's response to a velocity step. The FFT problem can best be solved by both designing a non-obtrusive sensor mount as well as utilizing a data acquisition system that is capable of capturing more than 500 points. The important point of this part of the result is that the sensor appears to be perfectly capable of measuring transitional and turbulent phenomena at the wall. Having shown that a transition type phenomena is occurring around a Reynolds' number of 90,000, which is reasonable for flow over a 30 degree leading edge (see Davies and Bernstein [10]), credibility is lent to other parts of the analysis in this work where it was assumed that a Mirels-type boundary layer existed.

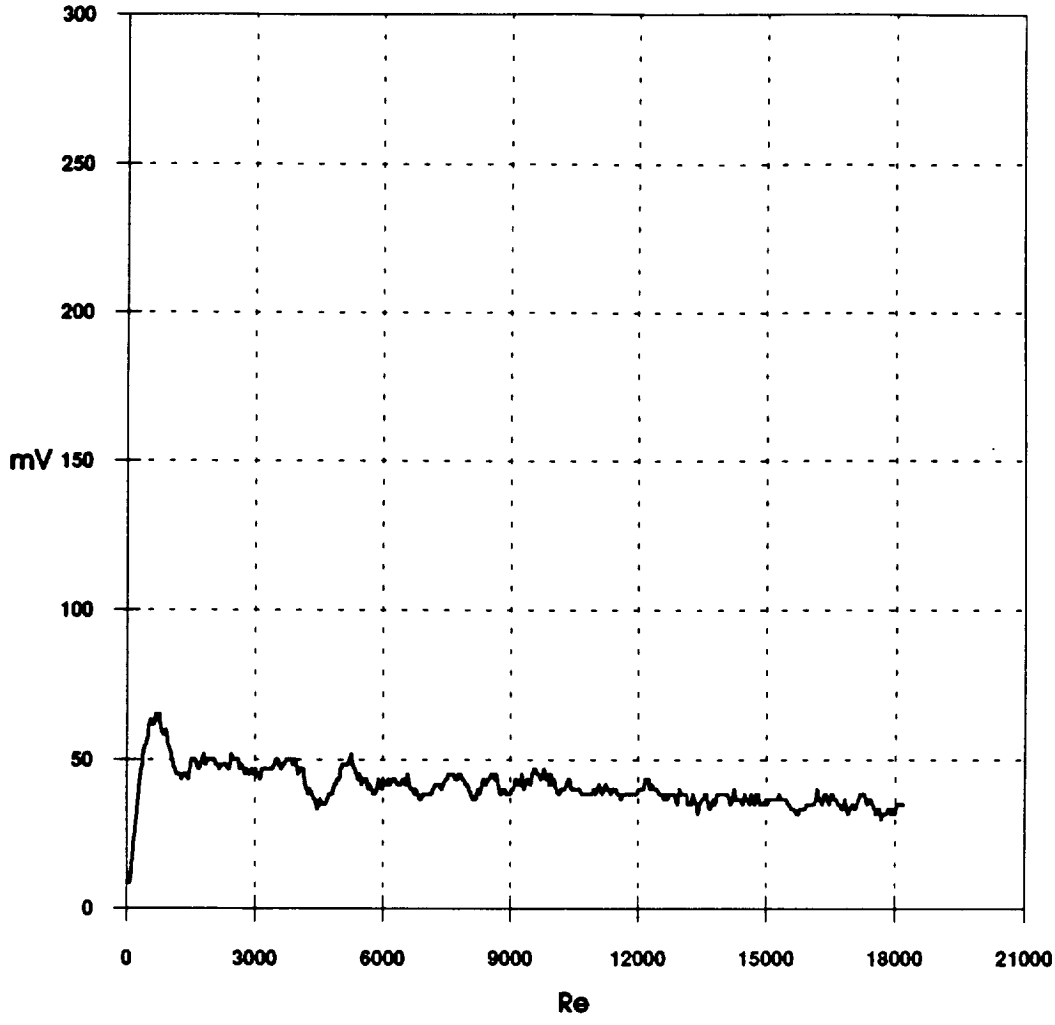

Figure 4.31. Reynolds' number stability analysis - case 1

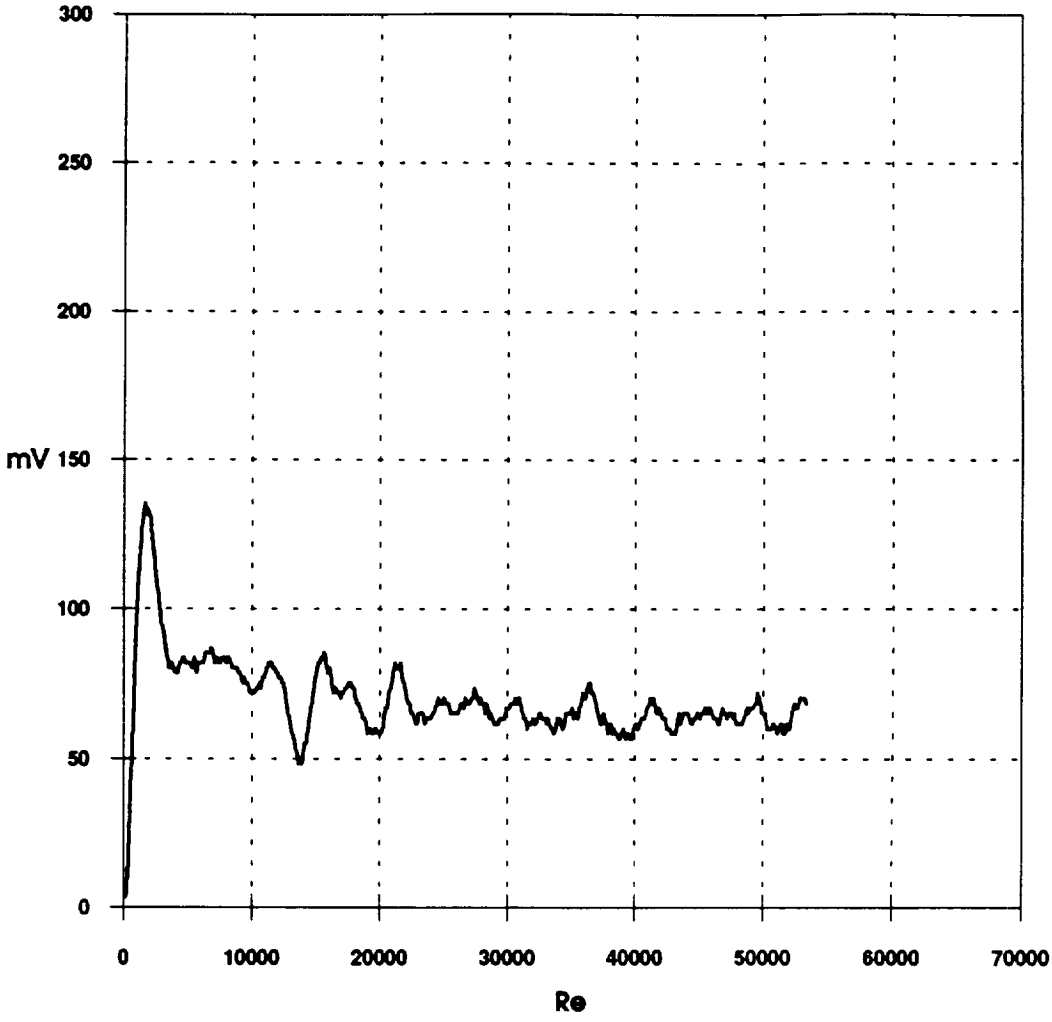

Figure 4.32. Reynolds' number stability analysis - case 2

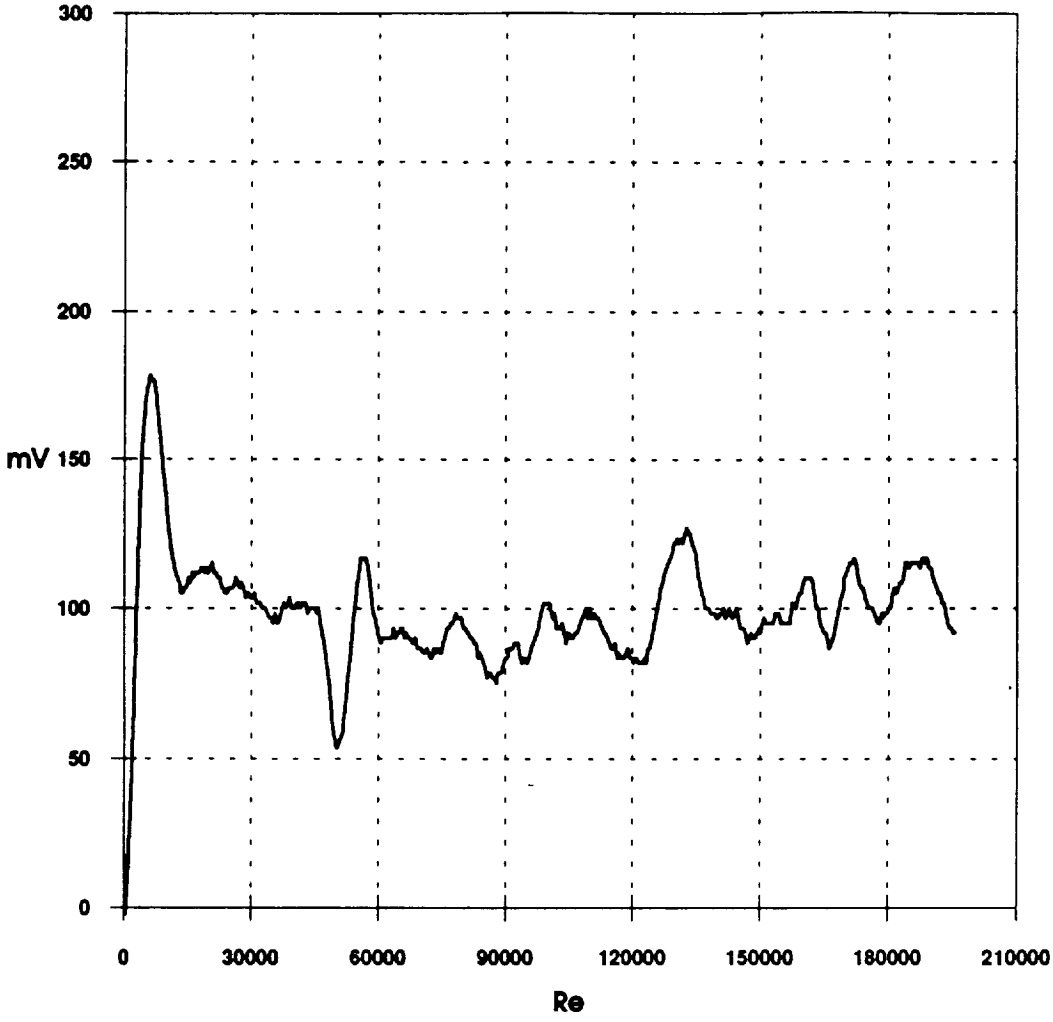

Figure 4.33. Reynolds' number stability analysis - case 3

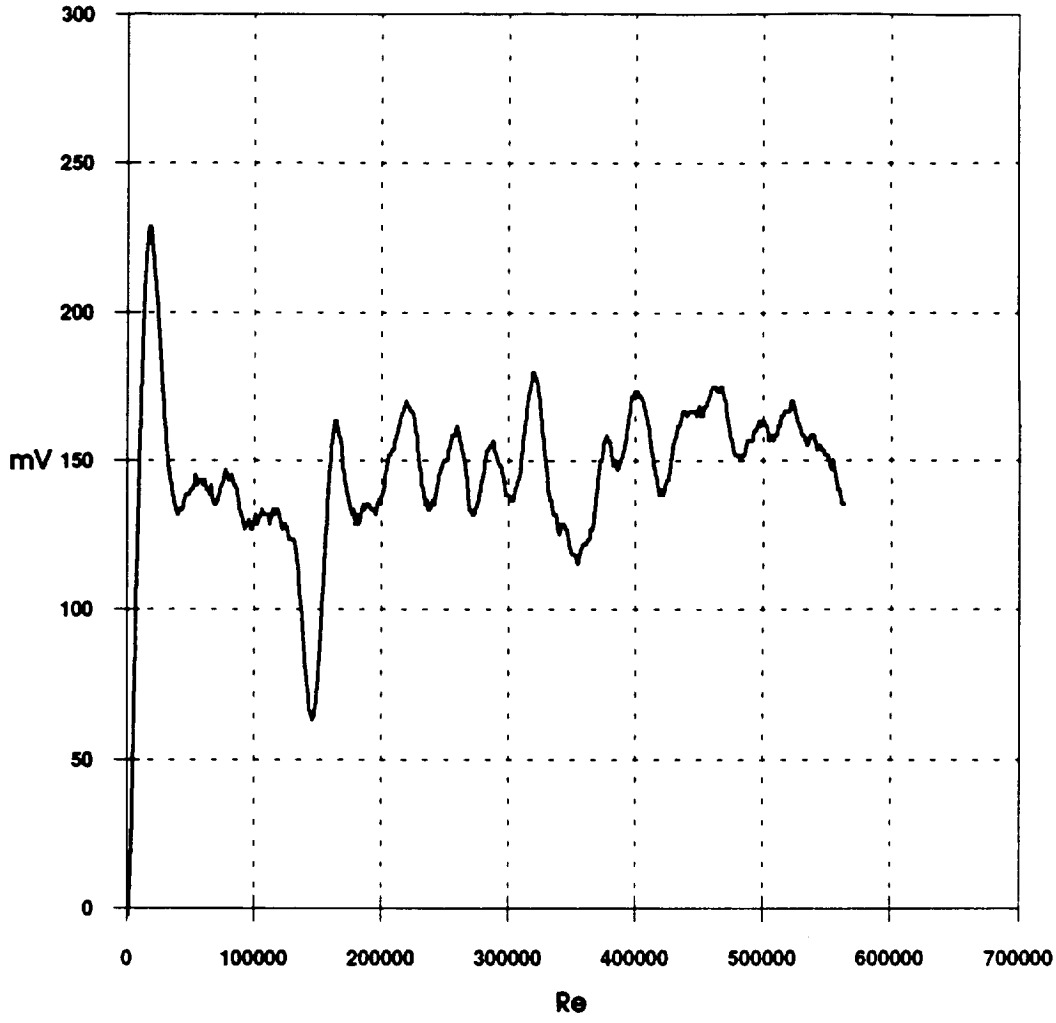

Figure 4.34. Reynolds' number stability analysis - case 4

5. CONCLUSIONS

Data has been provided in this work to detail the performance of flush-mount sensors through the variation of anemometer circuit architecture, sensor dimension and substrate material. The most important characteristics of a sensor are the sensitivity and the frequency response. Generally, there is a trade-off in the two characteristics such that a high frequency response flush-mount sensor has poor sensitivity and vice versa.

Frequency response of the anemometer system with a flush-mount sensor can be effectively varied in three ways. The first way is to vary the anemometer architecture. Utilizing an operational amplifier with the highest possible gain-bandwidth product will result in high frequency response by providing gain at high frequencies. The anemometer response may be further tuned electronically by adjusting the inductance in the circuit bridge as well as the offset voltage in the operational amplifier. Through the adjustment of these two parameters, the amplitude of the dynamic response overshoot may be altered as well as the exponential decay rate for the third order response. In the case of these two components, increased sensitivity can also be exchanged for a decrease in the frequency response performance.

Other architectural changes will make more minor improvements in the frequency response such as the use of resistors to isolate the inputs on the operational amplifier. This serves to match impedances in the circuit thereby reducing stray capacitances. A similar effect is achieved through the use of a 1:1 bridge rather than bridges with ratios such as 1:5 or 1:10. Use of a capacitor in parallel with a decompensated operational

amplifier will help to ensure stability out to higher frequencies by providing compensation to the operational amplifier. This helps create a robust system that is more reliable for high frequency response operation.

Frequency response may be improved by designing smaller sensors. A simple lumped capacitance heat transfer analysis showed that smaller sensors adjust more quickly to temperature changes and this was reflected very clearly in the comparison between the 5, 10 and 20 mil sensors on the glass substrate. Since the relationship between thermal capacity (based on sensor size) and frequency response is clearly shown, it is assumed that the same rule would apply to different metal film materials such that materials with smaller time constants based on the lumped capacitance model would respond faster when in use with a constant temperature anemometer. However, the lumped capacitance model is insufficient when it comes to accurately predicting the thermal behavior of the flush-mount hot film. The amount of power that the sensor dumps to the surrounding substrate is a function of the sensor dimensions as well as the ratio of the film conductivity to the substrate conductivity. The presence of substrate conduction invalidates the use of the lumped capacitance model for anything more than predicting basic trends.

As the sensor size decreases, architectural changes have a more significant effect on the frequency response. The 5 mil glass sensor benefited more from increases in the overheat as well as increases in the inductance compensation than either of the 10 or 20 mil glass sensors. However, the size of a sensor is limited by its sensitivity. The 5 mil glass sensor had a lower sensitivity than the 10 and 20 mil glass sensors. Gains in frequency response by reducing the sensor size will be countered by a decrease in sensitivity.

The relative amount of heat conducted to the substrate and convected to the fluid was made more clear by looking at the non-dimensional power dissipation, P^*, for different sensor dimensions. In terms of static power dissipation, larger sensors consumed

more power than the smaller sensors. However, with the smaller sensors, P^* was decreased, which was reflected in the sensitivity of the sensor. Smaller P^* implied that more heat was being conducted to the substrate than was being convected to the flow resulting in a decreased output level. The issue of decreased sensitivity was confirmed in sine wave testing in which the relative response amplitude was greater for larger sensors. With enough data, an empirical relationship between the frequency response and sensor sensitivity could be drawn to assist in the design of flush-mount sensors.

The non-dimensional power dissipation, P^*, was also recorded for the 20 mil sensors on the glass, alumina and aluminum substrates. In terms of static power dissipation, the alumina sensor consumed the largest amount of power while the glass consumed the least. However, P^* was greatest followed by the glass then alumina sensor. It is unclear as to why the aluminum sensor had superior performance. Soon after testing, the aluminum sensor failed. The superior performance could then have been a result of the sensor running hot. If it was running at a much higher temperature than the glass or alumina sensors, then the sensitivity would appear to be greater. However, the superior performance may be associated with the 6 micron polyimide layer on the aluminum substrate.

The greatest improvements in frequency response can be achieved by choosing the proper substrates upon which the flush-mount sensors will be deposited. It has been shown that substrate conductivity plays a strong role in the response of the sensor. The trend shows that for a given sensor dimension, higher conductivity substrates have faster frequency response than their lower conductivity counterparts. This trend holds true for electronic testing as well as velocity step testing. Recall the two simple models which analyzed the sensor as a semi-infinite substrate. Substrates with a higher β had a faster thermal response. In the case of this model, the experimental data followed this trend.

Comparisons were drawn to theory by Freymuth [16,17], Watmuff [41] and Kalumuck [21] with mixed success. Freymuth's third order theory served as a good tool for comparison of different anemometer configurations. Each configuration can be described with a time constant that reflects the third order behavior as well as the frequency response performance. However, when the experimentally determined time constants were used to predict the experimental response to a velocity step, the results were inaccurate. The time constant associated with the sensor was calculated for the 5, 10 and 20 mil glass sensors and it was found that the time constant, M, scaled closely to the dimensions of each sensor. The usefulness of this results remains in question. Freymuth's analysis was intended for hot wires rather than flush-mount films.

Freymuth provided a correction to his theory for flush-mount films that incorporated the Bellhouse-Schultz model for heat transfer from a hot film to a substrate. Theoretical results were shown for sensors of different Biot number and compared to experimental results. Biot number decreases with increasing sensor size for sensors on similar substrates and relative response increases with decreasing sensitivity. This is another confirmation of the sensitivity issue for different sensors.

Kalumuck's theory was concerned with representing the performance of different sensor designs through a Nusselt number for variations in the sensor conductivity ratio, aspect ratio and Peclet number. The purpose of his theory was to detail the heat transfer process between the film and substrate and to provide a means of representing the calibration of the sensor. Results from Kalumuck's theory were compared to velocity step testing results for the 20 mil glass, alumina and aluminum sensors. The results were closer than expected, which seems to open the possibility for quick sensor calibration in the shock tube. One shock tube run can provide the results for variation in Nusselt and Peclet number.

Finally, boundary layer stability was checked with the sensor as a proof of sensor capability as well as a check of the flow quality. Stability calculations indicate that the boundary layer transitions at a Reynolds' number of approximately 90,000 for the case where M = 0. A transition type phenomena was shown to occur at this Reynolds' number indicated by the sudden increase in heat transfer and the introduction of large scale fluctuations following the Re = 90,000 point.

6. SUGGESTIONS FOR FURTHER RESEARCH

This project was primarily involved with system refinement and the parametric study of substrate choice and sensor dimension. The substrate plays a very large role in the frequency response of a shear wall hot film, but how might this be quantified? Theoretical models have been devised to show the surface temperature distribution on the substrate in the vicinity of the sensor. Research efforts could be made to provide experimental data in support of these models. Current research in the Aerospace Sciences Laboratory of Purdue University involves the characterization of flows through the use of temperature sensitive paints. These paints could be utilized to define the thermal footprint associated with each sensor on each substrate in a variety of flow conditions. This might lead to a good empirical correlation of the ratio of conductive heat transfer to convective heat transfer from the sensor to the substrate and air.

The calibration of sensors still remains as an obstacle to the reliable use of a flush-mount hot film. Quite often, the sensor must be calibrated at conditions near to what the sensor will actually be used at. Understanding the heat transfer characteristics of the substrate as it ties in with the feedback response would help clear up this issue and provide a reliable means of calibrating a flush-mount sensor for all conditions. Kalumuck did a good job of modeling the film substrate interaction and experimental results seemed to compare well. The shock tube and Ludweig tube should be further investigated as a quick and simple means of calibrating flush-mount sensors resulting in calibrations similar to what Kalumuck described.

It becomes clear that the flow phenomena and the electrical phenomena associated with anemometry cannot be decoupled. Research has produced several good models that address either circuit stability or sensor heat transfer, but they always neglect some important aspect of the anemometry problem. This attempt to decouple the sensor from the anemometer never quite works. Theories that account for both effects have given good results for the hot wire, but not for the flush-mount hot film. These theories cannot accurately be applied to flush-mount hot films due to the heat loss to the substrate. The Bellhouse-Schultz model for heat transfer to the substrate stands as a suitable correction to some anemometry theory, but it is only one-dimensional and other theories prove the strong three-dimensional heat transfer behavior of a flush-mount hot film. Building a more comprehensive model could be approached by performing a much more rigorous study of both electrical and flow testing under different anemometer configurations. This would at least provide a better base of data for comparison to current theories and would result in a good empirical correlation such as the Biot number correlation discussed by Freymuth.

A constant current anemometer was designed and built towards the end of this project with the intention of running the sensors with the same shock conditions as the constant temperature cases. This would provide more information on the state of the flow and how well it compares to Mirels' solution. Constant current anemometry is more like running the sensors as thermometers where the frequency response is limited by the thermal capacity of the sensor material. Recall that the thermal models presented at the beginning of this thesis all treated the sensor as if it were connected to a constant current anemometer. It would be an excellent piece of work to compare the sensor behavior under constant temperature and constant current anemometry.

Substrate models for the flush-mount hot film can account for three dimensional heat transfer. However, the substrate is usually treated as semi-infinite. Evidence has shown that a thin insulating layer can significantly reduce the frequency response of a

flush-mount sensor on a high thermal conductivity substrate. One approach to designing a better sensor would be to gain a better understanding of the penetration depth, for velocity and voltage fluctuations, in a non-homogeneous layered substrate. The penetration depth of a fluctuation may be directly correlated to the frequency response of the sensor. If so, then optimizing substrate choice could become an easier task. For example, one of the highest conductivity substrates that could be used is diamond. Of course a whole model cannot be made from diamond but a diamond layer on a model could significantly increase the frequency response of the sensor. A layered substrate structure could be optimized for the heat wave penetration thickness into the substrate, thereby helping to minimize the amount of diamond to be used.

Perhaps the best direction for further research would be to draw a clear-cut relationship between the frequency response and sensitivity for different substrate types. As the substrate conductivity goes to the limit of infinity, what happens to the sensitivity, and what happens correspondingly if the substrate conductivity goes to zero? Obtaining more data in the flow condition for a larger array of homogeneous substrates would provide some interesting and useful data towards an empirical correlation relating frequency response and sensitivity. This relationship could also easily include the effect of sensor dimension. The end result would be some sort of curve that would assist in the optimization of sensor design.

BIBLIOGRAPHY

BIBLIOGRAPHY

1. Arts, T., Camci, C.; "Short Duration Heat Transfer Measurements"; Measurement Techniques in Turbomachines, Vol. 2, 1985.

2. Ajagu, C.O., Libby, P.A., LaRue, J.C.; "Modified Gauge for Time-Resolved Skin-Friction Measurements"; Review of Scientific Instruments, Vol. 53, No. 12, 1982.

3. Alfredsson, P.H., Johansson, A.V., Haritonidis, J.H., Eskelmann, H.; "The Fluctuating Wall-Shear Stress and the Velocity Field in the Viscous Sublayer"; Phys. Fluids, Vol. 31, No. 5, 1988.

4. Bellhouse, B.J., Schultz, D.L.; "The Measurement of Skin Friction in Supersonic Flow by Means of Heated Thin Film Gauges"; Reports and Memoranda No. 3490, 1965.

5. Bellhouse, B.J., Schultz, D.L.; "Determination of Mean and Dynamic Skin Friction, Separation and Transition in Low-Speed Flow With a Thin-Film Heated Element"; Journal of Fluid Mechanics, Vol. 24, 1966.

6. Bellhouse, B.J., Schultz, D.L.; "The Determination of Fluctuating Velocity in Air with Heated Thin-Film Gauges"; Journal of Fluid Mechanics, Vol. 29, 1967.

7. Brosh, A., Degani, D., Zalmanovich, S.; "Conjugated Heat Transfer in a Laminar Boundary Layer With Heat Source at the Wall"; Journal of Heat Transfer, Vol. 104, 1982.

8. Cole, K.D., Beck, J.V.; "Conjugated Heat Transfer from a Strip Heater with the Unsteady Surface Element Method"; AIAA/ASME 4th Joint Thermophysics and Heat Transfer Conference, AIAA-86-1242, 1986.

9. Cook, W.; "Response of Hot-Element Wall Shear Stress Gages in Unsteady Turbulent Flows"; AIAA 29th Aerospace Sciences Meeting, AIAA-91-0167, 1991.

10. Davies, W.R., Bernstein, L.; "Heat Transfer and Transition to Turbulence in the Shock-Induced Boundary Layer on a Semi-Infinite Flat Plate"; Journal of Fluid Mechanics, Vol. 36, Part1, 1969.

11. Diaconis, N.S.; "The Calculation of Wall Shearing Stress from Heat-Transfer Measurements in Compressible Flows"; Journal of the Aeronautical Sciences, Vol. 21, 1954.

12. Diller, T.E., Telionis, D.P.; "Time-Resolved Heat Transfer and Skin Friction Measurements in Unsteady Flow"; Advances in Fluid Mechanic Measurements, Springer-Verlag, 1989.

13. Fage, A., Falkner, V.M.; "On the Relation Between Heat Transfer and Surface Friction for Laminar Flow"; Aeronautical Research Council Report R & M 1408, 1931.

14. Flutie, K.J., Covert, E.E.; "Unsteady Measurement of Skin Friction in Adverse Pressure Gradient; A New Approach to a Well-Known Gauge"; AIAA 29th Aerospace Sciences Meeting, AIAA-91-0168, 1991.

15. Freymuth, P.; "Feedback Control Theory for Constant-Temperature Hot-Wire Anemometers"; Review of Scientific Instruments, Vol. 38, No. 5, 1967.

16. Freymuth, P.; "Frequency Response and Electronic Testing for Constant-Temperature Hot-Wire Anemometers"; Journal of Physics and Scientific Instruments Vol. 10, 1977.

17. Freymuth, P.; "Sine-Wave Testing of Non-Cylindrical Hot-Film Anemometers According to the Bellhouse-Schultz Model"; Journal of Physics E, Vol. 13, 1980.

18. Freymuth, P., Fingerson, L.M.; "Electronic Testing of Frequency Response for Thermal Anemometers"; TSI Vol 3, No. 4, 1977.

19. Houdeville, R., Juillen, J.C.; Skin Friction Measurements with Hot Elements"; VKI Lecture Series on Measurement Techniques in Aerodynamics, 1988.

20. Incropera, F.P., DeWitt, D.P.; Fundamentals of Heat and Mass Transfer, 3rd ed., John Wiley & Sons, 1990.

21. Kalumuck, K.M.; "A Theory for the Performance of Hot-Film Shear Stress Probes"; Ph.D. Thesis, M.I.T. Department of Aerospace Engineering, 1983.

22. Liepmann, H.W., Skinner, G.T.; "Shearing-Stress Measurements by Use of a Heated Element"; NACA TN 3268, 1954.

23. Ling, S.C.; Heat Transfer From a Small Isothermal Spanwise Strip on an Insulated Boundary"; Journal of Heat Transfer, Vol. 85, 1963.

24. Ludweig, H.; "Instrument for Measuring the Wall Shearing Stress of Turbulent Boundary Layers"; NACA TM 1284, 1950.

25. Mao, Z.X., Hanratty, T.J.; "The Use of Scalar Transport Probes to Measure Wall Shear Stress in a Flow With Imposed Oscillations"; Experiments in Fluids Vol. 3, 1985.

26. Menendez, A.N., Ramaprian, B.R.; "The Use of Flush-mounted Hot-Film Gauges to Measure Skin Friction in Unsteady Boundary Layers"; Journal of Fluid Mechanics, Vol. 161, 1985.

27. Mirels, H.; "Laminar Boundary Layer Behind Shock Advancing into Stationary Fluid", NACA TN 3401, 1955.

28. Mirels, H.; "Boundary Layer Behind Shock or Thin Expansion Wave Moving into Stationary Fluid", NACA TN 3712, 1956.

29. Murthy, V.S., Rose, W.C.; "Direct Measurements of Wall Shear Stress by Buried Wire Gages in a Shock Wave Boundary Layer Interaction Region"; date unknown.

30. Owen, F.K., Bellhouse, B.J.; "Skin Friction Measurements at Supersonic Speeds"; AIAA Journal, Vol. 8., No. 7, 1970.

31. Perry, A.E., Morrison, G.L.; "A Study of the Constant Temperature Hot-Wire Anemometer", Journal of Fluid Mechanics, Vol. 47, 1971.

32. Reda, D.C.; "Rise-Time Response of Nickel-Foil-On-Kapton-Substrate, Hot-Film, Shear-Stress Sensors"; AIAA 29th Aerospace Sciences Meeting, AIAA-91-0169, 1991

33. Roberts, G.T., Kilpin, D., Lyons, P., Sandeman, R.J., East, R.A., Pratt, N.H.; "Shock Tube Measurements of Convective Heat Transfer From a High Reynolds Number, Particle-Laden, Turbulent, Non-Steady Boundary Layer"; Proc. 15th Int. Symposium of Shock Waves and Shock Tubes, 1985.

34. Roberts, A.S.,Jr., Ortgies, K.R., Gartenberg, E.; "Transient Hot Film Sensor Response in a Shock Tube"; ODU Research Foundation, NASA Contractor Report 181838 under contract NAG1-735, 1989.

35. Roos, F.W.; "A Hot-Film Probe Technique for Monitoring Shock Wave Oscillations"; AIAA 17th Aerospace Sciences Meeting, A79-23559, 1979.

36. Roos, F.W., Bogar, T.J.; "Direct Comparison of Hot-Film Probe and Optical Techniques for Sensing Shock-Wave Motion"; AIAA 19th Aerospace Sciences Meeting, A81-20637, 1981.

37. Sandborn, V.A.; "Resistance Temperature Transducers"; Metrology Press, 1972.

38. Schneider, S.P.; "A Quiet-Flow Ludwieg Tube for Experimental Study of High Speed Boundary Layer Transition"; AIAA Third International Aerospace Planes Conference, A91-5026, 1991.

39. Schultz, D.L., Jones, T.V.; "Heat Transfer Measurements in Short-Duration Hypersonic Facilities"; Agardograph No. 165, 1973.

40. Tanner, R.I.; "Theory of a Thermal Fluxmeter in a Shear Flow"; Journal of Applied Mechanics, Vol. 34, 1967.

41. Watmuff; J. H.; "Increasing the Frequency Response of Constant Temperature Hot-Wire Systems for use in Supersonic Flow"; NASA Technical Brief ARC-12469, 1988.

42. White, F.M.; "Viscous Fluid Flow"; McGraw Hill, 2nd ed., 1990.

APPENDICES

APPENDICES

Appendix A: Anemometer Parts List

In the course of this thesis work, the anemometer underwent several changes in order to make it operate with a higher frequency response. The resulting anemometer designs are referred to as Anemometer Configuration Prototype (AC-P), Anemometer Configuration 1 (AC-1) and Anemometer Configuration 2 (AC-2). Most of the initial testing was done with the AC-P to ensure a working design. AC-1 was guided by the result of electrical testing data in the early workings with AC-P. AC-2 evolved after a more thorough understanding of the anemometer circuit was gained.

It is understood that this architecture is only one design in a large field of anemometer designs. The architecture employed for the anemometer design in this thesis is chosen primarily for historical reasons. This anemometer works with the operational amplifier operating at maximum gain. An operational amplifier at a higher gain means that the roll-off frequency will be lower for the system. This is not as large of a sacrifice as one might suspect due to the nature of the sensors that are subject to this research. The flush-mount sensors have an inherently low frequency response so the anemometer system can better take advantage of the maximum gain. A comparison for the cut-off frequency can be partially addressed electrically testing other anemometer architectures such as the IFA-100 anemometer designed by TSI. The IFA-100 narrowly outperforms the AC-2 design in terms of frequency response. However, the gain is greater for the AC-2 anemometer which explains the higher noise levels as well as the higher signal level for a given event.

A.1. AC-P Parts List

The following list details the parts used for the Prototype anemometer. A corresponding circuit design follows in Figure A.1.

4	1.0 μF 35 V capacitors
2	0.33 μF 35 V capacitors
2	100 μF 25 V capacitor
1	100 pF capacitor
2	100 Ω 1/4 W 1% resistors
3	4 kΩ 1/4 W 1% resistors
1	Digidecade variable resistor (1Ω-1000Ω)
1	2 kΩ trim pot resistor
1	40 Ω Vishay precision resistor
1	INA110 instrumentation amplifier
1	OP-27 operational amplifier (Gain/Bandwidth of 6)
1	TIP121 Darlington transistor
1	Milliameter

A.2. AC-1 Parts List

After initial work with the prototype anemometer was completed, the following changes were made resulting in Anemometer Configuration 1.

1. Removal of the milliameter from the feedback loop.
2. Removal of the Digidecade digipot and replacement with a 1% 1/8 W metal film fixed resistor.
3. Installation of a 1% 1 W metal film resistor for current limiting.
4. Minimal adjustment of offset null to eliminate start-up problems.
5. Connection of circuit board common to case and power in ground.
6. Replacement of the OP-27 operational amplifier with an OP-37 operational amplifier.

The following list details the parts used for Anemometer 1. A corresponding circuit design follows in Figure A.2.

4	1.0 μF 35 V capacitors
2	0.33 μF 35 V capacitors
1	1.0 μF 50 V capacitor
1	100 pF capacitor
2	100 μF 25 V capacitors
2	100 Ω 1/4 W 1% resistors
1	270 Ω 1 W 1% resistor
3	4 kΩ 1/4 W 1% resistors
1	100 kΩ 1/4 W 1% resistor
1	2 kΩ trim pot resistor
1	40 Ω Vishay precision resistor
1	INA110 instrumentation amplifier
1	OP-37 operational amplifier (gain bandwidth of 60)
1	TIP121 Darlington transistor

A.3. AC-2 Parts List

Further use and testing led to the following circuit changes resulting in Anemometer Configuration 2.

1. Installation of a 500 Ω precision potentiometer for current limiting control.
2. Installation of a Alcoswitch 10 position switch for fixed resistance selection.
3. Installation of a variable inductor for cable inductance compensation and tuning of frequency response.
4. Installation of permanent BNC cable connector for square wave testing
5. Installation of input isolation resistors on the input pins of the operational amplifier and transistor.
6. Installation of a trim capacitor for controlling the roll-off frequency of the operational amplifier.

The following list details the parts used for Anemometer Configuration 2. A corresponding circuit design follows in Figure A.3.

4	1.0 µF 35 V capacitors
2	0.33 µF 35 V capacitors
1	1.0 µF 50 V capacitor
1	100 pF capacitor
1	7-40 pF trim capacitor
2	100 µF 25 V capacitors
1	11-64 µH variable inductor
2	100 Ω 1/4 W 1% resistors
6	4 kΩ 1/4 W 1% resistors
1	100 kΩ 1/4 W 1% resistor
1	2 kΩ trim pot resistor
1	40 Ω Vishay precision resistor
1	INA110 instrumentation amplifier
1	OP-37 operational amplifier
1	TIP121 Darlington transistor
1	Alcoswitch 10 position switch
1	Spectrol 500 Ω precision potentiometer

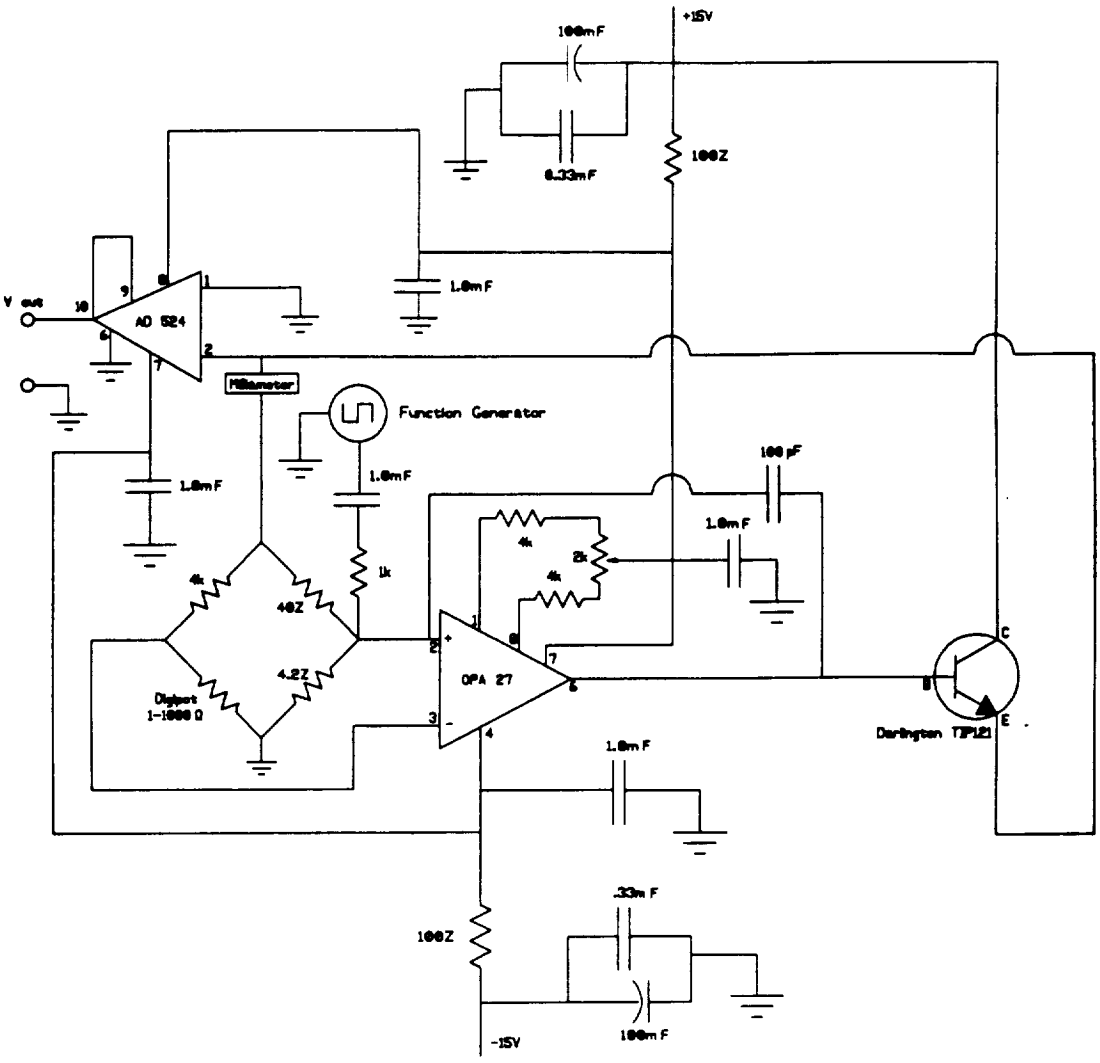

Figure A.1. Anemometer Configuration Prototype

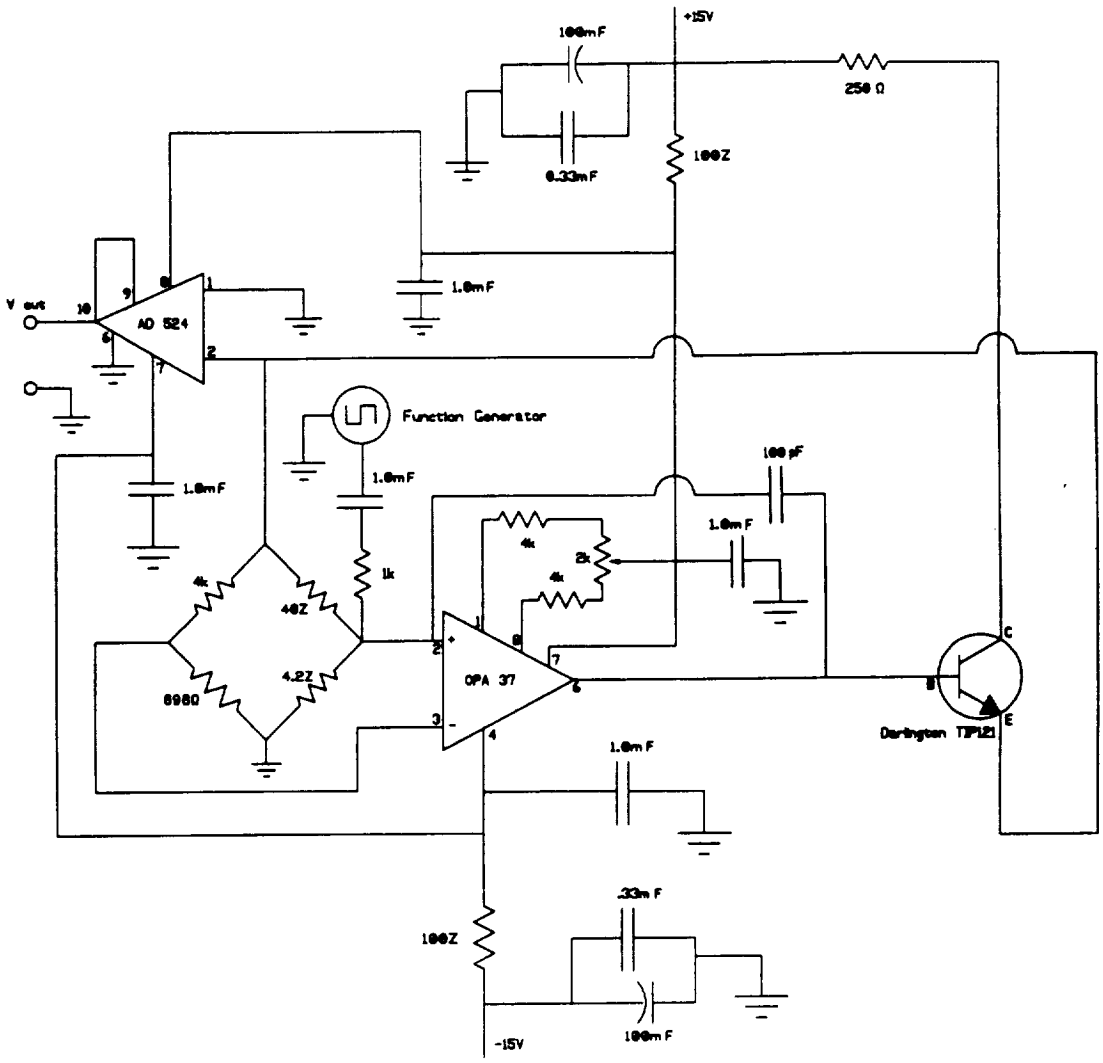

Figure A.2. Anemometer Configuration 1

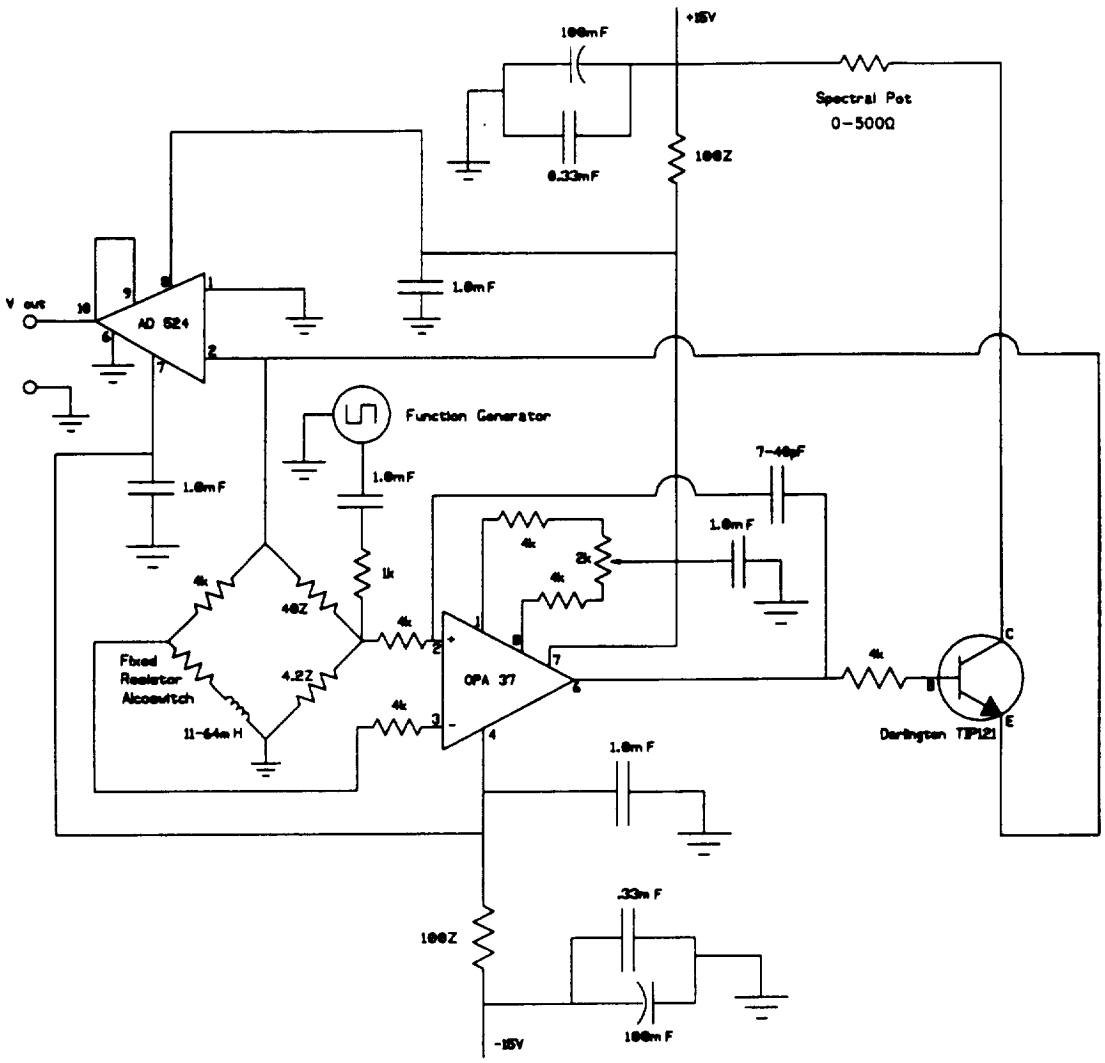

Figure A.3. Anemometer Configuration 2

Appendix B: Spice Modeling

SPICE is an software program that is capable of analyzing electrical circuits. It's intended use is to assist in the design of integrated circuits, however it was used in this project as a means of simulating the anemometer circuit and providing a "software testbed" for new anemometer components or subtle architectural changes. Some of the major effects due to subtle changes that were modeled with SPICE were:

Compensation Capacitor For Operational Amplifier: The roll-off capacitor (component C_1 on Figure B.1) is placed in parallel with the operational amplifier in order to control the gain-bandwidth product roll-off of the operational amplifier. The operational amplifier is built with a particular gain-bandwidth product, but at high frequencies, there may be unstable or non-ideal gain. By placing a capacitor in parallel, we can make the operational amplifier roll off the gain prematurely before the unstable mode is entered.

Control Resistance (Overheat Ratio): The control resistor (component R_1 on Figure B.1) is what sets the overheat of the anemometer circuit. A higher overheat correspond to a higher current level in the sensor and, therefore, a higher frequency response for the anemometer system.

Input Isolation Resistors: Input isolation resistors are put on the input posts of the operational amplifier (components R_6, R_7 on Figure B.1) The effect of introducing input isolation resistors on the posts of the operational amplifier not so much for the input impedance of the op amp as it is for the op amp looking out to the input. Doing this will help to match the impedance of the op amp looking out thereby increasing the frequency response as well as stability. This was suggested by Norwood Robeson of LaRC as a means of providing better stability and decreasing noise when designing high speed circuits with op amps.

Operational Amplifiers: The operational amplifier (component OP-37 on Figure B.1) is the most important piece of a constant temperature anemometer for this particular architecture. Operational amplifiers can be described with their gain bandwidth product which varies widely form op amp to op amp. The gain bandwidth product describes the op amp relationship between gain and frequency response. An op amp with a higher gain bandwidth product will provide a larger gain for a given frequency or amplify out to a higher frequency for a given gain.

An input model shown below in Figure B.2 was used for the SPICE program and a transient test was run to capture the response of the anemometer system to a square wave input similar to the wave that is input to the anemometer experimentally.

Some results obtained with SPICE are shown in the following plots. Figure B.3 shows how the anemometer response changes with overheat. SPICE shows that for a given input square wave, the response increases in speed and decreases in magnitude. This is consistent with the definition of operational amplifier gain-bandwidth product running in open loop mode. Forcing the anemometer to a higher roll-off frequency will be accompanied by a decrease in the magnitude of the output. The problem with this result is that the magnitude and frequency are far from what was experimentally determined. Responses for the flush-mount sensors was more on the order of 10^4 while this result indicates 10^5 and amplitudes were at least 10 if not 100 times greater than predicted by SPICE. This is to be expected because it is nearly impossible to model a hot wire or hot film using SPICE. Resistance can be specified as well as a temperature coefficient of resistance for components, but thermal time constants of materials cannot be modeled in SPICE.

Figure B.3 was for an anemometer using an OP-37 operational amplifier. Figure B.4 is for an anemometer using an OP-27 operational amplifier. The results follow the same trend as in Figure B.3, but the response times are longer and the response

amplitudes are smaller. Once again, this is consistent with the gain-bandwidth definition. The gain-bandwidth product for an OP-27 is approximately 6 MHz while the gain-bandwidth product for an OP-37 is approximately 60 MHz. In terms of trends for operational amplifier choice, this result is encouraging, but it is not as accurate as hoped, and it doesn't provide any more information than reading the component literature might provide.

Finally, Figure B.5 is a plot of the anemometer response to an identical input square wave for different level of capacitance compensation to the operational amplifier. The frequency response decreases slightly with a decrease in the compensation capacitance. This is consistent with predicted performance but it still is not accurate in its actual calculation of the frequency response.

The attempt to model the anemometer circuit with SPICE was largely a failure. While it is good for its accurate representation of a large library of integrated circuits, it is unable to account for the characteristics that make a hot wire or a hot film operate as they do i.e. thermal characteristics. Therefore, results from SPICE should be considered only as far as indicating the most basic trends.

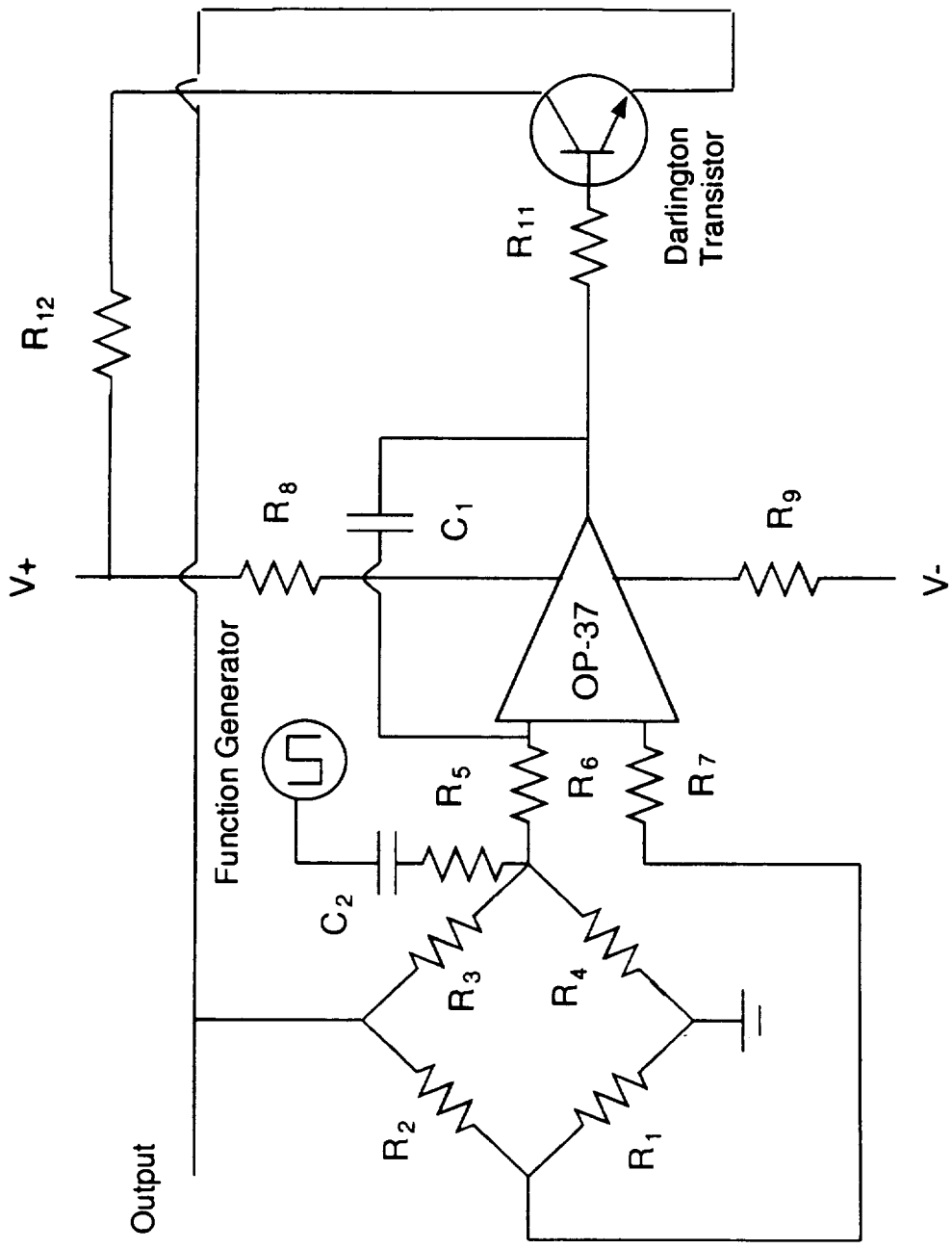

Figure B.1. Schematic of SPICE model used for anemometer circuit analysis

```
ANEM5.CIR ANEMOMETER CIRCUIT WITH SQUARE WAVE TEST
*This is the test step in voltage that is applied to the circuit
VTEST 12 0
PULSE(-3 3 0 1.000E-6 1.000E-6 499.0E-6 1.00E-3)
*This is the power supply voltage
V+ 10 0 DC +15
V- 6 0 DC -15
*These are the resistor values
R1 1 0 630
R2 3 1 4K
R3 3 2 40
R4 2 0 4.17
R5 2 11 100K
R6 2 4 01K
R7 1 5 1K
R8 9 10 50
R9 7 8 1K
*This can be used to replace C2 to make the circuit a voltage follower
*R10 4 7 0.01
R11 13 0 5K
*These are capacitor values
C1 11 12 1.0U
C2 4 7 1.0P
C3 3 13 100P
*This is the operational amplifier
XY=U1 4 5 10 6 7 OP37-LT
*This is the transistor
Q1 9 8 3 MOD1
*This is the library call for the IC's
.LIB NOM.LIB
*These are models of capacitors and resistors for the parametric study
*.MODEL RMOD RES(R=1)
*.STEP LIN RES RMOD(R) 500 800 50
*.MODEL CMOD CAP(C=1)
*.STEP LIN CAP CMOD(C) 1.0P 3.0P 1.0P
*This is a model for the transistor
.MODEL MOD1 NPN(BF=300)
*These are the program control commands that direct the analysis type
.TRAN 10.000N 20.000U 0 0
.PRINT TRAN V(13) V(12)
.END
```

Figure B.2. SPICE input model

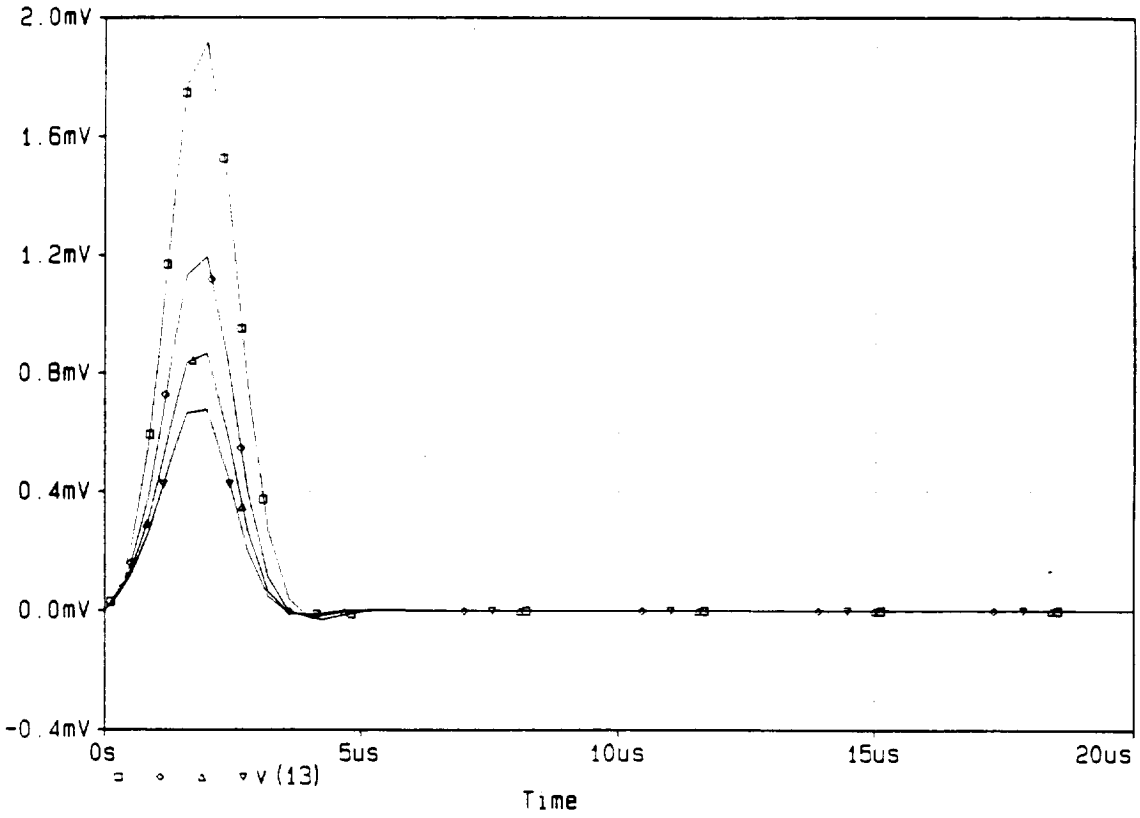

Figure B.3. Effect of increasing overheat on anemometer square wave response using OP-37

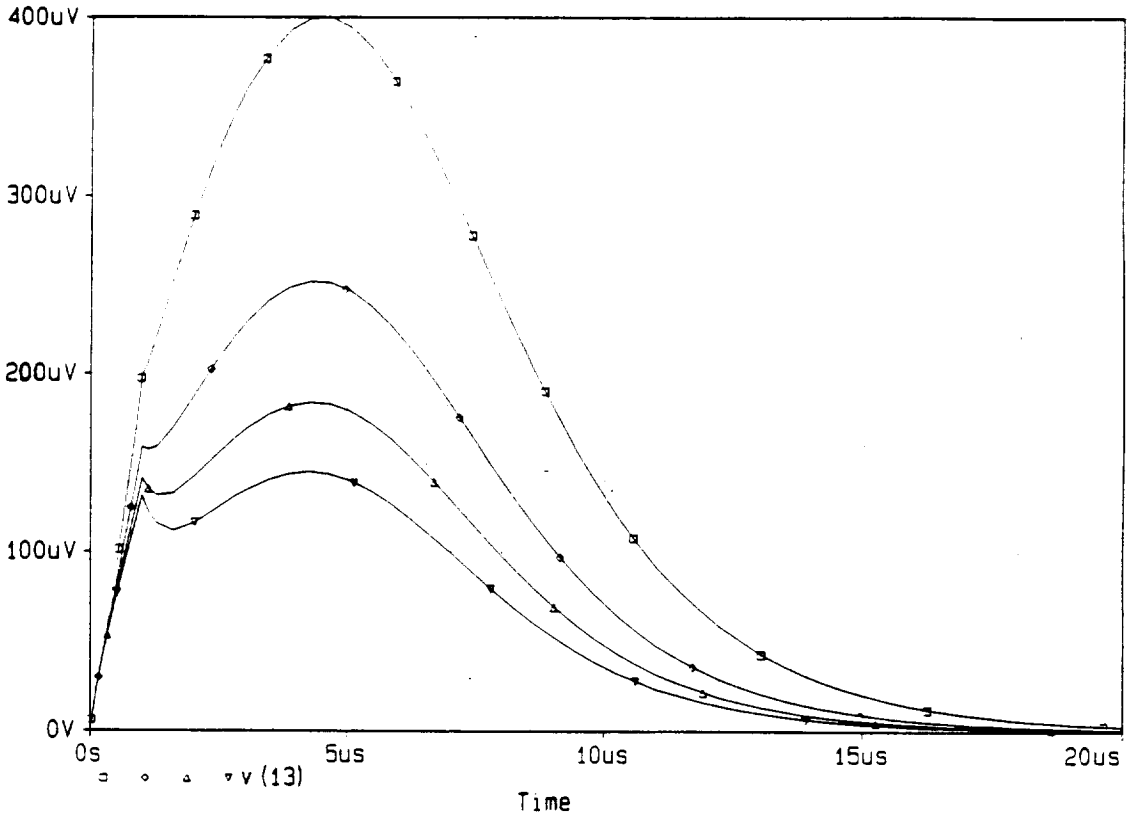

Figure B.4. Effect of increasing overheat on anemometer square wave response using OP-27

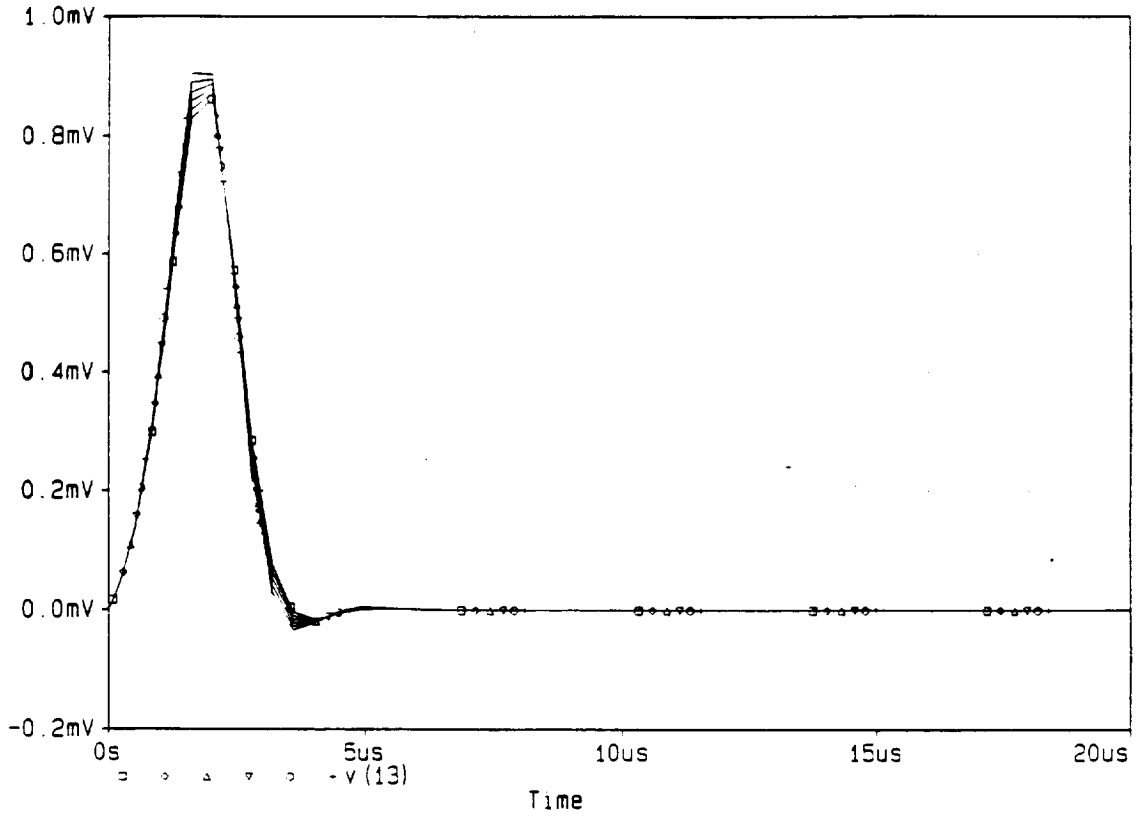

Figure B.5. Effect of controlling compensation to operational amplifier

Appendix C: Calibrations

Calibrations of the vital data acquisition instruments for this research are discussed and shown below in the following text.

C.1. Calibration Of The Validyne Pressure Transducer

A Validyne pressure transducer is used to monitor the pressure on the driver end of the shock tube. Because the rupture pressures for the Mylar in the shock tube do not exceed 20 psi, a 0-20 psi range diaphragm was installed in the Validyne in order to achieve the greatest pressure resolution. In order to calibrate the transducer, a Seegers pressure gauge was used in conjunction with a multimeter so that a relationship between output voltage from the transducer and gauge pressure could be drawn. The pressure was increased up to 20 psi and then decreased back down to 0 psi while taking data points in both directions. The hysteresis in the transducer was approximately 10 mV on the average. However, the hysteresis is unimportant in our transducer because we will only be interested in the pressure on the increasing leg of the calibration. This calibration was checked twice and then curve fitted to both first and second order polynomials. There was very little difference in the shape of the curves, so the first order curve was chosen to be sufficient. The pressure transducer calibration is:

$$\text{Pressure (psi)} = 4.756024\ (\text{Volts})$$

A plot of the experimental data along with the linear regression fit is shown in Figure C.1.

C.2. Calibration Of The Thermocouples

Two J-Type thermocouples (iron-constantan) are used as part of the data acquisition in the shock tube. One thermocouple is used to monitor the atmospheric

temperature, while the other thermocouple is used to monitor the temperature in the driver section of the shock tube during gas injection. It is assumed that gas is injected into the driver section at atmospheric temperature. However, there may be a decrease in the nitrogen temperature as the gas expands through the injection port. The J-Type thermocouples are hooked up with an Omega digital thermometer, but the calibration was checked against the freezing point and boiling point of water. The thermocouples were found to be accurate to a thermometer within 1 °C and the repeatability in a second calibration was identical. The calibrations for the thermocouples are given by:

$$\text{Atmospheric Thermocouple Temperature} = 0.99(\text{Digital Reading}) + 1.4$$

$$\text{Shock Tube Thermocouple Temperature} = 0.994(\text{Digital Reading}) + 1.0$$

Plots of the curve fits for both thermocouples are shown in Figure C-2.

C.3. Calibration Of The Skin Friction Sensors

It was necessary to calibrate the resistance of the skin friction sensors against temperature for two reasons. One reason was to provide the zero degree Celsius reference resistance, or what is called the cold resistance by most hot wire and hot film manufacturers so that all sensors could be referenced from a similar point for comparative purposes. The other reason was so that a sensor surface temperature could be defined for any operating point of the sensor. Applying an overheat sets an operating resistance for a sensor and knowing a sensors resistance can then give the operating temperature.

In order to perform the calibration, each sensor was placed on a Peltier heater and a thermistor was attached to the substrate near the sensor surface. Care was taken to minimize sensor exposure to convective currents and then a four-wire resistance

measurement of the sensor was made while moving the sensor through a temperature range of 0 to 90 degrees Celsius.

Plots of the predicted resistance trends, the experimental data for each sensor, and their corresponding linear regression fits are shown in the following seven figures. Table C.1 tabulates the calculated temperature coefficient of resistance for each sensor based on the experimental data.

Table C.1 Temperature coefficients of resistance for the sensors used in this research. For comparison typical values for nickel thin film TCR is 0.005 C^{-1} and nickel bulk TCR is 0.0067 C^{-1} (CRC Handbook of Chemistry and Physics)

Sensor Design	Lead Sensor TCR (C^{-1})	Rear Sensor TCR (C^{-1})
5 mil Glass	0.007396	N/A
10 mil Glass	0.006639	0.006082
20 mil Glass	0.005838	0.005227
20 mil Alumina	0.004478	0.004426
20 mil Aluminum	0.002830	N/A

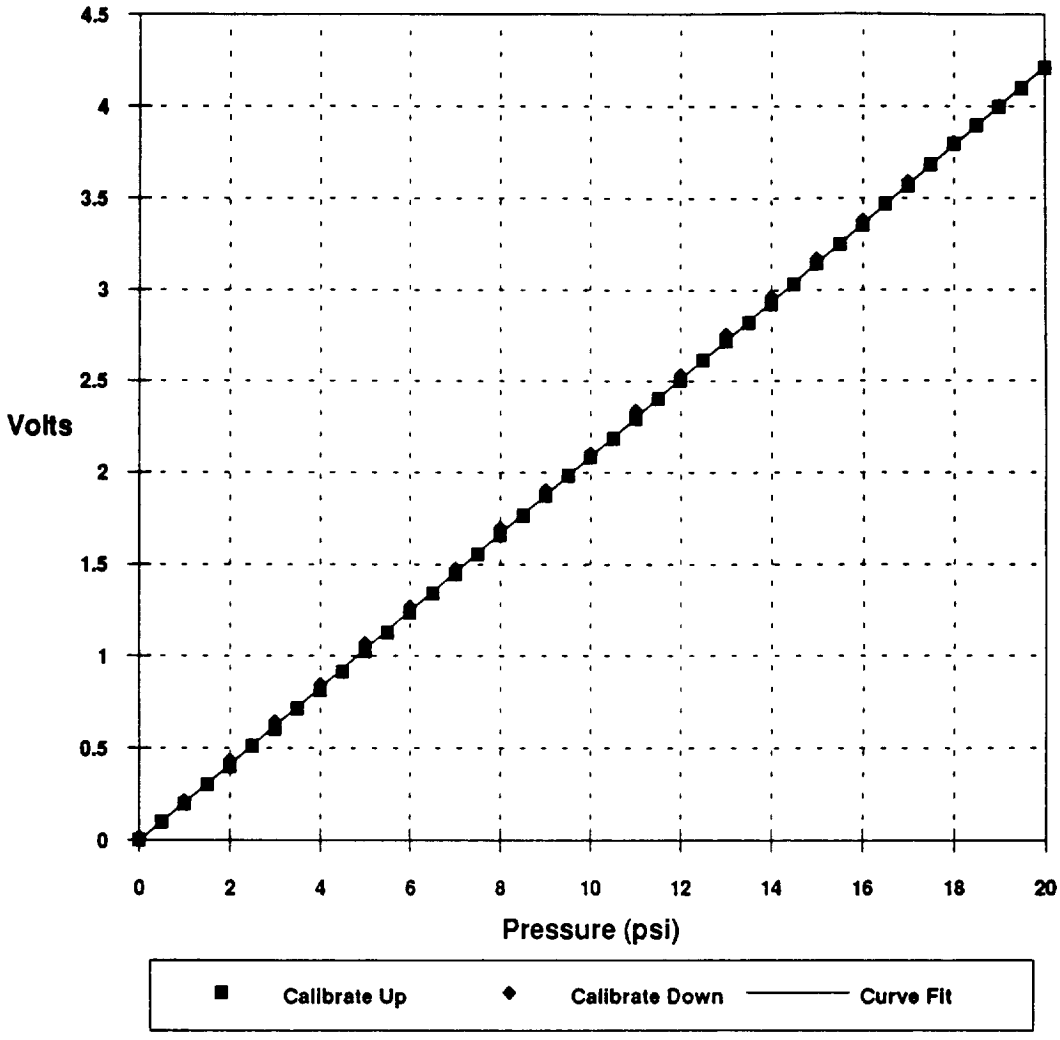

Figure C.1. Calibration of the pressure transducer used to monitor driver pressure

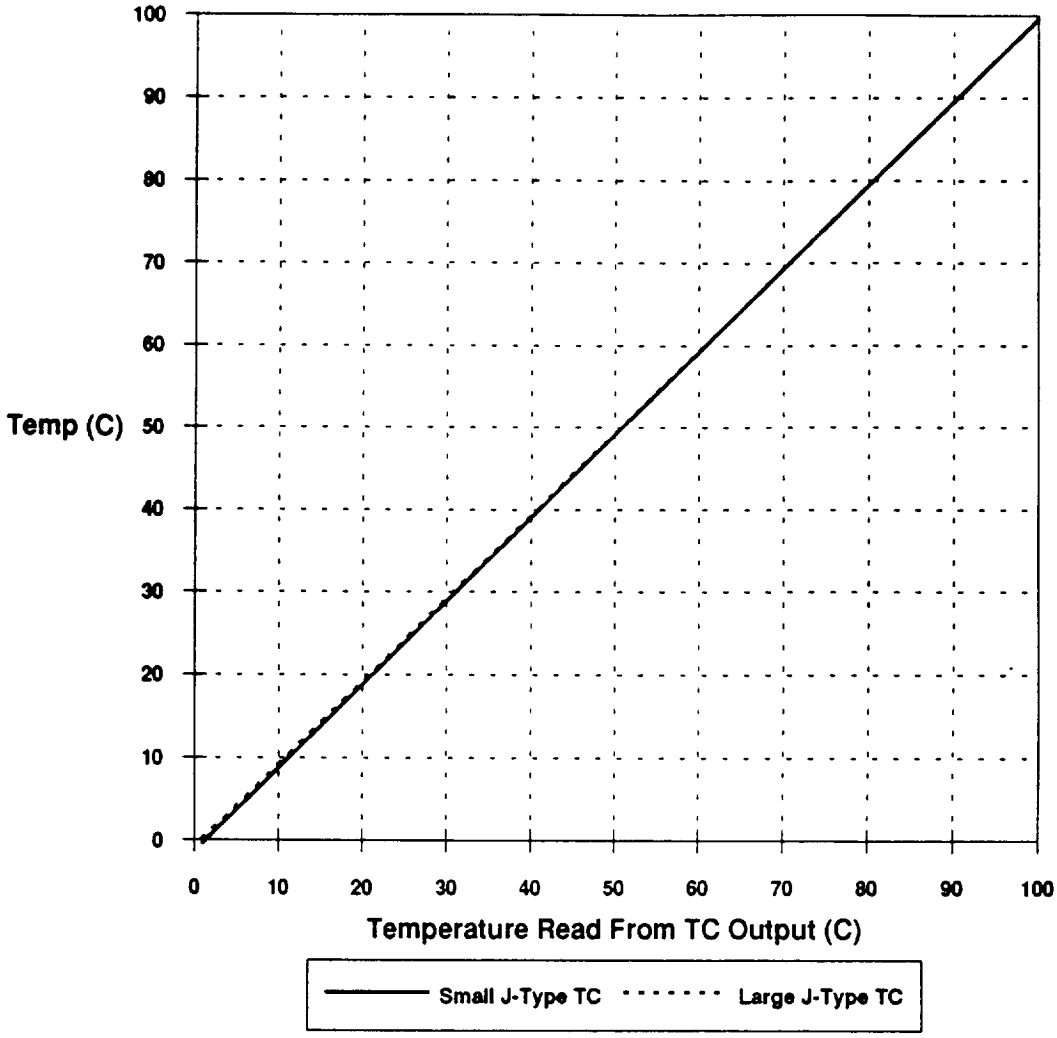

Figure C.2. Calibration of the thermocouples used to monitor shock tube and environmental temperature

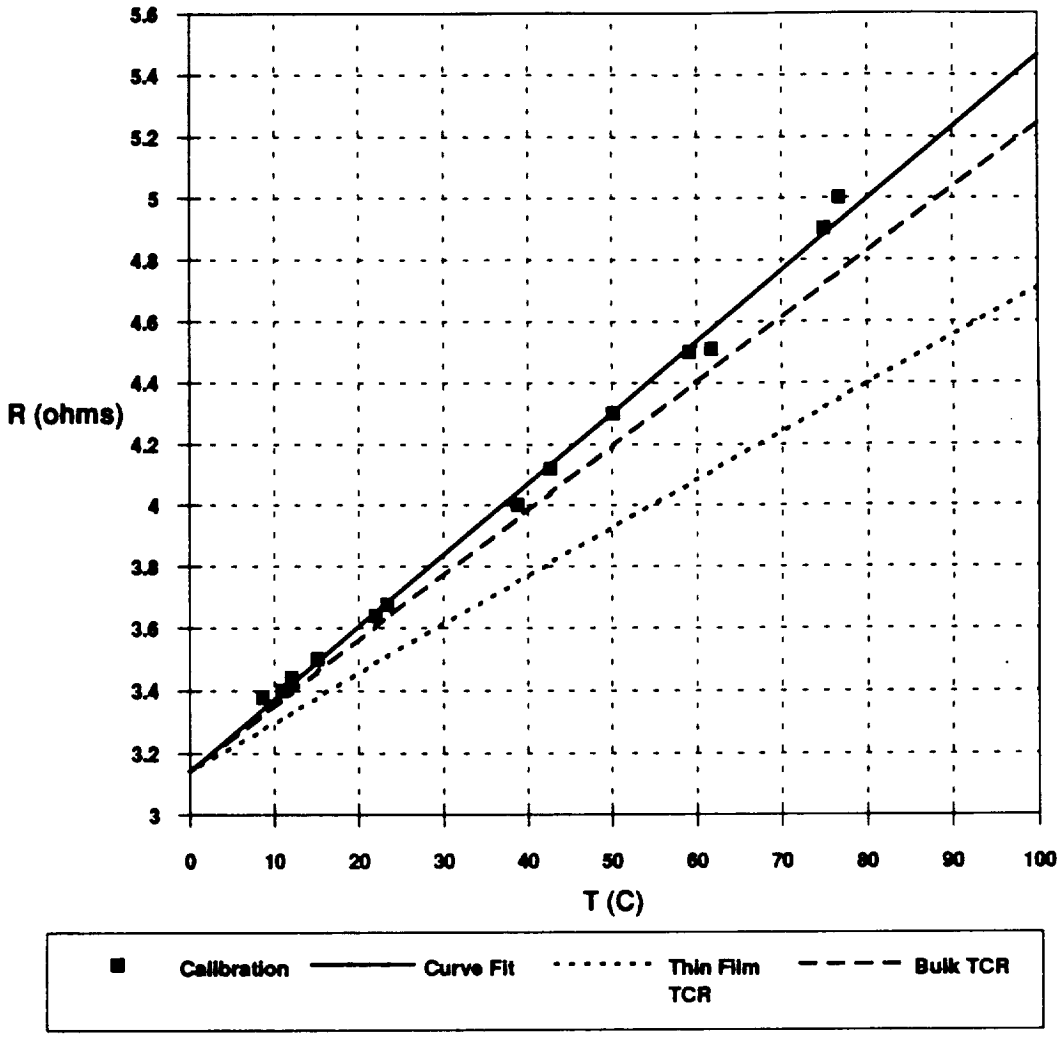

Figure C.3. Comparison of the theoretical and experimental thermal resistance calibration of 5 mil glass outer sensor

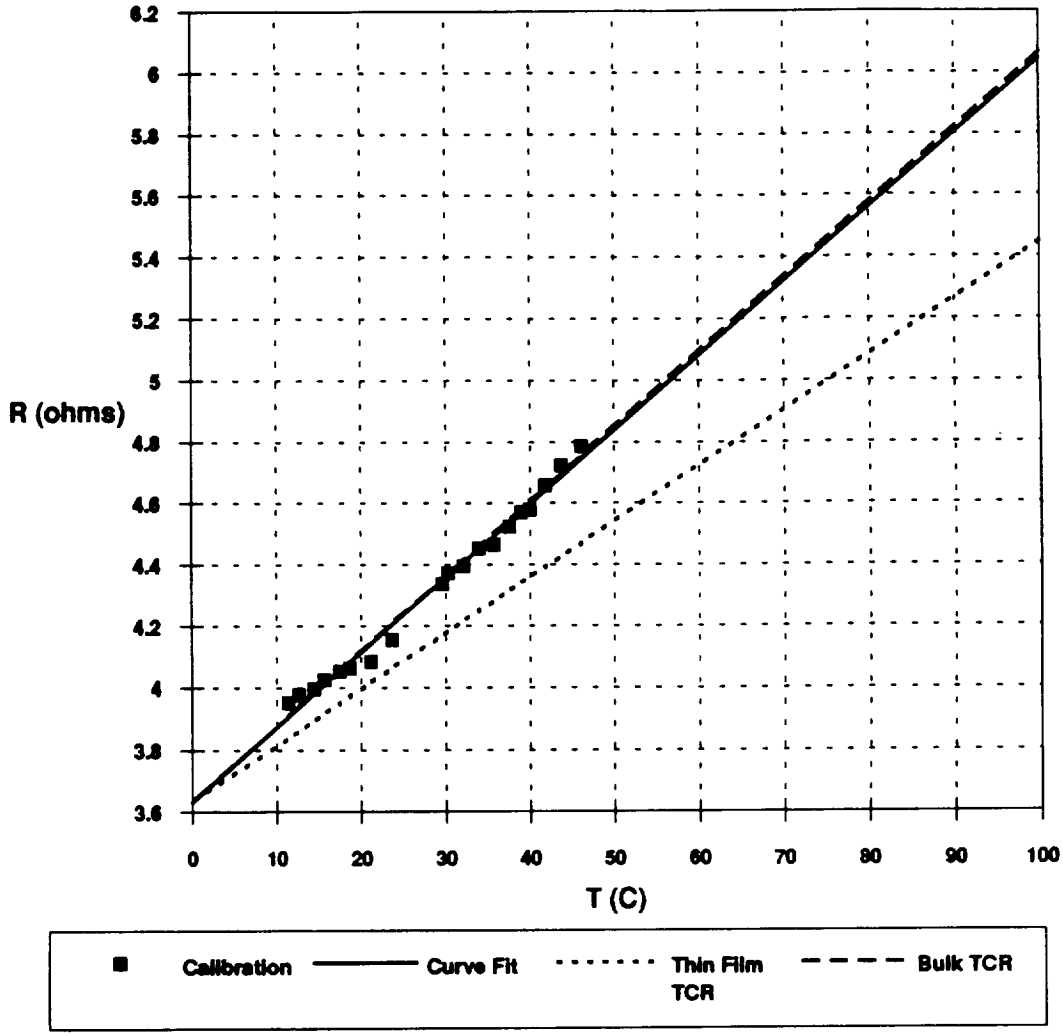

Figure C.4. Comparison of the theoretical and experimental thermal resistance calibration of 10 mil glass outer sensor

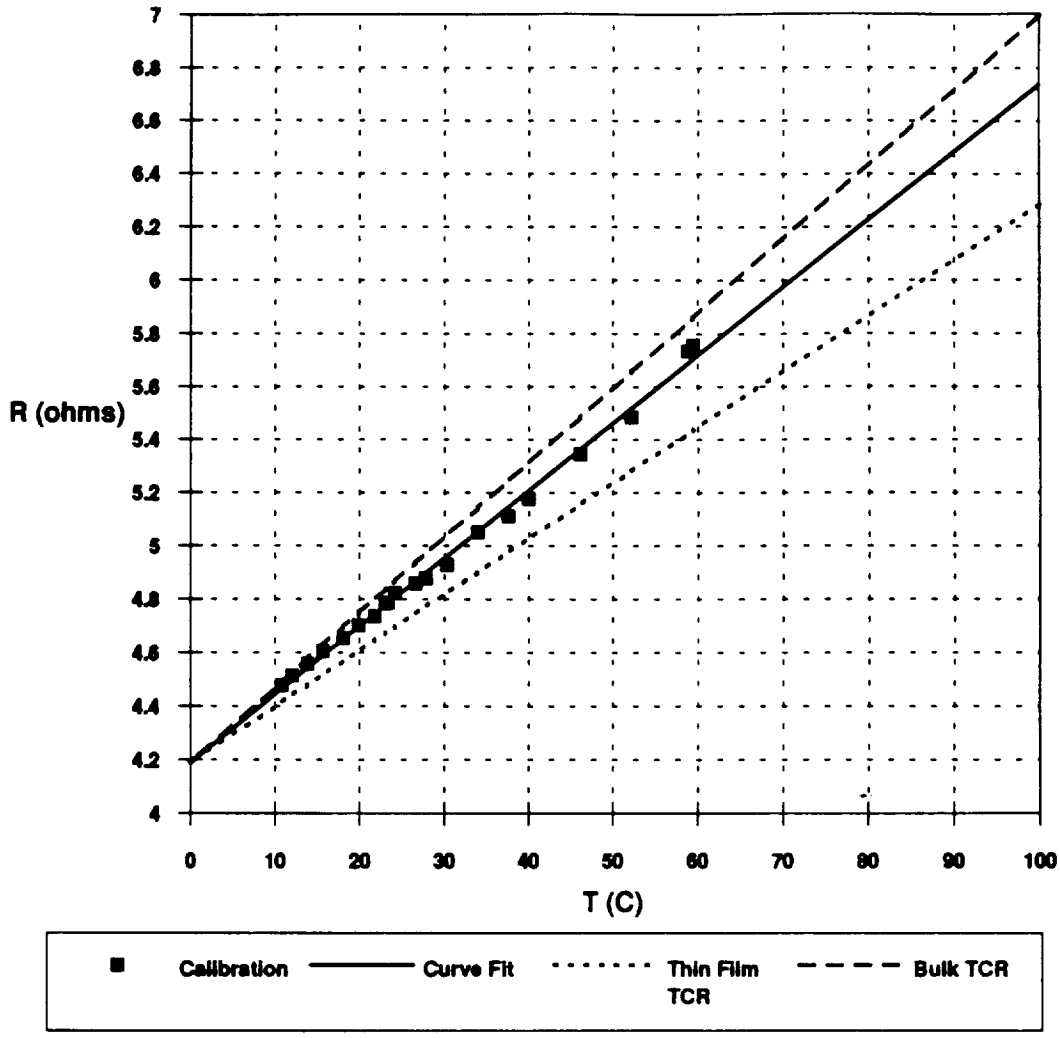

Figure C.5. Comparison of the theoretical and experimental thermal resistance calibration of 10 mil glass inner sensor

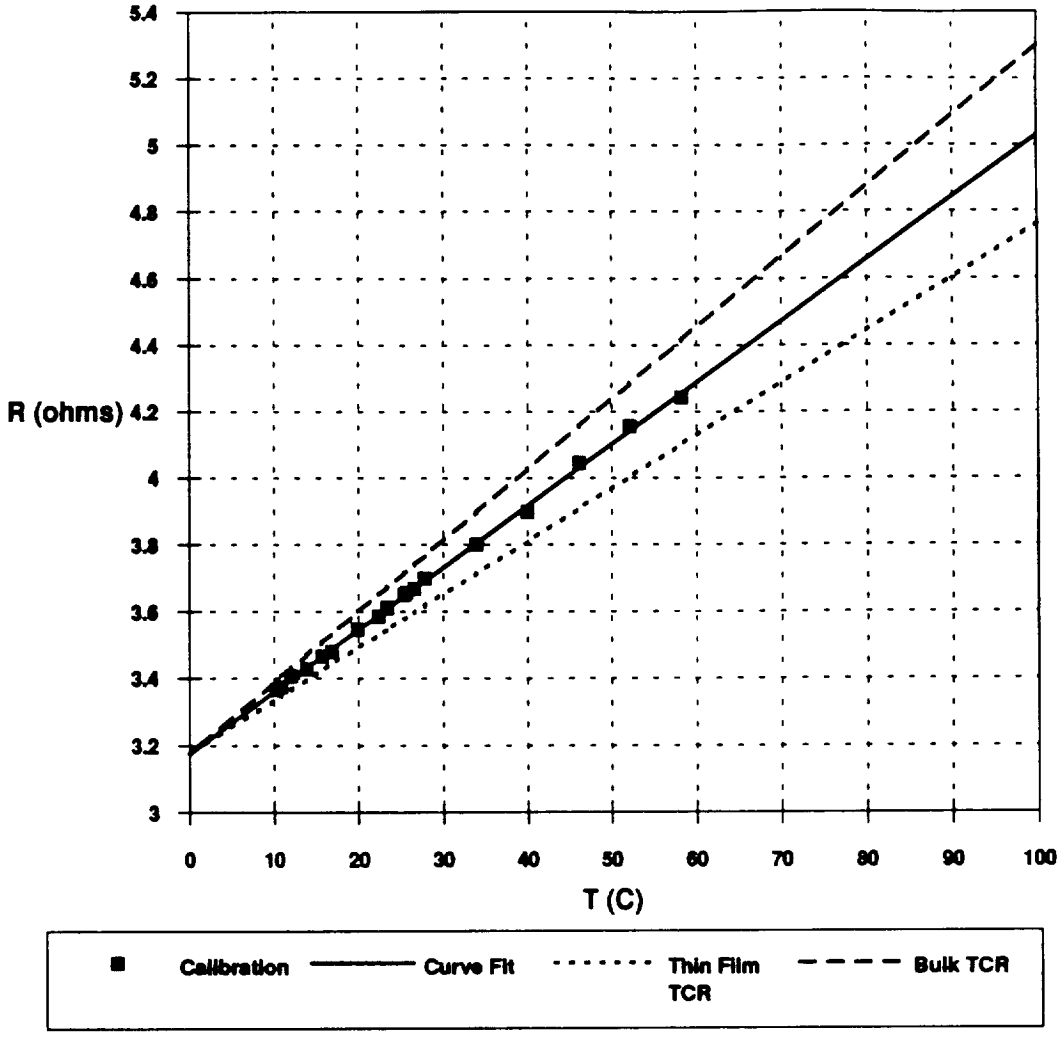

Figure C.6. Comparison of the theoretical and experimental thermal resistance calibration of 20 mil glass outer sensor

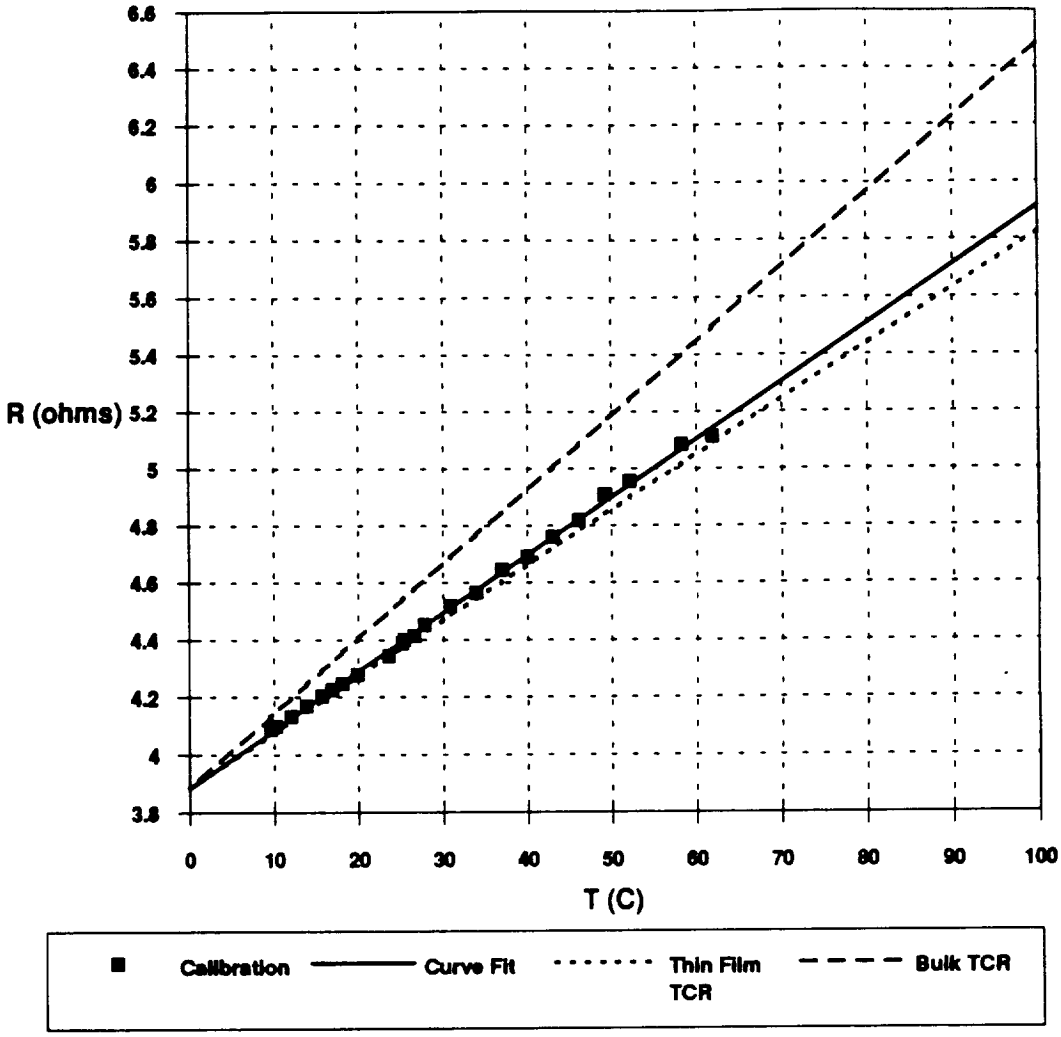

Figure C.7. Comparison of the theoretical and experimental thermal resistance calibration of 20 mil glass inner sensor

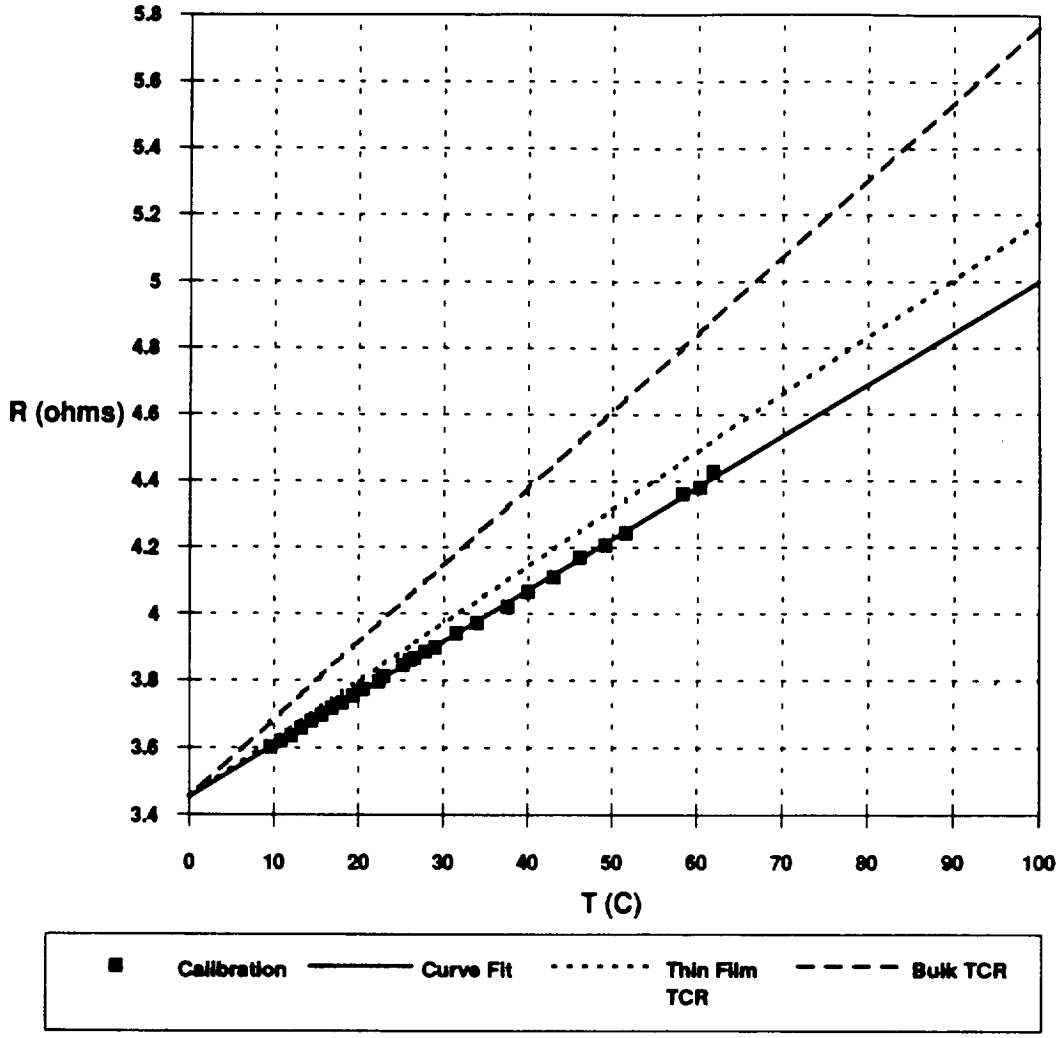

Figure C.8. Comparison of the theoretical and experimental thermal resistance calibration of 20 mil alumina outer sensor

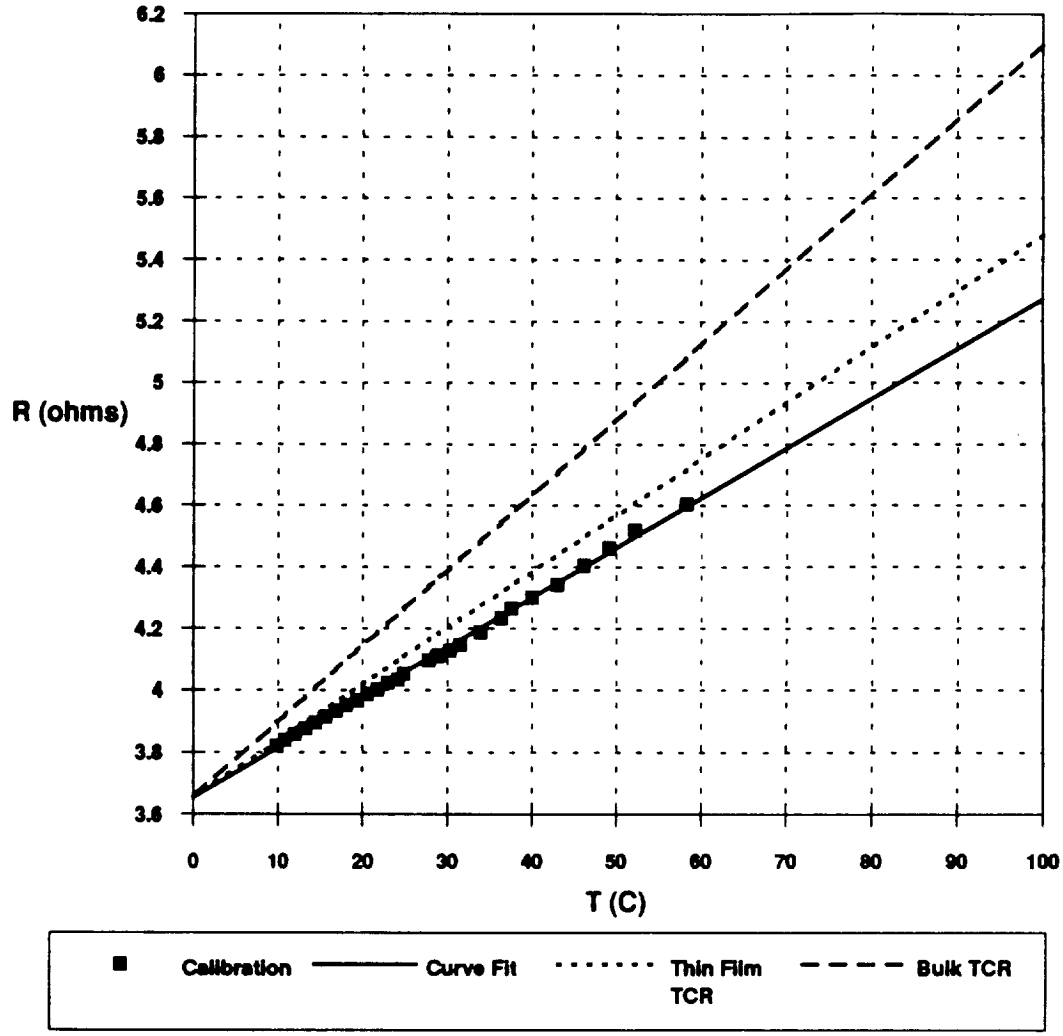

Figure C.9. Comparison of the theoretical and experimental thermal resistance calibration of 20 mil alumina inner sensor

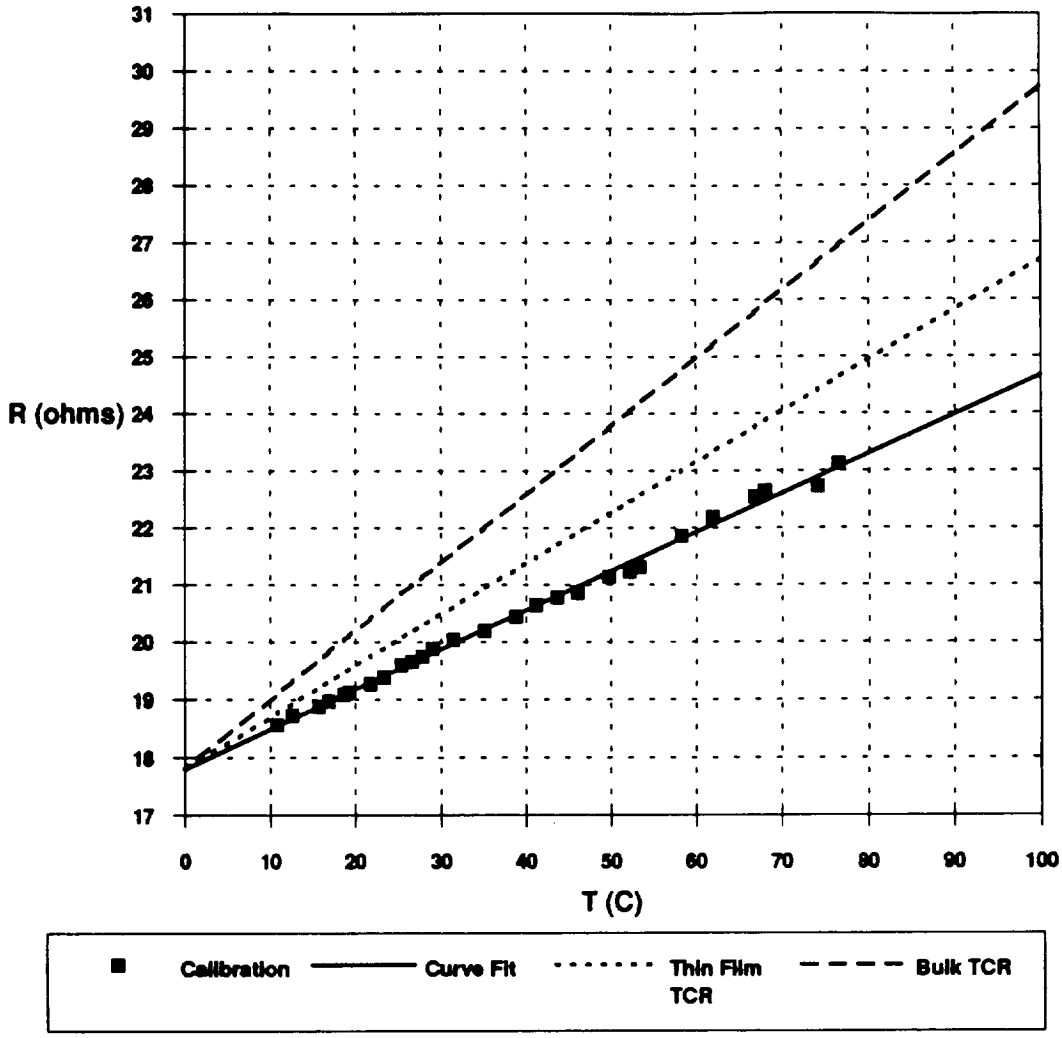

Figure C.10. Comparison of the theoretical and experimental thermal resistance calibration of 20 mil polyimide-aluminum outer sensor

Appendix D: Shock Analysis Program

In order to resolve data in the shock tube such as temperatures and velocities, a program is written based on normal shock relations in a shock tube. The only drawback of the code is that it does not account for attenuation of the shock. The use of the program is simple. It prompts the user to input the following:

Output file name: A filename is assigned and printed at the top of the output file for record keeping. Even though an output file name is assigned, the actual output is written to a file called "shock.dat"

Atmospheric pressure: This number should be typed in as mm Hg. It is the reference point for the other two pressure readings.

Atmospheric temperature: This number should be typed in as Kelvin. It is assumed that the driven end temperature is the same as the atmospheric temperature.

Driver pressure: The pressure transducer on the driver end of the shock tube is calibrated for psi gauge. Therefore the gauge pressure should be entered in psi.

Driver temperature: This number should be typed in as Kelvin. Generally, the driver temperature would be equal to the atmospheric temperature, but this input is available for when there is a slight change in the driver end temperature due to gas expansion during the charging of the driver section.

Driven pressure: A Heise gauge that reads in millimeters of mercury is used to record the driven end pressure. Therefore, this number should be typed in as mm Hg.

Once all of the data is entered, the program iterates for shock strength using an iterative method of bisections and generates a report of temperatures and velocities in the different regions of the shock tube during shock transit. The primary region of concern in this case is region 2, which is the region behind the shock.

Another shock program was written based on the first program to process a large variation in conditions for the shock tube. This was done in order to help choose what

conditions should be established in the shock tube to achieve the desired variation in flow velocity and shock strength. Figures D.1 and D.2 show trends in the shock strength and temperature behind the shock for different initial pressures in the driver and driven sections of the shock tube. Figure D.3 shows the variation of velocity behind the shock with the shock strength. Using these figures, approximate initial conditions can be determined for establishing the desired flow environment.

```
ccccccccccccccccccccccccccccccccccccccccccccccccccccccccccccccccccccccc
c                                                                      c
c   This program takes in the pressures and temperatures of the driver c
c   section and the driven section on the shock tube and generates a   c
c   report of pertinent information e.g. shock speed, strength, etc.   c
c   Written by Michael J. Moen 10-31-91.                               c
c                                                                      c
ccccccccccccccccccccccccccccccccccccccccccccccccccccccccccccccccccccccc
      implicit real(a-h,l-z)
      character*10 iname
      parameter(jmax=40,xacc=0.001)
      open(unit=4, file='shock.dat', status='unknown')
      print*, 'What is the output file name?'
      read*, iname
      print*, 'What is the atmospheric pressure (mm Hg)?'
      read*, pa
      print*, 'What is the atmospheric temperature (K)?'
      read*, ta
      print*, 'What does the driver pressure read (psi)?'
      read*, p4p
      p4=p4p+(14.696/760)*pa
      print*, 'What is the driver temperature (K)?'
      read*, t4
      print*, 'What does the driven pressure read (mm Hg)?'
      read*, p1p
      p1=p1p*(14.696/760)
      t1=ta
      gam1=1.4
      gam4=1.4
      R1=287.1
      R4=287.1
      a4=(gam4*R4*t4)**0.5
      a1=(gam1*R1*t1)**0.5
```

```
c    iterate for shock strength p2/p1
     x2=p4/p1
     x1=0.0
     fmid=(x2)*(1.0-((gam4-1.0)*(a1/a4)*(x2-1.0)/
    +    (((2.0*gam1)**0.5)*((2.0*gam1+(gam1+1.0)*
    +    (x2-1.0))**0.5))))**(2.0*gam4/(1.0-gam4))-(p4/p1)
     f=(x1)*(1.0-((gam4-1.0)*(a1/a4)*(x1-1.0)/
    +    (((2.0*gam1)**0.5)*((2.0*gam1+(gam1+1.0)*
    +    (x1-1.0))**0.5))))**(2.0*gam4/(1.0-gam4))-(p4/p1)
     if(f*fmid.ge.0.0) pause 'Root must be bracketed for bisection'
     if(f.lt.0.0)then
     rtbis=x1
     dx=x2-x1
     else
     rtbis=x2
     dx=x1-x2
     endif
     do 10 j=1,jmax
     dx=dx*0.5
     xmid=rtbis+dx
     fmid=(xmid)*(1.0-((gam4-1.0)*(a1/a4)*(xmid-1.0)/
    +    (((2.0*gam1)**0.5)*((2.0*gam1+(gam1+1.0)*
    +    (xmid-1.0))**0.5))))**(2.0*gam4/(1.0-gam4))-(p4/p1)
     if(fmid.le.0.0) rtbis=xmid
     if(abs(dx).lt.xacc.or.fmid.eq.0.0)then
     pstr=rtbis
     goto 11
     endif
  10 continue
     pause 'Too many bisections'
     goto 100
c    calculate shock values
  11 print*,'Shock Strength (p2/p1) = ',pstr
     print*,'Results are contained in file "shock.dat". Type "shout" to receive output.'
     ms=((gam1-1)/(2*gam1)+(gam1+1)*pstr/(2*gam1))**0.5
     m2=(1/gam1)*(pstr-1)*(pstr*((gam1+1)/(2*gam1)+(gam1-1)*pstr
    +  /(2*gam1)))**-0.5
     m3=(2/(gam4-1))*((((p4/p1)/pstr)**((gam4-1)/(2*gam4)))-1)
     t3=t4*(pstr/(p4/p1))**((gam4-1)/gam4)
     t2=t1*(1+pstr*(gam1-1)/(gam1+1))/(1+(gam1-1)/(pstr*(gam1+1)))
     u3=(2*a4)*(1-(pstr/(p4/p1))**((gam4-1)/(2*gam4)))/(gam4-1)
     u2=u3
     a2=u2/m2
     a3=u3/m3
     p2=pstr*p1
```

```
      p3=p2
      write(4,*),'Filename:  ', iname
      write(4,*),' '
      write(4,*),'Driving Pressure (psi) = ',p4
      write(4,*),'Driven Pressure (psi) = ',p1
      write(4,*),'Shock Strength (p2/p1) = ',pstr
      write(4,*),'Shock Mach = ',ms
      write(4,*),' '
      write(4,*),'Region 1'
      write(4,*),'--------'
      write(4,*),'Pressure (psi) = ',p1
      write(4,*),'Temperature (K) = ',t1
      write(4,*),'Sound Speed (m/s) = ',a1
      write(4,*),' '
      write(4,*),'Region 2'
      write(4,*),'--------'
      write(4,*),'Pressure (psi) = ',p2
      write(4,*),'Temperature (K) = ',t2
      write(4,*),'Sound Speed (m/s) = ',a2
      write(4,*),'Velocity (m/s) = ',u2
      write(4,*),'Mach = ',m2
      write(4,*),' '
      write(4,*),'Region 3'
      write(4,*),'--------'
      write(4,*),'Pressure (psi) = ',p3
      write(4,*),'Temperature (K) = ',t3
      write(4,*),'Sound Speed (m/s) = ',a3
      write(4,*),'Velocity (m/s) = ',u3
      write(4,*),'Mach = ',m3
      write(4,*),' '
      write(4,*),'Region 4'
      write(4,*),'--------'
      write(4,*),'Pressure (psi) = ',p4
      write(4,*),'Temperature (K) = ',t4
      write(4,*),'Sound Speed (m/s) = ',a4
  100 stop
      end
```

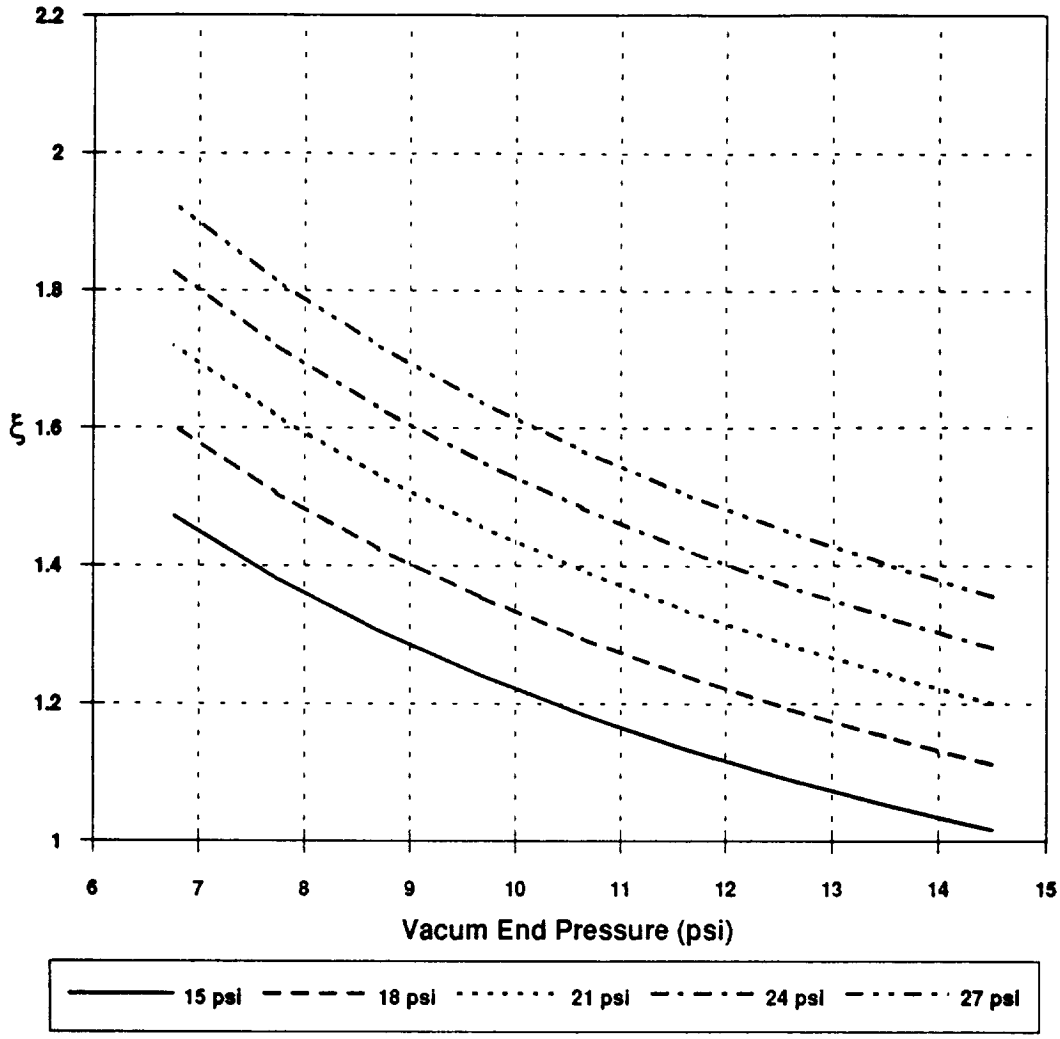

Figure D.1. Trends in shock strength for different initial driver and driven pressures

C-3

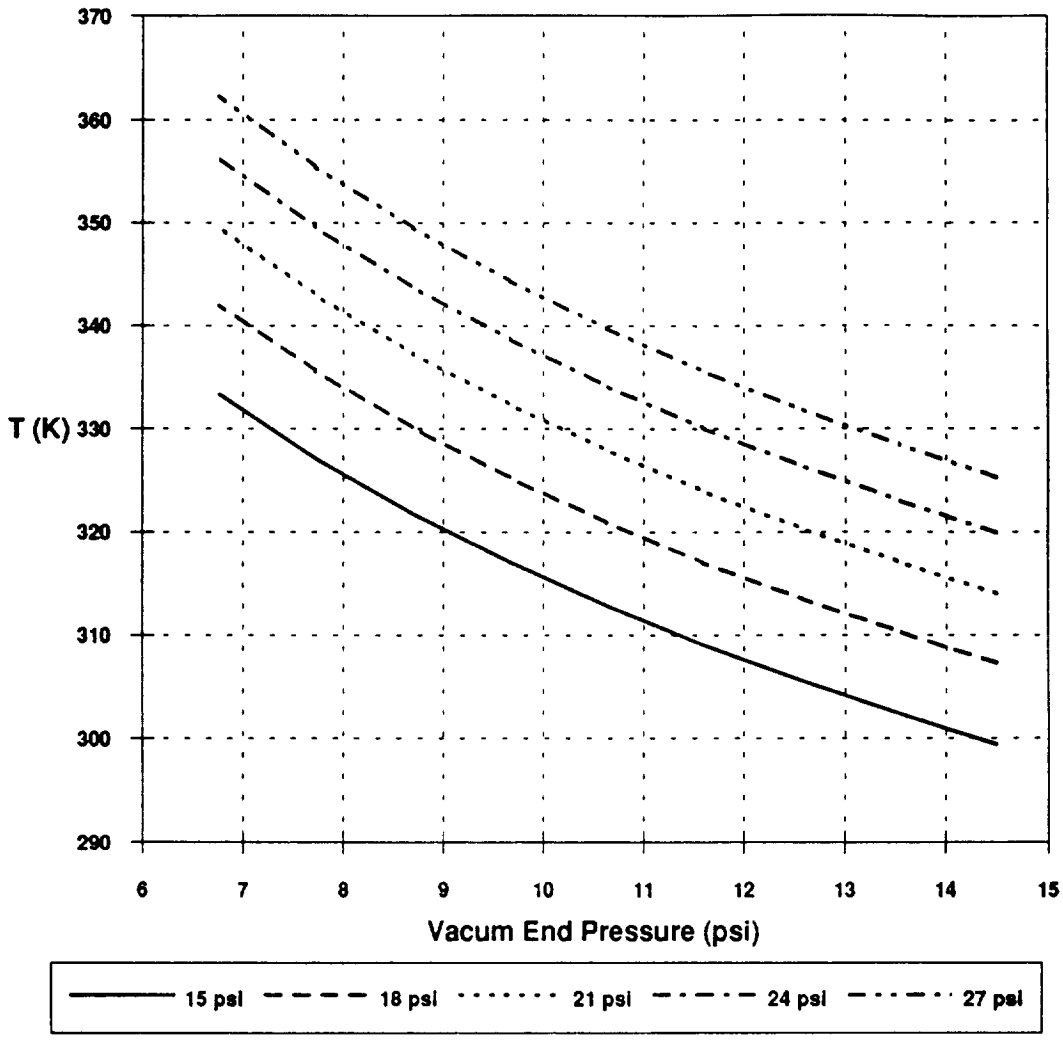

Figure D.2. Trends in temperature behind shock for different initial driver and driven pressures

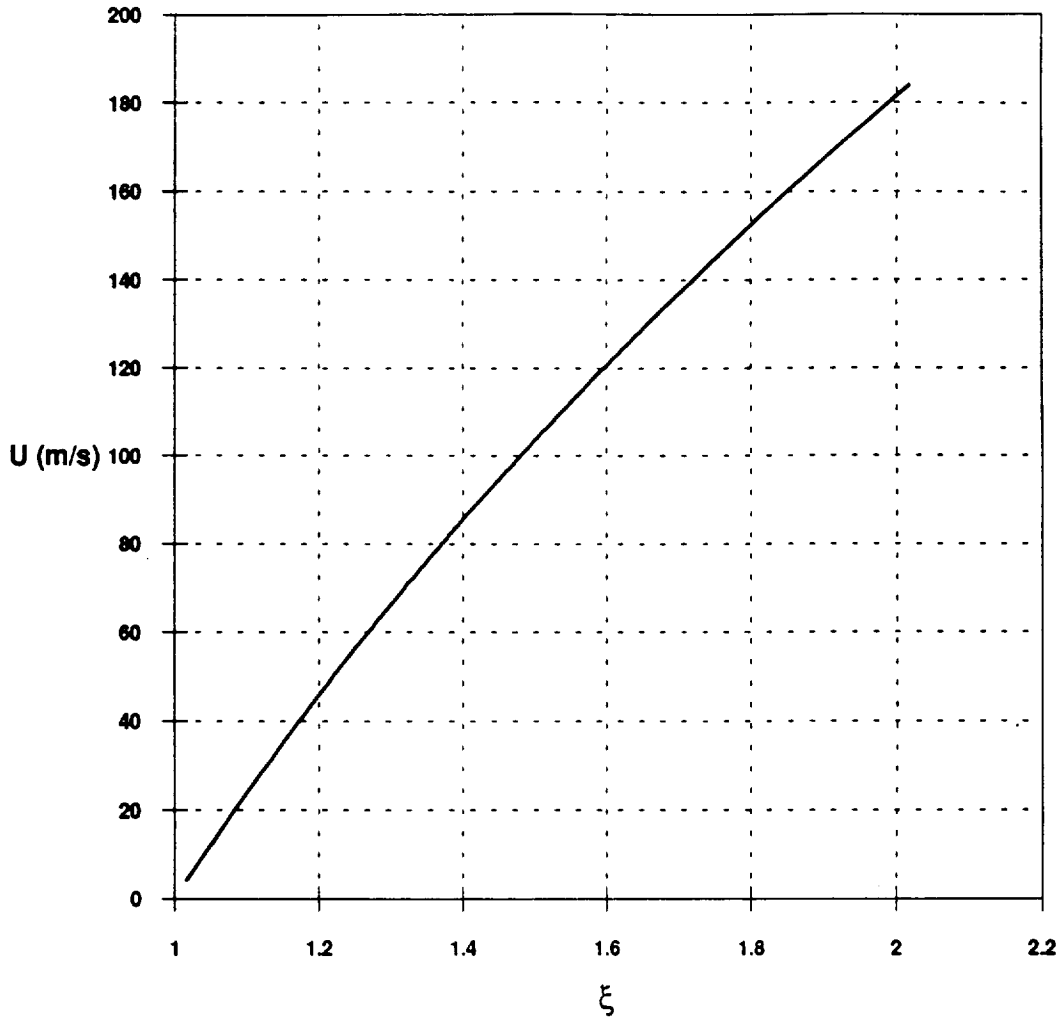

Figure D.3. Dependency of velocity behind shock on shock strength

Appendix E: Shock Tube Runs

The following pages contain information on the quality of the shock tube runs that were used in the sensor analysis. Each case was analyzed with the shock code and compared against the actual values that were measured. This point of comparison was in the shock velocity. Figure E.1 shows the deviation between the experimental and theoretical shock velocities for a number of the cases. For most of the cases, the error was less than one percent, which was deemed acceptable for this work. In only a few cases was the error greater than one percent, but in no cases was it greater than four percent.

Another issue was the repeatability of the signal for a given shock wave. This criteria was checked before the bulk of the testing. Figure E.2 shows two similar strength shocks passing over the thin film sensor. The response is nearly identical for the two shocks with exception to the later part of the response, which may be deemed turbulent boundary layer. At about 0.3 milliseconds, a phenomena arises in which the signal "bounces". This is believed to be due to the design of the sensor support where a geometric step exists in the juncture between the sensor and the mount. A pressure surge is fed back upstream into the subsonic region behind the shock wave after the shock wave passes over the step on the sensor mount. Only after all necessary data was taken was the mount redesigned by removing most of the step. The mount was then tested in similar flow situations as had been established for the experimental data. Figure E.3 shows an identical sensor before and after the mount redesign. The redesigned sensor mount shows a significantly decreased "bounce" in the signal, which seems to prove that the step on the sensor mount was the cause of the unexpected flow fluctuation.

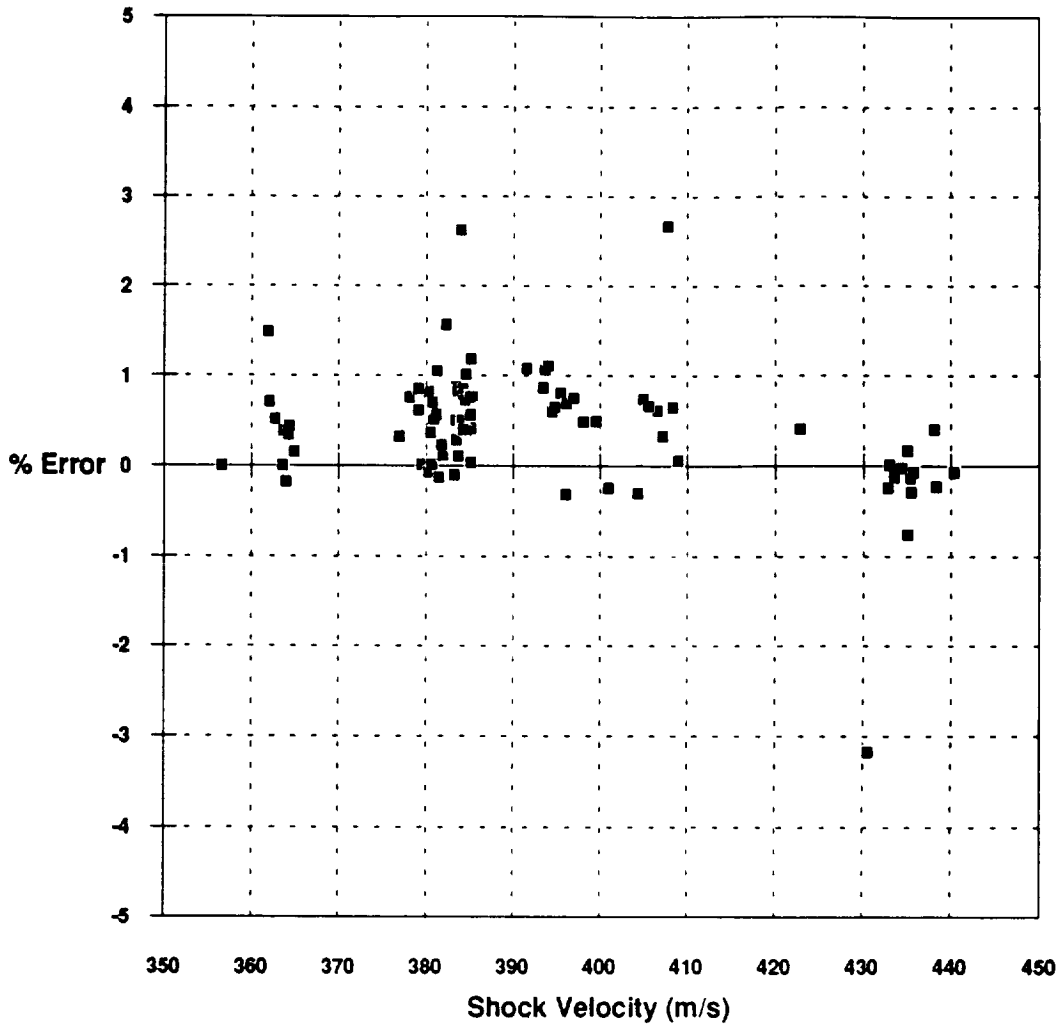

Figure E.1. Error between experimental and theoretical shock velocities established in the shock tube

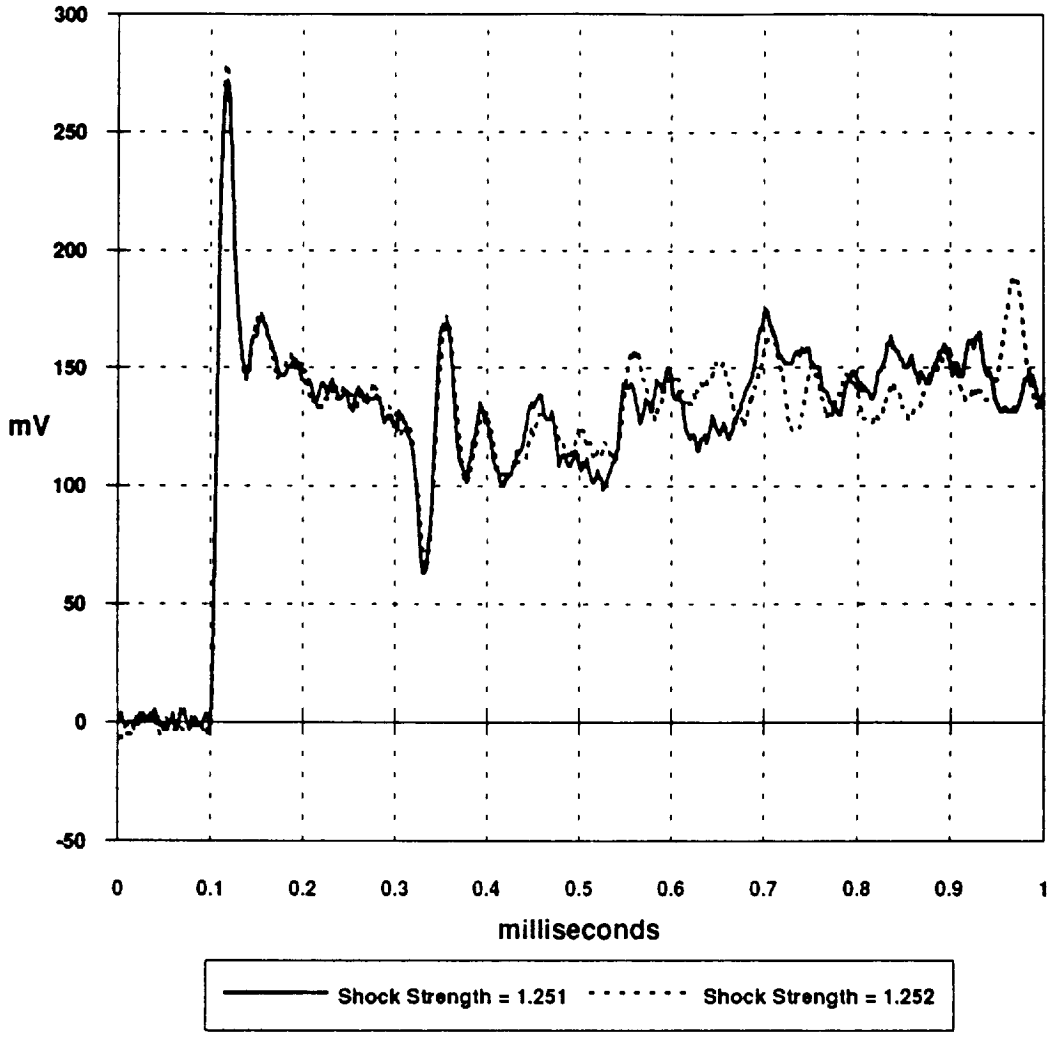

Figure E.2. Repeatability of anemometer signal for near identical shock events

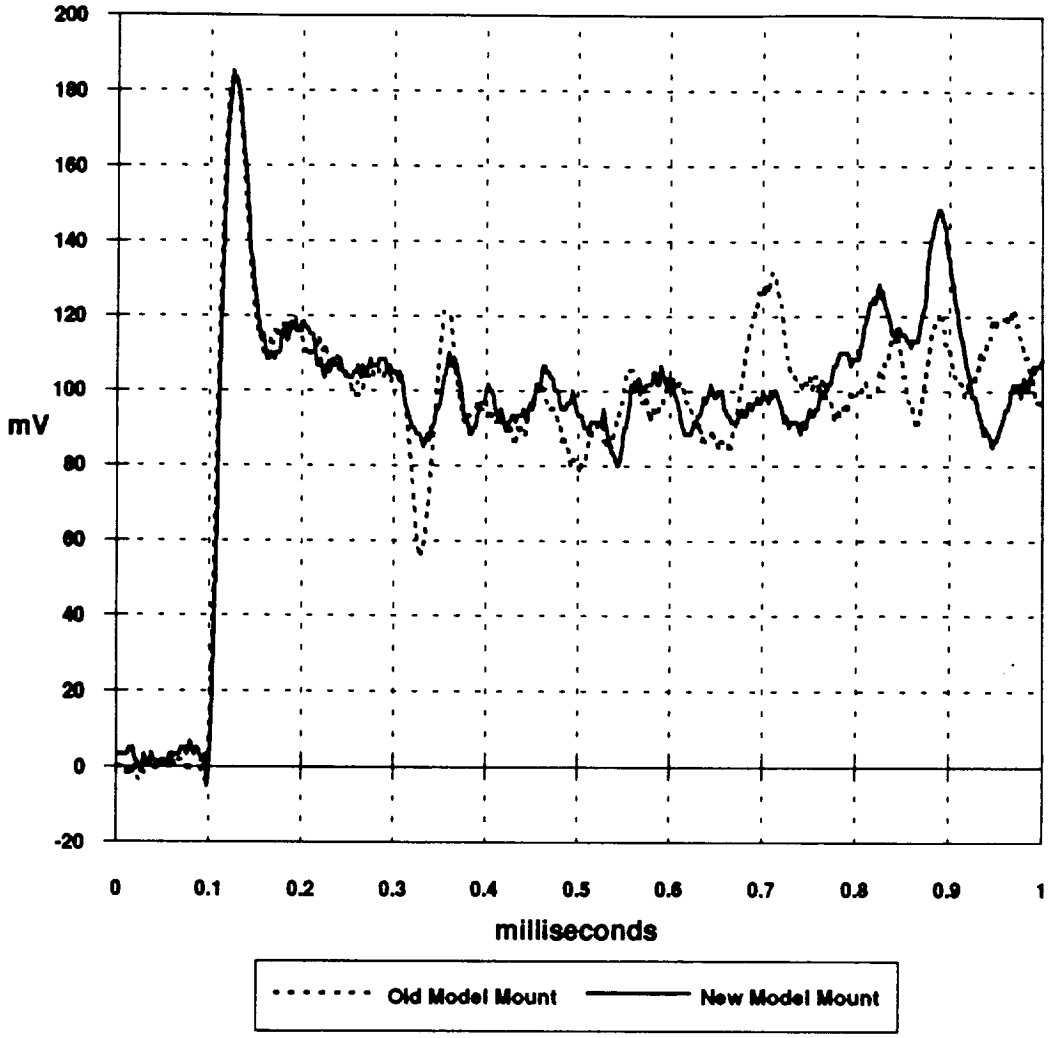

Figure E.3. Reduction of flow anomaly by redesigning sensor base plate mount

Appendix F: Shock Thickness Estimation

When it comes to shock waves, the shock front is generally treated as a discontinuity where properties "jump" to different values. In this simplified case, the Rankine-Hugoniot equations are used to describe and analyze the jump. As shocks become weaker, the thickness of the shock front increases, but the Rankine-Hugoniot relations can still be used to describe the jump in properties. However, when the dimension of an object that is being tested in a shock tube becomes very small, then it might be of interest to consider the shock front as a case of continuum flow. This is the case with the sensors used in this research, so to ensure that the shock structure will not interfere with the sensor analysis, a classical shock analysis for continuum flow is consulted to estimate the shock thickness.

The classical shock analysis for continuum flow first defines a key parameter that is referred to as the fundamental gasdynamic derivative. This can be found from the relationship for the velocity change that occurs along a fluid streamline.

$$udu + vdP = 0 \qquad (1)$$

As pressure changes there is a corresponding change in the speed of sound

$$dP = \left(\frac{dP}{dc^2}\right)_s dc^2 \qquad (2)$$

where the speed of sound can also be written as

$$c^2 = \left(\frac{\partial P}{\partial \rho}\right)_s = -v^2 \left(\frac{\partial \rho}{\partial v}\right)_s = \frac{-v^2}{(\partial v / \partial \rho)_s} \qquad (3)$$

If the derivative of (3) is taken with respect to P, then the following equation is found.

$$\left(\frac{\partial c^2}{\partial P}\right)_s = 2v\left(\frac{c^4}{2v^3}\left(\frac{\partial^2 v}{\partial P^2}\right)_s - 1\right) \tag{4}$$

Within (4), the following term in equation (5) is referred to as the fundamental gas dynamic derivative.

$$\frac{c^4}{2v^3}\left(\frac{\partial^2 v}{\partial P^2}\right)_s = \Gamma \tag{5}$$

Further manipulation shows that Γ can also be stated as

$$\Gamma = \frac{v^3}{2c^2}\left(\frac{\partial^2 P}{\partial v^2}\right)_s = \frac{1}{c}\left(\frac{\partial R}{\partial \rho}\right)_s \tag{6}$$

where R is called the acoustic impedance defined as

$$R = \rho c \tag{7}$$

Since the shock waves used to calibrate the sensor will be weak shock waves, a weak shock approximation is used to estimate the shock thickness. Certain criteria should be satisfied to fit the definition of a weak shock. These are

$$\frac{P_2 - P_1}{\rho_1 c_1^2} << 1.0 \tag{8a}$$

$$-\frac{u_2 - u_1}{c_1} << 1.0 \tag{8b}$$

$$-\frac{v_2 - v_1}{v_1} << 1.0 \tag{8c}$$

It should also be noted that the entropy change for a weak shock wave is at best only one-third the order of magnitude of the pressure differential across the shock. Therefore, the entropy change is negligible for the weak shock approximation. Although these criteria should be met, certain shocks may still be treated as weak even if some of the requirements are strained such as

$$\frac{P_2 - P_1}{\rho_1 c_{1^2}} = 0.50 \tag{9}$$

To estimate the shock thickness, the shock is held in a stationary (observer moving with shock) reference frame, and the flow is treated as one-dimensional. It is also assumed that the shock thickness, D, is small compared to the shock front curvature, R. Furthermore, the fluid is assumed to be in equilibrium meaning that it may be treated with the linear transport equations. Finally, the phenomena of thermal radiation and diffusion within the shock are neglected. The governing equations are written from the one-dimensional Navier-Stokes equations.

Continuity:
$$\frac{\partial(\rho u)}{\partial x} = 0 \tag{10a}$$

Momentum:
$$\rho u \frac{\partial u}{\partial x} + \frac{\partial P}{\partial x} - \frac{\partial}{\partial x}\left(\frac{4}{3}\mu' \frac{\partial u}{\partial x}\right) = 0 \tag{10b}$$

Energy:
$$\rho u \frac{\partial}{\partial x}\left(h + \frac{u^2}{2}\right) - \frac{\partial}{\partial x}\left(\frac{4}{3} u\mu' \frac{\partial u}{\partial x}\right) - \frac{\partial}{\partial x}\left(k \frac{\partial T}{\partial x}\right) = 0 \tag{10c}$$

where

$$\frac{4}{3}\mu' = \frac{4}{3}\mu + \mu_v \tag{11}$$

If the three governing equations are integrated once and set equal to some arbitrary constants, they become

Continuity: $$\rho u = C_1 \tag{12a}$$

Momentum: $$\rho u^2 + P - \frac{4}{3}\mu' \frac{\partial u}{\partial x} = C_2 \tag{12b}$$

Energy: $$h + \frac{u^2}{2} - \frac{4}{3}\frac{\mu'}{\rho}\frac{\partial u}{\partial x} - \frac{k}{\rho u}\frac{\partial T}{\partial x} = C_3 \tag{12c}$$

The applicable boundary conditions are

At $x = -\infty$:		At $x = \infty$:	
	$u = u_1$		$u = u_2$
	$\mu = \mu_1$		$\mu = \mu_2$
	$P = P_1$		$P = P_2$
	$\rho = \rho_1$		$\rho = \rho_2$
	$\frac{\partial u}{\partial x} = 0$		$\frac{\partial u}{\partial x} = 0$
	....		....

(13)

Now, returning to the equation for momentum with the boundary conditions at $x = -\infty$, it becomes

$$\rho_1 u_1^2 + P_1 = C_2 \tag{14}$$

so that

$$\rho_1 u_1^2 + P_1 = \rho u^2 + P - \frac{4}{3}\mu' \frac{\partial u}{\partial x} \tag{15}$$

or this can be written as

$$-\frac{4}{3}\mu' \frac{\partial u}{\partial x} = (P_1 - P) + \rho_1 u_1^2 - \rho u^2 \tag{16}$$

and taking continuity at x = -∞ results in

$$\rho_1 u_1 = C_1 \tag{17}$$

so that the momentum equation can be written as

$$-\frac{4}{3}\mu' \frac{\partial u}{\partial x} = (P_1 - P) + \rho_1 u_1 (u_1 - u) \tag{18}$$

In order to evaluate the equations, it is necessary to define a point within the shock structure at which the equations will be evaluated. The midpoint of the slope of the velocity curve that defines the shock structure is used as follows.

$$u = u_1 + \frac{u_2 - u_1}{2} \tag{19}$$

In addition, the shock thickness is defined as

$$\Delta_m = \frac{u_2 - u_1}{u_x} = \frac{u_2 - u_1}{\partial u / \partial x} \tag{20}$$

Now, pressure is calculated by going back to continuity. Continuity is written in terms of the specific volume

$$u = \frac{C_1}{\rho} = C_1 v \tag{21}$$

so that at the midpoint for evaluation, the velocity relationship can be written as

$$v = v_1 + \frac{u_2 - u_1}{2C_1} \tag{22}$$

Now pressure, P(v,s), can be expanded around its thermodynamic variable such that

$$P - P_1 = \left(\frac{\partial P}{\partial v}\right)_s (v - v_1) + \frac{1}{2}\left(\frac{\partial^2 P}{\partial v^2}\right)_s (v - v_1)^2 + \left(\frac{\partial P}{\partial s}\right)_v (s - s_1) + \quad \ldots \tag{23}$$

Because this is a weak shock estimation, all terms for v - v_1 higher than the second order term are eliminated. In addition, all terms that involve a change in the entropy are dropped for reasons explained earlier. Therefore, equation (21) becomes

$$P - P_1 = \left(\frac{\partial P}{\partial v}\right)_s (v - v_1) + \frac{1}{2}\left(\frac{\partial^2 P}{\partial v^2}\right)_s (v - v_1)^2 \tag{24}$$

Using continuity again, this can be written as

$$P - P_1 = \left(\frac{\partial P}{\partial v}\right)_s \frac{(u_2 - u_1)}{2\rho_1 u_1} + \left(\frac{\partial^2 P}{\partial v^2}\right)_s \frac{(u_2 - u_1)^2}{8\rho_1^2 u_1^2} \tag{25}$$

If a substitution is made using the gas dynamic derivative, equation (23) becomes

$$P - P_1 = -\rho_1 c_1^2 \frac{(u_2 - u_1)}{2u_1} + \rho_1 c_1^2 \Gamma_1 \frac{(u_2 - u_1)^2}{4u_1^2} \tag{26}$$

Now this expression may be substituted in for the pressure into the momentum equation to yield

$$-\frac{4}{3}\mu'\frac{\partial u}{\partial x}=\rho_1 c_1^2\frac{(u_2-u_1)}{2u_1}-\rho_1 c_1^2\,\Gamma_1\frac{(u_2-u_1)^2}{4u_1^2}+\rho_1 u_1(u_1-u) \tag{27}$$

Then additional substitutions are made using the shock thickness definition and the shock Mach number which results in

$$-\frac{8}{3}\frac{\mu'}{\rho_1 c_1\Delta_m}=\frac{1}{M_{1n}}-M_{1n}-\frac{\Gamma_1(u_2-u_1)}{2M_{1n}^2 c_1} \tag{28}$$

Now, if the weak shock condition is used that says

$$-\frac{(u_2-u_1)}{c_1}=\frac{2(M_{1n}-1)}{\Gamma_1} \tag{29}$$

then equation (26) further simplifies to

$$\frac{8}{3}\frac{\mu'}{\rho_1 c_1\Delta_m}=M_{1n}-\frac{1}{M_{1n}^2} \tag{30}$$

but for weak shock waves, it may be said that

$$\frac{1}{M_{1n}^2}=1 \tag{31}$$

and for dilute gases, the viscosity may be approximated as

$$\mu'=\rho c\Lambda=\rho_1 c_1\Lambda_1 \tag{32}$$

so that the thickness relation becomes

$$\frac{8}{3}\frac{\Lambda_1}{\Delta_m} = M_{1n} - 1 \tag{33}$$

and the final weak shock thickness approximation is stated as

$$\frac{\Delta_m}{\Lambda_1} = \frac{8}{3(M_{1n} - 1)} \tag{34}$$

Figure F.1 plots the shock front thickness against the Mach number for air at standard conditions ($\Lambda = 6.6 \times 10^{-8}$ m). The weakest shock wave that was used as data had a Mach number of 1.05. Even in the case of smallest sensor tested at this Mach number, the sensor has a streamwise length approximately 40 times greater than the shock front thickness. Therefore, the shock thickness is not a concern in regards to affecting the data quality.

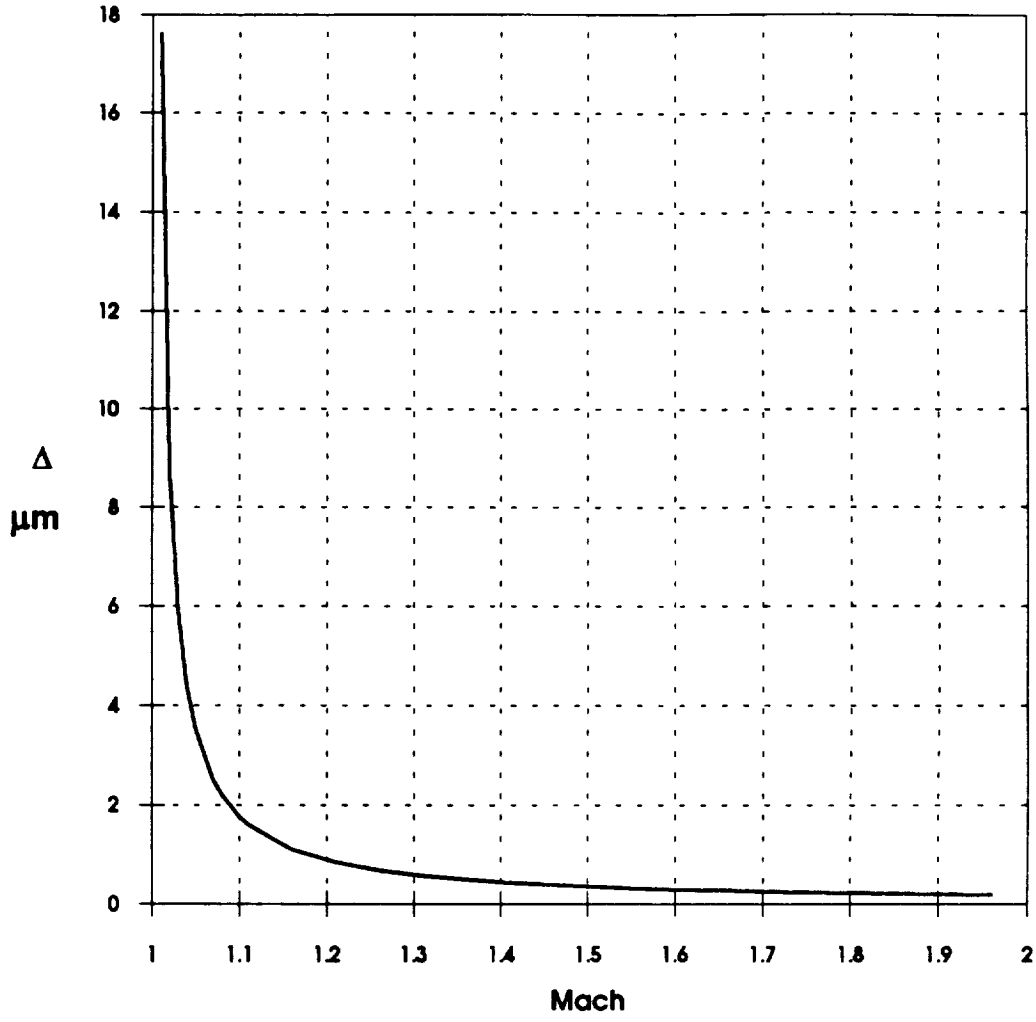

Figure F.1. Shock front thickness for normal shock wave advancing into stagnant fluid at standard conditions

Appendix G: Data Acquisition Program Source Code

Below is the text of the data acquisition program written for the Gould (DSO) 400 digital oscilloscope in the BASIC language. This program is capable of reading a channel of stored digital data from a triggered event.

```
' Written by Michael J. Moen.
' This program will download raw data from the Gould 400.
' The scope must be set for the following:
'
'   (1) 9600 Baud, 8 Data Bits, 1 Stop and No Parity.
'   (2) Download Data in Binary Mode
'
'
'-------------------------------------------------------
'
'          Starts off main program
'
KEY OFF
OPEN "com1:9600,n,8,1,cs0,ds0" FOR RANDOM AS #1
OPTION BASE 0
DIM ch1%(501), vdat(501), tim(501)
vb = 30
tb = 50
refave = 128
con1:
GOSUB menu:
con2:
answer$ = INKEY$
IF answer$ = "" THEN GOTO con2:  ELSE choice = VAL(answer$)
IF choice < 1 OR choice > 6 THEN BEEP: GOTO con1:
ON choice GOSUB display, ref, set, down, plot, done
GOTO con1:
'
' -------------------------------------------------------
'
menu:           'Prints the main menu
'
CLS : SCREEN 0, 1: WIDTH 80
LOCATE 2, 17: COLOR 15, 0: PRINT "Gould (DSO) 400 Data Retrieval Program"
LOCATE 3, 17: PRINT "-------------------------------------"
COLOR 7, 0
```

```
LOCATE 5, 18: PRINT "(1) Display Scope Status"
LOCATE 7, 18: PRINT "(2) Set Ground Reference For Output"
LOCATE 9, 18: PRINT "(3) Specify Time And Voltage Base"
LOCATE 11, 18: PRINT "(4) Download Data From Channel 1"
LOCATE 13, 18: PRINT "(5) Show Preliminary Plot"
LOCATE 15, 18: PRINT "(6) Exit"
LOCATE 18, 18: PRINT "Please enter choice [ 1 to 6 ]";
LOCATE 21, 28: COLOR 15, 0: PRINT "Statistics:"
LOCATE 22, 28: PRINT "----------"
COLOR 7, 0
LOCATE 24, 13: PRINT "Voltage Base = "; vb; " Time Base = "; tb; " Ground = ";
refave
RETURN
'
' ---------------------------------------------------------
'
display:          'Displays scope error status
'
CLS : SCREEN 0, 1: WIDTH 80
buffer = LOC(1)
IF buffer > 0 THEN dummy$ = INPUT$(LOC(1), 1)
PRINT #1, "ST?"
FOR delay = 1 TO 1000: NEXT delay
buffer = LOC(1)
IF buffer = 0 THEN
BEEP: LOCATE 4, 4: PRINT "Comm Problem - Try Again You Bobo": GOTO con3:
END IF
scope.data$ = INPUT$(LOC(1), 1)
IF scope.data$ <> "ST?=0" THEN
LOCATE 4, 4: PRINT "Error Free - Ready For Transfer"
ELSE
LOCATE 4, 4: PRINT "Scope Error - Check The Following"
LOCATE 7, 4: PRINT "Scope Set At 9600 Baud, 8 Data Bits, 1 Stop and No Parity"
LOCATE 9, 4: PRINT "Download Data in Binary Mode"
LOCATE 11, 4: PRINT "Block Length = 0"
END IF
con3:
LOCATE 16, 4: PRINT " Hit any Key to Continue ";
con4:
answer$ = INKEY$
IF answer$ = "" THEN GOTO con4:
RETURN
'
' ---------------------------------------------------------
'
```

```
ref:          'Sets ground reference to subtract from data file
WIDTH 80: CLS
header$ = "": comma.flag% = 0
refave = 128
'
LOCATE 4, 5: PRINT "Please Choose Ground Reference Option:"
LOCATE 6, 5: PRINT "(1) Use Default Ground Reference For Output File"
LOCATE 8, 5: PRINT "(2) Establish Ground Reference For Output File"
LOCATE 10, 5: PRINT "(3) Specify Ground Reference For Output File"
LOCATE 12, 5: INPUT "Select (Default = 1):  ", none%
IF none% = 2 THEN
LOCATE 16, 5: PRINT "Program Establishing Ground Reference"
LOCATE 17, 5: PRINT "Please Stand By..."
'
PRINT #1, "ST1"              'send command
FOR delay = 1 TO 2000: NEXT delay
'
'                       Read Header
con8:
char$ = INPUT$(1, 1)
IF char$ = "," THEN comma.flag% = comma.flag% + 1
IF comma.flag% = 2 THEN GOTO con7:
header$ = header$ + char$
GOTO con8:
'                       Read Transfer Format
con7:
format$ = INPUT$(2, 1)
IF format$ <> "#B" THEN BEEP: RETURN
'                       Read Transfer Amount
amount$ = INPUT$(2, 1)
'                       Read Data Samples
sum = 0
FOR sample% = 1 TO 500
ch1%(sample%) = ASC(INPUT$(1, 1))
sum = sum + ch1%(sample%)
NEXT sample%
dummy$ = INPUT$(LOC(1), 1)
refave = sum / 500
GOTO con9
ELSEIF none% = 3 THEN
LOCATE 16, 5: PRINT "Please Specify Point To Be Used For Ground Reference"
LOCATE 18, 5: INPUT "Point (8 to 248):  ", refave
ELSE
refave = 128
END IF
```

```
con9:
RETURN
'
' ------------------------------------------------------------
'
set:        'Sets oscilloscope time and voltage base to create output file
WIDTH 80: CLS
header$ = "": comma.flag% = 0
'
LOCATE 4, 5: PRINT "Please Specify Oscilloscope Voltage Base"
LOCATE 6, 5: INPUT "Volts/Division:  ", vb
LOCATE 9, 5: PRINT "Please Specify Oscilloscope Time Base"
LOCATE 11, 5: INPUT "Time/Division:  ", tb
RETURN
'
' ------------------------------------------------------------
'
down:       'Downloads data from CH1 to a data file
'
WIDTH 80: CLS
header$ = "": comma.flag% = 0
'
LOCATE 4, 5: INPUT "Enter name of data file to create"; file$
OPEN file$ FOR OUTPUT AS #8
LOCATE 10, 5: PRINT "Downloading Data From The Scope"
LOCATE 12, 5: PRINT "Please Standby ...";
'
PRINT #1, "ST1"             'send command
FOR delay = 1 TO 1000: NEXT delay
'
'                   Read Header
con6:
char$ = INPUT$(1, 1)
IF char$ = "," THEN comma.flag% = comma.flag% + 1
IF comma.flag% = 2 THEN GOTO con5:
header$ = header$ + char$
GOTO con6:
'                   Read Transfer Format
con5:
format$ = INPUT$(2, 1)
IF format$ <> "#B" THEN BEEP: RETURN
'                   Read Transfer Amount
amount$ = INPUT$(2, 1)
'                   Read Data Samples
xs = 0
```